
# Turbulence model and Immersed Boundary method development in TELEMAC-3D for offshore structure modelling

Yue YIN

*School of Engineering, University of Liverpool*

March 2017

# Abstract

In recent years, increased evidences suggest that offshore structures such as wind farms, tidal turbine farms, piles of bridge and breakwater have great impact on the hydrodynamics and hence may have a strong influence on the sediment transport at a site. The open-source hydrodynamic suite of software TELEMAC has been used for the study of such environmental influence around Unite Kingdom. However, the use of the 3-D version of the software, TELEMAC-3D is restricted by how structures are accounted for in the meshes, as water columns have the same number of layers all over the domain. Moreover, a large scale farm has a large impact on turbulence mixing in the coastal regional scale, and this is not properly understood. The PhD project focuses on 3-D hydrodynamics and development of an 3-D unstructured capability using an immersed boundary method to account for obstacles in the flow. Two large eddy simulation models (the 2eddy LES model and the Wall-adapted Large Eddy model) have been incorporated into TELEMAC-3D to get a more realistic and effective representation of the turbulence mixing and to account for the unsteadiness of the flow past the structures. The simulations have been performed using High Performance Computing to enable large scale applications using TELEMAC-3D and fine spatial and temporal resolutions in 3-D. The implementations carried out in the code are fully parallel. The numerical models have been validated for two laboratory scale cases, including the flow around a circular cylinder and the flow over a submerged structure. Then a far-field simulation at the southern North Sea has been carried out, where the hydrodynamics and morphological impacts of the London Array offshore wind turbine farm have been investigated. The numerical results of turbulence model implementation indicate that both turbulence models have good performance in the representation of the flow past a cylinder in laboratory scale. However in the large scale application, only the 2eddy LES

model is successfully applied because the WALE model relies on a very fine mesh in the vertical direction. The implementation of IBM suggested that when dealing with an obstacle going from the bottom though the surface of the water, the immersed boundary method offers good accuracy in the prediction of surrounding flow structures. For the submerged obstacles, they can be simulated by TELEMAC-3D by implementing the Immersed Boundary method. Although the accuracy is limited currently, qualitative analysis can still be performed.

# Acknowledgements

I would like to express my sincere thanks to my primary supervisor, Dr. Ming Li who has given me a lot of advice in hydrodynamics, sediment transport modelling and also to write the thesis. I would also like to show my sincere gratitude to my second supervisor, Dr. Charles Moulinec for his guidance and continuous support throughout the whole PhD project especially in programming and in High Performance Computing. I am also grateful to all my colleagues at STFC Daresbury Laboratory including Prof. David R. Emerson, Dr. Xiaojun Gu, Dr. Malgorzata Zimon, Dr. Stefano Rolfo, Dr. Jianping Meng and Dr. Jian Fang for their great help in learning about numerical methods.

I also would like to thank EPSRC and EDF Energy, who, through an iCASE studentship supported this study. The technical support from the Computing Services of the University of Liverpool and from the Hartree Centre were also greatly appreciated.

Finally, I do like to thank my parents and my wife. My family gave me a lot of support both materially and mentally. I really appreciated my wife's good cooking skills and her warm care.

# Contents

# List of Figures

# List of Tables

# Nomenclature

| | |
|---|---|
| $\Delta\rho$ | Variation of density |
| $\Delta t$ | Time step |
| $\delta_{ij}$ | Kronecker symbol |
| $\eta$ | Water surface elevation |
| $\eta^{n+1}$ | Water surface elevation in the new time step |
| $\eta^{n}$ | Water surface elevation in the last time step |
| $\nu$ | Dynamic viscosity |
| $\nu_(t,h)$ | Horizontal turbulence viscosity |
| $\nu_(t,v)$ | Vertical turbulence viscosity |
| $\nu_t$ | Turbulence viscosity |
| $\Omega_{ij}$ | Rotation rate tensor |
| $\overline{S}_h$ | The strain rate tensor for horizontal direction |
| $\overline{S}_v$ | The strain rate tensor for vertical direction |
| $\rho$ | fluid density |
| $\rho_0$ | reference density |
| $\theta_{u_1}$ | Implicitation coefficient for the velocity |
| $\vec{n}$ | Normal vector to the walls |

| | |
|---|---|
| $\vec{U}$ | Velocity vector |
| $\vec{w_s}$ | Sediment settling velocity |
| $A_b$ | Bed load coefficients |
| $A_s$ | Suspended load coefficients |
| $C$ | Mass conservation for a tracer |
| $C_D$ | Quadratic drag coefficient |
| $C_h$ | Coefficient of the 2eddy LES model in horizontal direction |
| $C_s$ | Coefficient of the Smagorinsky model |
| $C_v$ | Coefficient of 2eddy LES model in vertical direction |
| $C_w$ | Coefficient of WALE turbulence model |
| $d_{50}$ | Median grain diameter |
| $d_{90}$ | Grain diameter for which 90% of the grains by mass are finer |
| $F_{x_i}$ | Source term |
| $f_{x_i}^{ibm}$ | Immersed Boundary forces |
| $Fr$ | Froude number |
| $g$ | Gravity acceleration |
| $g_{ij}$ | Velocity gradient tensor |
| $h$ | Water depth |
| $i_p$ | The number of $i^t h$ layers |
| $L_h$ | The length-scale for horizontal direction |
| $L_v$ | The length-scale for vertical direction |
| $n_p$ | Total number of the layers |

| | |
|---|---|
| $p$ | Pressure |
| $p_d$ | Dynamic pressure |
| $p_h$ | Hydrostatic pressure |
| $p_{atm}$ | Atmosphere pressure |
| $Q_b$ | Sand transport rate of bed load |
| $Q_s$ | Sand transport rate of suspended load |
| $Re$ | Reynolds number |
| $S_{ij}$ | Strain rate tensor of the filtered velocities |
| $t$ | Time |
| $u_0$ | Orbital velocity of the waves |
| $u_i$ | i=1,2,3 the velocity components along Cartesian coordinates |
| $u_i^b$ | i=1,2,3 the velocity components at the bottom |
| $u_i^C$ | Velocity components obtained from advection step |
| $u_i^n$ | Velocity components in the last time step |
| $u_i^n$ | Velocity components of the last time step |
| $u_i^s$ | i=1,2,3 the velocity components on the surface |
| $u_i^{hyd}$ | Velocity components of hydrostatic step |
| $u_i^{n+1}$ | Velocity components in the new time step |
| $u_{cr}$ | Critical entrainment velocity |
| $x_3^*$ | Vertical spatial component in transformed mesh |
| $x_i$ | i=1,2,3 the Cartesian components |
| $Z_b$ | Bottom elevation |
| $Z_s$ | Free surface elevation |

# Chapter 1

# Introduction

With the rapid expansion of the offshore marine energy industry, it has become important for coastal engineers to be able to predict the impact of the construction of structures on offshore waves, tides and sediment transport.

For instance, as one of the typical offshore structures, offshore wind turbine farms (OWF) get more and more interesting nowadays due to the highly increasing demand in renewable energy sources. More than 12,000 kms of coastline enables the UK to have a huge advantage on sea and ocean energy utilisation. There is an abundance of wind energy resource which is potentially enough to supply 20% of the current electricity demand [2]. In particular, the UK's exposure to Atlantic winds makes a large amount of wind energy resources available. Similar to offshore wind farm (OWF), a tidal turbine farm is also of great interest in hydro-power. Because of the existence of a large number of headlands and islands, which concentrate the tidal flows, the UK has the largest tidal energy potential resource in Europe [3]. Developing and building offshore wind turbine farms and tidal turbine farms around the UK will contribute towards the power demands in the future and bring many benefits to the society and the economy, such as cutting down carbon emissions, providing new jobs and industries.

However increased evidence indicate that such large number of structures in the coastal area are expected to has a significant impact on the surrounding environments including currents, waves, turbulence, sediment transport and also on the vegetation and living animals. In turn these changes in the marine environment would influence the performance of the devices, the efficiency in power generation and their structure

stability. Therefore, more studies must be carried out, such as for instance, the flow past an offshore wind turbine foundation or a tidal turbine has to be better understood as its wake perturbs the flow around other turbines; what type of farm distribution is more efficient should be also investigated; moreover the impact of farms on the seabed must be studied to investigate their effect on sediment morphology, current distribution, and environment or ecology.

Due to the limitation in computation capability, the research on flow-structure interaction is usually divided into two aspects: near-field modelling and far-field modelling. Previously, in near-field modelling, e.g. within 4-6 diameters of the structure several approaches including the traditional CFD modelling of a flow past a cylinder for the wind turbine foundation and actuator disc theory, blade element momentum model, and full geometry model used to represent a tidal turbine have been simulated by numerical models [4–8]. However these approaches mainly focus on the details of the structures itself. As a result, they are difficult to be taken into far-field applications due to the high computing demand.

In far-field modelling, e.g. beyond 10-20 diameters of the structure, several coastal engineering models such as FVCOM [9], Delft3D [10], TELEMAC [11] have been widely used to simulate the potential impacts of the structures at regional scale or energy resources available. However, simulating the environmental impacts of offshore structures is limited due to the following reasons.

Firstly, the turbulence models used in the current ocean models are not suitable for the study of the wake in details. The most common approach nowadays is to solve the Reynolds Averaged Navier-Stoke equations (RANS) which are based on the knowledge of the properties of flow turbulence to give approximate time-averaged solutions to the Navier-Stokes equations. Although time-averaged values for the velocity field can be represented in the results, the instantaneous velocity profile and vortex shedding could not be reproduced.

Secondly, the dimension of the offshore structure is normally far smaller than the whole simulation domain which might cross regions spanning hundreds of thousands of square kilometres. One difficulty in this case is to generate a mesh containing complex geometry and the cell size needs to vary from a few centimetres around the offshore

structure to a few kilometres around boundary. The RANS model cannot account for the different scales of physical processes involved in the simulation , i.e. the wake behind the turbine foundation in the order of metre to the tide or surface wave length of kilometres. The details of enhanced turbulence around a small scale offshore structure are diminished in the temporal and spatial averaging processes, which often leads to limited far-field impacts as we see in these model outputs.

Thirdly, most of the current 3-D coastal models are using a sigma transform to represent the 3-D topography. The strategy of the sigma transform is to copy several times the same 2-D mesh in the vertical direction. However the representations of submerged obstacles with vertical walls can not be easily handled, as each water column contains the same number of prisms.

As compromise to the aforementioned limitations, in the current far-field modelling, a common approach is to use an additional force to represent the wind turbine foundation or tidal turbine, rather than using an obstacle to represent it directly [12–15]. The precision of this approach is clearly in question.

Therefore, this PhD research aims to develop a new 3-D flow simulation algorithm, which can simulate the flow field around an off-shore structure at large scale, and investigate its impact on the coastal zone. New turbulence models based on Large Eddy Simulation (LES) will be employed to represent the turbulence generation and dissipation at different scales. To represent the structure submerged under the water surface, the immersed boundary method will be implemented. These developments will be realised in the open source TELEMAC-3D package.

## 1.1 Aim and Objectives

Several objectives are identified:

1. Develop a better representation of the far-field hydrodynamics around an offshore structure in a realistic flow environment (turbulence modelling).

2. Develop a better representation of an offshore structure by a 3-D numerical model (immersed boundary method).

3. Implement the new model in a regional scale application with a large scale offshore structure (offshore wind farm) presence.

## 1.2 Methodology and approach

The development of the current numerical model enables it to simulate the environment impact on offshore structure which plays a crucial role in structure design and consultation work.

1. Advanced turbulence modelling: The flow in the wake of an offshore structure such as an offshore wind turbine foundation is time-dependent and fully turbulent. It is therefore desirable to use Large Eddy Simulation. This provides a more realistic and effective representation of the flow field. In situations where there is a large number of turbines, large scale turbulence is one of the crucial processes that determines the hydrodynamics. Moreover, sediment morphology depends on the shear stress on the seabed and this is strongly affected by turbulence.

2. In the representation of the 3-D flow structure, the current version of TELEMAC-3D (v7p1), the hydrodynamics code used in this research, relies on an integration along the vertical axis to calculate the velocity field and the mesh motion. A sigma transform is used to solve the transport equation and the same number of layers is used for each water column. However due to the sigma mesh transform, flows around submerged obstacles can not be easily handled, especially when they have vertical solid walls. In order to represent the obstacles in the water, the aim of the present study is to implement an immersed boundary method strategy to the code. The principle of the method is to simulate the flow around structures by applying forces which impede the flow along the solid boundaries. An additional force, which is to replace the actual reaction force on the solid surface, is added to the momentum equations of the Navier-Stokes equations. This method does not alter the parallel performance of the code.

3. The largest simulations are performed on a Cray CX30, namely ARCHER, the UK National Facility and production simulations on STFC Daresbury Laboratory

by an iDataPlex Cluster. High Performance Computing enables large scale applications, and a numerical model with very fine spatial and temporal resolutions is used, leading to a better 3-D representation of the obstacles coupled with an advanced LES turbulence closure.

4. In modelling the flow around a farm of marine turbines the 3-D unstructured version of the code configurations are investigated, with both aligned and staggered distributions of cylindrical obstacles on the seabed. The application considers a wide range of geological configurations, such as sandbanks, deep channels and estuaries.

## 1.3 Structure of the thesis

The structure of the thesis is organised as follows:

Chapter 2 presents the literature review relative to this study. The reviews are separated into two parts. Firstly, the impact of offshore structures on the coastal environment is reviewed. Secondly the numerical models developed and used in recent studies are investigated.

Chapter 3 introduces the numerical model used in this project including the turbulence models and the immersed boundary method.

Chapter 4 validates new turbulence models with laboratory scale test cases. The flow past a cylinder in a flume is simulated and the numerical results are benchmarked with experimental data.

Chapter 5 shows the validation of the immersed boundary method for two test cases. The first one is the flow past a full cylinder and the second one is the flow past a cylinder with a finite height. The comparison between numerical results and measurement data are illustrated in this chapter.

Chapter 6 presents two large scale applications of the turbulence model and the immersed boundary method. Both the impact of offshore wind farms in the Thames Estuary and tidal turbine farms in an ideal channel are simulated.

Chapter 7 discusses the numerical results and summarises the work in this study. Finally, some potential future work is listed.

# Chapter 2

# Literature Review

In this chapter, recent researches related to this PhD project are reviewed. Firstly, the common offshore structures in engineering and their impacts on the coastal environment is briefly introduced, followed by the numerical models of recent water-structure interaction simulations. Near-field modelling is briefly presented, before far-field modelling is reviewed in details focusing on the following aspects: hydrodynamic , turbulence and sediment transport modellings.

## 2.1 Offshore structure

Offshore structures are buildings or facilities which are installed in a marine environment, usually for the production and transmission of electricity, oil, gas and other resources [16]. Different types of offshore structural systems have been developed including offshore wind turbines, tidal turbines or oil platforms over the past decades. In this study, two types of offshore structure including offshore wind turbine farms and tidal turbine farm are selected as the object of the numerical modelling.

### 2.1.1 Offshore wind turbine foundation types

There exist several very different designs of offshore wind turbine foundation, depending on the different application conditions. The common types of currently used foundations can be classified as follows [17]:

- **Mono pile** - made of a steel or concrete pile which is on into the seabed directly.

- **Gravity foundation** - It consists of a large base and a pile constructed from either concrete or steel. The base rests on the seabed, thus the turbine is dependent on gravity to remain erect.

- **Tripod foundation** - It is similar to the design in oil and gas industry, the foundation being supported by a tripod foundation and each end of the tripod is driven into the seabed.

Most current OWFs built in the UK are located in the shallow coastal areas and are used monopile foundations [18]. Therefore in this study, only monopile foundation OWF is taken into consideration.

### 2.1.2 Tidal turbine types

Following the technological innovation, a number of tidal turbines have been designed. According to their physical arrangements, they can be classified into three main types: horizontal axis, cross flow and vertical axis [19]. Figure 2.1 shows a horizontal tidal

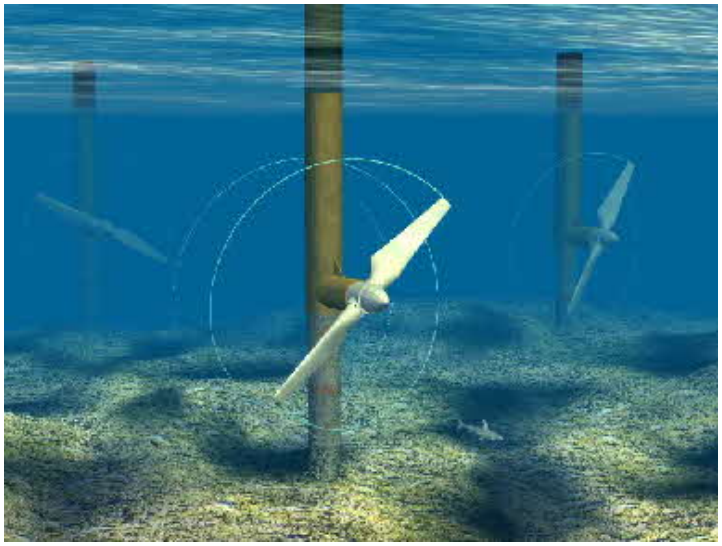

**Figure 2.1:** horizontal axis tidal turbine.

turbine. This kind of turbine has a bladed rotor device, rotating in a plane perpendicular to the axis. The rotor drives a generator via a gearbox, which is similar to a wind turbine. Figure 2.2 gives two examples of cross flow turbines. The cross flow turbines have rotor axes orthogonal to the water flow but parallel to the water surface.

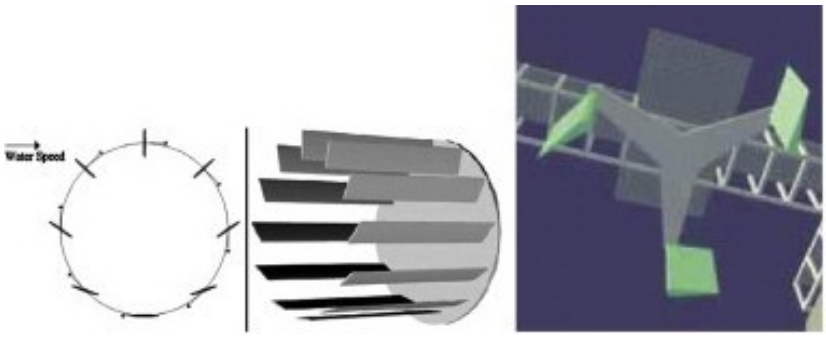


**Figure 2.2:** Cross-flow turbines.

These turbines are also known as floating waterwheels. These are mainly drag-based devices (cross flow turbines) and inherently less efficient than their lift-based counterparts (horizontal turbines). Another drawback of these turbines is the large quantity of material required to build them, which makes them expensive [20].

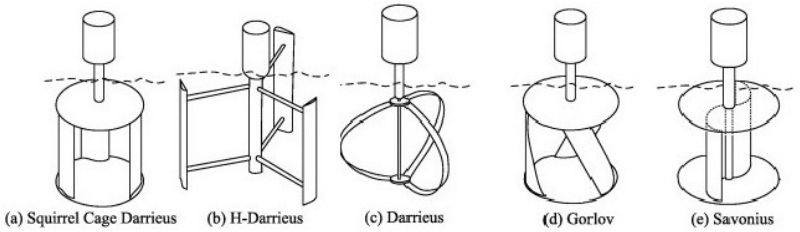


**Figure 2.3:** Vertical axis tidal turbines.

Figure 2.3 shows several tidal turbines based on the vertical-axis type. These types of devices were first developed for the wind industry, but research into this configuration decreased due to the fact they are theoretically less efficient than the horizontal devices. However, this research has been revived for the tidal industry [21]. Darrieus-type turbine is the most common one in this field, followed by H-Darrieus- or Squirrel-cage Darrieus-types. However they have not been taken into hydro applications as operational and performance issues are still assessed [22, 23]. The Gorlov turbine is another kind of vertical-axis type of turbine, where the blades have an helical structure shape [24]. The Savonious turbine with straight or skewed blades also belongs to also in this family [22, 23].

Except for the tidal turbine mentioned above, there are other innovative concepts including vortex-induced vibration, Venturi, fluttervane and fan belt that can be used

to extract energy from tidal stream [25]. However before they can be commercialised, more experiments and tests should be performed at laboratory scale.

Currently, horizontal and vertical turbines are still considered as the two main competitors of the field. Comparing with the vertical turbines which are still in test stage, horizontal turbines have been used in tidal energy conversion industry [26] because of their structure which is similar to the wind turbines and has proven its application to wind industry. The current tendency shows that horizontal-axis-type turbines will still be preferred in the short-term future for shallow water applications. Therefore a number of research are devoted to the investigation of the effects of these type of turbines in marine environment.

The numerical model in this study will be based on horizontal turbines. The impacts of horizontal turbine farms will be investigated.

## 2.2 Impact of offshore structure on the coastal environment

Having offshore structure such as OWF or tidal turbine farm in the coastal area has significant impacts on the surrounding environments including currents, waves, turbulence, sediment transport and also on the vegetation and living animals. In turn, these surroundings would influence the tidal turbines' efficiency in power generation and their structure stability.

### 2.2.1 Single turbine impact

Many laboratory experiments and numerical modelling exercises have been carried out to investigate the turbine impacts based on individual turbine structures [27–29]. The exact form of the wake created by a turbine may be device-specific, but the fundamental flow characteristics can be decomposed in a way that there is a significant acceleration around the structure, together with a low pressure area in the wake zone where complex 3-D turbulence eddies are generated.

The turbulence kinetic energy is observed to increase around the turbine blade tip due to the rotation of the blades and the presence of the structure. Such enhanced

turbulence field gradually dissipates behind the structure in the wake region. Mycek et al [30, 31] investigated the turbulence effects on the behaviour of tidal turbines through an experiment with 1/30 scale prototypes of horizontal axis turbines. He pointed out that the ambient turbulence intensity condition plays a significant role on the wake shape. Moreover, regarding to the power generation efficiency, the higher turbulence intensity rate, the better performance of the downstream turbine with a given distance. This work is of great importance for the arrangement of tidal turbine arrays.

Due to the complex turbulent flow observed around a turbine, the bed shear stress increases immediately behind the turbine structure which plays an important role in sedimentation. Hill et al [32, 33] did a series of experiments to study the interactions between sediment transport and tidal turbines. In the experiments, he found the local scour formation and depth around tidal turbines are amplified comparing with the experiment where only a support tower was tested. This is due to the presence of the rotor which increases the local shear stress directly downstream of its location. The distance between the rotor bottom tip and the sediment layer is a key factor of this impact. Although the author can not find the difference between the impacts of a single turbine and aligned turbines on the far-field sediment transport or morphodynamic characteristics of the channel, he could predict that larger arrays of turbines may decrease the transport capacity in the channel, possibly impacting inter-array transport, near-by channel bank stability, and far-field sediment transport characteristics, more than a single or two turbine array would.

### 2.2.2 Large scale turbine farm impact

The large scale turbine farm impacts are mainly caused by the conjuction of far wake behind each individual structure. On the one hand, this far wake can influence the power coefficient of the power generation itself. In the investigation of the interaction between different tidal turbine array configurations, Chen et al [34] and Rao et al [35] point out that the best performance of tidal turbine arrangement is a single-row setting. In multiple-row settings, the efficiency of the inside turbines are significantly affected by the upstream wakes. On the other hand, the far wake behind the turbine farm would influence the surrounding environment including sediment transport and coastal mor-

phology changes. A large scale impact of offshore wind farms on suspended sediments was captured by the Landsat-8 satellite. It is shown in figure 2.4 (Vanhellemont and Ruddick [36]). In this satellite photo, a turbid wake of several kilometre length can be clearly observed behind each individual structure. Due to the difficulty of in-situ measurement at a wind farm site, the environmental impact of these wakes and the source of the suspended material are still unclear, but such large wake size indicates that more research should be carried out.

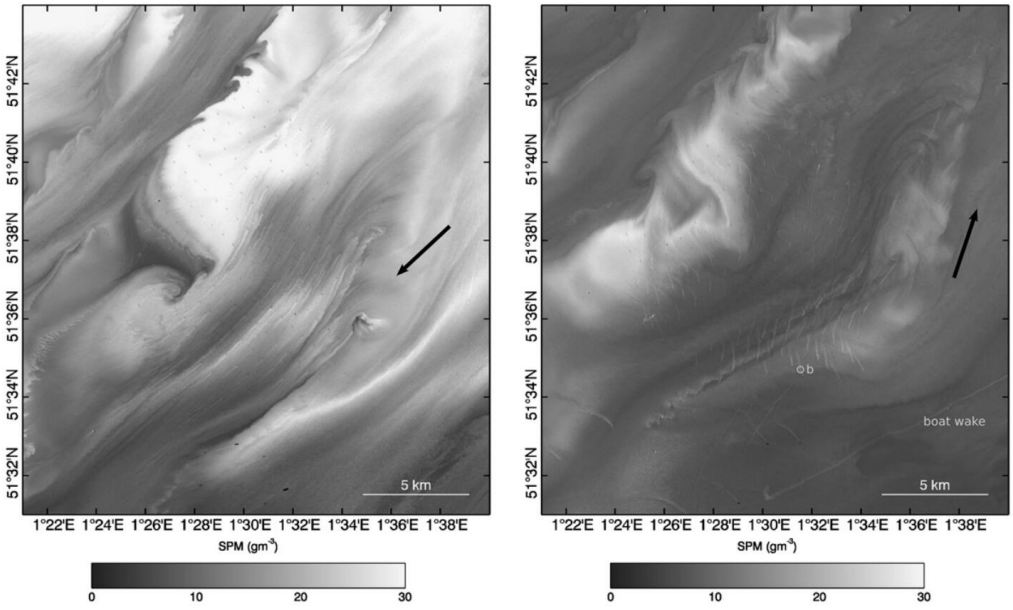


**Figure 2.4:** Details of wake around the London Array site as shown in the processed Landsat-8 image

The sedimentation around a turbine farm at large scale was estimated numerically by Thiébot et al [37]. The effect of tidal stream turbines was investigated at real scale (Alderney, France). The results show that tidal energy extraction modifies the bed load and suspended sediment transport and globally reduces the sediment fluxes. As a result, the mass balance perturbations of sediment deposition reach 20% in the whole test domain.

More details of numerical modelling is reviewed in the next section.

## 2.3 Numerical modelling

Offshore strucutures such as marine turbines are usually installed in shallow water regions and are influenced by a number of factors including current, wave, tide and turbulence. On the one hand, in order to obtain accurate flow conditions in the site of interest, the numerical model would cover thousands of square kilometres [38–41]. On the other hand, the few meters around each turbine are also of interest to better understand turbulence past the turbines and sediment transport around them. Due to the limitation in computation capability, these studies are normally divided into two aspects: near-field modelling and far-field modelling.

### 2.3.1 Boundary between near field and far field models

The near field is located directly around a turbine, where coherent turbulent structures generated by the turbine can be observed. A shear layer along the wake boundary is generated by the difference in velocity between the low speed zone in the wake and the free stream flow. In the shear layer eddies are formed, which help to mix the lower velocity fluid in the wake with the higher velocity fluid surrounding the wake. This mixing process transfers momentum into the wake and increases the flow velocity. The distance downstream where the shear layer becomes thick enough to meet the turbine wake axis is used to mark the end of the near wake region and the start of the far wake. In wind turbine studies, this transition point is detected between two to five rotor diameters downstream of the turbine (Vermeer et al [42]). This typical length of boundary is also used for the research of tidal turbine cases.

In the simulation of near field impacts, most studies are carried out in laboratory flumes. At this scale, the real tide phenomenon, rising and falling of water elevation, is often not considered. Instead, a steady or unsteady flow condition [43, 44] is given directly to represent the tidal current. The impact of complex variation of bathymetry is also limited due to the small spatial scale involved.

Under the combined effect of tide and bathymetry, the influence of tidal turbines can be stretched for some considerable distance from the structures ($>$ 5 diameter of the turbine pile). For example, Divett et al [45] studied a number of tidal turbines installed in a channel which influence the flow regime through the entire channel. Such

far-field impacts are necessary to be investigated through either laboratory experiment, or by far-field numerical modelling. Different from the near-field modelling in which the flows are more isotropic, in far-field modelling, the horizontal scale is much larger than the vertical scale. The Coriolis force becomes an important factor due to the geostrophic contribution. Although tide and wave propagation can be simulated, the details of the turbine structure are difficult to be represented due to its small scale. Based on these previous studies, it is generally accepted that the boundary between near-field and far-field is located at 5 diameters of the turbine.

### 2.3.2 Near field modelling

Most near-field modelling is carried out using computational fluid dynamics (CFD) software. The current flow is calculated by solving the Navier-Stokes (or non-hydrostatic) equations. The details of pressure changes around the structure and its coupling with the flow velocities are particularly important adjacent to the stream devices. To simulate the impact of a tidal turbine, the most straight way is to represent the turbine structure in the simulation domain by its full geometry, and to mesh at sufficient resolution to capture the flow around the blades [5, 8]. The model is time-stepped, the rotational position of the blades incremented, and performance characteristics and wake velocities are calculated. If implemented with sufficient spatial and temporal accuracy, this approach can be accurate and provide details of the flow field and turbine performance. However this approach requires a lot of computing power to carry out the calculations.

A more efficient technique consists in representing the turbine structures by adding source terms to the governing equations. The Reynolds Averaged Navier-Stokes (RANS) Actuator Disc (AD) theory and Blade Element Momentum (BEM) models are two of the most common approaches to parametrise a tidal turbine in numerical models. The former is popular in investigating the wake impact by considering the tidal turbine as a constant sink of momentum, where a similar force can be simulated as would be imposed by a turbine [43, 44, 46–49]. The BEM model approach is composed of two separate theories, the momentum theory and the blade element theory. This approach is computationally efficient and can accurately predict the performance of a turbine

across a range of tip speed ratios, blade types, pitch angles, and inflow conditions [6, 7, 50–53]. However, the BEM approach does not provide any detail of the flow field around the device, as for example wake velocities.

The focus of near-field modelling is typically placed on the performance of the individual turbine configuration, power potential and impacts to the flow dynamics adjacent to the structure (within approximately 10 diameters distance). The potential impacts on much larger scale process, such as large scale tidal circulation, coastal regional morphology and sediment path way, are not possible to investigate using such an approach due its high computational cost. Similarly, when a turbine farm is considered, the typical modelling method is based on far-field modelling as discussed in the following section.

### 2.3.3 Far-field modelling

#### Hydrodynamic modelling

The large scale tidal current motions are usually studied by ocean models. These models might be 1-D, 2-D, or 3-D.

Neill et al [54] and Bryden et al [55] implemented a 1-D morphological model to study the impact of tidal stream turbines in a tidal river channel. The time-varying free surface and velocity were calculated by the 1-D continuity equation with the assumption that the water elevation at the boundary varies according to the tidal cycle. However these studies dealt with a single turbine deployment. The study area was limited to a channel due to the spatial dimension of the model.

In most of far-field study cases, the horizontal length scale is usually much greater than the vertical length scale. Therefore two-dimensional depth-averaged horizontal models have been extensively employed since they benefit from computational efficiency. The shallow water equations [56] are widely applied in those models. The equations are derived from depth-integrating the Navier-Stokes equations. Integrating vertically allows the vertical velocity to be removed from the equations. Additional forces including wind, the Coriolis forces and the bottom friction, for instance can be implemented in the momentum equations to better account for physical phenomena. Fan et al [57], Suursaar et al [58] and Vethamony et al [59] applied different 2-D hydro-

dynamic models to investigate the sea level variations due to wind and tidal effects. In their studies, the shallow water equations are discretised by the finite difference method, hence a structured mesh is used. This numerical technique obviously limits the model in dealing with complicated coast lines. Other numerical techniques including the finite volume method and finite element methods on unstructured grid are also used to solve shallow water equations[60–62]. These approaches allow for detailed spatial resolution in the areas of interest at low computational costs. Although the in above studies, good agreement can be found in the comparison of numerical prediction and measured data, the depth-averaged nature of the algorithms means that the vertical variations cannot be resolved which is typically important for flow around vertical structures.

More recently, 3-D numerical models are developed so that the 3-D incompressible Navier-Stokes equations in sigma ($\sigma$) coordinates are solved. Balas and Özhan [63] applied a 3-D model to investigate the flow in the Göksu Lagoon (Turkey). The authors indicated that the numerical model shows a good agreement compared with field data and that even if the water is shallow, the reversal of the flow in the vertical plane can be captured. In this study, the 3-D incompressible Navier-Stokes equations are solved based on two assumptions: (i) hydrostatic pressure distribution, i.e. the weight of the fluid balances the pressure, (ii) the Boussinesq approximation, i.e. the density differences are neglected unless the differences are multiplied by the gravity. Traditionally, the hydrostatic approximation is applied to reduce the computational costs. This approximation is valid in large scale studies with coarse grid resolution. Numerical model can only obtain good result if the flow acceleration is weak [64]. However with faster computers and gradually smaller grid sizes, more studies are performed with non-hydrostatic ocean models [65] in which the non-linear pressure distribution adjacent to the structure can be resolved.

#### Representation of the offshore structure

Due to the limitation in computation capability, the mesh used for large scale simulation is far than in a near-field simulation, hence the structure can not be recognised by the mesh directly. To represent an offshore structure such as a tidal turbine, the common approach is to use an external force instead.

For example, a 2-D hydro-environmental model known as DIVAST (Depth Averaged Velocity And Solute Transport) has been used to simulate the coastal hydro-environment [66, 67]. This approach has been modified by Ahmadian et al [12, 13] to investigate the hydro-environmental impact of tidal stream turbines at large scale. In their studies, tidal turbines are represented by considering a thrust and drag force as external forces. These are added to the shallow water momentum equation at some nodes of the mesh where the turbines are allocated. In other words, in this far field modelling, the impact of the tidal turbine farm is replaced by the impact of forces.

A similar approach to that in Ahmadian et al [12] [13] is used by Work et al [14]. In order to simulate the far field effects on flow velocities and water levels introduced by tidal turbines, an additional drag force was calculated in the Regional Ocean Modelling System (ROMS) which indicated the dissipation of power extraction. In another far-field application [15], the tidal turbine was represented in terms of nonlinear Rayleigh friction in the momentum equation. In this case, the quadratic Rayleigh friction formulation, instead of axis thrust, is used to simulate the turbine drag in a 3-D momentum equation. Other popular ocean modelling software including Delft3D, FVCOM are also modified for the investigation of far field tidal turbines impact [34, 35, 68]. Extra source terms are added to the momentum equations for the representation of the tidal turbines.

The common point of the aforementioned far-field approaches is that the real structure of a tidal turbine is replaced by a forcing term in the momentum equation, with different expressions. Although some validations with experimental data have been carried out and results show reasonable agreement, the reliability of these approaches, however, is still in question. For instance, in the work of Ahmadian et al [12], the model validation were conducted in an idealised channel, against the results of a previously published 1-D model [69]. Very often, these added forcing terms are capable of reproducing the averaged effects, i.e. the time-mean effects on flow reduction, or the spatially averaged wake effects behind the structure. However, the details of the flow dynamics around the tidal turbine and supporting structures are not represented. Subsequently, the following far-field effects are often limited very close to the structure itself. But recent remote sensing imagery reveals that the suspended sediment

concentrations changed noticeably within 15 km from the turbine array, which is far more than the distance involved in the validation [36]. Such far distance effects indicate that the impacts from individual structures may not be represented sufficiently by the temporal and spatial averaged terms as in the above studies. It is necessary to simulate the near-field effects to a certain extent so that the far-field process can be represented properly.

Rather than using an additional force, an obstacle represented by its own geometry will be more natural for far field simulations. However this approach is limited by the mesh resolution used in most existing oceanographic/coastal models, including TELEMAC [11], Delft3D [10], MIKE21 [70] and FVCOM [9], among others. In these 3-D modelling systems, the meshes used are all based on the sigma coordinate system in the vertical. This kind of mesh structure is made of prisms. In order to prepare the mesh of the 3-D flow domain, a 2-D mesh made of triangles which covers the computational domain (the bottom) in a plane is first constructed. The second step consists in duplicating that mesh along the vertical direction in a number of curved surfaces known as planes. Between two such planes, the links between the split triangles make up prisms. The drawback of this mesh is that it can not recognise any structure on the seabed or submerged structures. Therefore to represent a tidal turbine directly, fundamental modifications are needed in far-field modelling due to the current limitations of mesh.

**Turbulence modelling**

Turbulence modelling plays a significant role in oceanography/coastal modelling not only due to its importance in mixing the flow field, but also because the sediment diffusion depends on the turbulent eddies.

- Reynolds Averaged Navier-Stokes equations

The most common approach is to solve the Reynolds Averaged Navier-Stokes (RANS) equations which are based on the knowledge of the properties of flow turbulence to give approximate time-averaged solutions to the Navier-Stokes equations. Different closures might be used, depending on the order required, including mixing length [71]; k-$\varepsilon$ [72],

k-$\omega$ [73]. Keshtpooret et al [64] used the k-$\varepsilon$ closure to investigate the mechanisms of the morphologic evolution of scour holes within the Indian River Inlet. The mixing coefficient and consequently bed shear stress are calculated by the k-$\varepsilon$ closure. The author indicated that the turbulence was enhanced due to the flow separation within developed scour holes and thus it was the dominant mechanism for further scour hole development. Leupi et al [74] applied the same approach to simulate cohesive sediment dynamics in estuaries. He pointed out that the k-$\varepsilon$ closure needed very small time steps to predict accurate result, while the bed morphology (solid-phase flow) required a long time simulation.

Regarding the wake representation, Chen et al [34] implemented the k-$\varepsilon$ closure to investigate the impact of different configurations of tidal turbine arrays near an island. The turbine structures are represented by additional source terms. The wake impacts are visible in the numerical results, however these results only showed time-averaged values for the velocity field. The instantaneous velocity profile and vortex shedding phenomena could not be reproduced in the results.

In addition, the turbulence modelling approach used in most of these RANS models is limited to the scale similar to the physical processes involved, i.e. tide or surface wave length (from about 100 m to a few km) or boundary geometry, such as the estuary size (about 100 m). The enhanced turbulence around small scale tidal turbine structures is simply treated as a sub-grid process. Inevitably, the details of these effects are diminished in the temporal and spatial averaging process, which often leads to limited far-field impacts as we see in these model outputs.

- Large Eddy Simulation

A more advanced approach to account for turbulence is to use Large Eddy Simulation (LES). This approach is based on the assumption that the small eddy scales are more isotropic, and less affected by boundary conditions, than the large scales [75]. This feature enables the model to separate the turbulent flow into large and small parts by a filtering process based on an energy cascade. The large eddies are simulated by the calculation explicitly, while the small eddies are treated by using a sub grid-scale model. Mathematically, the flow field is separated in a resolved and a sub-grid part, which represent the large and small eddies respectively. In ocean and coastal engineering

modelling, due to the great difference between the length of horizontal and vertical scales, the diffusion coefficient in the two directions should be treated separately. The LES closure is commonly used in the horizontal direction. Rao et al [35] investigated the efficiency of different tidal turbine array settings using the ocean modelling software FVCOM. In their study, the turbine structures are represented by drag forces. The Smagorinsky LES parameterisation [76] was used in the horizontal direction, and the vertical mixing was calculated using the Mellor and Yamada mixing scheme[77] . The numerical results showed that the wake length of the turbine structure is significantly influenced by additional turbulence injection. The average length of the wake flow is about 20 time of the structure diameter, however some longer wake lengths were also found when flow speed was increased.

Effects of different coefficients of Smagorinsky LES closure were tested by Shapiro et al [78]. In their work, the effect of the horizontal diffusion parameterisation was calibrated by measurements in the Black Sea. The authora pointed out that a small Smagorinsky coefficient could destroy the strong anticyclonic eddy in the study area. In order to realistically represent mesoscale eddies, a much smaller coefficient for the horizontal diffusion [79] should be applied.

The Smagorinsky LES model is isotropic and the eddy viscosity is evaluated as the product of a length scale $\Delta$, proportional to the grid size. Due to the anisotopic grids in ocean/coastal engineering modelling, it is difficult to find a proper single length scale for the model. Based on the traditional Smagorinsky closure, a two-eddy-viscosities sub-grid scale Smagorinsky model was employed by Roman et al [80] to deal with mesh anisotropy. Through the comparison with the classic standard Smagorinsky model, the new model showed its dramatic superiority in the simulation of a turbulent plane channel flow with increasing grid anisotropy. Petronio et al [81] implemented this model to simulate wind-driven sea circulation in coastal areas. According to the comparison, the flow velocity profile showed a good agreement with field measurements. Specifically, the authors pointed out that the model reproduces well the vertical profile of the angle of the horizontal velocity component at the locations of the field measurements.

**Sediment transport and morphology**

In coastal modelling, the sediment transport is normally divided into bed load and suspended load. Bed load refers to sediment particles that move by rolling, sliding, and hopping (or saltating) over the bed. Suspended load refers to particles being carried in the lower to middle parts of the flow in the water column. Therefore the calculation of sediment transport is based on a function of various flow (velocity, water depth, wave height, etc.) and sediment (grain diameter, relative density, settling velocity, etc.) parameters.

- Bed-load transport

A large number of semi-empirical formulae exist to calculate the bed-load transport rate including the Meyer-Peter and Müller [82], Engelund-Hansen [83] and Einstein-Brown [84]. Most use the assumption of threshold conditions for the onset of erosion (e.g. Meyer-Peter and Müller [82], van Rijn [85] ). Others are based on a similar energy concept (e.g. Engelund-Hansen [83] ) or a statistical approach (e.g. Einstein-Brown [84], Bijker[86] ) Most sediment transport formulae are based on experiments performed under fluvial, unidirectional flows. These formulae show a rapid variation of the bed-load transport prediction, as a function of the mean flow intensity. Therefore, an increase of the current velocity by 10% will result, depending on the formula being used, in an increase of the transport rate of over 30% (Meyer-Peter), 60% (Engelund-Hansen) or almost 80% (Einstein-Brown). Any error made when calculating the hydrodynamics will be significantly amplified in the sediment transport rate calculations. On the other hand, under variable flow conditions (e.g. a tidal regime), the average transport will be highly influenced by strong currents and will not be directly related to the mean flow. Therefore the bed-load formula should be selected carefully depending on both the local sediment and flow conditions.

For example, the Meyer-Peter and Müller formula has been validated for coarse sediments in the range of 0.4 mm to 29 mm. The Einstein-Brown formula is recommended for gravel larger than 2 mm and a large bed shear stress [84]. The Engelund-Hansen formula predicts both bed-load and suspended load. It is recommended for fine sediments, in the range 0.2 mm $< d_{50} <$ 1 mm but only suitable under equilibrium

conditions (quasi-steady and uniform flow) [87]. The van Rijn formula was proposed to calculate the bed-load transport rate for particles of size 0.2 mm $< d_{50} <$ 2 mm [85]. The effects of waves can be taken into account by the sediment formulae, i.e. by the Bijker [86], Bailard[88], Dibajnia and Watanabe [89] formula.

Fairley [90] numerically simulates the cumulative impact of tidal stream turbine arrays on sediment transport. In his study, the sediment transport is calculated using the van Rijn equations [85]. The variables used in the calculation of sediment transport are taken from a hydrodynamic model. The two models are fully coupled at each time-step such that computed changes to bed level are fed to the hydrodynamic module to allow for accurate prediction of currents. The drawback of this approach is that small time-steps are required.

In the investigation of the effect of the stream tidal turbine on the bed-load transport, the numerical models always cover a long period (weeks - months). In order to obtain a long period bed-load transport results more efficiently, Thiébot [37] introduced a tidal-average critical stress to control the bed-load erosion process. Rather than calculating the critical stress at each time-step, the critical stress exceedance is calculated by averaging over a 1-month-long simulation. The results are expressed in terms of magnitude and direction and are therefore representative of the direction and magnitude of the bed-load sediment flux.

- Suspension load transport

The suspended sediment concentration in equilibrium is given by the Rouse profile [91]. The Rouse profile characterises sediment concentrations because the Rouse number includes both turbulent mixing and settling under the weight of the particles. Turbulent mixing results in the net motion of particles from regions of high concentrations to low concentrations. Because particles settle downward, for all cases where the particles are not neutrally buoyant or sufficiently light that this settling velocity is negligible, there is a net negative concentration gradient as one goes upward in the flow. The Rouse profile therefore gives the concentration profile that provides a balance between turbulent mixing (net upwards) of sediment and the downwards settling velocity of each particle.

In most suspended sediment models for coastal seas, the suspended sediment concentration $C$ is normally solved by the advection diffusion (mass-balance) equation as follows:

$$\frac{\partial C}{\partial t} + \nabla \cdot (C\overrightarrow{U} + C\overrightarrow{w_s}) = \nabla \cdot (\upsilon_t \nabla C) \tag{2.1}$$

where $\vec{U}$ is the velocity vector. $\upsilon_t$ is the turbulent diffusivity coefficient ($m^2/s$). $\overrightarrow{w_s} = (0, 0, -w_s)$ is the sediment settling velocity (m/s). The sediment particles are considered as passive scalars with an additional settling velocity term.

Ashall et al [92] implemented this approach to investigate the variability in suspended sediment concentration due to tidal power extraction. The suspended sediment concentration obtained by the numerical model shows a good agreement with the field observed data.

### 2.3.4 Immersed Boundary Method

The strategy based on triangular elements to mesh the bottom of the field, and using layers of triangle elements to simulate 3-D flows is a clear limitation to simulate flows around submerged obstacles, as each water column contains the same number of prisms. It is then possible to generate a mesh around a cylinder going through the free surface, but not around a submerged cylinder, for instance. In order to account for the obstacles in water, Immersed Boundary (IB) methods are very good options.

The IB method was firstly introduced by Peskin [93] in 1973 to simulate the blood flow in the heart. This approach was used to model elastic capillary and artery walls. Nowadays, a variety of approaches have been developed in the simulation of fluid-structure interaction (FSI) problems.
In general, immersed boundary methods can be divided into diffused interface and sharp interface methods.

In the diffused interface IB method, immersed bodies are represented by singular forces, using discrete delta functions or mask functions for penalisation methods. Following different method to calculate the force, it can be further classified as classic IB method, direct forcing IB method and penalisation method. In the classic IB method, IB forces are represented by appropriate constitutive laws depending on the realistic

force condition. This approach is more suited for FSI problems with elastic boundaries for instance where the spring feature of the wall can be introduced by Hook's law. For rigid boundary, the immersed boundary can be represented by direct forcing methods [94, 95]. The idea of this approach is to calculate the IB force based on the momentum equations discretised in time. To incorporate direct forcing in the classic diffused interface IB method, the quantities on the background and immersed boundary meshes can be transferred by employing discrete delta functions of the classic formulation. Another approach which can be used to calculate IB force is called penalisation method [96]. In this method, the solid obstacles are modelled as porous media with vanishing porosity.

In order to keep the model numerically stable, the fictitious body forces used in the aforementioned methods have to be distributed smoothly over the immersed boundaries. However due to the implementation of discrete delta function/mask function, the immersed boundaries are not sharp. These drawbacks can be overcome by several sharp interface methods such as cut-cell methods or immersed interface methods.

In cut-cell methods, the mesh cells are cut by the interface to fit the immersed boundary. The fluxes across the faces of the cut-cells are reconstructed from the surrounding regular cells and immersed boundaries [97]. Due to the difficulty to re-arrange the topology of the cut-cells (for instance, after cutting a rectangle cell, the shape of the remaining cell can be either a pentagon, a quadrangle or a triangle), this approach is easier to be used in 2D [98–100] than 3D [101, 102]. Another method which makes the IB force sharper was introduced by Leveque and Li [103]. Similar to the classic IB method, this approach uses a singular force to represent the effects of the immersed interface, however instead of using a discrete delta function, a jump condition is implemented in the finite difference scheme. This method helps to represent the effects of non-smooth solutions which could be caused by singular forces at the immersed boundaries or the discontinuous substance properties across the immersed interfaces.

## 2.4 Summary

Literature studies have been carried out in this chapter. Following the comparison of different types of existing offshore structures, the numerical model in this project is based on offshore wind turbine and horizontal tidal turbines because these facilities

have been widely installed around the UK and play significant role in energy extraction.

The presence of offshore wind turbine farms and tidal turbines significantly impacts the coastal environment including currents, waves, turbulence, sediment transport, vegetation and living animals. A number of studies have been carried out to investigate these impacts both in the near- and far-field by numerical modelling. In near-field modelling, various CFD software are used to predict the flow field around a turbine structure and good agreement is found between experiment and numerical results. There have been several numerical approaches for representing tidal turbines in near-field e.g. actuator disc theory, blade element momentum model, and even full geometry model. These approaches need high resolution around the structure and require a large amount of computational resource.

In far-field modelling, due to the huge difference between the horizontal and vertical scales, ocean modelling/coastal engineering software is preferred because of the reduced computational cost. In the model, people usually represent the turbine farms by additional forces. This approach reduces the computation cost, however the details of the flow around the turbine structures can not be accurately predicted. It has become clear that the overall impacts of the whole farm are not simply a multiplication of individual turbine impacts by the total number of structures. The interaction between individual structures can also influence the overall effect considerably. Therefore, representing each individual turbine structure is important when large scale turbine farms are concerned, which means that the horizontal mesh resolution needs to be small enough to be comparable to the turbine size.

In general, the aim of this study is to implement the common method of CFD to ocean model and improve the capability of the ocean model of offshore structure modelling. Therefore, regarding the simulation of the hydrodynamics impact of offshore wind farm, an approach similar to modelling the flow past a cylinder will be used in which each individual turbine foundation will be represented explicitly in the mesh as a circular cylinder with high resolution around its boundary. The calculation of this application is extremely time consuming, hence high performance computation is compulsory.

For the tidal turbine simulation, the meshes used in ocean model/coastal engineer-

ing are not sufficient to account for the submerged structure in the simulation. The reviews of Immersed Boundary method indicate that this technology offers an alternative to enforce no-slip boundary in Navier-Stokes equations by introducing additional forces, hence the submerged structure can be represented. By applying the Immersed Boundary method, the tidal turbine structure is represented as a submerged circular cylinder in the computational mesh. Although the blade rotation effect is neglected, this approach can be still used to predict the impact of tidal turbines on far-field environment as at such large scale, the impact of blade rotation is considerably small.

The choice of the turbulence models is also important in large scale simulation because of the balance between the required precision and time consumption of calculation. LES will be a good turbulence model in this project due to its ability to capture unsteadiness of the flow. In order to improve the simulation of the flow field around a tidal turbine farm at large scales, the coastal engineering software, TELEMAC-3D, is used as a numerical solver. The details of the numerical modelling are discussed in the next chapter.

# Chapter 3

# Numerical Model

The TELEMAC suite has been widely used to simulate the coastal or riverine hydraulics. [104–107]. It is chosen in this study for the following reasons:

- Firstly, comparing with other coastal environmental software (Delft3D, Mike21), the usage of triangular mesh makes the code more flexible in the representation of bathymetry with complex geometry.
- Secondly, this model has very good performance on distributed memory computers [108].
- Thirdly, the TELEMAC suite has multiple modules which allow to simulate various physical processes. Not only hydraulics, but also wave propagation or sediment transport can be studied.
- Finally, this model is programming friendly. It is an open-source code that users can input or modify it's code easily.

The development and implementation of new turbulence model and immersed boundary method is based on the existing code, TELEMAC-3D, which is one of the modules of the TELEMAC System [11]. TELEMAC is a powerful integrated modelling tool developed by EDF (France). It contains multiple modules which are used to represent various physical processes.

This chapter focuses on the numerical model used in this study. Firstly the methodology of the hydrodynamics software TELEMAC-3D is introduced. Then the imple-

mentation of new turbulence models and immersed boundary method are discussed in details.

## 3.1 Three-dimensional Navier-Stokes equations for free surface flows

### 3.1.1 Formulation

The three dimensional flow is represented by the 3D Navier-Stokes equations.

In Cartesian coordinates and non-conservative form, the equations are written as:

$$\frac{\partial u_1}{\partial x_1} + \frac{\partial u_2}{\partial x_2} + \frac{\partial u_3}{\partial x_3} = 0 \tag{3.1}$$

$$\frac{\partial u_1}{\partial t} + u_1\frac{\partial u_1}{\partial x_1} + u_2\frac{\partial u_1}{\partial x_2} + u_3\frac{\partial u_1}{\partial x_3} = -\frac{1}{\rho}\frac{\partial p}{\partial x_1} + \nu\left(\frac{\partial^2 u_1}{\partial x_1^2} + \frac{\partial^2 u_1}{\partial x_2^2} + \frac{\partial^2 u_1}{\partial x_3^2}\right) + F_{x_1} \tag{3.2}$$

$$\frac{\partial u_2}{\partial t} + u_1\frac{\partial u_2}{\partial x_1} + u_2\frac{\partial u_2}{\partial x_2} + u_3\frac{\partial u_2}{\partial x_3} = -\frac{1}{\rho}\frac{\partial p}{\partial x_2} + \nu\left(\frac{\partial^2 u_2}{\partial x_1^2} + \frac{\partial^2 u_2}{\partial x_2^2} + \frac{\partial^2 u_2}{\partial x_3^2}\right) + F_{x_2} \tag{3.3}$$

$$\frac{\partial u_3}{\partial t} + u_1\frac{\partial u_3}{\partial x_1} + u_2\frac{\partial u_3}{\partial x_2} + u_3\frac{\partial u_3}{\partial x_3} = -\frac{1}{\rho}\frac{\partial p}{\partial x_3} - g + \nu\left(\frac{\partial^2 u_3}{\partial x_1^2} + \frac{\partial^2 u_3}{\partial x_2^2} + \frac{\partial^2 u_3}{\partial x_3^2}\right) + F_{x_3} \tag{3.4}$$

where $(x_1, x_2, x_3)$ are the Cartesian coordinates, $(u_1, u_2, u_3)$ are the velocity along $x_1$, $x_2$ and $x_3$ direction respectively. $\rho$ is the water density, $t$ is the time, $\nu$ is the dynamic viscosity, $p$ is pressure, $g$ is the gravity constant, $(F_{x_1}, F_{x_2}, F_{x_3})$ is a potential extra force (it could be the wind, the Coriolis force or an Immersed Boundary force, for instance).

### 3.1.2 Decomposition of the pressure

In order to solve the free-surface elevation directly by the Navier-Stokes equations, the pressure term in equations 3.2, 3.3 and 3.4 is decomposed into a hydrostatic part and a dynamic part:

$$p = p_h + p_d \tag{3.5}$$

where $p_h$ represents the hydrostatic pressure and $p_d$ the dynamic pressure.

The hydrostatic pressure is defined by the following equation:

$$p_h = \rho g(\eta - x_3) + p_{atm} \tag{3.6}$$

where $\eta$ is the water surface elevation.

Under the Boussinesq approximation, this gives:

$$p_h = p_{atm} + \rho_0 g(\eta - x_3) + \rho_0 g \int_{x_3}^{\eta} \frac{\Delta\rho}{\rho_0} dx_3 \tag{3.7}$$

where $\rho_0$ and $\Delta\rho$ are reference density (1,024 kg m$^3$) and the variation of density respectively; $p_{atm}$ is the atmospheric pressure.

The hydrostatic pressure is thus a function of the free-surface elevation $\eta$. It can be obtained by solving the depth-averaged continuity equation. The detail of this solution is described in the following sections.

The dynamic pressure is coupled to the velocity field and can be solved by Chorin and Teman projection scheme [109].

### 3.1.3 Hydrostatic Navier-Stokes equations

In large scale simulations, the model domain usually covers thousands of square kilometres. The horizontal dimension of the water body is far larger than the vertical dimension. Therefore the diffusion, source terms and acceleration in the vertical direction can be neglected. In this case, if the pressure at one point only depends on the weight of the column of water above it, the Navier-Stokes equations can be simplified to a hydrostatic version.

In view of hydrostatic hypothesis, the Navier-Stokes equations are re-written as follows: Mass conservation:

$$\frac{\partial u_1}{\partial x_1} + \frac{\partial u_2}{\partial x_2} + \frac{\partial u_3}{\partial x_3} = 0 \tag{3.8}$$

Momentum equation:

$$\frac{\partial u_1}{\partial t} + u_1\frac{\partial u_1}{\partial x_1} + u_2\frac{\partial u_1}{\partial x_2} + u_2\frac{\partial u_1}{\partial x_3} = -g\frac{\partial \eta}{\partial x_1} + \nu\left(\frac{\partial^2 u_1}{\partial x_1^2} + \frac{\partial^2 u_1}{\partial x_2^2} + \frac{\partial^2 u_1}{\partial x_3^2}\right) + F_{x_1} \tag{3.9}$$

$$\frac{\partial u_2}{\partial t} + u\frac{\partial u_2}{\partial x_1} + u_2\frac{\partial u_2}{\partial x_2} + u_3\frac{\partial u_2}{\partial x_3} = -g\frac{\partial \eta}{\partial x_2} + \nu\left(\frac{\partial^2 u_2}{\partial x_1^2} + \frac{\partial^2 u_2}{\partial x_2^2} + \frac{\partial^2 u_2}{\partial x_3^2}\right) + F_{x_2} \tag{3.10}$$

Pressure:

$$p = p_{atm} + \rho_0 g(\eta - x_3) + \rho_0 g \int_{x_3}^{\eta} \frac{\Delta\rho}{\rho_0} dx_3 \tag{3.11}$$

### 3.1.4 Boundary

The boundary conditions have to be applied when solving the Navier-Stokes equations however their forms for free surface flows are complex. They include:

- A free surface of the water evolving with time;
- An impermeable bottom;
- Structures with impermeable walls such as bridge piles, dykes, for instance;
- Open boundaries such as upstream and downstream limits of a river, or for instance, in this study, the tide variation is used as the open boundary.

To start with, the boundary conditions will be established at the free surface and at the bottom and, subsequently, at the walls and open boundaries.

#### Free surface

The kinematic boundary condition as shown in the following equation is applied to the free surface.

$$\frac{d}{dt}(x_3 - \eta) = 0 \tag{3.12}$$

The assumption to build this equation is that the fluid particle is adjacent to the surface, thus the velocity of the fluid is the same as the velocity of the free-surface. If the velocity of a point fixed on the surface has the components $u_1^s$, $u_2^s$ and $u_3^s$, the equation 3.12 can be re-written with Euler variables:

$$u_3^s - \frac{\partial\eta}{\partial t} - u_1^s \frac{\partial\eta}{\partial x_1} - u_2^s \frac{\partial\eta}{\partial x_2} = 0 \tag{3.13}$$

where $u_i^s$ is the velocity components at the surface. $\eta$ is the surface elevation.

#### Bottom

At the bottom, similar equation is obtained as:

$$u_3^b - \frac{\partial Z_b}{\partial t} - u_1^b \frac{\partial Z_b}{\partial x_1} - u_2^b \frac{\partial Z_b}{\partial x_2} = 0 \tag{3.14}$$

where $u_i^b$ the velocity components at bottom. $Z_b$ represents the bottom elevation.

#### Walls

On the walls, an impermeability condition is applied as:

$$\vec{U} \cdot \vec{n} = 0 \tag{3.15}$$

where $\vec{U}$ represents the fluid velocity on the solid boundary and $\vec{n}$ is the normal vector to the walls.

#### Open boundaries

On the open boundaries, additional information is needed, as for instance the pressure, the water depth, the velocity or the discharge.

### 3.1.5 Discretisation of the Navier-Stokes equations

#### Three dimensional mesh

In this study, the simulation domain is represented by a three dimensional mesh. To build it, an unstructured triangular mesh is generated from the bottom first and then this 2-D mesh is repeated along the vertical in superimposed layers. As shown in figure 3.1, the mesh in 3-D is made of prisms with six nodes, their quadrangular sides being vertical.

In this study, two different methods are used for coupling the horizontal mesh with the vertical direction.

The first method makes planes evenly spaced along the vertical which means starting with the coordinate nodes $(x_1, x_2)$ of the 2-D mesh, then defining the elevation for each point of the 3D mesh with coordinates $(x_1, x_2, x_3)$, according to the formula:

$$x_3(x_1, x_2, i_p) = Z_b(x_1, x_2) + \frac{i_p - 1}{n_p - 1}(Z_s(x_1, x_2) - Z_b(x_1, x_2)) \tag{3.16}$$

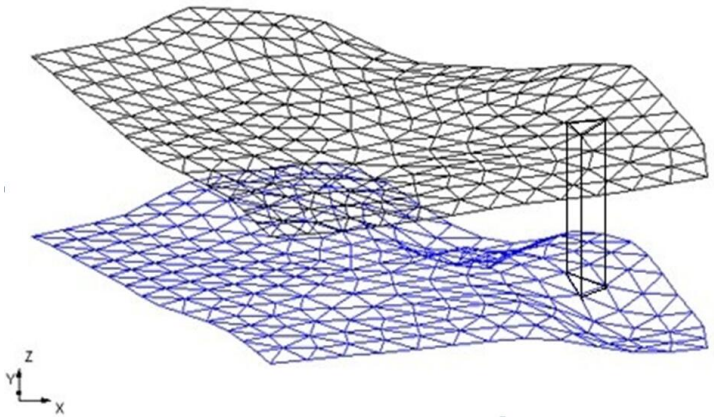


**Figure 3.1:** 3D mesh of calculation domain

$Z_b$ always being the bottom elevation, $Z_s$ the free surface elevation and $i_p$ is the index of the plane under consideration (planes range from 1 to $n_p$ going from the bottom to the free surface). In this case, the vertical coordinate ${x_3}^*$ of each plane in the transformed mesh is simply $\dfrac{i_p - 1}{n_p - 1}$.

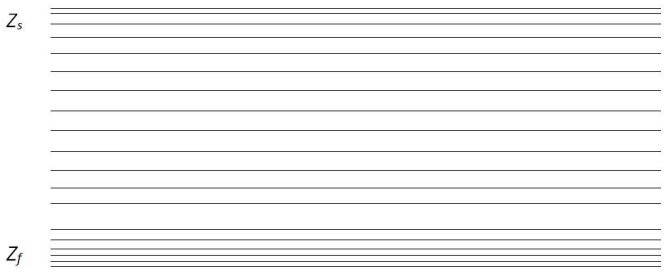


**Figure 3.2:** Example of vertical distribution of the planes

The second method is based on unevenly distributed planes along the vertical. The turbulence effect can be represented more precisely by having high resolution close to the boundaries (near surface and bottom). When the total number of planes is controlled, this approach helps create more planes close to both bottom and surface layers but fewer planes in the middle as shown in figure 3.2.

The vertical coordinate ${x_3}^*$ of each plane in the transformed mesh is given by the following formula:

$$ {x_3}^*(ip) = \sigma_0 e^{k_a - \frac{(1-\sigma_0)k_a^2}{2k_m}} - \sigma_0 \tag{3.17} $$

$$k_m = 2\frac{\ln(1+1/\sigma_0)}{1+\sigma_0} \tag{3.18}$$

$$k_a = k_m\frac{i_p-1}{n_p-1} \tag{3.19}$$

where $\sigma_0$ is a relaxation coefficient. In this study, $\sigma_0 = 0.05$.

**Sigma transform**

During the calculation, the free-surface of the domain varies as a function of time. A sigma transform is applied in the vertical direction to deal with the vertical motion of the planes. A mapping from ($Z_b$, $Z_s$) to (0,1) is used as follows.

And the following change of variables is used:

$$x_3^* = \frac{x_3 - Z_f}{Z_s - Z_b} = \frac{x_3 - Z_b}{h} \tag{3.20}$$

where $Z_b$ and $Z_s$ are the bottom elevation and surface elevation respectively, $h$ being the water depth.

**Fraction Step method**

The equations of motion with free-surface are solved by following steps:

1. Advection step:

   The advection terms are calculated by:

$$\frac{u_i^C - u_i^n}{\Delta t} + (u_i^n \cdot \nabla)u_i^n = 0 \tag{3.21}$$

$$\tag{3.22}$$

   where $\Delta t$ is the time-step; $u_i^n$ are the velocity components at the old time-step, and $u_i^C$ is the result of this advection step.

2. Hydrostatic step:

   In this step, the hydrostatic pressure assumption, equation 3.11, is used. Firstly, the free-surface $\eta$ is solved by the depth-averaged continuity equation, as:

$$\begin{aligned}\frac{\eta^{n+1}-\eta^n}{\Delta t} + \eta^n\Big[\theta_u\big(\frac{\partial u_1^{n+1}}{\partial x_1} + \frac{\partial u_2^{n+1}}{\partial x_2} + \frac{\partial u_3^{n+1}}{\partial x_3}\big) \\ +(1-\theta_u)\big(\frac{\partial u_1^n}{\partial x_1} + \frac{\partial u_2^n}{\partial x_2} + \frac{\partial u_3^n}{\partial x_3}\big)\Big] = 0\end{aligned} \tag{3.23}$$

where $\theta_u$ is an implicitation coefficient for the velocity.

Then the velocity components are obtained by calculating the (hydrostatic) momentum equations following the hydrostatic assumption:

$$\frac{u_i^{hyd} - u_i^C}{\Delta t} = -g\ \theta_h\ \nabla(\eta^{n+1} - \eta^n) - g\ \nabla(\eta^n) + \nabla \cdot (\nu\ \nabla(u_i)) + F_i \tag{3.24}$$

3. In the hydrostatic version, $u_i^{hyd}$ (i=1,2) is the final 2D horizontal velocity, and then the vertical velocity $u_3^{n+1}$ is calculated by the three-dimensional continuity equation.

4. In the non-hydrostatic version, momentum equation for $u_3$ is added as:

$$\frac{\partial u_3}{\partial t} + (u_3 \cdot \nabla)u_3 = -\frac{1}{\rho_0}\frac{\partial p_d}{\partial x_3} + \nabla \cdot (\nu\ \nabla(u_3)) \tag{3.25}$$

where the $p_d$ is the non-hydrostatic pressure which can be solved by a Poisson equation.

Finally, the free-surface can be updated again by the depth-averaged continuity equation.

**Finite element method**

In TELEMAC, the Navier-Stoke equations are discretised by finite element method (FEM). This approach is based on two principal ideas: an interpolation method and a variational method known as 'weighted residuals'. The interpolation discretises the unknown and the variational principle discretises the equation.

For example, let's consider our equations are in the form of:

$$L(u) = f \tag{3.26}$$

The general idea is to replace an unknown function $u$, which belongs to an infinite dimensional space, by an approximation $u_h$ defined on a finite dimensional space N. This is an approximation and we cannot always ensure that $L(u_h) = f$. We simply try to minimize $L(u_h) - f$ and this will be the goal of the variational method.

TELEMAC offers different interpolation functions depending on the mesh used for calculations. The TELEMAC-3D mesh structure is made of prisms(eventually split in tetrahedrons). Therefore in this study, we stick on the interpolation of PRISM.

Figure 3.3 shows a prism with 3 vertical rectangular faces, and two triangular faces, one at the bottom and one at the top, and which are not necessarily horizontal. This mesh structure is the same as the one used in our simulations.

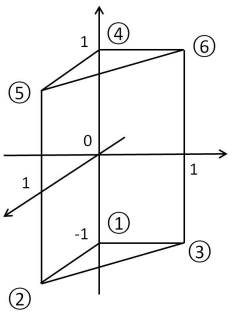


**Figure 3.3:** reference element for a prism

In figure 3.3, the numbers in circles indicate local numbering of the nodes.

The Basis functions $\Psi_j$ corresponding to the nodes $j$ of the reference element are:

$$\Psi_1 = (1-\alpha-\beta)\big(\frac{1-\gamma}{2}\big) \tag{3.27}$$

$$\Psi_2 = \alpha\big(\frac{1-\gamma}{2}\big) \tag{3.28}$$

$$\Psi_3 = \beta\big(\frac{1-\gamma}{2}\big) \tag{3.29}$$

$$\Psi_4 = (1-\alpha-\beta)\big(\frac{1+\gamma}{2}\big) \tag{3.30}$$

$$\Psi_5 = \alpha\big(\frac{1+\gamma}{2}\big) \tag{3.31}$$

$$\Psi_6 = \beta\big(\frac{1+\gamma}{2}\big) \tag{3.32}$$

The basis function $\varphi_i$ on any prism in the $\Omega$ mesh are obtained by creating the $\Psi_i$ functions with the isoparametric transformation F, transforming the reference prism into this prism of any type.

The $\Psi_i$ function which appear in the definition of F are the same as the basis function defined on the reference element since the reference element chosen is isoparametric(the interpolation nodes are also the geometric nodes). In our case, the expressions

of F can be simplified since:

$$x_1 = x_4 \quad ; \quad y_1 = y_4 \tag{3.33}$$

$$x_2 = x_5 \quad ; \quad y_2 = y_5 \tag{3.34}$$

$$x_3 = x_6 \quad ; \quad y_3 = y_6 \tag{3.35}$$

The following is therefore obtained for F:

$$\begin{cases} x = (1-\alpha-\beta)x_1 + \alpha x_2 + \beta x_3 \\ y = (1-\alpha-\beta)y_1 + \alpha y_2 + \beta y_3 \\ z = [(1-\alpha-\beta)z_1 + \alpha z_2 + \beta z_3]\left[\frac{1-\gamma}{2}\right] + [(1-\alpha-\beta)z_4 + \alpha z_5 + \beta z_6]\left[\frac{1+\gamma}{2}\right] \end{cases} \tag{3.36}$$

The following is deduced for the$\varphi_i$ functions: $\varphi_i(x,y,z) = \Psi_i(F^{-1}x, y, z)$

Having restricted out function $u$ to a representation $u_h$, based on a discrete number of unknowns $u_i$, we now wish to minimize $L(u_h) - f$. The variational method states that the dot product $\int_\Omega (L(u_h) - f)\varphi_i d\Omega$ is zero for some functions $\varphi_i$ called test functions. The choice of these functions defines the variants of the finite element method. In this study, we select the Galerkin technique which consists in choosing test functions equal to the basis functions: $\varphi_i = \Psi_i$. When $u_h$ is decomposed as $\sum_{i=1}^{n} u_i \Psi_i$, the variational method will clearly lead to a linear system of unknowns $u_i$.

## 3.2 Turbulence modelling

The flow around piles of wind turbines or around marine turbines is very turbulent. TELEMAC-3D offers the user several options for turbulence modelling to compute the turbulent eddy viscosity: (i) a constant viscosity model; (ii) a mixing length model; (iii) a k-$\epsilon$ two equation model; and (iv) a space/flow dependent eddy viscosity following Smagorinsky (1963), which is commonly called Large Eddy Simulation (LES).

The constant viscosity model is only sufficient when the flow is governed by the pressure gradient and advection. The mixing length model is used to describe the velocity profile in the vicinity of a wall. The k-$\epsilon$ model comprises a couple of equations solving the balance equations for k (turbulent energy) and $\epsilon$ (turbulent dissipation). This approach can only give a time averaged mean value for the velocity field. The

Smagorinsky model can be used to compute instantaneous velocity profiles, however there are two drawbacks in the current turbulence approach. The first one is that it uses the same length scale both in horizontal and vertical. Due to the strong grid anisotopy in coastal engineering modelling, it is difficult to find a proper single length scale for the model. The second drawback is that it only takes the strain rate of the turbulent structure into consideration but not the rotation rate.

Therefore, in this study, two new turbulence models including the 2eddy LES model [80] and the Wall-Adapting Local Eddy-Viscosity (WALE) model [110] are implemented in TELEMAC-3D, in an attempt to circumvent the 2 aforementioned drawbacks.

### 3.2.1 The 2eddy LES turbulence model

This model is based on the assumption [75], which pointed out that the large eddies of the flow are dependent on the geometry while the smaller scales are universal. This feature enables the model to separate the turbulent flow into large and small parts by a filtering process based on an energy cascade. The large eddies are computed, while the small eddies are modelled by using a sub grid-scale model.

The smagorinsky model is the first ever derived LES turbulence model. The smallest turbulent scales would naturally appear in the numerical solutions if the size of the finite elements would allow the reproduction of all the mechanisms including the viscous dissipation of very small vortices. Only in the formation of smaller vortices, where turbulence is inhibited by the mesh, modelling takes place.

The classic Smagorinsky model is computed as:

$$\nu_t = C_s^2 \Delta^2 \sqrt{2 S_{ij} S_{ij}} \tag{3.37}$$

where $\nu_t$ is the turbulent viscosity, $S_{ij}$ the strain rate tensor of the filtered velocities, with:

$$S_{ij} = \frac{1}{2}\left(\frac{\partial u_i}{\partial x_j} + \frac{\partial u_j}{\partial x_i}\right) \tag{3.38}$$

where $C_s$ is a dimensionless coefficient to be calibrated and $\Delta$ is the mesh size derived in 2-D or 3-D from the surface or from the volume of an element.

Based on the assumption that the small scales tend to isotropy, the standard Smagorinsky model relies on the small and isotropic mesh elements. The eddy vis-

cosity is evaluated as the product of a length-scale $C_s\Delta$, proportional to the grid size, and a velocity scale $C_s\Delta|S_{ij}|$.

In order to solve large scale fluid mechanics, the mesh used in coastal engineering is normally anisotropic and there is a big difference between the horizontal and vertical element size. It is difficult to define a single length-scale for both horizontal and vertical directions. A newly developed Large Eddy Simulation model, namely the 2eddy LES turbulence model [111] is used.

The 2eddy LES model shares similar ideas as to these of the Smagorinsky model, but uses different length-scales in the horizontal and vertical directions respectively. Two turbulence viscosities $\nu_{t,h}$ and $\nu_{t,v}$ are commonly used in geophysical fluid dynamics [111], with $h$ and $v$ representing the horizontal and the vertical component respectively. The diffusive term of the Navier-Stokes equations is calculated for each velocity component i, as:

$$D_i = \frac{\partial}{\partial x_1}\nu_h\frac{\partial u_i}{\partial x_1} + \frac{\partial}{\partial x_2}\nu_h\frac{\partial u_i}{\partial x_2} + \frac{\partial}{\partial x_3}\nu_v\frac{\partial u_i}{\partial x_3} \tag{3.39}$$

where $\nu_h = \nu + \nu_{t,h}$ and $\nu_v = \nu + \nu_{t,v}$. Adopting the 2eddy LES model to reproduce the sub-grid stress as in the Smagorinsky model we have:

$$\nu_{t,h} = (C_h L_h)^2|\overline{S}_h| \tag{3.40}$$

$$\nu_{t,v} = (C_v L_v)^2|\overline{S}_v| \tag{3.41}$$

where $C_h$ and $C_v$ are the coefficient of the model and $L_h$ and $L_v$ are the length-scales for the horizontal and vertical directions respectively. In the original model for structured grids, $L_h$ and $L_v$ are computed as:

$$L_h = \sqrt{\Delta {x_1}^2 + \Delta {x_2}^2} \tag{3.42}$$

$$L_v = \Delta x_3 \tag{3.43}$$

Where $\Delta x_i$ are the spacing in the $i^{th}$ direction.

For unstructured grids (finite elements for instance), defining $\Delta x_1$ and $\Delta x_2$ is not easy. The L are here computed from the volume element and the vertical spacing $\Delta x_3$. $\Delta x_3$ is obtained by calculating the vertical distance between two nodes. $L_h$ is then approximated by $L_h = \sqrt{V_{element}/\Delta x_3}$, where $V_{element}$ is the volume of the element.

The strain rate tensors, in both directions, namely $|\overline{S}_h|$ and $|\overline{S}_v|$ are decomposed as:

$$|\overline{S}_h| = \sqrt{2S_{11}^2 + 2S_{22}^2 + 2S_{12}^2} \tag{3.44}$$

$$|\overline{S}_v| = \sqrt{2S_{13}^2 + 2S_{23}^2 + 2S_{33}^2} \tag{3.45}$$

The coefficients of the model need calibration and this is still an open issue, as the model has not been tested on a wide range of configurations. An ideal test case should be able to catch the anisotropic behaviour of the unresolved turbulent scales. Roman et al [80] has applied the 2eddy LES model to investigate the hydrodynamics of Muggia Bay in Italy. The turbulence mixing in a 20 m depth bay was successfully reproduced. This simulation environment is similar to the one of this study. Therefore in this study, $C_h$ and $C_v$ are set to 0.005 and 0.25 respectively which is the same as the recommended values in [80].

### 3.2.2 Wall-Adapting Local Eddy-Viscosity turbulence model

In LES, the eddy-viscosity $\nu_t$ must not change when the frame of reference is changed. Clearly the velocity gradient tensor $g_{ij} = \dfrac{\partial u_i}{\partial x_j}$ is a good choice to represent the velocity fluctuations at the length scale $\Delta$. The Smagorinsky model is based on the second invariant of the symmetric part $S_{ij}$ of this tensor. However there are two major drawbacks associated with this choice:

- This invariant is only related to the strain rate of the turbulent structure but not the rotation rate.
- It does not offer a proper wall-scaling to get a good prediction of the friction coefficient.

In order to overcome the aforementioned disadvantages, a new turbulence model named Wall-Adapting Local Eddy-Viscosity (WALE) [112] is also tested. In this approach, a better operator with the traceless symmetric part of the square of the velocity gradient tensor is considered as follows:

$$S_{ij}^d = \frac{1}{2}\left(g_{ij}^2 + g_{ji}^2\right) - \frac{1}{3}\delta_{ij} g_{kk}^2 \tag{3.46}$$

where $g_{ij}^2 = g_{ik}g_{kj}$ and $\delta_{ij}$ is the Kronecker symbol. Einstein summation is used here. The anti-symmetric part of $g$, $\Omega$ is represented by:

$$\Omega_{ij} = \frac{1}{2}\left(\frac{\partial u_i}{\partial x_j} - \frac{\partial u_j}{\partial x_i}\right) \tag{3.47}$$

The tensor defined by equation 3.46 can be rewritten in terms of

$$S_{ij}^d = S_{ik}S_{kj} + \Omega_{ik}\Omega_{kj} - \frac{1}{3}\delta_{ij}\left[S_{mn}S_{mn} - \Omega_{mn}\Omega_{mn}\right] \tag{3.48}$$

By using equation 3.48 and making use of the Cayley-Hamiltion theorem for linear algebra, this quantity can be developed as:

$$S_{ij}^d S_{ij}^d = \frac{1}{6}\left(S^2S^2 + \Omega^2\Omega^2\right) + \frac{2}{3}S^2\Omega^2 + 2IV_{S\Omega} \tag{3.49}$$

with the notations:

$$S^2 = S_{ij}S_{ij}$$

$$\Omega^2 = \Omega_{ij}\Omega_{ij}$$

$$IV_{S\Omega} = S_{ik}S_{kj}\Omega_{ik}\Omega_{kj}$$

According to equation 3.49, an LES model based on $S_{ij}^d S_{ij}^d$ will detect turbulence structures with either strain rate, rotation rate or both. The expression for the eddy-viscosity reads as:

$$\nu_t = (C_w\Delta)^2 \frac{\left(S_{ij}^d S_{ij}^d\right)^{3/2}}{\left(S_{ik}S_{kj}\right)^{5/2} + \left(S_{ij}^d S_{ij}^d\right)^{5/4}} \tag{3.50}$$

In equation 3.50, the spatial operator $\left(S_{ij}^d S_{ij}^d\right)^{3/2}$ behaves like $x_2^3$ near a wall. $\left(S_{ik}S_{kj}\right)^{5/2}$ and $\left(S_{ij}^d S_{ij}^d\right)^{5/4}$ scale the operator and make it in the proper dimension of frequency for subgrid scale model formulation. $C_w$ is the constant which was suggested, i.e. $C_w^2 \approx 10.6C_s^2$ [110]

### 3.2.3 The implementation in TELEMAC-3D

In the code of TELEMAC-3D, two new subroutines are created to compute the viscosity by the 2eddy LES model and WALE model respectively. Following the programming rule in the existing code, the formulations shown in the last two sections are written.

The Navier-Stokes equations are discretised by the finite element method (FEM), therefore most of the variables in the calculation are written in the form of $u_h = \sum_{i=1}^{n} u_i \Psi_i$. For example, the velocity gradients are calculated as:

$$(\nabla u)_i = X_{MUL} \int_{\Omega} \Psi_i \overrightarrow{grad}(u_i) d\Omega \tag{3.51}$$

where $X_{MUL}$ is a multiplication factor; $\Psi_i$ is the test function.

This subroutine computes the integral over the domain of the gradient multiplied by the test function at prism level. It considers the averaged gradient multiplied by a surface which is the integral of test functions on the domain. Then this surface is considered to be $\Delta^2$. For instance, if we calculate the Smagorinsky viscosity:

$$\upsilon_t = C_s^2 \sqrt{2 S_{ij} S_{ij}} \tag{3.52}$$

Actually, what we have is written as follows:

$$S_{ij} = \frac{1}{2}\left(\frac{\partial U_i}{\partial x_j} V_{element} + \frac{\partial U_j}{\partial x_i} V_{element}\right) \tag{3.53}$$

In 2-D this approach is correct as the extra area that we get from the gradient formulation stands for the square of the mesh size. However, in 3-D we get an extra volume.

A correction was made in the calculation of strain rate tensor $S_{ij}$, so that the exact velocity gradients could be computed. The formula of the velocity gradients are written as:

$$VEC(i) = \frac{XMUL}{volume} \int_{\Omega} \Psi_i \nabla(F) d\Omega \tag{3.54}$$

Then the turbulence viscosity is computed by equation 3.40 3.41 or equation 3.50

## 3.3 Immersed Boundary Method

The immersed boundary method used here is based on direct forcing method which relies on forces applied to some nodes of the mesh, which impedes the flow along the

solid boundaries. The additional IB force replaces the actual reaction force on the solid surface and is activated by using source terms in the momentum equations of the Navier-Stokes equations. The forcing step is added in the 'hydrostatic' step where the hydrostatic velocity is solved.

The forcing step in the current modified model can be represented as:

$$\frac{u_1^{n+1} - u_1^C}{\Delta t} = -g(\frac{\partial \eta}{\partial x_1}) + \nu\left(\frac{\partial^2 u_1}{\partial x_1^2} + \frac{\partial^2 u_1}{\partial x_2^2} + \frac{\partial^2 u_1}{\partial x_3^2}\right) + F_{x_1} \tag{3.55}$$

$$\frac{u_2^{n+1} - u_2^C}{\Delta t} = -g(\frac{\partial \eta}{\partial x_2}) + \nu\left(\frac{\partial^2 u_2}{\partial x_1^2} + \frac{\partial^2 u_2}{\partial x_2^2} + \frac{\partial^2 u_2}{\partial x_3^2}\right) + F_{x_2} \tag{3.56}$$

$$\tag{3.57}$$

where $u_i^C$ are the velocity components obtained from the previous advection step and $F_{x_i}$ contains the buoyancy terms.

Following [113], the force terms are obtained by rearranging equations 3.57 and substituting $u_1^{n+1}$, $u_2^{n+1}$, $u_3^{n+1}$ with the desired velocity at the solid node. By applying non-slip boundary conditions at the solid surface, the IB force terms are defined as:

$$F_{x_1}^{ibm} = \begin{cases} \dfrac{0 - u_1^C}{\Delta t} + g(\dfrac{\partial \eta}{\partial x_1}) \\ -\nu\left(\dfrac{\partial^2 u_1}{\partial x_1^2} + \dfrac{\partial^2 u_1}{\partial x_2^2} + \dfrac{\partial^2 u_1}{\partial x_3^2}\right) - F_{x_1} \text{ , on the boundary node} \\ 0 \text{ , elsewhere} \end{cases}$$

$$F_{x_2}^{ibm} = \begin{cases} \dfrac{0 - u_2^C}{\Delta t} + g(\dfrac{\partial \eta}{\partial x_2}) \\ -\nu\left(\dfrac{\partial^2 u_2}{\partial x_1^2} + \dfrac{\partial^2 u_2}{\partial x_2^2} + \dfrac{\partial^2 u_2}{\partial x_3^2}\right) - F_{x_2} \text{ , on the boundary node} \\ 0 \text{ , elsewhere} \end{cases}$$

Because the finite element method is used to discretise the equations, the value of one node relies on the values of the surrounding nodes. Therefore, although the velocities on the IB nodes can be set to zero by applying the additional force (this is because of the assumption that the boundary of an obstacle is accounted for during meshing), small velocity fluctuations can still be observed inside the obstacle. In order to keep the model stable, a zero velocity condition is applied on all the nodes inside of the obstacle at each time-step. When dealing with submerged structures in the water, the vertical zero velocity condition is used at all immersed boundary nodes.

## 3.4 Sediment transport modelling

The total transport rate at each computational node is split into bed-load and suspended-load transport. For the bed-load simulations, the Soulsby-Van Rijn formula is used as it is suitable for use in cases with combined currents and waves. The transport rate is represented by the following equations:

$$Q_{b,s} = A_{b,s}u\big[\big(u^2 + 2\frac{0.018}{C_D}u_0^2\big)^{0.5} - u_{cr}\big]^{2.4} \tag{3.58}$$

where $u_0$ is the orbital velocity of the waves, $C_D$ is the quadratic drag coefficient due to the current. This formula considers the sand transport rate both of bed load $Q_b$ and suspended load $Q_s$. $A_{b,s}$ are the bed load and suspended load coefficients which are computed as:

$$A_b = \frac{0.005h(d_{50}/h)^{1.2}}{[g(s-1)d_{50}]^{1.2}} \tag{3.59}$$

$$A_s = \frac{0.012d_{50}D_*^{-0.6}}{[g(s-1)d_{50}]^{1.2}} \tag{3.60}$$

where $d_{50}$ is the median grain size, $D_*$ is the dimensionless grain size defined as:

$$D_* = \big[\frac{g(s-1)}{\nu^2}\big]^{1/3}d_{50} \tag{3.61}$$

The critical entrainment velocity $u_{cr}$ is defined as:

$$u_{cr} = 0.19d_{50}^{0.1}\log_{10}\big(\frac{4h}{d_{90}}\big)\text{if } 0.1\ mm \leq d_{50} \leq 0.5\ mm \tag{3.62}$$

$$u_{cr} = 8.5d_{50}^{0.6}\log_{10}\big(\frac{4h}{d_{90}}\big)\text{if } 0.5\ mm \leq d_{50} \leq 2\ mm \tag{3.63}$$

where $d_{90}$ is the characteristic of the coarser grains that 90% of the grains by mass are finer.

The three dimensional suspended sediment concentration is calculated by considering the local mass conservation of a tracer. The equation is written as

$$\frac{\partial C}{\partial t} + \nabla\cdot(Cu + Cw_s) = \nabla\cdot(\nu_t\nabla C) \tag{3.64}$$

where $\nu_t$ is the turbulent diffusivity coefficient $(m^2s^{-1})$. $\overrightarrow{w_s} = (0, 0, -w_s)$ is the sediment settling velocity $(ms^{-1})$.

## 3.5 The TELEMAC system

In this study, the open-source TELEMAC-3D software is used as a tool to numerically model the 3D hydrodynamics.

TELEMAC-3D is part of a processing chain, namely the TELEMAC system [11]. This system also includes a sediment transport module SISYPHE and a wave module TOMAWAC. Triple coupling of these modules gives all the requirements to perform simulations of hydrodynamic flow, contaminant and sediment transport. The details of a full model operation procedure can be found in figure 3.4.

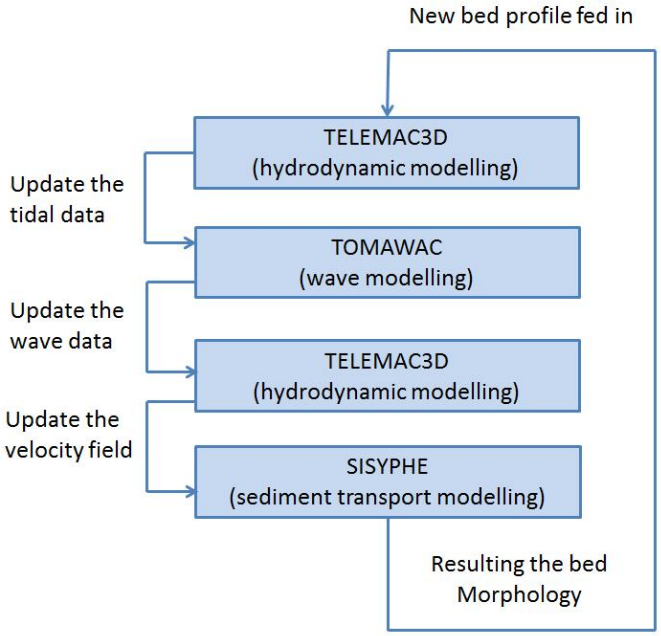


**Figure 3.4:** Simulation procedure with the TELEMAC modelling system

The files to perform a simulation include a steering file, a mesh file, a boundary file, and potentially a Fortran file. The steering file contains all the parameters which will be used in that simulation. The mesh file contains all the mesh information (for instance the number of nodes and elements, the initial value of each node.). The boundary conditions are defined on all the boundary nodes. The Fortran file allows the user to modify and use their owe code.

# Chapter 4

# Turbulence model validation

This chapter illustrates the validation of the implementation of the 2eddy LES model [80] and the wall-adapted local-eddy viscosity (WALE) model [112]. The laboratory experiment of Roulund et al. [114] is used to calibrate the models.

### 4.0.1 The experiment

Roulund et al. [114] conducted a rough rigid bed experiment with a vertical circular pile in a steady current. A pile of a diameter D = 0.536 m was sealed along its perimeter on a rigid bed covered by a single layer of crushed stones, the roughness height of which was k = 0.77 cm. It was conducted in a 28 m long and 4 m wide flume. The water depth was maintained at 0.54 m. The approach velocity was 0.326 m/s, which was obtained from the integration of the velocity profile. Only velocity measurements were carried out in this test. The measurements were conducted using a two-component DANTEC 'pen-size' laser-Doppler anemometer (LDA) in the plane of symmetry upstream and downstream of the pile. The focal length of the pen-size probe with a specially built adaptor was 8 cm. The measurement volume (dx dy dz) was 1.5 mm, 0.12 mm, 0.12 mm. In this study, the influence of the horseshoe vortex and the lee wake vortex flow processes around the pile was investigated. The author pointed out that the Reynolds number and the boundary-layer thickness have significant impact on the turbulence around the structure.

To further investigate the capability of the new turbulence approach, both turbulence models are used in the simulation of the flow around a circular cylinder and their

results compared to the laboratory measurement of Roulund et al [114].

## 4.1 Model setup

The validation of the two new turbulence implementations use the same computational mesh, boundary conditions and parameter settings.

### 4.1.1 Computational domain

Following Roulund et al [114], the simulation domain is set to be 50 m long by 4 m wide. The bed is assumed to be flat with a constant depth of 0.54 m. A cylinder with a diameter of 0.53 m (D) is placed at 13 m downstream of the inlet as in figure 4.1.

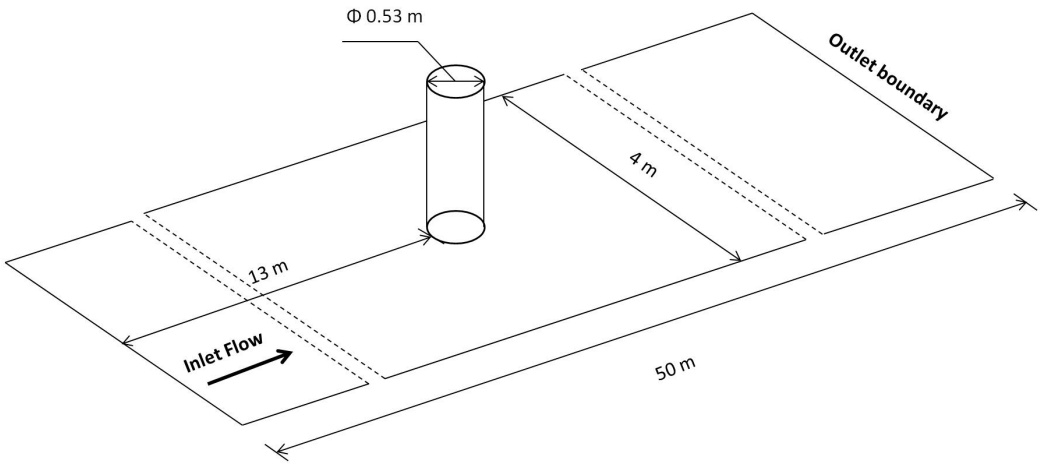


**Figure 4.1:** Geometry of the computed domain.

### 4.1.2 Computational mesh

To assess the mesh dependency of the solution, three meshes with different grid density are used. An initial mesh, called *mesh1* is generated using 47,546 triangular elements in the 2-D horizontal plane and 50 non-equally distributed vertical layers across the water depth. The mesh around the cylinder up to 5 m behind the cylinder is refined to capture the wake dynamics. As comparison, two other 2-D meshes, *mesh2* and *mesh3* are generated with 91,628 elements and 282,740 elements respectively, the same vertical

distribution being used for these 2 meshes as well. A zoom of the difference between the three meshes can be found in figures 4.2, 4.3 and 4.4.

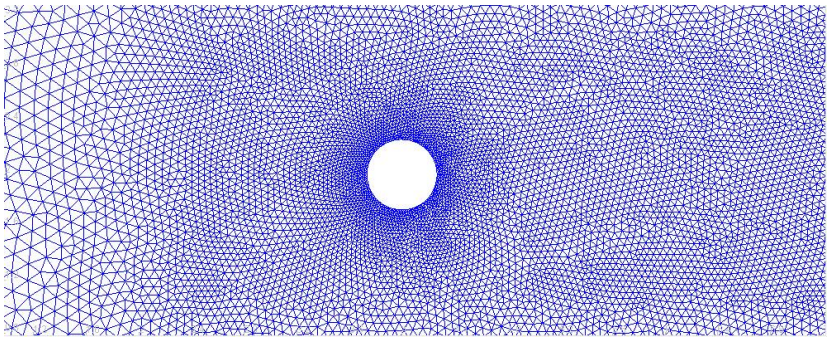

**Figure 4.2:** mesh1 with 47,546 triangular elements

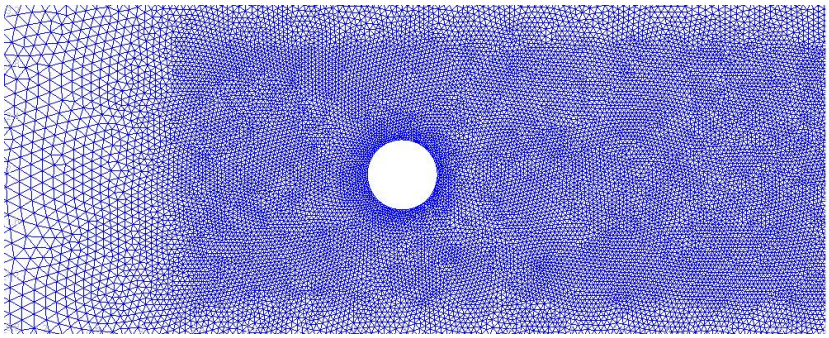

**Figure 4.3:** mesh2 with 91,628 triangular elements

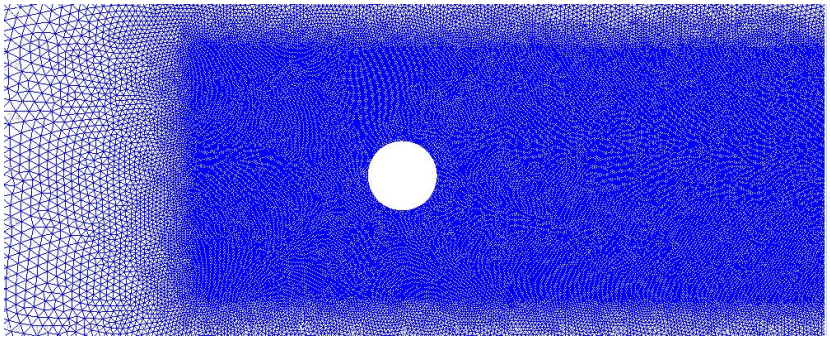

**Figure 4.4:** mesh3 with 282,740 triangular elements

In *mesh1*, the element average edge size behind the cylinder is about 0.05 m. In *mesh2* and *mesh3*, the element average edge size behind the cylinder reduces to 0.035 m and 0.02 m respectively. All three meshes have the same resolution around the circular cylinder.

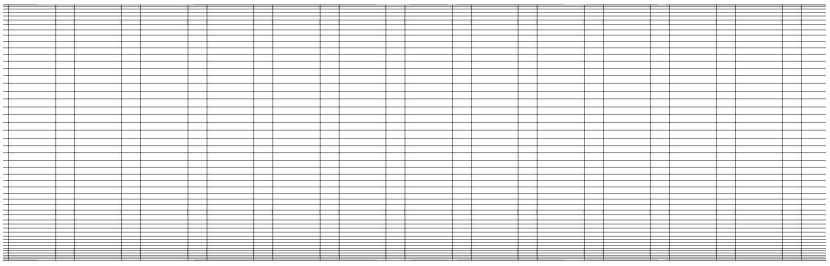

**Figure 4.5:** The vertical mesh with 50 non-equally mesh

In the vertical direction, 50 non-equally distributed sigma transform layers are used. The distance between consecutive layers is specified according to equation 3.17. The minimum distance between two layers is found at the bottom and surface, which is about 0.003 m. In the middle of the mesh, the distance between two layers is about 0.015 m.

### 4.1.3 Boundary conditions

Apart from the free surface which is directly treated by the solver, the boundaries of the computational domain include inlet, outlet, walls and bottom.

1. *Inlet*: At the inlet, a flow rate Q is specified. The value of Q is calculated from the horizontal velocity, which follows the same flow settings as in Roulund et al's experiment.

2. *Outlet*: At the outlet, prescribed elevations are given.

3. *Wall*: The walls of the flume and pile are set as solid walls. Sidewall friction is not accounted for in this study.

4. *Bottom*: The bed roughness is specified in both smooth bed and rough bed conditions according to the experiment.

### 4.1.4 Parameter settings

Table 4.1 summarises the test conditions for the cylinder case. Two conditions from the experiment in [114] are used, one for a smooth bed and the other one for a rough

bed. In the rough bed simulations, the bottom friction is modelled by the Nikuradse law and the friction coefficient $ks$ is set to 0.1 cm.

In the table, the Reynolds number $Re$ reads,

$$Re = \frac{UD}{\nu} \tag{4.1}$$

where $U$ is the mean flow velocity and $D$ is the diameter of the cylinder. Also mentioned in the table, the Froude number $Fr$ is defined as

$$Fr = \frac{U}{\sqrt{gh}} \tag{4.2}$$

in which $h$ is the water depth.

| Test | 1 | 2 |
|---|---|---|
| Bed | Rigid | Rigid |
| Smooth bed/rough bed | Smooth | Rough |
| Water depth $h$ (m) | 0.54 | 0.54 |
| Mean Flow velocity $U$ $(ms^{-1})$ | 0.326 | 0.326 |
| Pile diameter $D$ $(m)$ | 0.54 | 0.54 |
| $Re$ | $1.7 \times 10^5$ | $1.7 \times 10^5$ |
| $Fr$ | 0.14 | 0.14 |
| Bed Nikuradse equivalent sand Roughness $ks(cm)$ | - | 0.1 |
| Mesh | $mesh1/mesh2/mesh3$ | $mesh1/mesh2/mesh3$ |

**Table 4.1:** Test conditions for the numerical modelling

In all the tests, a time step of 0.01 s is chosen to keep the maximum Courant number below 0.8.

The Courant number is defined as:

$$C = U_{mean}\frac{\Delta t}{\Delta x} \tag{4.3}$$

where $U_{mean}$ is the depth-mean flow velocity and $\Delta x$ is the smallest element size.

In order to ensure that the flow is fully developed, each test is run for 30 minutes and the last 100 seconds of the instantaneous results are collected for analysis and comparison.

## 4.2 Validation of the model

In the appendix, two conference papers from the author [115, 116] related to the turbulence modelling validation are attached. In order to have a more comprehensive view, the behaviour of TELEMAC existing turbulence models is discussed. The same laboratory scale case of the flow around a constant circular cylinder is studied.

In [115], the Smagorinsky turbulence model is used in the horizontal direction and the mixing length model in the vertical direction. Both turbulence models exist in the current version of TELEMAC (v7p1). The paper points out that the coastal model TELEMAC-3D can be used at laboratory scale. It performs well when simulating steady flows, such as the flow in front of a structure/cylinder. However, the existing Smagorinsky model shows very mesh dependent results. The vortex shedding behind the structure is only resolved by the very fine mesh.

[116] compares the performance of the new implemented WALE model and the existing Smagorinsky model. In this research, the Smagorinsky model is used in both horizontal and vertical directions. The numerical results indicate that, in the circular cylinder test case, both turbulence models show good agreement in front of the cylinder. However behind the cylinder, the result of the WALE model is clearly better than that of the constant Smagorinsky model.

In the following section, the tests of the validation of two new turbulence models, i.e. the 2eddy LES and the WALE model, are discussed. According to [117], the vortex shedding behind the cylinder is expected.

### 4.2.1 Mesh setup

The validation of the new turbulence model implementation begins with some mesh sensitivity tests. The computations are performed with three different size meshes, *mesh1*, *mesh2* and *mesh3*. The details of these meshes can be found in section 4.1.2. All three meshes deal with 50 horizontal layers unevenly distributed. The smooth bed condition is used for the mesh dependency test.

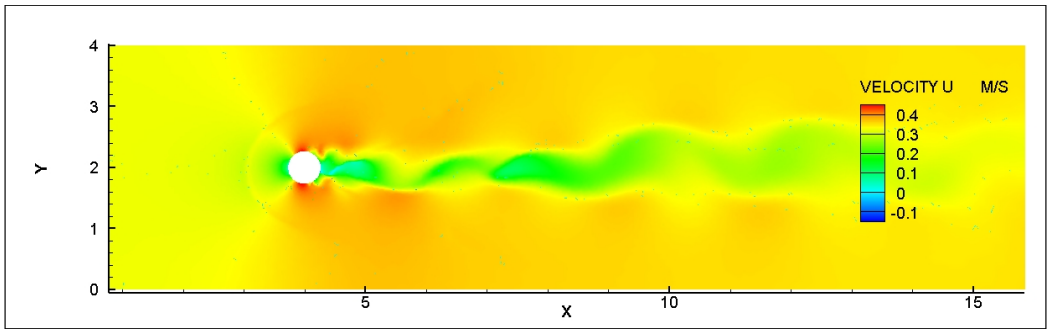


(a) *mesh1*

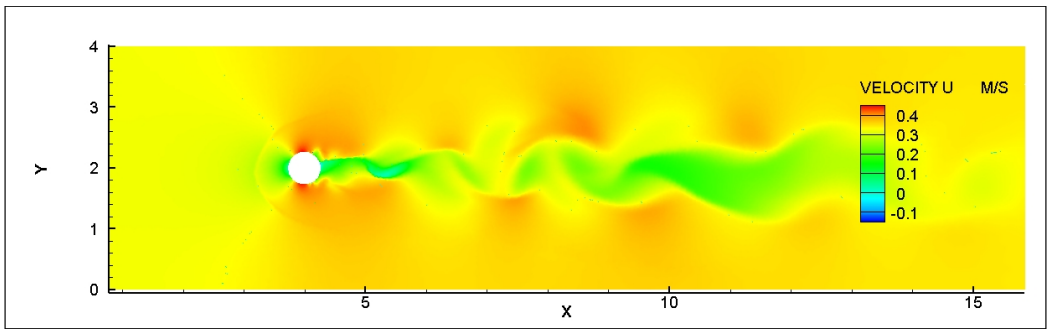


(b) *mesh2*

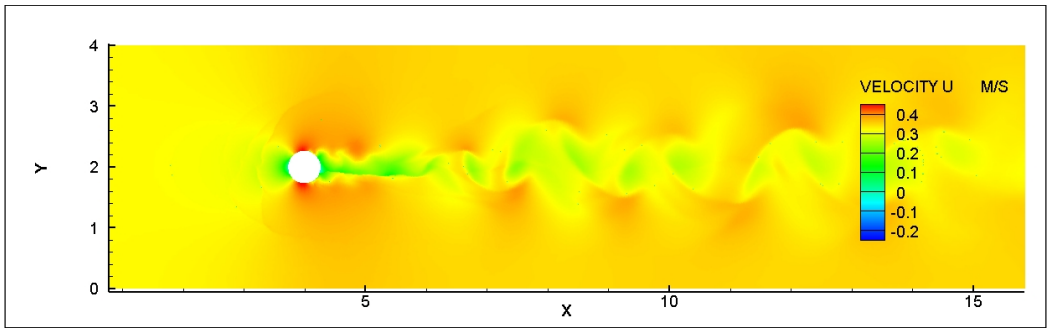


(c) *mesh3*

**Figure 4.6:** Instantaneous velocity distribution at the surface layer for the different meshes, using the 2eddy viscosity LES model

### 4.2.2 2eddy LES model

Firstly, the computed instantaneous velocity distribution is compared for different mesh resolutions. Figure 4.6 (a) (b) (c) illustrate the surface instantaneous velocity distribution around the pile in the smooth bed condition obtained using the 2eddy viscosity LES model for three different meshes respectively. In the figures, the low speed of the

flow is denoted in green and the high speed of the flow is denoted in red. Overall similar flow patterns can be found in the results of the three different meshes. The flow velocity decreases in front of the cylinder and accelerates at the sides of the cylinder. A decrease in velocity in the wake of the pile can be clearly observed. A vortex shedding (no data are available for comparison) is captured in all test cases. There is another remarkable fact that in front of the cylinder, all three results show a fan-shaped separation. This is similar to the bow wave effect [118] in ship design. A bow wave is the wave that forms at the bow of a ship when it moves through the water. In this study, the bow wave effect indicates the loss of momentum and represents a significant proportion of the wave resistance. The following result show that there is a dramatic increase of water surface in this area.

The major difference of the velocity profile in these three figures is found in the wake region. The numerical result of the coarsest mesh (figure 4.6 (a)) shows a more continuous low speed region. The vortex separation in the wake is not obvious. However the shedding of smaller size eddies in wakes in figure 4.6 (b) and (c) is noticeable. In the result of the finer meshes (figure 4.6 (c)), the wake is composed by a series of small low speed vortices. According to the concept of LES turbulence modelling, the size of the mesh plays the role of cutoff filter. All turbulent structures smaller than the filter size are modelled. Therefore the finer the mesh is in the numerical model, the more details of the turbulence structure are simulated.

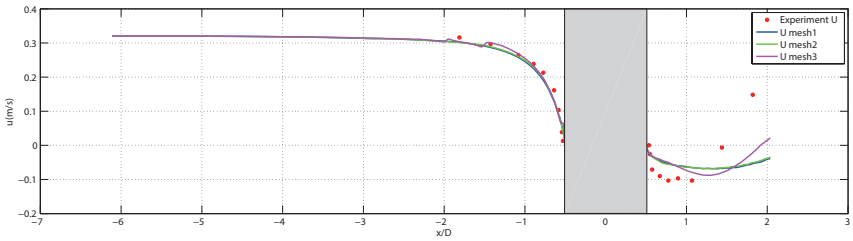


**Figure 4.7:** Mean horizontal velocity component obtained by the 2eddy viscosity LES model using different mesh sizes (smooth bed test)

Figure 4.7 compares the time averaged streamwise velocity profiles in the middle layer over the central cross section using different mesh sizes for the smooth bed test. The time averaging is obtained by averaging 100 instantaneous numerical results after

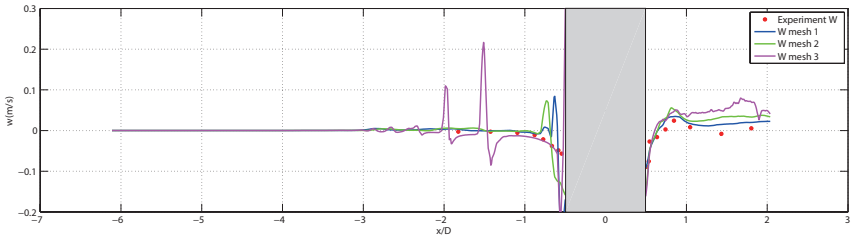


**Figure 4.8:** Mean vertical velocity component obtained by the 2eddy viscosity LES model using different mesh sizes (smooth bed test)

the flow in a fully developed channel. In the figures, the symbols denote the experimental data obtained by Roulound et al [114]. The blue, green and purple curves represent the numerical results obtained by using *mesh1*, *mesh2* and *mesh3* respectively. It is clear that, the three computed velocity profiles in front of the circular cylinder show a very good agreement with the experimental data. The flow speed reduces from 0.36 $ms^{-1}$ at the inlet boundary to 0 $ms^{-1}$ at the cylinder wall. In the wake area behind the structure, all three cases show the flow recovery, however the result obtained from *mesh3* shows a slight different distribution, e.g. a shorter recovery distance and comparing with the experiment data, a better agreement in the minimum value of flow velocity.

The comparison of the time averaged vertical velocity is illustrated in figure 4.8. The main differences are found in front of the cylinder. Two noticeable spikes are found in the vertical velocity distribution obtained by *mesh3*. The largest one is located at 1 diameter in front of the cylinder and another smaller one is at about 1.5 diameter far in front of the cylinder. In general, the vertical velocity tends to zero at a position far from the structure because without any disturbance at the inlet, the flow in the channel tends to be in the horizontal direction. With the presence of the cylinder, the vertical velocity also increases in front of the structure. However the spikes found in the velocity distribution are not caused by the flow fluctuation but a small vortex generated in front of the cylinder. As discussed above, small vortex structures can be resolved by the high mesh resolution. In the simulation based on *mesh3*, two extra vertical vortices are found in front of the cylinder at the bottom. These vortices can not be averaged through the time averaging in 100 s and therefore the vertical velocity increases dramatically. However the results of the three different meshes all show good

agreement in the comparison to the flow behind the cylinder. The vertical velocity increases from a large negative value to a positive value then reduces. This is due to the anticlockwise vertical vortex generated behind the structure.

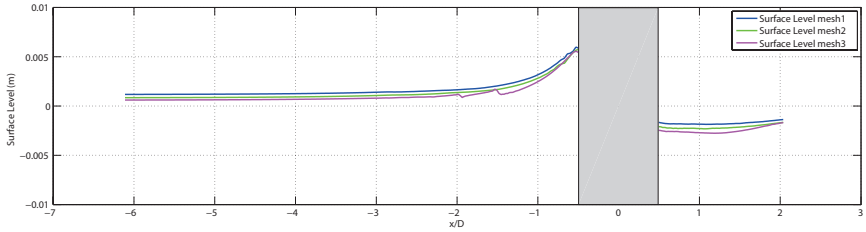


**Figure 4.9:** Mean surface elevation obtained by the 2eddy viscosity model using different mesh sizes (smooth bed test)

Figure 4.9 presents the mean surface levels obtained from the three different meshes. Similar trend is found that there is a dramatic surface rise in front of the cylinder and a gentle recovery behind the cylinder. Although the test with the finer mesh slightly underestimated the surface levels, the peak elevations obtained by the three cases are almost the same.

### 4.2.3 WALE model

The results of the mesh sensitivity tests obtained by the WALE turbulence model are presented in this section.

Figure 4.10 (a) (b) (c) illustrate the instantaneous surface velocity distribution using *mesh1*, *mesh2* and *mesh3* respectively. Similar to the results obtained by the 2eddy viscosity LES model, all three cases show low flow velocity in front of and behind the cylinder and high flow velocity at the sides of the cylinder. The vortex structure based on the difference in velocity distribution arises from the mesh density is similar by using WALE model. The size of the eddies is in much closer range than that in the 2eddyLES model results. The bow effects are also remarkable and are found in the front of the cylinder.

Comparing with the 2eddy viscosity LES model, the WALE model show less mesh dependence. The coarser mesh is still capable of representing small coherent structures. This is due the fact that the WALE model considers both rotation rate and strain rate of the turbulent structure. In figure 4.10 (c), small vortices observed in the wake region

are mainly associated with rotation effect.

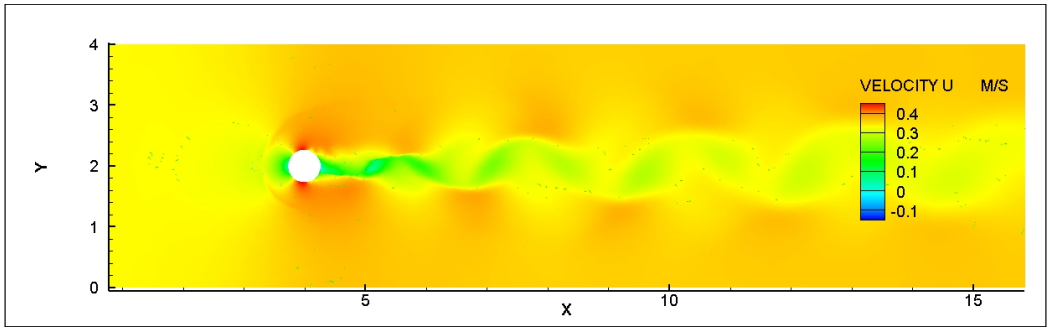


(a) *mesh1*

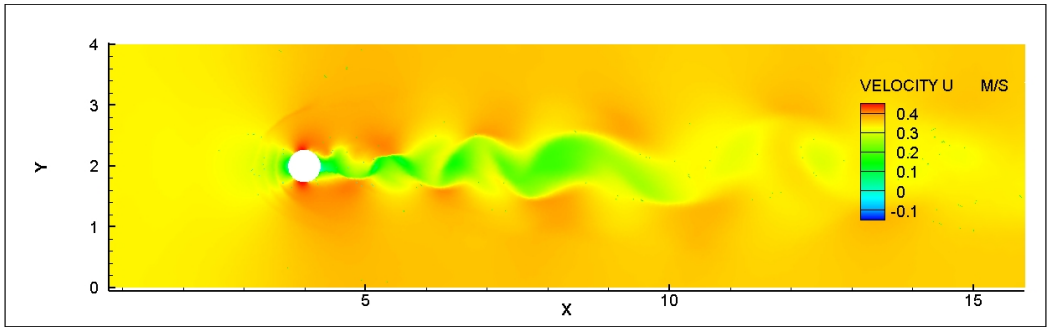


(b) *mesh2*

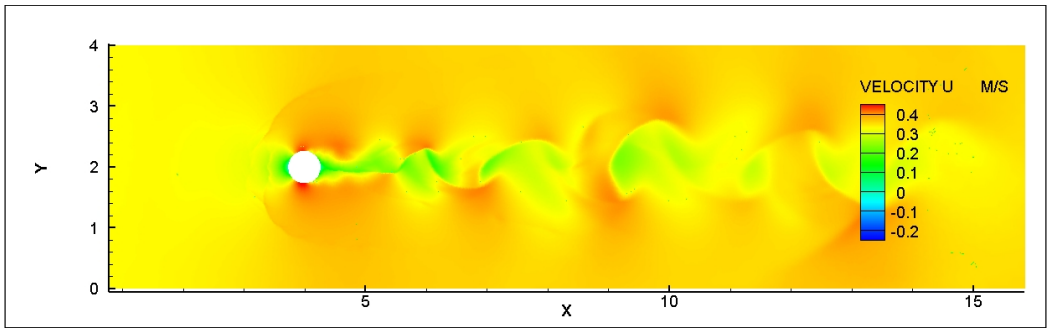


(c) *mesh3*

**Figure 4.10:** Instantaneous velocity distribution at surface layer with different mesh, using the WALE model

In the comparison of time-averaged velocity components, the WALE model also shows less mesh dependency. Figure 4.11 presents the time-averaged streamwise velocities obtained by using the three different meshes. In front of the cylinder, there is a very good agreement between all three numerical results and experimental data. Behind the cylinder, the recovery feature is captured but small variations are also seen

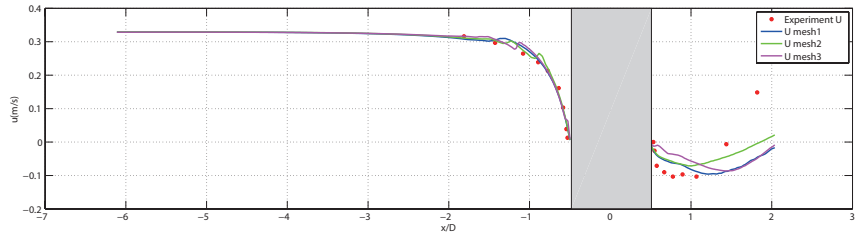


**Figure 4.11:** Mean horizontal velocity component obtained by the WALE model using different mesh sizes (smooth bed test)

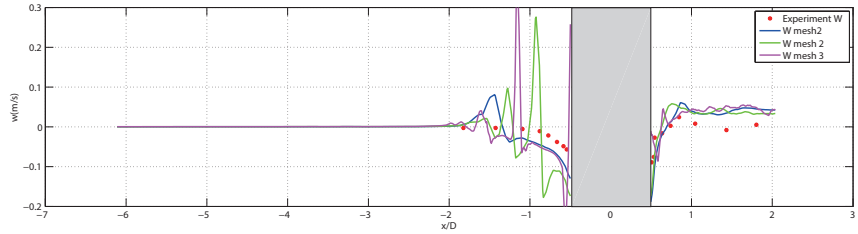


**Figure 4.12:** Mean vertical velocity component obtained by the WALE model using different mesh sizes (smooth bed test)

in the figure.

Figure 4.12 shows the computed vertical velocity along the central plane in comparison with the data. All numerical results obtained by different meshes have spikes in front of the cylinder but the location is different. This is due to the fact that small vortices are generated using all three meshes. In the result of *mesh1*, there is only one small spikes which is located at about 1 diameter in front of the cylinder. However two large spikes are found in the results of *mesh2* and *mesh3* respectively. This similar feature as in the 2eddy LES model seem suggest that the time averaging required to get the mean flow is much longer than the 100 s.

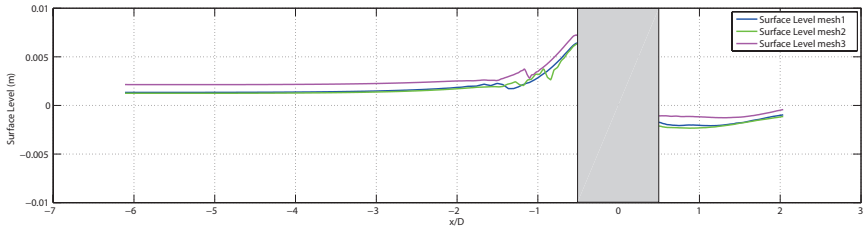


**Figure 4.13:** Mean surface elevation obtained by the WALE model using different mesh sizes (smooth bed test)

In contrast with the comparison of the surface elevation with the 2eddy viscosity LES model, using the WALE model with a finer mesh (*mesh3*) slightly over predicts the surface level as shown in figure 4.13.

It is clear that the mesh resolution does influence the numerical results in the present LES simulation, however this impact of the model accuracy is limited as demonstrated in the similarities in these comparisons of the mean flow. For this reason, all the following figures show numerical results based on *mesh1*.

## 4.3 Model result

The aforementioned model calibration shows limited model results. The following section presents more detailed results from both turbulence models.

### 4.3.1 Flow structure obtained from the 2eddy LES model

The details of the flow structure obtained by the 2eddy LES model are illustrated in figure 4.14.

Figure 4.14 shows the distribution of the magnitude of the instantaneous velocity around a cylinder at the free surface, middle and bottom layer respectively. In all three layers, similar flow patterns can be found with a decrease of velocity in the wake of the pile and a flow acceleration at the sides of the pile. However it is obvious that the wake illustrated in the free surface and middle layer is much longer than that at the bottom layer. In comparison with that near the surface, velocity accelerations at both sides of the pile play significantly larger roles in the flow pattern near the bed region.

In addition, the reduction in velocity in the wake region is noticeable, particularly from the middle layer downwards to the bed, a region with negative flow velocity can be seen clearly at about 2 to 3D downstream. The reversed flow is more obvious at the bed surface.

The pattern of vortex shedding in the wake region remains similar at the top and middle layer. But further downwards close to the bed, such coherent structure has been reduced to a very small region close to the cylinder.

Figures 4.15 and 4.16 visualise the velocity vectors in front of and behind the cylinder respectively, using a vertical cross-section view. Before the flow is split by the

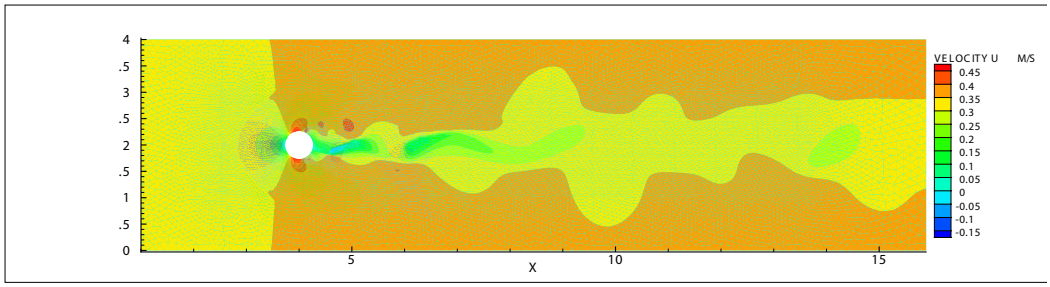


(a) Surface layer Z = 0m

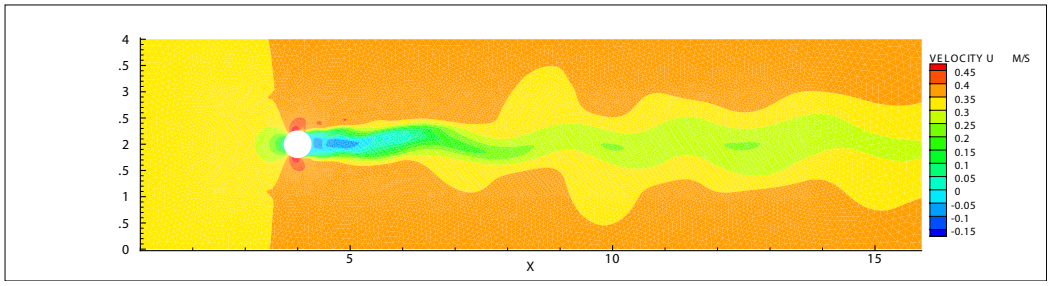


(b) Middle layer Z = -0.27m

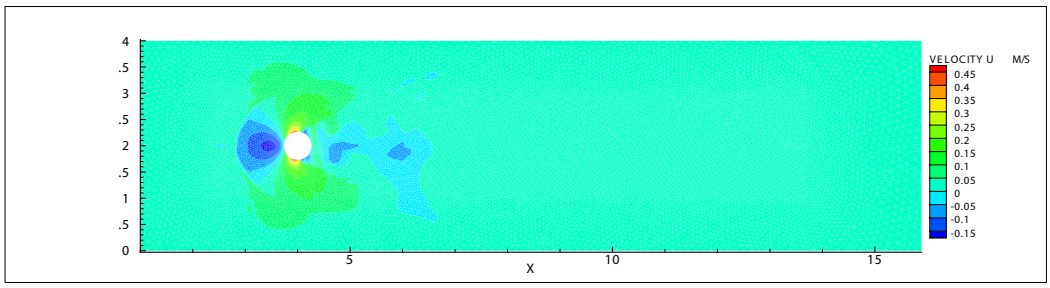


(c) Bottom layer Z = -0.54m

**Figure 4.14:** Horinzontal velocity distribution at different layers. Obtained from 2eddy LES model and smooth bed condition

cylinder (shown in figure 4.15), an uniform flow with log profile in the vertical direction is obtained by the numerical model. This distribution remains until about 0.6D in front of the cylinder, then the flow starts reducing the velocities and changing directions. A vortex can be clearly found at the bottom in front of the cylinder, which is also well known as 'horseshoe vortex' located about 0.25D at the front of the cylinder. A downwards flow is clearly seen immediately in front of the cylinder.

When the flow passes the cylinder (as shown in figure 4.16), two vortices are generated immediately behind the structure. Flows in opposite direction are found further

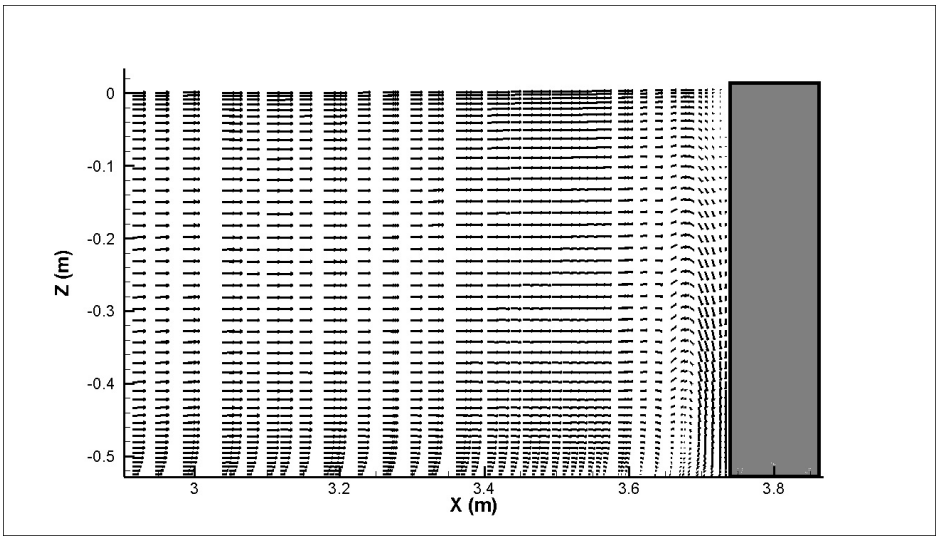


**Figure 4.15:** Velocity vector diagram in vertical cross section, in front of the cylinder

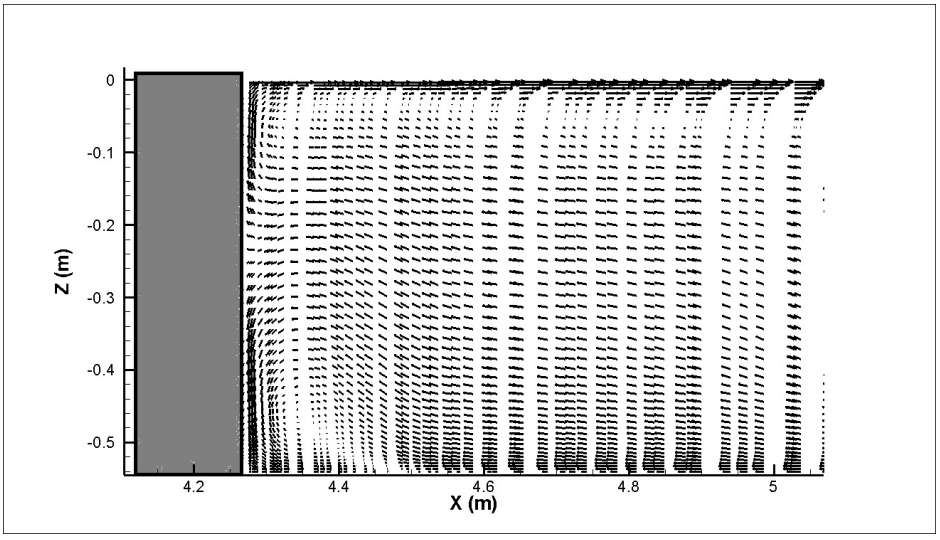


**Figure 4.16:** Velocity vector diagram in vertical cross section, behind the cylinder

downstream, e.g. the flow at the free surface goes downstream, however an opposite upstream flow is found close to the bottom.

The vortex shedding phenomenon is clearly illustrated in figure 4.17. It depicts a sequence of velocity vectors and streamline plots at depth of Z = -0.27 m. From these figures, the unsteady behaviour of the wake is evident. The vortices are created at the back of the cylinder and detach periodically from either side of the structure.

In the investigation of the turbulence, the Q criterion is a widely used as a vortex detection criterion for LES results [119]. Q is the second scalar invariant of the velocity

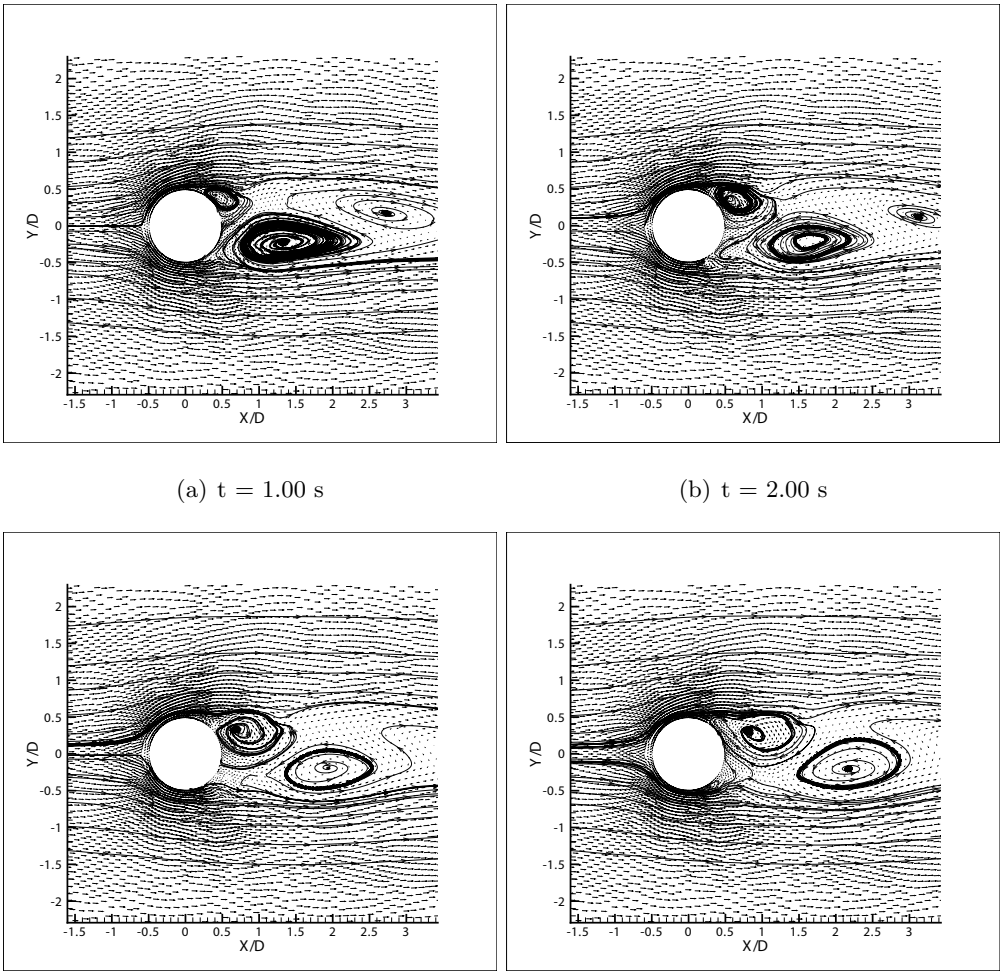


(a) t = 1.00 s

(b) t = 2.00 s

(c) t = 3.00 s

(d) t = 4.00 s

**Figure 4.17:** Horizontal velocity vector and streamlines for unsteady flow simulation during one period of vortex shedding. Smooth bed; horizontal cross-section at Z = -0.27 m

derivative tensor and can be expressed for incompressible flows as:

$$Q_{criterion} = (\Omega_{ij}\Omega_{ji} - S_{ij}S_{ji})/2 \tag{4.4}$$

where $S_{ij}$ and $\Omega_{ij}$ are the symmetric and the anti-symmetric part of the velocity derivation tensor respectively. This expression highlights that positive regions of the Q field are associated with the fact that rotation is dominant over the shear. In fact it represents the local balance between shear strain rate and vorticity magnitude, defining vortices as areas where the vorticity magnitude is greater than the magnitude of rate-of-strain [120–123].

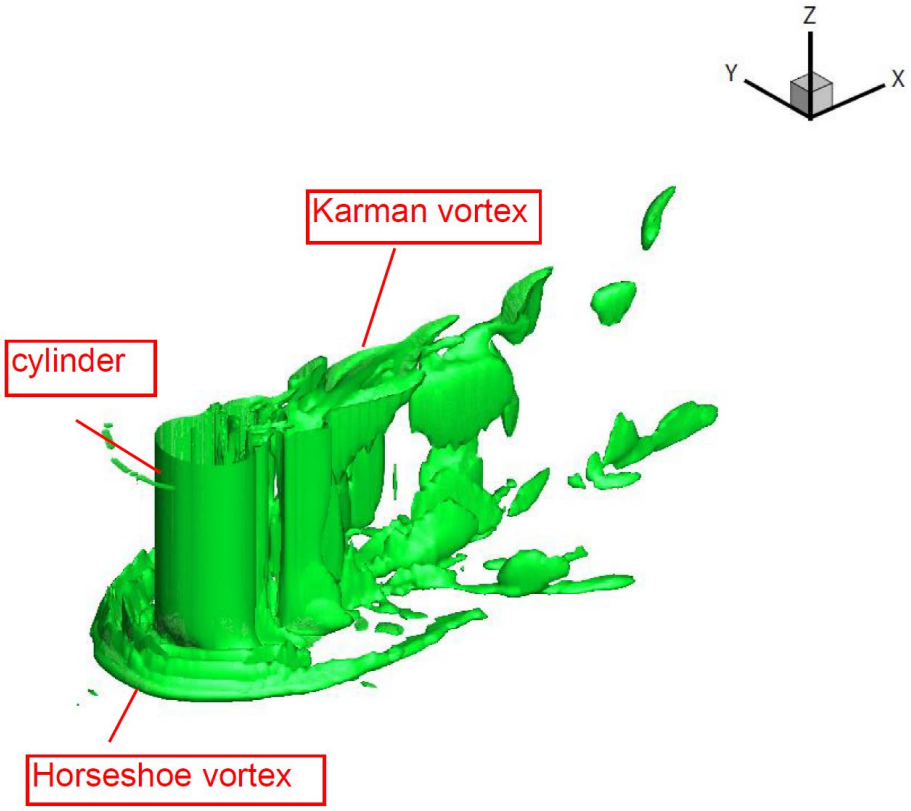


**Figure 4.18:** Vortex identification plotting Q criterion iso-surfaces (3-D view)

Figures 4.18 and 4.19 use the Q criterion to visualise the vortex structure obtained by the 2eddy LES turbulence model in a 3-D view and a top view respectively. In the figures, the iso-surface of the Q criterion is displayed and each closed bar indicates a vortex. A horseshoe vortex is clearly represented in front of the cylinder. Although the vortex in the wake area close to the cylinder is disordered, vortex shedding is still visible after a distance.

### 4.3.2 Flow structure obtained from the WALE model

The horizontal velocity profiles in different layers across the central plane obtained from the WALE model are represented in figure 4.20. Similar velocity distribution to that in the 2eddy LES model is found. Although the upstream flow reduces speed in front of the cylinder, a negative value is only found at the bottom layer which indicates that a horseshoe vortex is only produced in this area. Moreover, in the wake area there is no recovery flow at the surface layer but in the middle and bottom layers. Again, similar

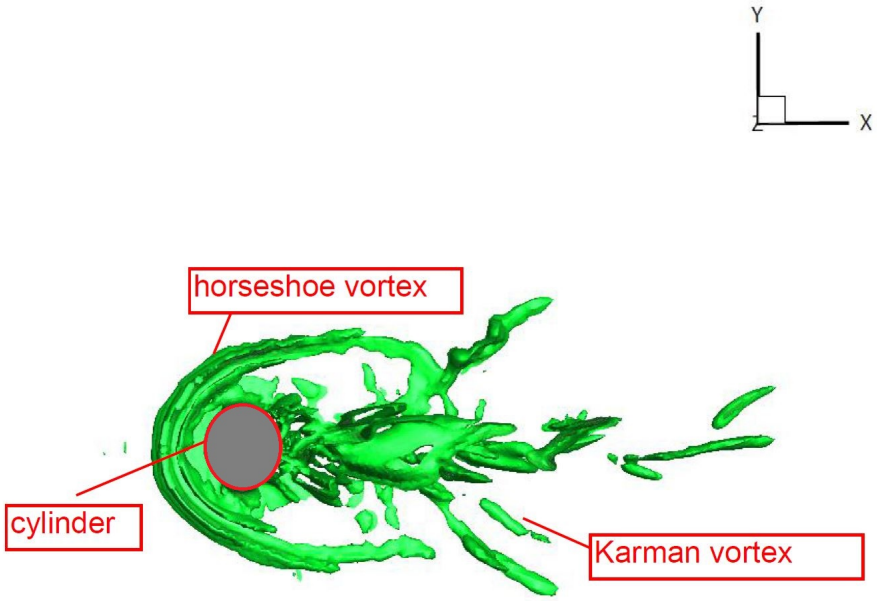


**Figure 4.19:** Vortex identification plotting Q criterion iso-surfaces (Top view)

to that in the 2eddy LES model results, the reduction near the lower part of the water column is stronger which produces negative flow velocity, especially close to the bed surface. The vortex structure is largely dominated by the shedding at the upper part of the water body with much reduced strength near the bed. However, the width of the Karman vortex street in the wake is narrower than that in the 2eddy LES case and various small coherent structure is seen in the middle layer, which suggests the vortex shedding in the cross-width direction is limited.

Figures 4.21 and 4.22 illustrate the velocity vector distribution in a vertical cross-section for the WALE model results. The horseshoe vortex is clearly seen at the bottom, in front of the cylinder, however comparing the 2eddy model with the WALE model, the position is further upstream. The core of this horizontal vortex is located at about 2D in front of the structure. As opposed to the 2eddy LES model results where the horizontal and vertical dimensions of the horseshoe vortex are similar, the horizontal size of the vortex obtained from the WALE model is about 6 times its vertical size. However in the wake region, the WALE model also shows similar flow pattern as the 2eddy LES model with two vortices against the cylinder wall, the size of the vortex in

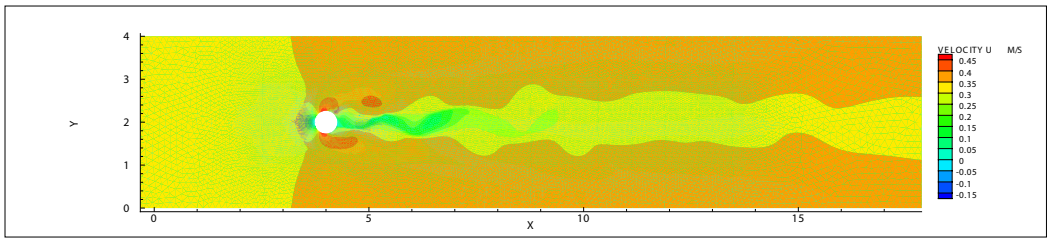


(a) Surface layer Z = 0m

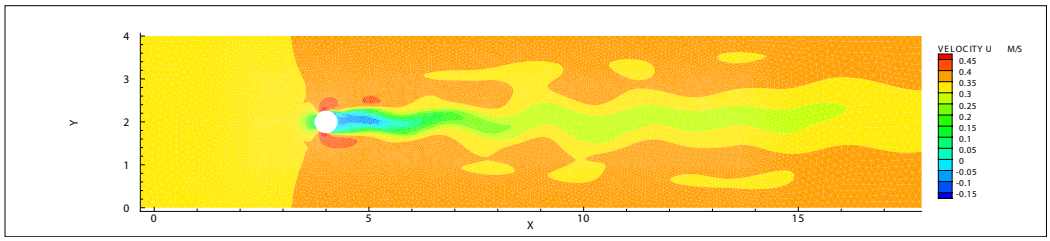


(b) Middle layer Z = -0.27m

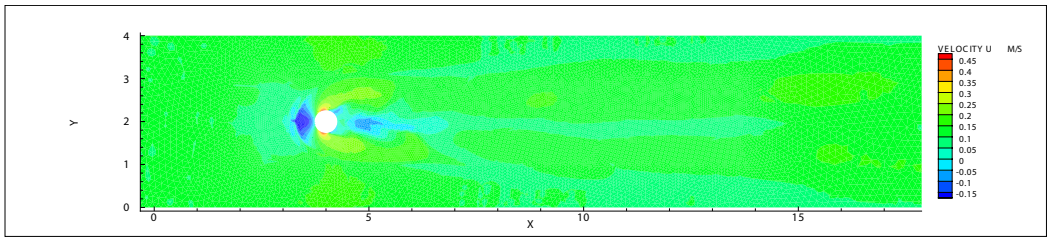


(c) Bottom layer Z = -0.54m

**Figure 4.20:** Horinzontal velocity distribution at different layers. Obtained from the WALE model and smooth bed condition

the 2eddy LES model is bigger.

The vortex shedding captured by the WALE model is illustrated in figure 4.23. The result covers 4 seconds and a full vortex shedding can be found during this period. Similar to the vortex shedding phenomenon obtained by the 2eddy LES model, the vortices are created at the back of the cylinder and detach periodically from either side of the structure.

In the visualisation of the Q criterion (see figure 4.24 and 4.25), the numerical result obtained by the WALE model indicates that a similar vortex structure as for the 2eddy viscosity LES model is observed. Both horseshoe vortex and Kármán vortices shedding are found in front of and behind the cylinder respectively. However, the WALE model exhibits a longer tail of horseshoe vortex at the sides of the cylinder.

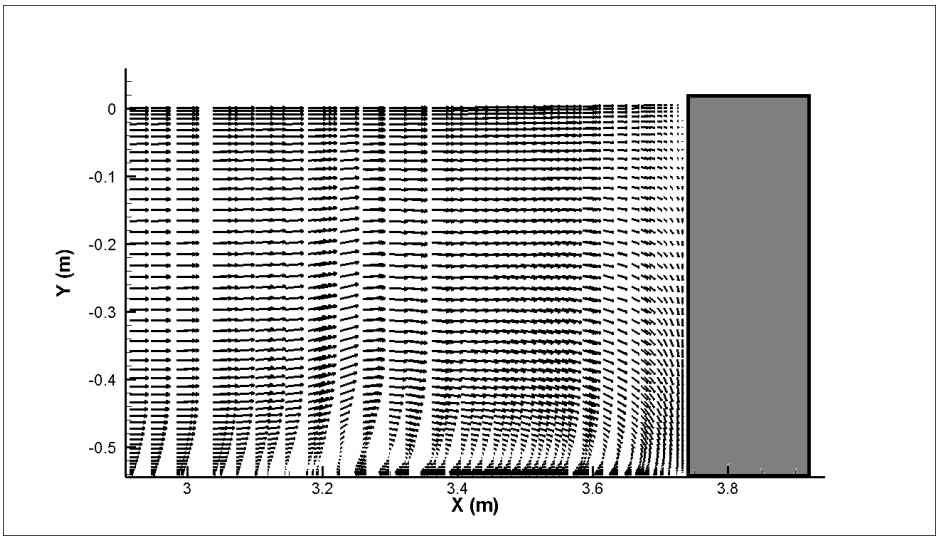


**Figure 4.21:** Velocity vector diagram in vertical cross section, in front of the cylinder

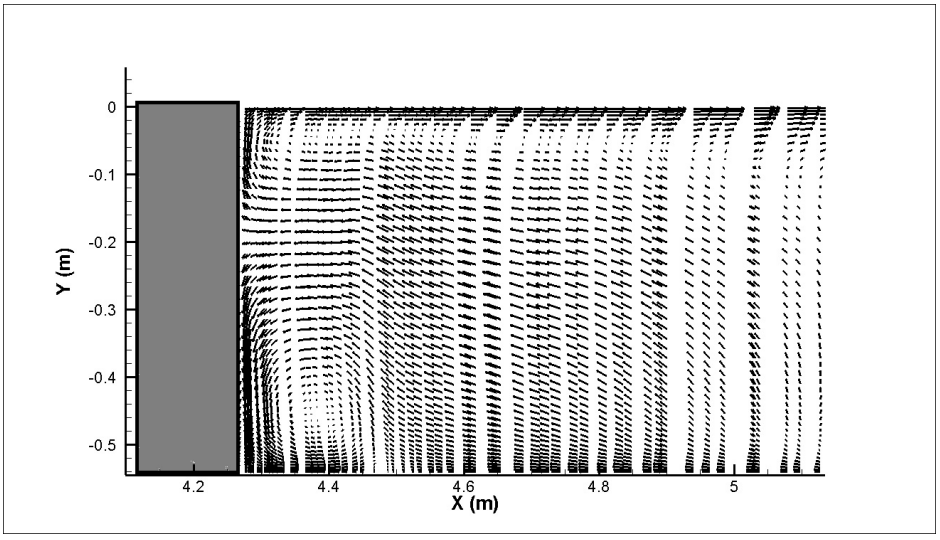


**Figure 4.22:** Velocity vector diagram in vertical cross section, behind the cylinder

### 4.3.3 Comparison between the 2eddy LES model and WALE model

To further illustrate the difference between the 2Eddy LES model and the WALE model, results from these two are compared and discussed in detail in the following section.

Figure 4.26 compares the turbulence kinetic energy (TKE) obtained by both turbulence models. TKE is the mean kinetic energy per unit mass associated with eddies in turbulent flow. The results obtained by both turbulence models show a common

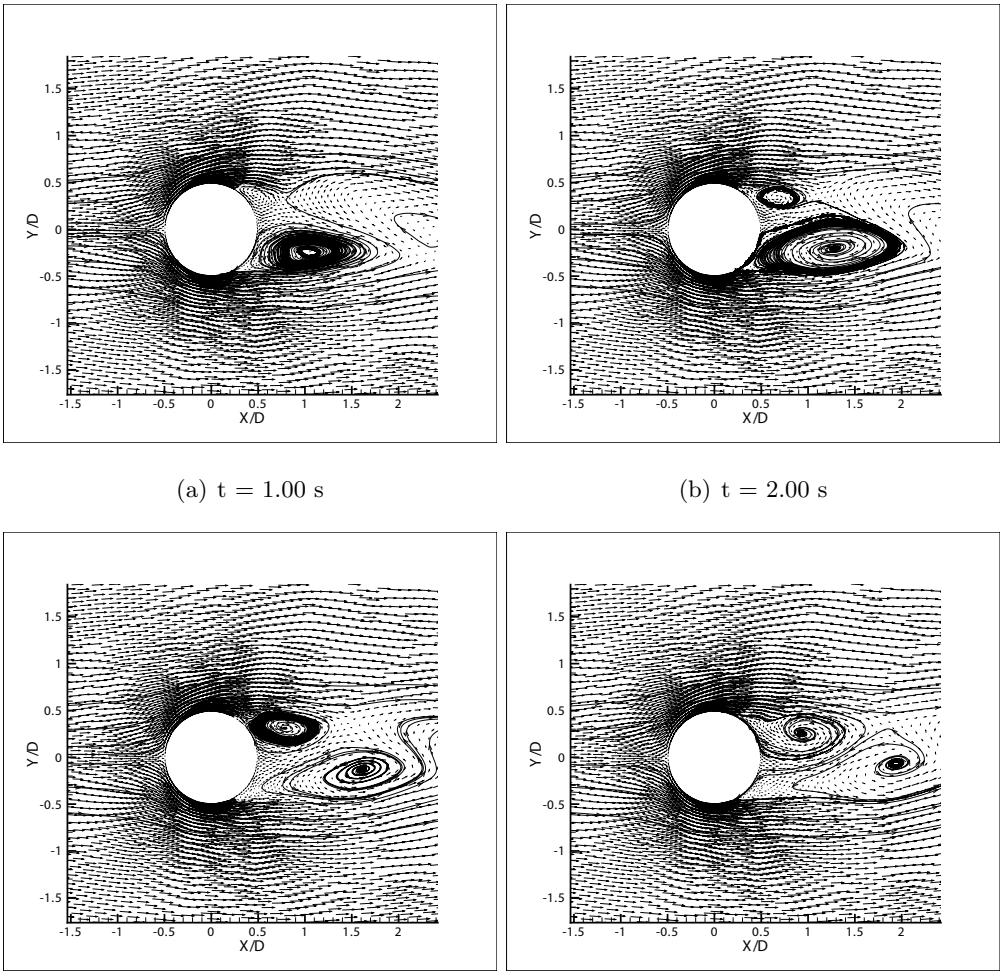


(a) t = 1.00 s

(b) t = 2.00 s

(c) t = 3.00 s

(d) t = 4.00 s

**Figure 4.23:** Horizontal velocity vector and streamlines for unsteady flow simulation during one period of vortex shedding. Smooth bed; Horizontal cross-section at Z = -0.27 m

feature that in the range of X = 4.05 m and X = 4.2 m, there is high TKE along the cylinder which continuously diffuse downstream. This is generated by the separation of flow and cylinder wall at about X = 4.05 m. A different trend is observed in front of the cylinder, the result obtained by the 2eddy LES model show high TKE values, whereas the WALE model does not show. This indicate that very strong turbulent flow in front of the cylinder is only represented by the 2eddy LES model.

Figures 4.27 and 4.28 illustrate the time evolution instantaneous velocities in a 100 s period, obtained by the 2eddy LES model and WALE model respectively. The point is located at 1D behind the cylinder. Strong fluctuating velocities are seen clearly in the

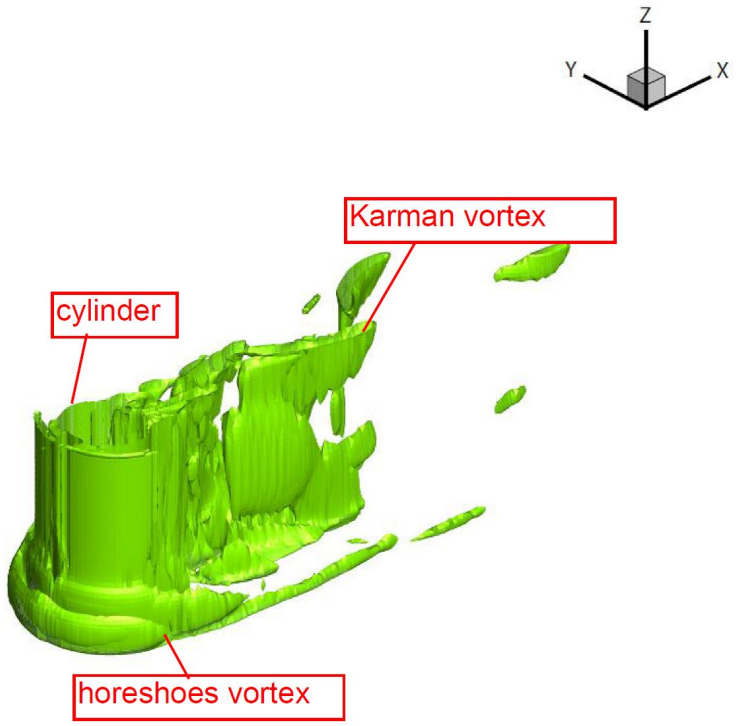


**Figure 4.24:** Vortex identification using Q criterion iso-surfaces (3D view)

figures. By counting the peak of instantaneous velocity under time-averaged velocity, the shedding frequency can be estimated. The frequency obtained by the 2eddy LES model is 0.13 Hz and it of the WALE model is 0.15 Hz. As suggested in [124], the Strouhal number St as defined by St = fD/U, where D is cylinder diameter, U is mean flow velocity, can be used to quantify the vortex shedding frequency f. In the present case, the Reynolds number Re is approximately $2 \times 10^5$, given U is 0.32 $ms^1$ and D as 0.54 m, the diagramme of St against Re in [124] indicates the St is in the range of 0.2 to 0.35, which leads to f is in the range of 0.12 Hz to 0.21 Hz. This is very similar to the present model results.

The pressure coefficient obtained by both turbulence models is shown in figure 4.29. Here the pressure coefficient ($C_p$) is calculated as:

$$C_p = \frac{p - p_\infty}{\frac{1}{2}\rho_\infty U_\infty^2} \tag{4.5}$$

where $p$ is the pressure at the point at which pressure coefficient is being evaluated; $p_\infty$ is the pressure in the free stream; $\rho_\infty$ is the free stream fluid density; $U_\infty$ is the free

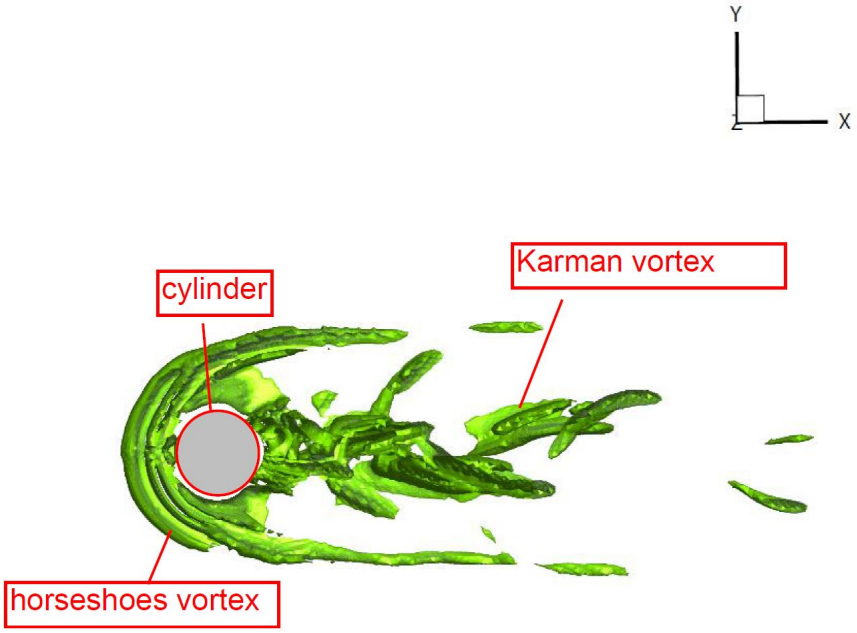


**Figure 4.25:** Vortex identification using Q criterion iso-surfaces (Top view)

stream velocity of the fluid. In the figure, the pressure coefficient obtained from both turbulence models shows a drop trend in the first half of the cylinder. This down trend is replaced by a rising trend after about 90 degrees from forward the stagnation point and ends with a constant value at about 150 degrees. The peak of pressure coefficient obtained by the 2eddy LES model is about twice as small as the one of the WALE model.

Figure 4.30 illustrates a series of comparison of the computed time averaged streamwise velocity distributions in different layers. This test is carried out using the smooth bed condition. The results obtained by the 2eddy viscosity LES model and the WALE model are represented by blue and green curves respectively. Red dots are for the measurement data. Generally, the tendency is for the velocity to decrease in front of the cylinder and to recover behind it, for both turbulence models. The 2eddy viscosity LES and WALE models produce similar results in the wake area, although the distance of flow recovery in both cases are slightly longer than for the experimental data. In front of the cylinder, a big difference between the two turbulence models can be found

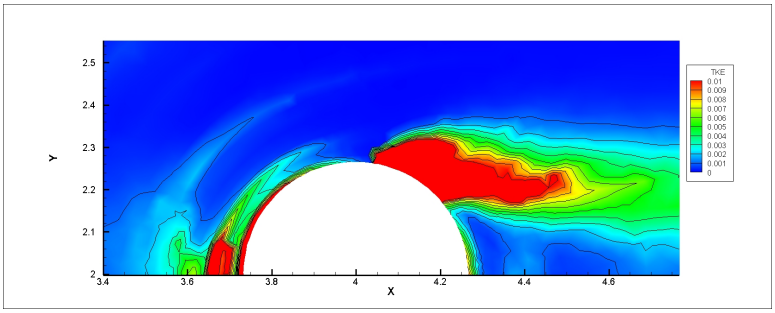


(a) 2eddy LES model

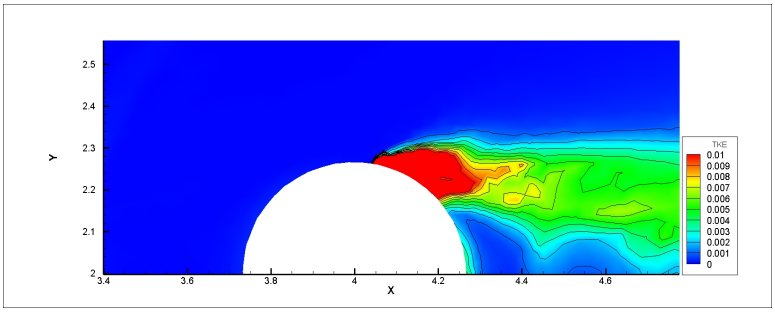


(b) WALE model

**Figure 4.26:** Turbulence kinetic energy (TKE) obtained by 2eddy LES model and WALE model. Z = -0.27 m

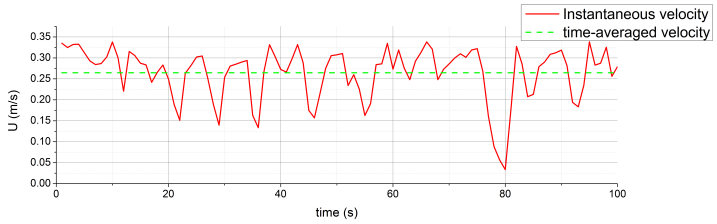


**Figure 4.27:** Instantaneous velocity in 100 s period obtained by the 2eddy LES model.

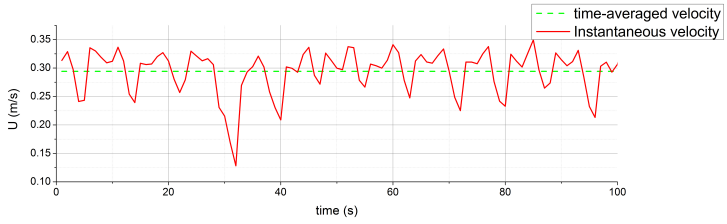


**Figure 4.28:** Instantaneous velocity in 100 s period obtained by the WALE model.

especially at the layers close to the bottom.

At the layer Z = -0.34 m (63 % of the water depth), mean horizontal velocities

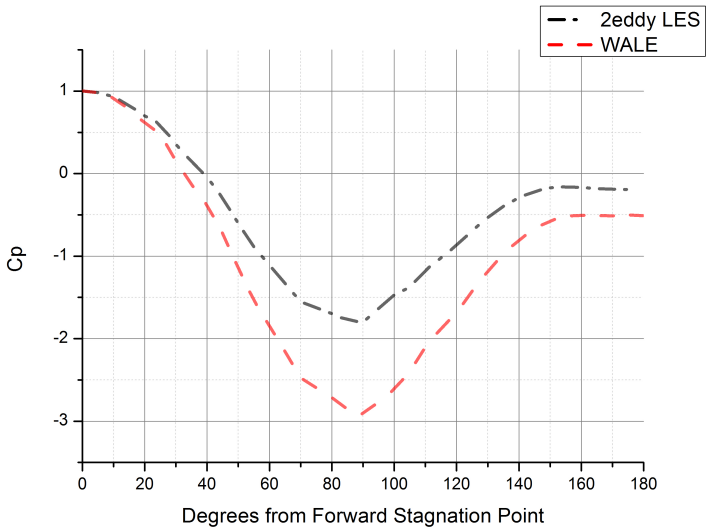


**Figure 4.29:** Mean pressure coefficient around the cylinder

obtained from the two models match the experiment data well in front of the cylinder. In the wake area, the velocity obtained by the WALE model reduces to the same peak as in the experiment, however the 2eddy viscosity LES model slightly under-predicts this peak value. A similar velocity distribution is found at the layer of Z = -0.44 m (81 % of the water depth), however a clear velocity drop is observed at about 1D distance before the cylinder. At the layer of Z = -0.49 m (91 % of the water depth), the results obtained from the 2eddy viscosity LES model still show good agreement in front of the cylinder, but the velocities are under-estimated by the WALE model. Behind the cylinder, the two turbulence models show good agreement for the velocity decrease, but a slower increase behind it is found comparing with the experimental data. At the layer Z = -0.52 m (96 % of the water depth) and -0.53 m (98 % of the water depth), both turbulence models under-predict the velocity in front of the cylinder. Behind the cylinder, the experimental data show a significant feature that the flow velocity slightly increases before reducing to negative values, and then recovering to reach the outlet speed, which is represented by the numerical model.

In the result of the WALE model, the dramatic drop of velocity is taken place at about 1D in front of the cylinder, which is the same position of the vertical vortex on the bottom (shown in figure 4.21). This vertical vortex has an effect on the velocity

distribution, and this effect becomes bigger with depth increase.

Figure 4.31 illustrates the comparison of the mean vertical velocity distributions in the case of the smooth bed condition. In front of the cylinder, at the first three layers (Z = -0.34 m , Z = -0.44 m and Z = -0.49 m), the experimental data show that the vertical velocity maintains a 0 $ms^{-1}$ value at the beginning and then decreases to a large negative value when reaching the cylinder. The 2eddy viscosity LES model shows a good agreement except for a small positive velocity spike which is found in front of the cylinder due to the impact of vertical vortex on the bottom. This spike is also found in the WALE model results, however its location is farther away from the cylinder.

At the last two layers (Z = -0.52 m and Z = -0.53 m) in front of the cylinder, the experiment shows a small positive velocity spike before decreasing to a negative speed. This is not represented by the numerical simulations. Behind the cylinder, both the 2eddy viscosity LES and WALE models show a good agreement as vertical velocities increase from a negative value to a positive value and then drop to about 0 $ms^{-1}$. The 2eddy viscosity LES model performs slightly better in the layers Z = -0.34 m and Z = -0.44 m when the peak of velocity behind the cylinder is overpredicted by the WALE model.

A similar comparison is conducted for the rough bed condition. Figure 4.32 shows mean horizontal velocity distributions obtained using the *mesh3* 2-D triangular element distribution with 50 vertical layer distributions. In front of the cylinder, the mean velocity profiles obtained from the numerical model show a tendency to decrease, which is also observed in the experimental data. Good agreement are found at layers above Z = -0.447 m (83% of the water depth) by both numerical models. At the layer of Z = -0.497 m (92% of the water depth) and Z = -0.517 m (96% of the water depth), the mean velocity profiles obtained by the 2eddy viscosity LES model still match the experiment well, however there is a big difference between the WALE model results and the experimental data. At the bottom, where Z = -0.537 m (99% of the water depth), both numerical models under-predict the horizontal velocities.

In the wake part, although a very good agreement can be found at the layer of Z = -0.347 m, the velocity profiles obtained by both two numerical models are over-estimated close to the surface and under-estimated close to the bottom. The 2eddy

viscosity LES model preforms better than the WALE model to catch the flow recovery tendency.

The vertical velocity distributions in the rough bed configuration are illustrated in figure 4.33. Both the 2eddy viscosity LES model and the WALE model show very good agreement in front of the cylinder. Big differences are observed behind the cylinder. The numerical results indicate that the vertical velocity increases from large negative values to about 0 $ms^{-1}$, even though the experimental data show the opposite.

Figures 4.34 and 4.35 present the amplification of the bed shear stress obtained by the 2eddy viscosity LES module and the WALE model respectively. For the comparison, the smooth bed experimental results of Hjorth [125] is illustrated in figure 4.36. Here the amplification of the bed shear stress is defined by:

$$\alpha_\tau = \frac{|\tau_0|}{\tau_\infty} \tag{4.6}$$

where $\tau_0$ is the bed shear stress and $\tau_\infty$ is the undisturbed bed shear stress.

The 2eddy viscosity LES model and the WALE model show similar results in the bed shear stress distribution with a large bed shear stress at the side of the cylinder and a small shear stress in front of and behind the cylinder. However comparing to the experiment, the location of the maximum bed shear stress obtained by the numerical models is slightly different from the experiment. In the experiment, the maximum bed shear stress is located at about 45 degrees from the upstream direction, but that of the numerical model can be seen at about 90 degrees from the upstream direction.

## 4.4 Discussion

This chapter illustrates the simulation of the flow past a circular cylinder, using two turbulence models, the 2eddy LES and the WALE model. The simulation takes place at laboratory scale and the results are benchmarked with the Roulund's experiment data [114]. The aim of this work is to validate the capability of the new turbulence models in the simulation of far-field hydrodynamics to assess the environment impact around the offshore structures including offshore wind turbine farm and tidal turbine farm.

The main reason for using the cylinder test to validate new model implementations

is that the hydrodynamics procedure of the flow past a circular cylinder is similar to the one around offshore wind turbine foundations. Therefore the capability of new turbulence models can be illustrated in a straightforward manner.

As the large-eddy simulation approaches are subgrid-scale-based models, which depend (through the filter size) on the area of each triangular element of the horizontal mesh, assessing the mesh independency of both models is of great importance. In the author's previous works [115, 116], existing turbulence models in TELEMAC-3D were investigated. It is noticed that using the constant Smagorinsky approach in the horizontal direction and a mixing length model in the vertical direction shows very mesh-dependent results and the unsteady flow state can be only represented by an extremely fine mesh. This is due to the fact that Smagorinsky model normally requires a very fine mesh to capture the isotropic turbulence structure.

The 2eddy LES model relies on the horizontal and vertical turbulence to be modelled separately. This feature reduces the demand for an extremely fine mesh and the size of the vertical mesh does not follow the same trend as the horizontal mesh size. According to the numerical results using the 2eddy LES model, the unsteady flow state is well captured by all three different size meshes and and the vortex shedding behind the cylinder is clearly represented. This is a big improvement comparing with using the existing turbulence model.

The WALE model improves the turbulence modelling for these simulations in the other way as the rotation rate of turbulence is taken into account. Actually the rotation rate is a fundamental feature of turbulence however it is neglected by most LES approaches. The numerical results obtained by the WALE model indicate that the unsteady flow state can be represented by all different mesh sizes and they show the feature of mesh independence. When using the same coarse mesh as the 2eddy LES model used, more small vortex structures can be captured.

To compare the implementation of the two new turbulence models, the velocity components along the center line at different vertical layers are investigated. The 2eddy viscosity LES model and the WALE model have similar numerical accuracy in the representation of the flow structure at layers ranging from -0.2 m to -0.44 m, however at layers close to the bottom, the 2eddy LES model performs better than

the WALE model. This may be due to the fact that the WALE model requires more isotropic element resolution than the 2eddy viscosity model as different constants are used for the horizontal and vertical directions. Although 50 layers are used in the vertical direction, the aspect ratio of the elements, between the horizontal and vertical directions is still large, especially in the area near the structure.

To summarize, the 2eddy LES model and WALE models are both suitable to simulate the flow past a circular cylinder. Comparing with the existing turbulence approaches of TELEMAC-3D, both new turbulence models show less mesh sensitivity and the unsteady flow state can be represented by a fairly coarse mesh. The 2eddy viscosity LES model offers better accuracy than the WALE model to simulate the flow close to the bottom, however more vortex structure can be captured by the WALE model.

Overall, both turbulence models are capable of reproducing the time-averaged flow field and turbulence quantities.

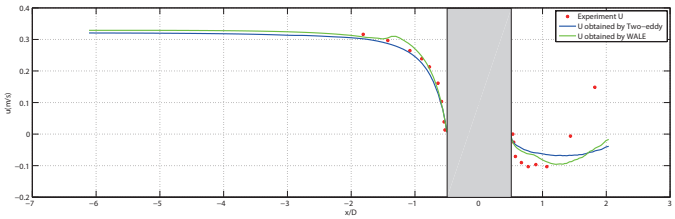


(a) At the layer of Z = -0.34 m

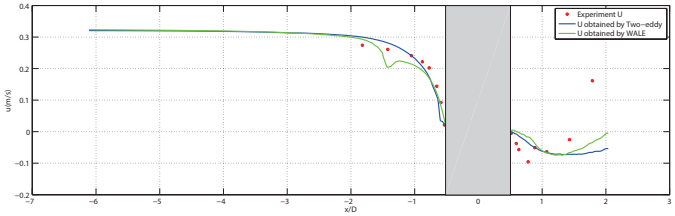


(b) At the layer of Z = -0.44 m

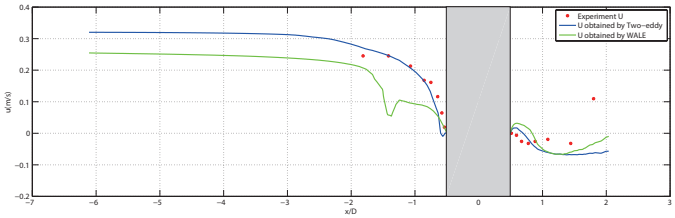


(c) At the layer of Z = -0.49 m

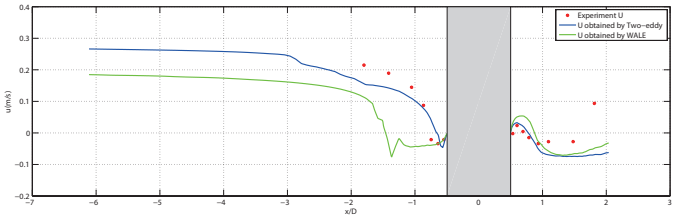


(d) At the layer of Z = -0.52 m

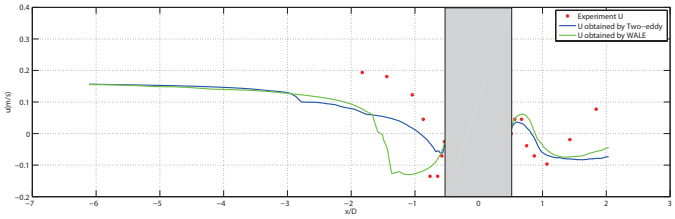


(e) At the layer of Z = -0.53 m

**Figure 4.30:** Mean horizontal velocity at different layers. Smooth rigid bed with *mesh1*

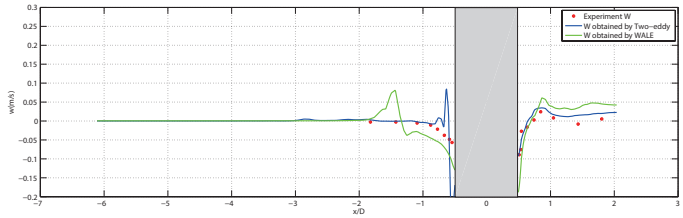


(a) At the layer of Z = -0.34 m

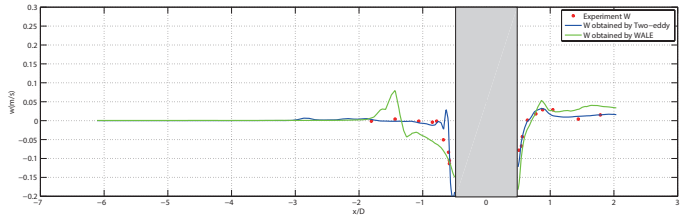


(b) At the layer of Z = -0.44 m

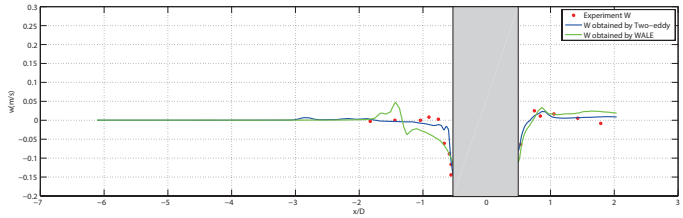


(c) At the layer of Z = -0.49 m

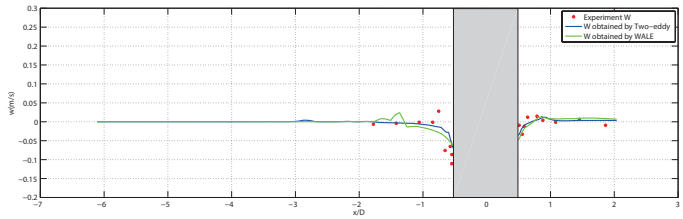


(d) At the layer of Z = -0.52 m

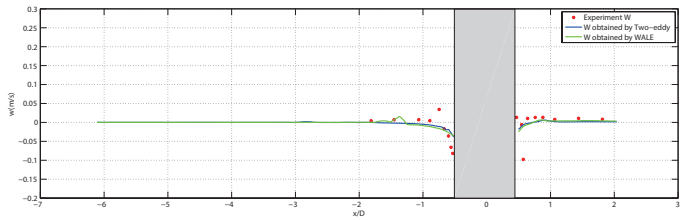


(e) At the layer of Z = -0.53 m

**Figure 4.31:** Mean vertiacl velocity at different layers. Smooth rigid bed with *mesh1*

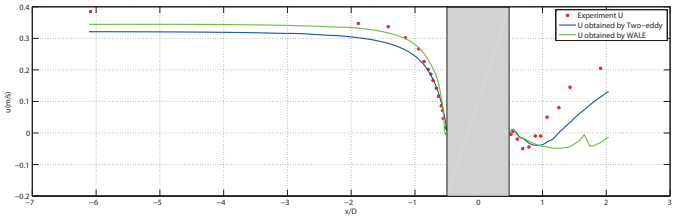


(a) At the layer of Z = -0.047 m

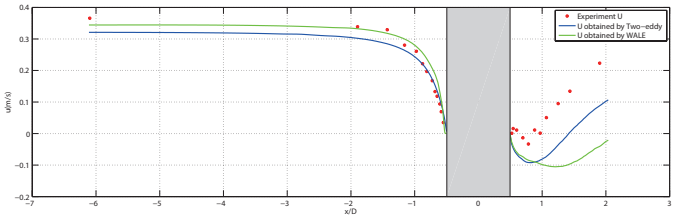


(b) At the layer of Z = -0.147 m

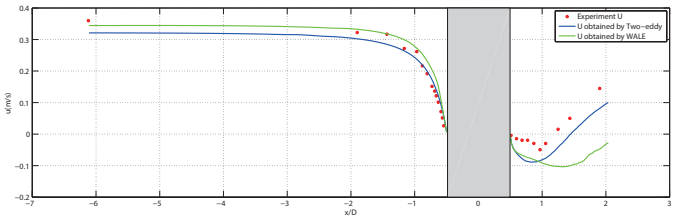


(c) At the layer of Z = -0.247 m

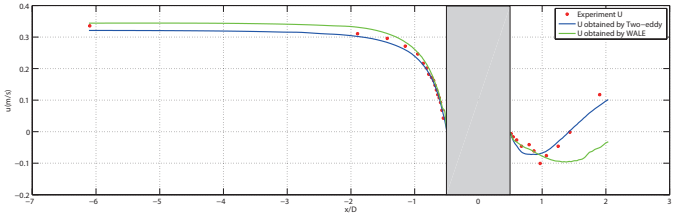


(d) At the layer of Z = -0.347 m

**Figure 4.32:** Mean horizontal velocity at different layers. Rough rigid bed with *mesh1* (cont.1)

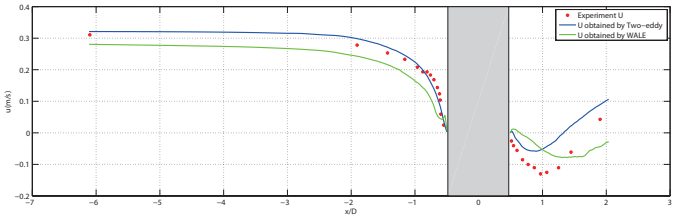


(a) At the layer of Z = -0.447 m

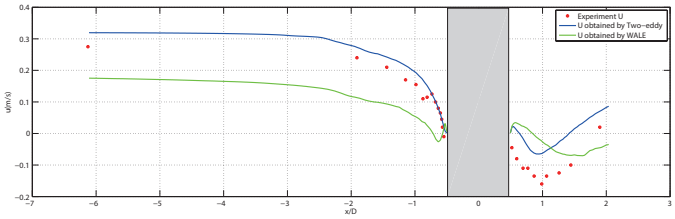


(b) At the layer of Z = -0.497 m

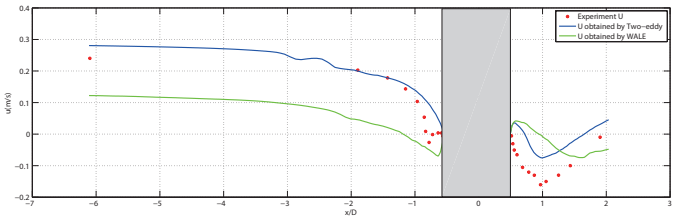


(c) At the layer of Z = -0.517 m

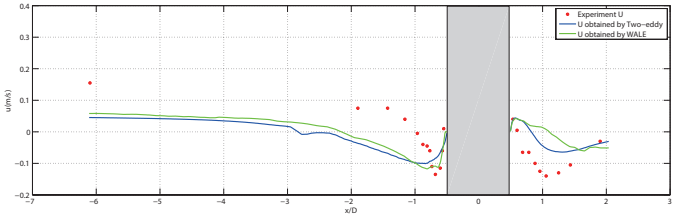


(d) At the layer of Z = -0.537 m

**Figure 4.32:** Mean horizontal velocity at different layers. Rough rigid bed with *mesh1* (cont.2)

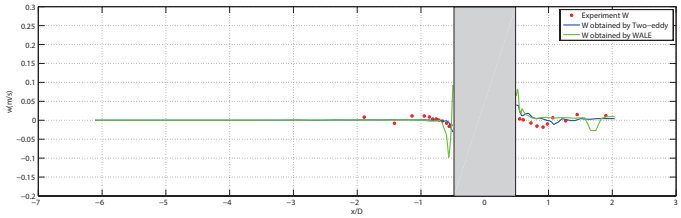


(e) At the layer of Z = -0.047 m

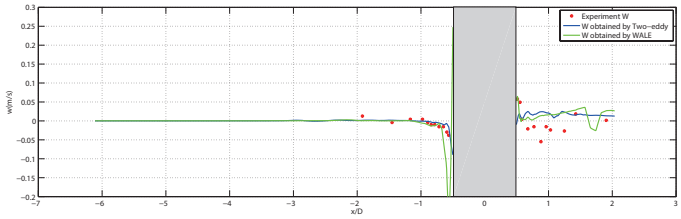


(f) At the layer of Z = -0.147 m

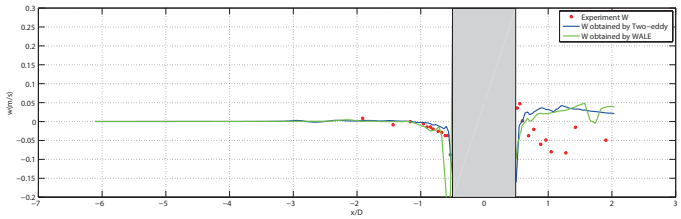


(g) At the layer of Z = -0.247 m

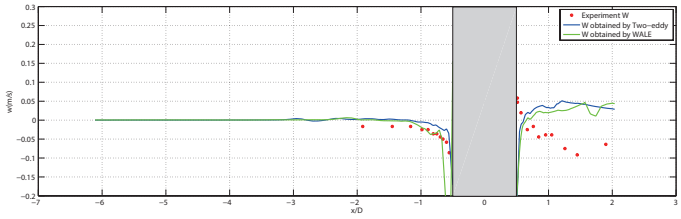


(h) At the layer of Z = -0.347 m

**Figure 4.33:** Mean vertical velocity at different layers. Rough rigid bed with *mesh1* (cont.1)

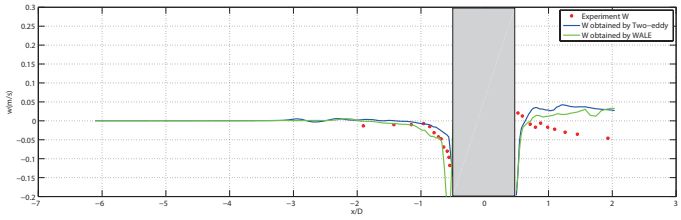


(a) At the layer of Z = -0.447 m

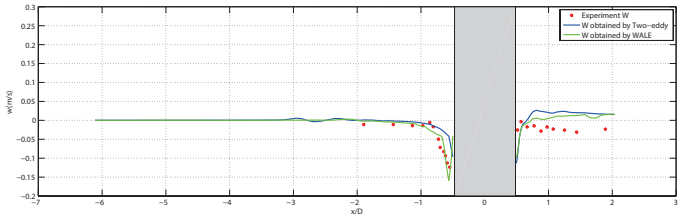


(b) At the layer of Z = -0.497 m

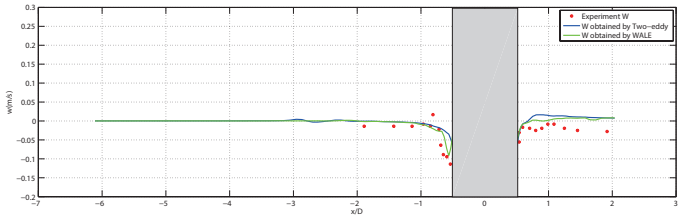


(c) At the layer of Z = -0.517 m

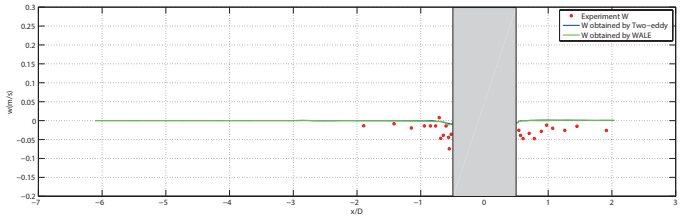


(d) At the layer of Z = -0.537 m

**Figure 4.33:** Mean vertical velocity at different layers. Rough rigid bed with *mesh1* (cont.2)

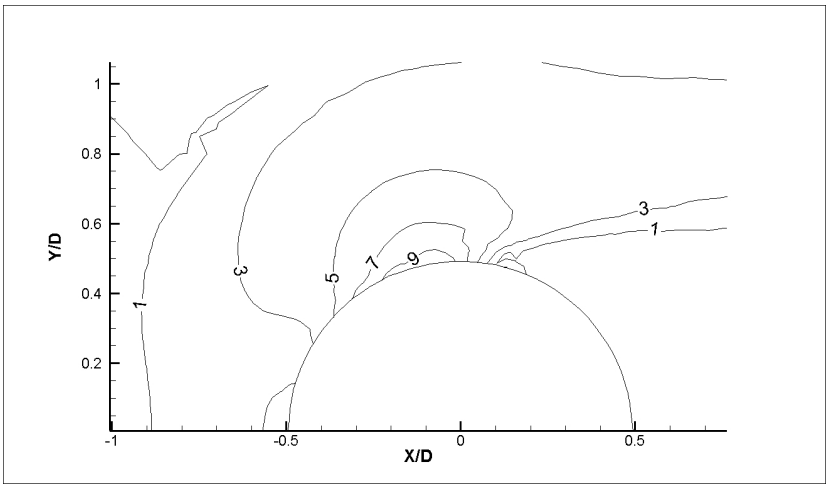


**Figure 4.34:** Bed shear stress amplification. 2eddy LES model

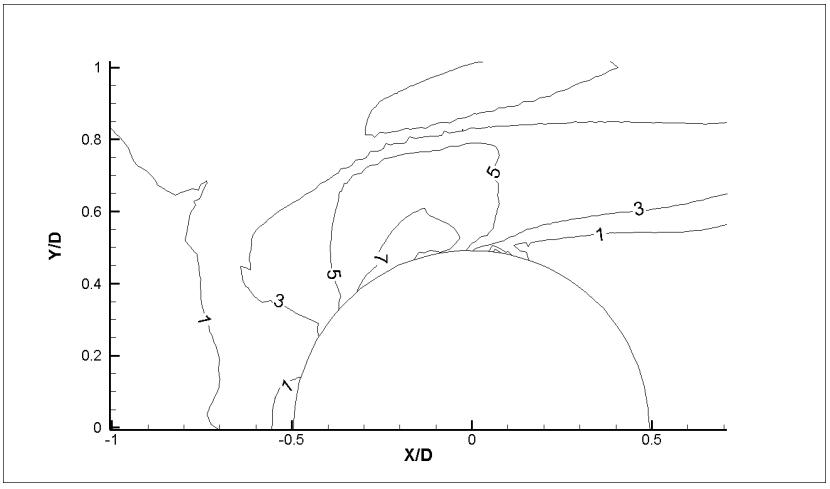


**Figure 4.35:** Bed shear stress amplification. WALE model

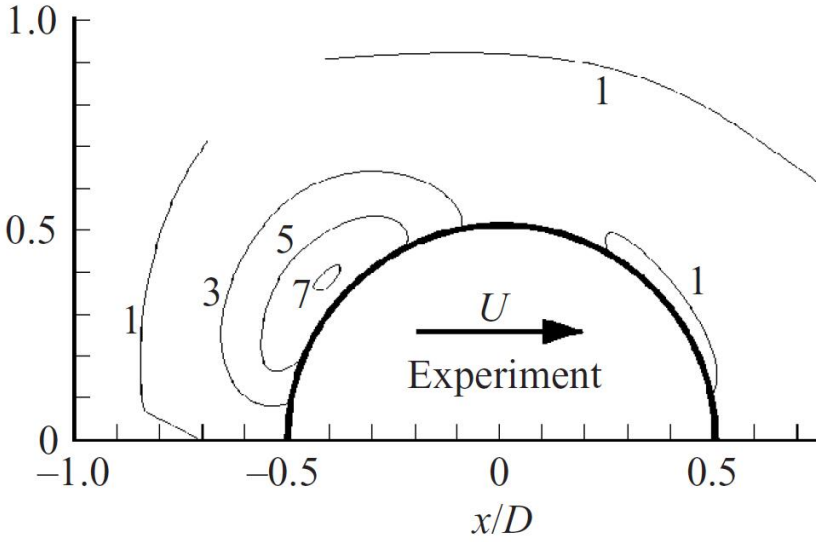


**Figure 4.36:** Bed shear stress amplification. Experiment (Hjorth 1975)

# Chapter 5

# Immersed boundary method validation

This chapter presents the validation of immersed boundary method of two laboratory scale cases. The first test case is the same as the one used in Chapter 4 for the flow past a circular cylinder. The second test case is the simulation of the flow past a submerged cylinder. The implementation of the immersed boundary method for a full structure and a submerged structure is slightly different and the changes are discussed. Both numerical results are benchmarked with laboratory experiments [1, 114] respectively.

## 5.1 CASE I: flow past a full cylinder

The Immersed boundary method is firstly used to represented a structure which is set in the water. The same case of the flow past a circular cylinder therefore is selected to validate the immersed boundary method implementation. Rather than representing the cylinder as an island in the mesh, an immersed boundary force is implemented to describe it.

### 5.1.1 Computational domain and mesh

Following the test case used in Chapter 4, the flume of simulation is set to 40 m long and 4 m wide. The bed is assumed to be flat with a constant depth of 0.54 m. The area containing the cylinder (100 nodes in 2-D to account for the cylinder) and the wake part

are refined. The mesh of the simulation domain contains 48,764 elements in 2-D and has 50 unevenly distributed horizontal layers. As shown in figure 5.1, the footprint of the the cylinder is represented directly in the mesh, however the boundary nodes of the cylinder are marked as immersed boundary nodes which can be seen clearly in figure 5.2 (the boundary between the blue mesh and the red mesh is the immersed boundary). Such type of mesh (body-fitted-like mesh) is used to avoid any interpolation while using the immersed boundary method.

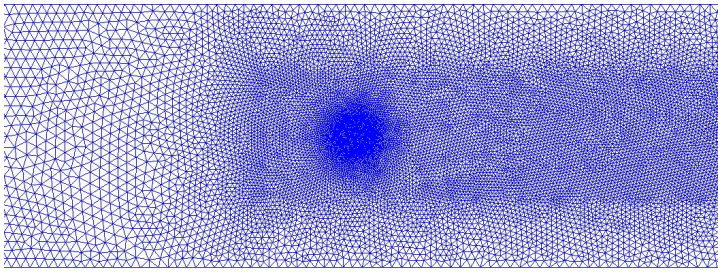

**Figure 5.1:** Snapshot of the computed domain

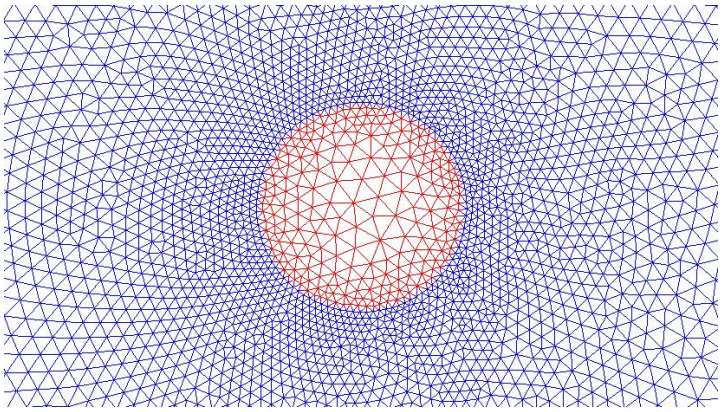

**Figure 5.2:** Snapshot of the computed domain

On the implementation side, the loop for masking the nodes inside the cylinder is created before the calculation loop beginning in the main code 'telemac3d.f'. The distance between each node and the cylinder center is computed. If this distance is smaller than the cylinder radius, the node will be masked and considering as the cylinder solid boundary. The global number of each boundary node is stored in variable CYLINDER_NODE(:). The radius of the cylinder is 0.27 m.

In this study, the code is written as:

```
      CYLINDER_X = 4.D0
      CYLINDER_Y = 2.D0
      CYLINDER_INNER_RADIUS = 0.24D0
      CYLINDER_OUTER_RADIUS = 0.29D0
      N_IBM = 1

       DO NP = 1,NPLAN
         DO I=1,NPOIN2
          IJK = (NP-1)*NPOIN2+I



         NODE_DISTANCE = SQRT( (MESH3D%X%R(IJK)-CYLINDER_X)**2
     &                      +(MESH3D%Y%R(IJK)-CYLINDER_Y)**2 )
         IF (NODE_DISTANCE .LE. CYLINDER_OUTER_RADIUS .AND.
     &       NODE_DISTANCE .GE. CYLINDER_INNER_RADIUS ) THEN

             CYLINDER_NODE(N_IBM) = IJK

             write(13,*) NP,CYLINDER_NODE(N_IBM)

             N_IBM = N_IBM+1

         ENDIF

        ENDDO
       ENDDO
       N_IBM = N_IBM-1
```

### 5.1.2 Boundary conditions

Except for the implementation of the immersed boundary, the inlet, outlet, wall and bottom conditions are the same as the ones used in Chapter 4. They are summarised

as follows:

1. *Inlet*: At the inlet, a flow rate Q is specified. The value of Q is expressed from the horizontal velocity, which follows the same flow settings as in Roulund's experiment.

2. *Outlet*: At the outlet, prescribed elevations are given.

3. *Wall*: The walls of the flume are set as solid walls. Sidewall friction is not accounted for in this study, therefore all the walls are smooth.

4. *Bottom*: Smooth bed conditions are considered.

For the cylinder representation, an immersed boundary force is applied on the selected nodes describing the boundary of the cylinder. Zero velocity conditions are applied to all the nodes inside of the cylinder.

### 5.1.3 Model setup

The parameters used in this test case are the same as the ones listed in Chapter 4. Details can be found in table 4.1. Only the case with the smooth bed condition is used for the IB method validation. The 2eddy viscosity LES model is applied for the representation of the turbulence impact.

### 5.1.4 Numerical results

The results obtained by the implementation of the immersed boundary method are very similar to the one shown in chapter 4.

The instantaneous horizontal flow distributions obtained from the numerical model are plotted in figure 5.3. Three figures show the velocity profiles at the surface, middle (Z=-0.27 m) and bottom layers respectively. The turbulent flow due to the cylinder obstacle can be seen clearly at the surface and middle layers. All the figures show the deceleration of the flow in front of the cylinder and behind the cylinder. There is also a dramatic acceleration at each side of the cylinder. In the bottom layer, rather than the long oscillating wake, a fast velocity area at the sides of the cylinder plays a more significant role in the flow structure.

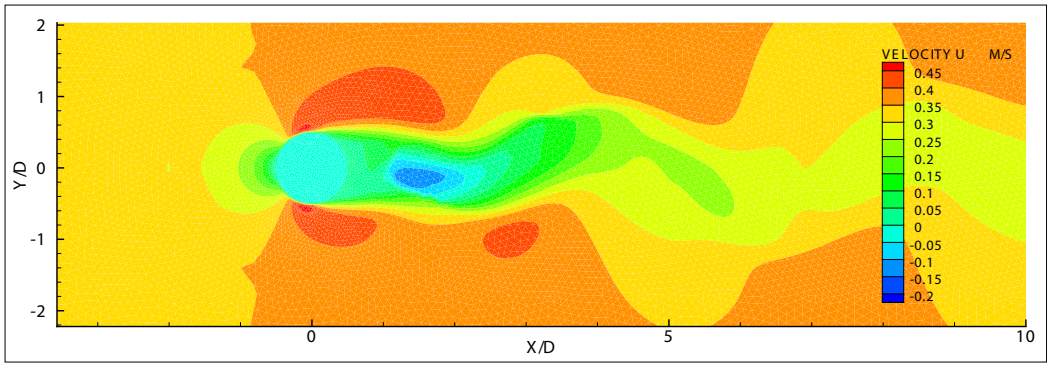


(a) Surface layer Z=0 m

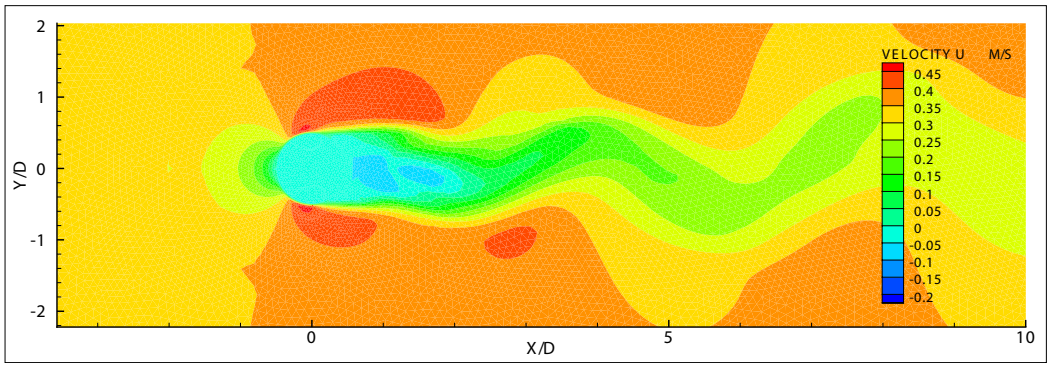


(b) Middle layer Z=-0.27 m

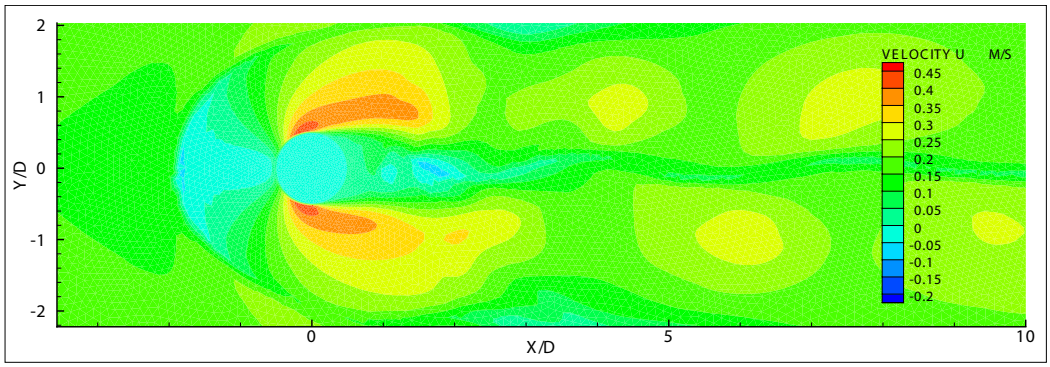


(c) Bottom layer Z=-0.54 m

**Figure 5.3:** Horizontal velocity distribution at different layers using the IB method. Obtained from the 2eddy LES model and smooth bed condition

Comparing with the numerical results obtained by using an 'hollow mesh', shown in figure 4.14, we found several differences. Firstly, in the previous results, the return flow (negative flow velocity) is only found in the middle layer and bottom layer, however in the results of immersed boundary implementation, it was also found at the surface layer.

Moreover, figure 4.14 shows that the size acceleration flow at the sides of cylinder is smaller than the diameter of the cylinder, but in figure 5.3, the length of the acceleration flow is about three times the diameter of the cylinder.

In the further investigation of the horizontal flow distribution, the averaged horizontal velocity magnitude is computed by averaging 100 instantaneous data. The result is represented in figure 5.4

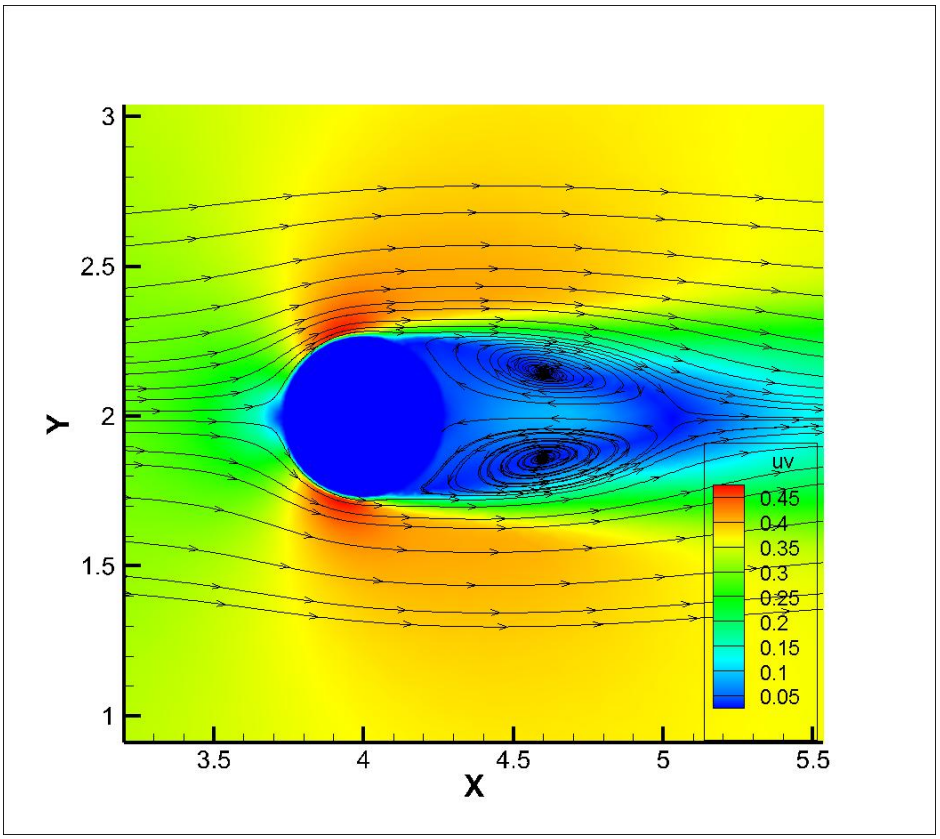


**Figure 5.4:** Averaged horizontal velocity magnitude and stream lines at Z=-0.27 m

As shown in this figure, the velocities inside the cylinder are kept to zero. The streamlines indicate the route of the flow past the cylinder. Under the effect of the immersed boundary forces which are applied to the cylinder boundary nodes, the upstream flow splits in front of the cylinder and then accelerates at each side. After the detachment of the flow around the cylinder, a pair of symmetric vortices is clearly found behind it.

Figures 5.5 and 5.6 illustrate the velocity vectors in a vertical cross-section along the center line. A horseshoe vortex is found in front of the cylinder close to the bottom,

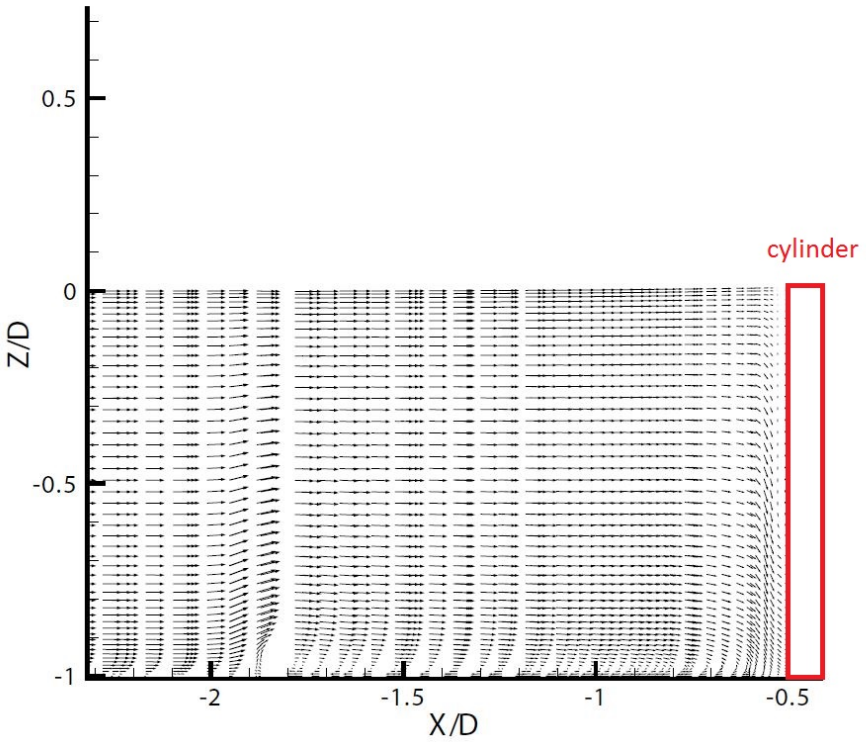


**Figure 5.5:** Velocity vectors in the vertical cross-section along center line. Flow in front of the cylinder

however the shape of this vortex is quite flat compared to the results obtained by the classical approach ('hollow mesh') test case. The horizontal size of this vortex is about 1.5D and the vertical one is only 0.1D. Behind the cylinder, two vortices are generated immediately behind the cylinder structure exhibiting a similar pattern as in the 'hollow mesh' test case.

The unsteadiness of the flow is shown in figure 5.7, which covers a full vortex shedding period. The flow route is represented by both vectors and streamlines. The shedding of the vortices from the two sides of the cylinder is clearly exhibited.

Quantitatively, the numerical results obtained by immersed boundary method are benchmarked with Roulund's experiment [114]. Figure 5.8 shows the averaged horizontal velocity at different heights. Experimental data and numerical model results are represented by red dots and blue curves respectively. Generally, the flow velocities show a deceleration trend in front of the cylinder and a recovery trend behind the cylinder.

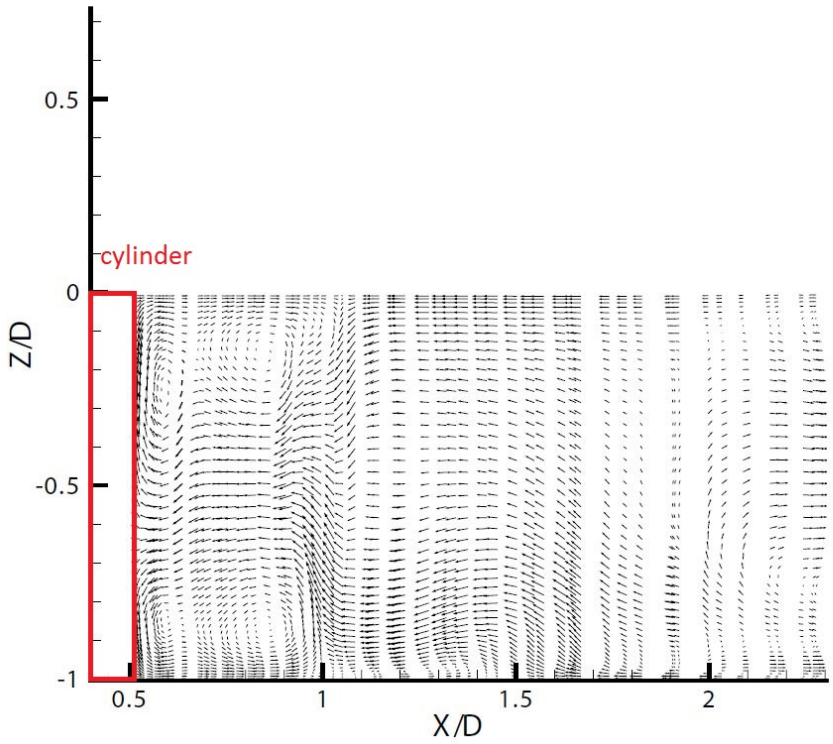


**Figure 5.6:** Velocity vectors in the vertical cross-section along center line. Flow behind the cylinder

In front of the cylinder, a very good agreement can be found at layer of Z=-0.34 m, Z=-0.44 m and Z=-0.49 m. However differences are found for the layer Z=-0.52 m and Z=-0.53 m where the numerical model underpredicts the flow velocities. In the wake area, at the layer of Z=-0.34 m, Z= -0.44 m and Z=-0.49 m, the experimental data show that the flow reduces to a negative value first and then recovers to the value of the upstream velocity. At two layers below (Z= -0.52 m and Z= -0.53 m), both results indicate that there is a very small increase before the flow recovery. All the flow features represented by the experimental data are captured by the numerical model although the length of these recovery is over estimated.

Averaged vertical velocities at different layers are illustrated in figure 5.9. Numerical results exhibit the same patterns as the experimental data both in front of and behind the cylinder. A spike is found in front of the cylinder at the layer of Z=-0.34 m and Z=-0.44 m which is similar to the results obtained using the 'hollow mesh'. The main

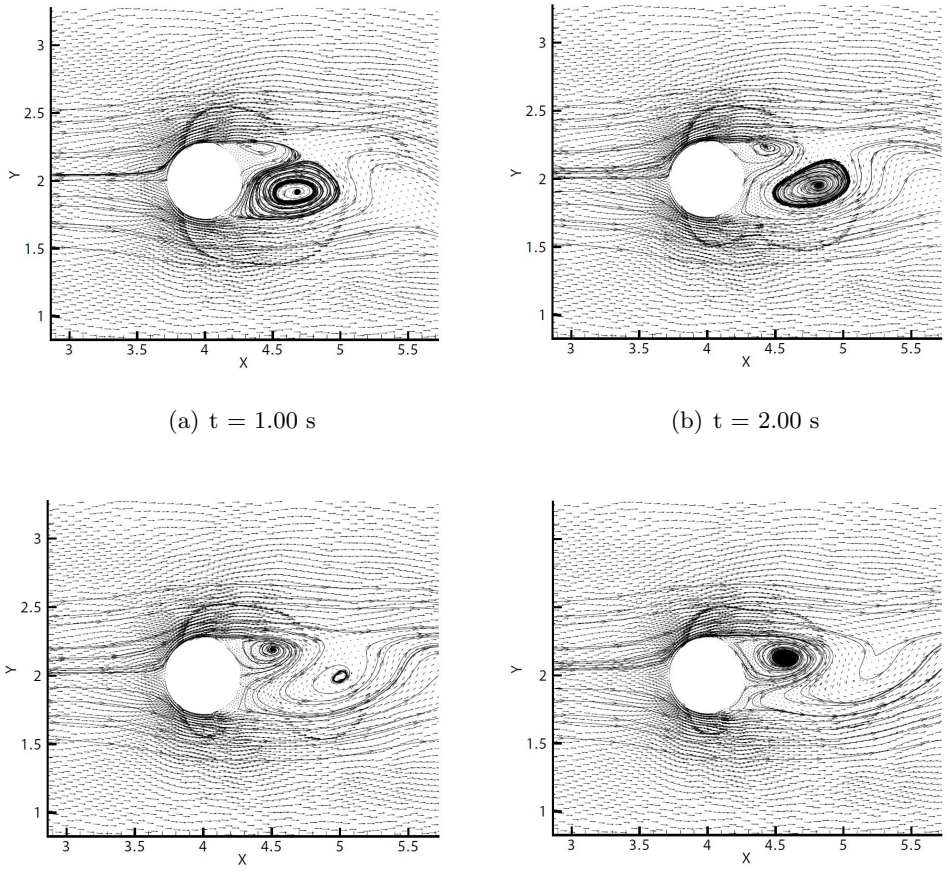


(a) t = 1.00 s

(b) t = 2.00 s

(c) t = 3.00 s

(d) t = 4.00 s

**Figure 5.7:** Horizontal velocity vector and streamlines for unsteady flow simulation during one period of the vortex shedding. Horizontal cross-section at Z=-0.27 m

reason lead to this spike is that a horseshoe vortex was generated in front of the cylinder and then the local vertical velocity is increased.

Due to the lack of measurement data, numerical results can not be validated further downstream, however a comparison between the numerical results obtained using the immersed boundary method and the 'hollow mesh' classical strategy is presented in figure 5.10

The averaged horizontal velocity obtained using the immersed boundary test and the 'hollow mesh' test are represented by a red line and a black line respectively. As shown in this figure, both tests show the same result in front of the cylinder. A small difference is found in the wake region. Between 0.5D to about 18D, the flow

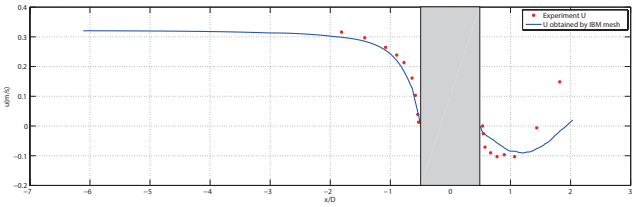


(a) At the layer of Z=-0.34 m

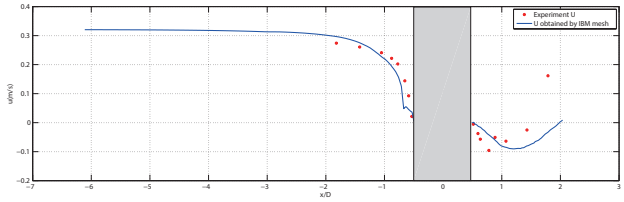


(b) At the layer of Z=-0.44 m

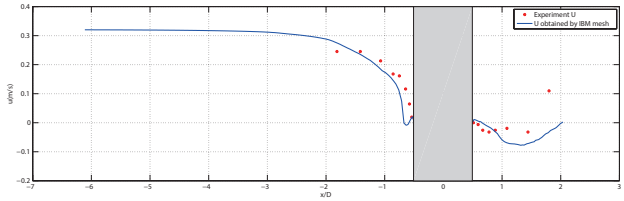


(c) At the layer of Z=-0.49 m

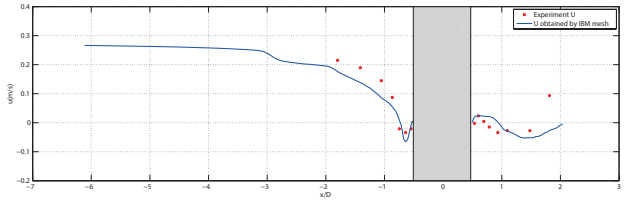


(d) At the layer of Z=-0.52 m

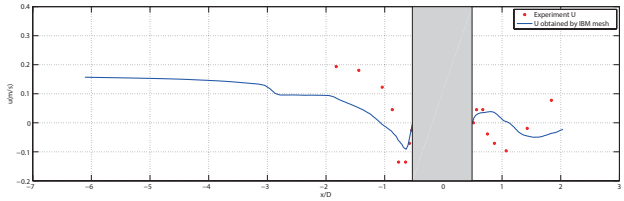


(e) At the layer of Z=-0.53 m

**Figure 5.8:** Mean horizontal velocity at different layers. Smooth rigid bed using *mesh1* resolution

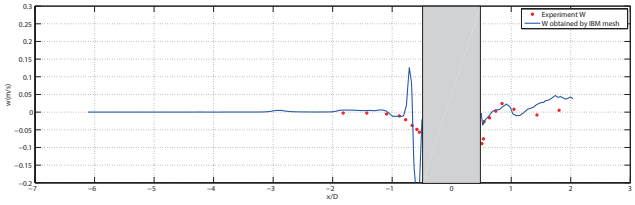


(a) At the layer of Z=-0.34 m

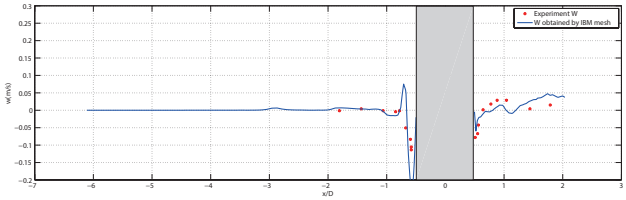


(b) At the layer of Z=-0.44 m

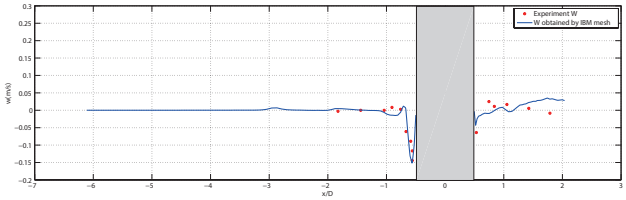


(c) At the layer of Z=-0.49 m

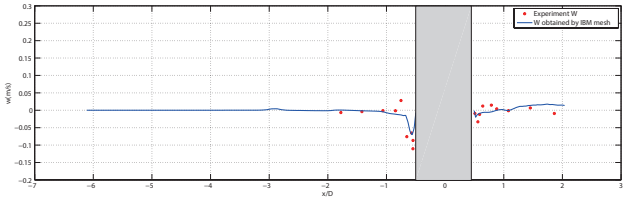


(d) At the layer of Z=-0.52 m

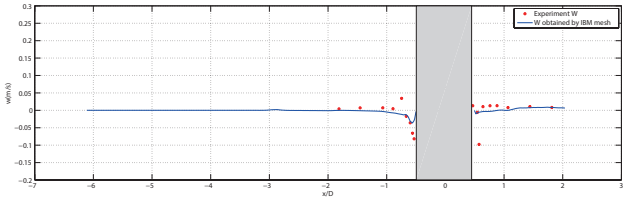


(e) At the layer of Z=-0.53 m

**Figure 5.9:** Mean vertical velocity at different layers. Smooth rigid bed with *mesh1* resolution

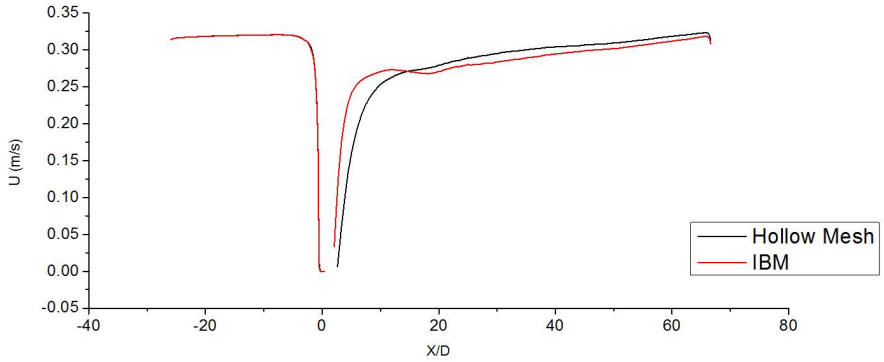


**Figure 5.10:** Mean horizontal velocity along the center line at the layer of Z=-0.27

obtained using the immersed boundary method shows a faster recovery, however from 18D downstream on, the velocity predicted by the 'hollow mesh' test is higher than the one of the IB test.

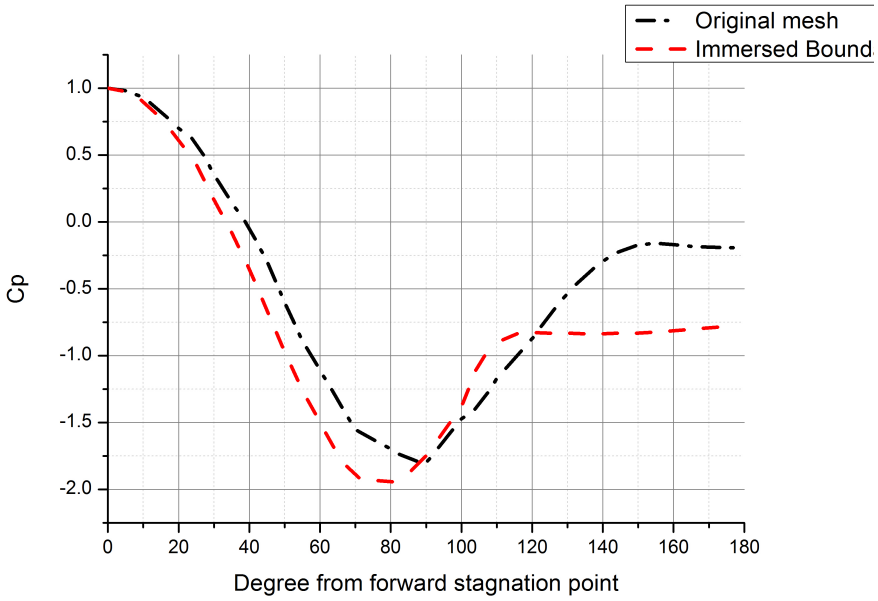


**Figure 5.11:** Mean pressure coefficient around cylinder.

The mean pressure coefficient around the cylinder obtained by using the 'hollow mesh' and the immersed boundary method is shown in figure 5.11. It can be seen that the pressure coefficient of both numerical results exhibit a decrease trend in the first half of the cylinder, and then recover to a constant negative value. The lowest pres-

sure coefficient of the immersed boundary method appeared at about 80 degrees from forward of the stagnation point, however this peak using the original model is found at about 90 degrees. Furthermore, in the end of the curves, the pressure coefficient of the immersed boundary method is about twice as large as it of the original model which means that the flow calculated by the immersed boundary method is more turbulent behind cylinder.

Figure 5.12 illustrates a series of time-averaged horizontal velocities along 6 different sections crossing the flume. They are located at 2 m, 0.5 m in front of cylinder, in the middle of the cylinder and at 0.5 m, 1.5 m, 2.5 m behind the cylinder respectively. In these figures, the x-axis indicated the width of the flume. Similar velocity distribution is found in front of the cylinder ( see figure 5.12 (a) and (b)), that the velocity reduced from an initial speed at the side of the flume to a low speed in the middle of the flume. This peak obtained by the immersed boundary method is slightly lower than the one in the original model. Figure 5.12 (c) shows the velocity distribution crossing the cylinder and the acceleration at the side of the cylinder is clearly represented by the numerical models. Behind thecylinder, both numerical results show the feature that flow has a gradual acceleration from the side of the flume to about 2/3 of the flume width and then it is replaced by a dramatic reduction. An higher reduction rate and lower flow speed are found in the result of immersed boundary method.

Figure 5.13 presents the turbulence kinetic energy (TKE) distribution around cylinder in the middle layer obtained by the 'hollow mesh' and the immersed boundary method respectively. It is noticed that there is a big difference between two results of the TKE distribution along the boundary of the cylinder. In front of cylinder, both model results show high TKE, however in the test of using immersed boundary method, the TKE along the cylinder wall is very small. This is due to the face that zero velocities are calculated on the boundary nodes of the cylinder. This also effects the TKE behind the cylinder. The result of 'hollow mesh' (see figure 5.13 (a)) indicates that at both sides of the cylinder, there is a high TKE region and this high TKE continuously diffuse towards downstream along the side of cylinder. In the middle behind the cylinder, the TKE maintains in a low value. A different picture is found in the result of immersed boundary method, two high TKE regions are found behind cylinder with a

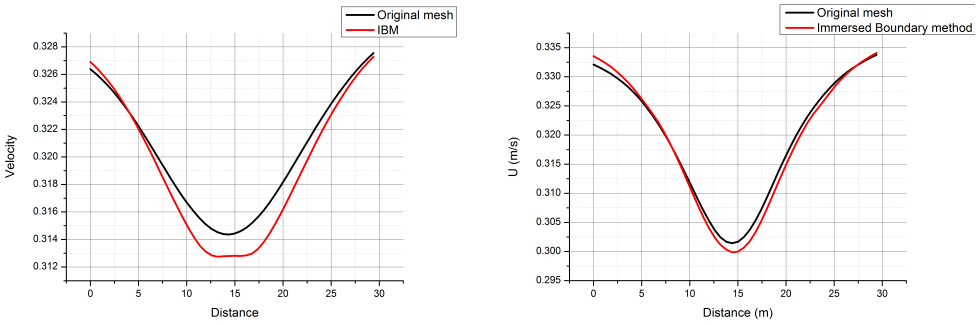


(a) section 1




(b) section 2

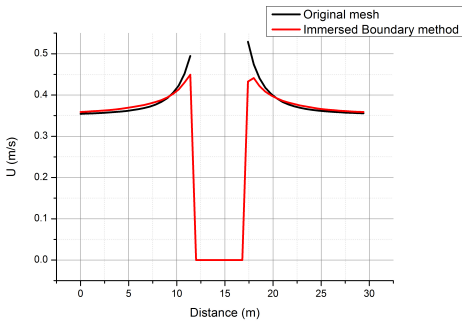


(c) section 3

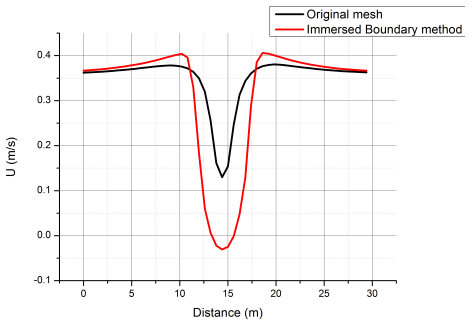


(d) section 4

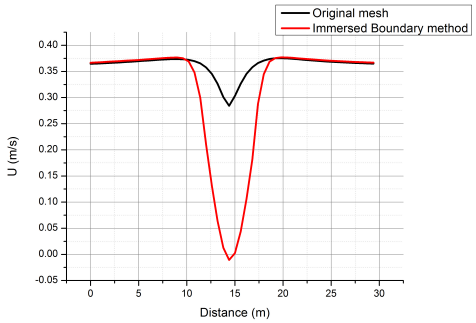


(e) section 5

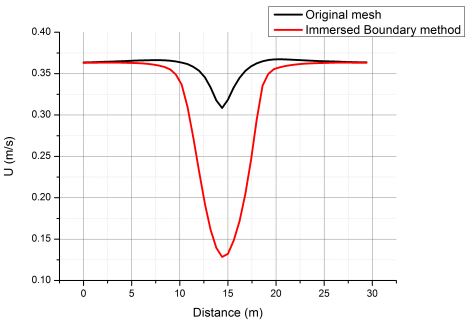


(f) section 6

**Figure 5.12:** Mean horizontal velocity distribution along severl different cross sections in the flume

distance of about 1 diameter. Although these high TKE regions are separated at the distance between 1 to 2 diameter, they have a mixing after 2 diameter and diffuse to downstream.

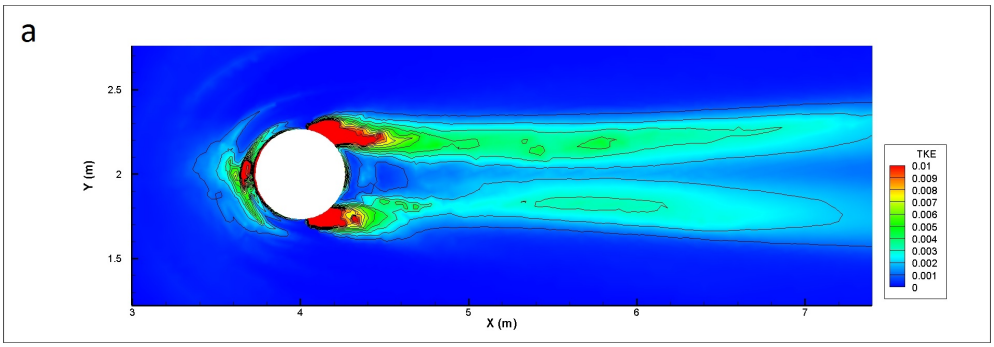


(a) TKE obtained by the 'hollow mesh' test

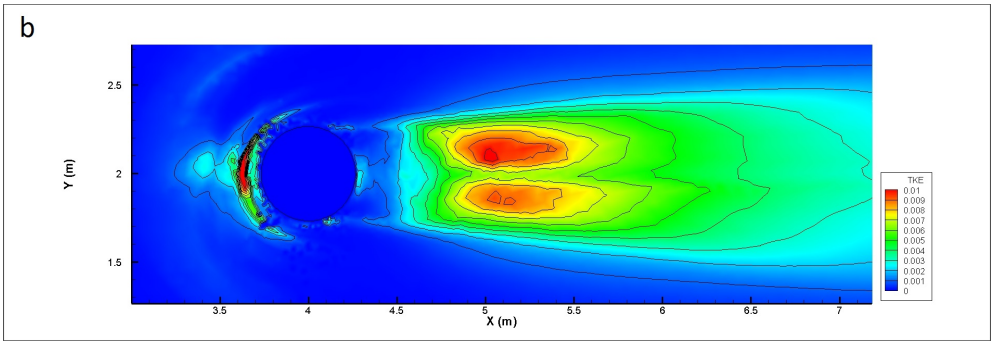


(b) TKE obtained the immersed boundary test

**Figure 5.13:** Turbulence kinetic energy (TKE) distribution around circular cylinder in the middle layer obtained by two methods of structure representation, the 'hollo mesh' and the immersed boundary method

## 5.2 CASE II: flow past a submerged cylinder

In the second test case, the immersed boundary method is implemented to simulate the flow past a submerged cylinder with finite height. Following Palau-Salvador's experiment [1], cylinders with $h$=0.20 m height and two different diameters (0.04 m and 0.08 m respectively) are simulated using the immersed boundary method.

### 5.2.1 Computational domain and mesh

Palau-Salvador's experiment [1] used a tank with constant water level of 3 m. This water depth is also used in the numerical models. As shown in figure 5.14, the width and length of the numerical model is set to 4h (0.8 m) and 13h (2.6 m) respectively. The cylinder is placed at 3h (0.6 m) downstream the inlet.

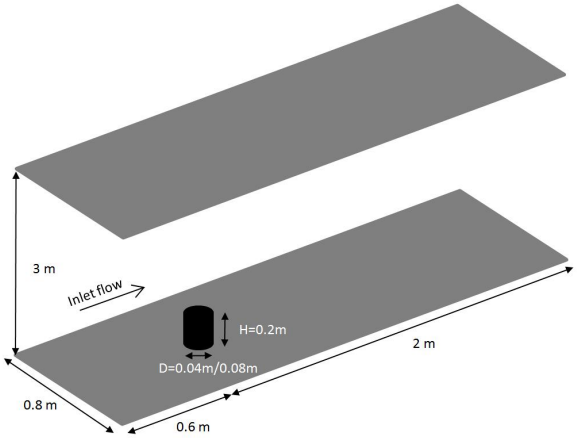


**Figure 5.14:** Computational domain of the flow passing a finite height cylinder

In total, the mesh of the numerical model contains 37,372 elements in 2-D and 50 layers in the vertical direction. Similar to the mesh used in case I, there are 100 nodes located at the cylinder boundaries. The mesh around the cylinder is refined. In the vertical direction, as shown in figure 5.15, a height of first 30 layers from the bottom are fixed, in order for the cylinder to keep its constant height during the simulation.

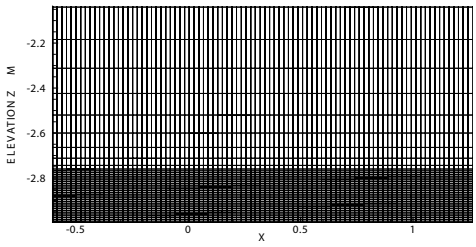


**Figure 5.15:** Vertical mesh used in the numerical model of the flow passing a finite height cylinder

### 5.2.2 Boundary conditions

In this study, the same boundary conditions as in the previous case are used. They are summarised as follows:

1. *Inlet*: At the inlet, a flow rate Q is specified. The value of Q is expressed from the horizontal velocity, which follows the same flow settings as in Roulund's experiment.

2. *Outlet*: At the outlet, prescribed elevations are given.

| Test | 1 | 2 |
|---|---|---|
| Bed condition | Smooth Rigid | Smooth Rigid |
| Water depth $h$ (m) | 3 | 3 |
| Mean Flow velocity $U(ms^{-1})$ | 0.54 | 0.54 |
| Pile diameter $D(m)$ | 0.04 | 0.08 |
| Re Number | $2.2 \times 10^4$ | $4.4 \times 10^4$ |

**Table 5.1:** Test conditions for the numerical modelling

3. *Wall*: The walls of the flume are set as solid walls. Sidewall friction is not accounted for in this study, therefore all the walls are smooth.

4. *Bottom*: Smooth bed conditions are considered.

For the cylinder representation, an immersed boundary force is applied on the selected nodes describing the boundary of the cylinder. Zero velocity conditions are applied to all the nodes inside of the cylinder.

### 5.2.3 Model setup

The key parameters of the numerical model are summarised in the table. A constant flow velocity of 0.54 $ms^{-1}$ was set at inlet boundary. The Reynolds number based on the two pile diameters are $2.2 \times 10^4$ and $4.4 \times 10^4$ respectively. A time step of 0.001 s is chosen to keep the maximum Courant number below 0.6. 5.1

### 5.2.4 Results

The horizontal velocity distributions at the layer of $Z = h/2$ are illustrated in figures 5.16 and 5.17. The numerical results obtained from the 0.04 m diameter cylinder case and the 0.08 m diameter cylinder case show similar pattern that the flow reduces speed in front of the cylinder and then recovers is behind it. Streamlines in the figures indicate that the upstream flow is separated by the structure and then pushed to the side of cylinder. After the flow detaches from the cylinder wall, small vortices are generated in the wake area. In comparison with the instantaneous pictures of Palau-Salvador's experiment, the width of the wake tail in the numerical results is slightly over-predicted.

In the previous investigations of the flow past a full cylinder, a remarkable feature is the flow acceleration at both sides of the cylinder. This high speed area should appear adjacent to the cylinder wall, however the result of figure 5.16 and figure 5.17 indicated that although there are accelerations at the sides of cylinder, these accelerations are found at about 3 diameter behind the cylinder.

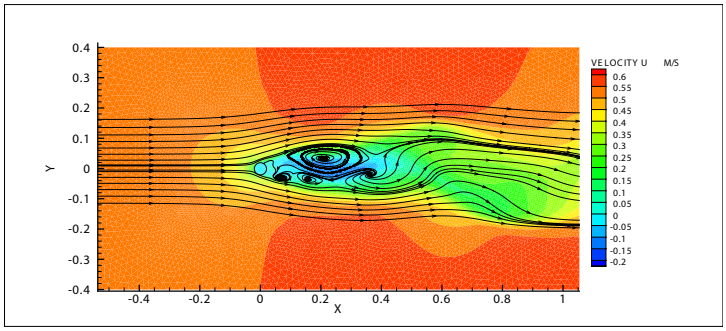


a: numerical model

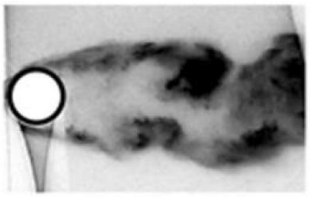

b: Experiment

**Figure 5.16:** Horizontal velocity distribution at layer of $h/2$ of the cylinder D=0.04m. (a) Numerical results. (b) Instantaneous pictures of Palau-Salvador's experiment[1]

The horizontal velocity distributions along the center line are shown in a vertical cross-section view (see figure 5.18). The numerical results show that the flow accelerates at the top of the cylinder and decelerates in the wake part. The vertical vortices behind the cylinder are seen clearly both in the 0.04 m diameter case and the 0.08 m diameter case. However in the figure showing the 0.04 m diameter results, the horizontal velocity colour bands indicate that there is a strong velocity fluctuation in front of the cylinder. The reason of this impact might be due to the effect of the forcing on the immersed boundary nodes. Because the same configuration is used in both cylinder cases, these velocity wiggles may also come from the quality of the mesh used in the 0.04 m diameter case.

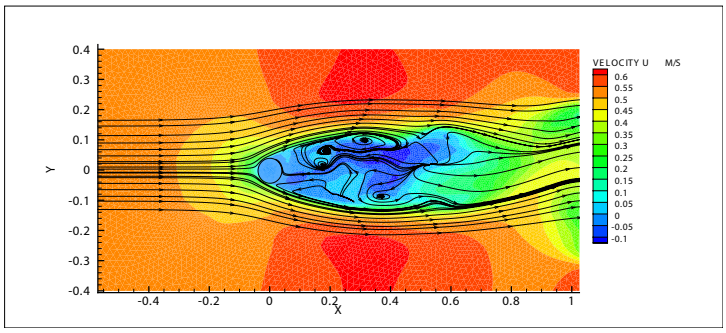


a: numerical model

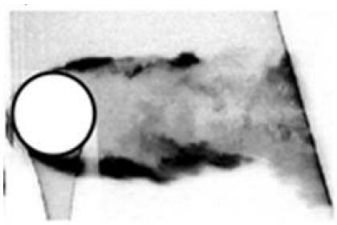

b: Experiment

**Figure 5.17:** Horizontal velocity distribution at layer of $h/2$ of the cylinder D=0.08m. (a) Numerical results. (b) Instantaneous pictures of Palau-Salvador's experiment[1]

Figure 5.19 presents the root mean square of the horizontal (uu) and vertical (ww) fluctuations in the centre plane. This shows the turbulence intensity around the submerged cylinder. In general, strong horizontal and vertical velocity fluctuations are found in both cylinder cases. However these fluctuations are not located just behind the cylinder but with some few distance of it. In the study of the 0.04 m diameter case, some small horizontal fluctuations are represented on the top behind the cylinder. The strongest horizontal fluctuation is found 7 diameter behind the cylinder, and the same is observed for the vertical fluctuation. In the 0.08 m diameter case, the zone of horizontal fluctuation is closer, i.e. about 4 diameters, however the vertical fluctuation zone is still at about 8 diameters downstream of the cylinder.

Figure 5.20 uses the Q criterion to visualise the vortex structure obtained by both numerical tests. The spike shown in figure 5.20 (a) proves the founding of figure 5.18(a) that there is a strong velocity fluctuation in front of the cylinder. The vortex structures including the horseshoe vortex at the bottom of and in front of the cylinder, the tip

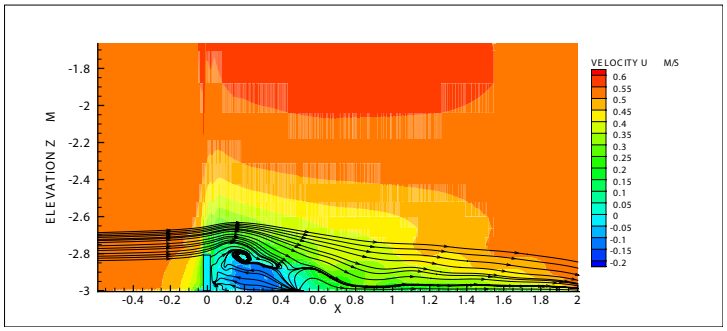


a: D=0.04m

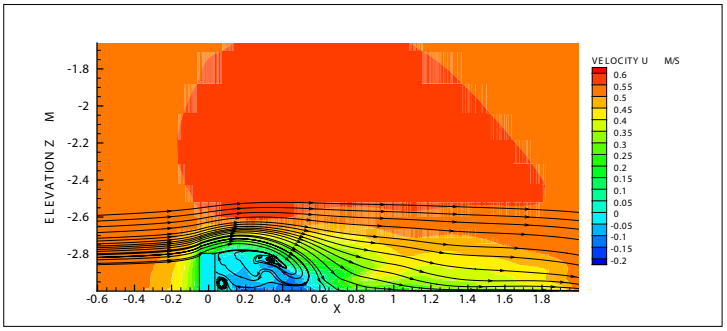


b: D=0.08m

**Figure 5.18:** Horizontal velocity distribution along the center line in the vertical cross-section view.

vortex above the cylinder and the trailing vortex behind the cylinder are represented clearly by the numerical models. In the case of a larger cylinder diameter (0.08 m), more vortices are present in the flow, which are also captured by the numerical models.

The averaged horizontal velocity obtained by the numerical models are compared with the measurement data obtained by Palau-Salvador [1]. Figure 5.21 illustrates this comparison along the centre line at layer of Z/h=0.6. The red dots and red curve represent the measurement data and numerical results, respectively, both obtained for the 0.04 m diameter cylinder case. The green dots and green curve represent the measurement data and numerical results obtained for the 0.08 m cylinder case. In front of the cylinder, both numerical results show a good agreement with the experimental data in that the flow reduces speed gradually from the inlet speed to zero, showing the effectiveness of the immersed boundary method. However in the wake area, large over estimations are found in the numerical results, compared to the measurement data. Although in figure 5.21, all profiles show the recovery trend, the distance of this trend is far more over predicted by the numerical models, which might partly be explained

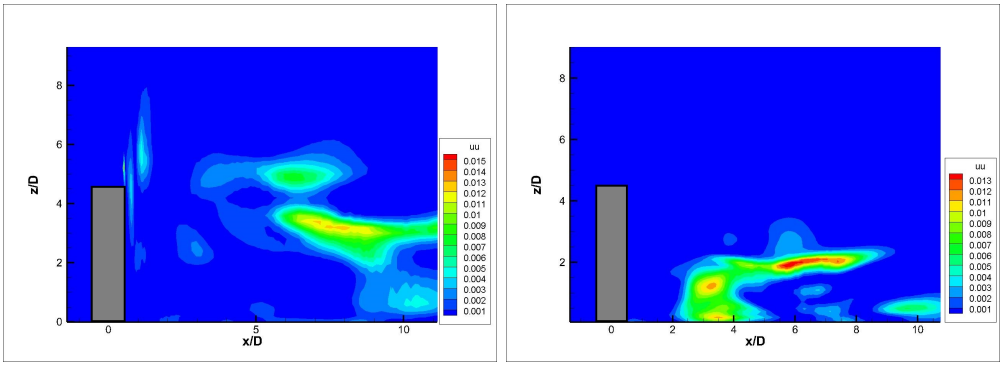


(a) D=0.04 m




(b) D=0.08 m

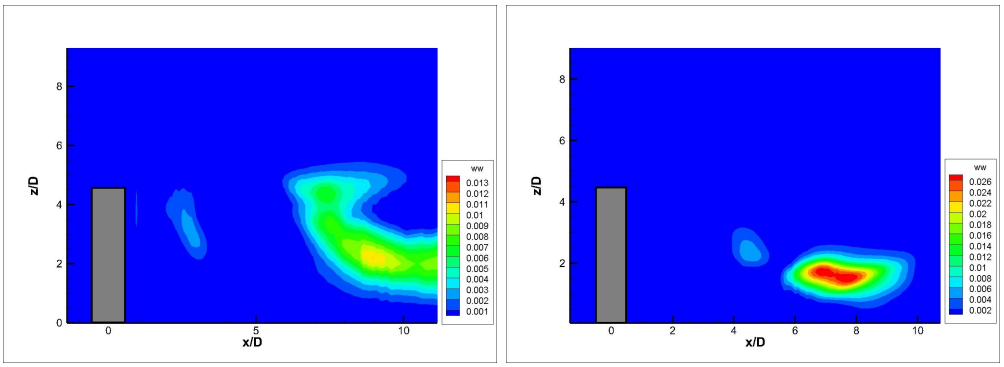


(c) D=0.04 m




(d) D=0.08 m

**Figure 5.19:** Root mean square of the streamwise (uu) and vertical (ww) fluctuations in the centre plane

by the use of LES turbulence models, which, for the other cases (full cylinder using IB method or 'hollow mesh' methods) also tend to overestimate the length of the horizontal vortex past cylinders.

## 5.3 Discussion

In this study, the immersed boundary method is tested. Two laboratory scale cases including the flow passing a full cylinder and the flow around a finite-height cylinder are used for the validation. The immersed boundary force is calculated in the 'hydrostatic step', therefore they are only used in the source term of the horizontal momentum equation. Because the vertical velocity is predicted through the mass conservation equation, a zero velocity condition is applied for the vertical component.

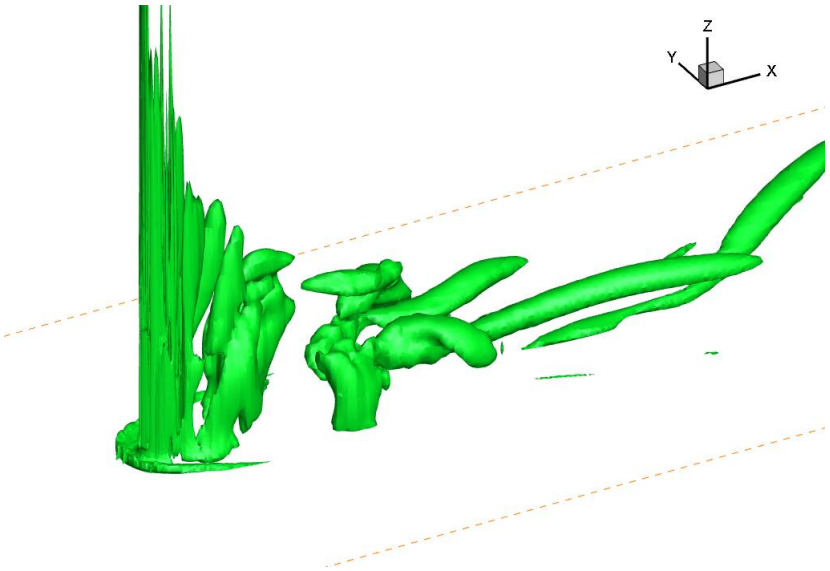


a: D=0.04m

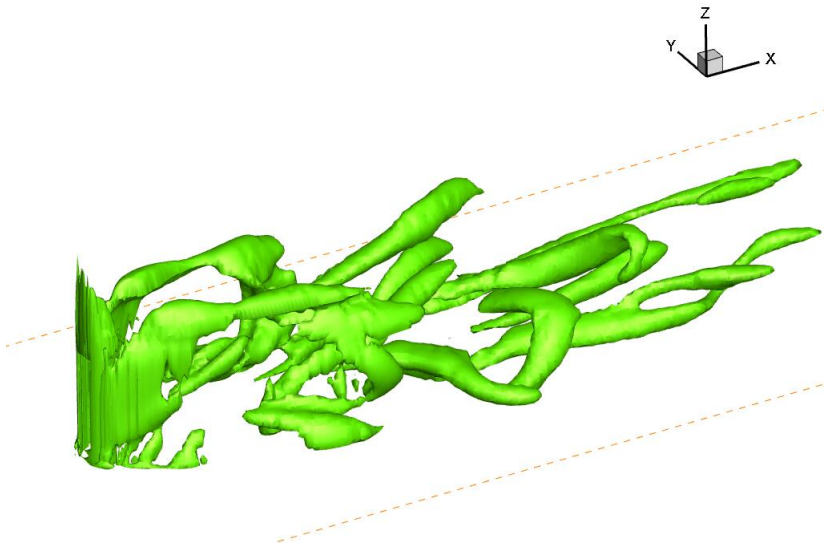


b: D=0.08m

**Figure 5.20:** horizontal velocity distribution along center line in vertical cross-section view

In the full cylinder case, the immersed boundary successfully represents the structure in the water. The feature of the flow past a circular cylinder is well captured including the reduced flow in front of cylinder, the flow acceleration beside cylinder and the vortex shedding behind cylinder. In comparison with the original simulation, the implementation of the immersed boundary increases the motion of water, hence the

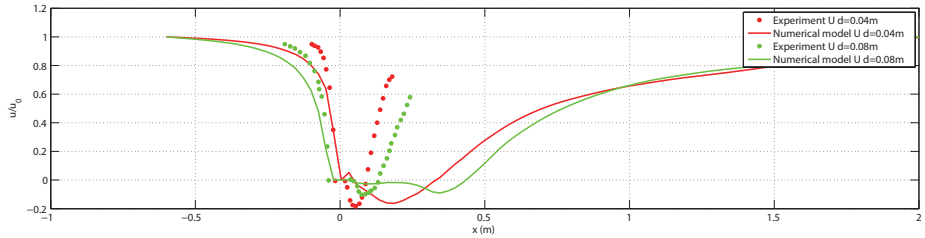


**Figure 5.21:** Stream-wise and horizontal mean-velocity along the center line at the layer of z/h =0.6 as a function of x

flow around cylinder becomes more turbulent. This is because in the original model (representing the cylinder by a 'hollow mesh'), the wall of the cylinder is considered as a smooth wall. However when implementing the immersed boundary method, the velocity on the cylinder wall is set to zero and this is equal to a non-slip boundary condition. Consequently, the flow become more turbulent due to the friction on the cylinder wall.

In the finite-height cylinder test case, although the general flow feature can be simulated by the numerical model and the vortex structure can be seen in the results, there is a big difference between the numerical model and the experimental data, especially in the length of wake recovery. The main problems appear for the representation of the flow structure above the top of the structure. This may be related to the inherent numerics in the software. For example, different advection schemes need to be investigated or the integration step along the vertical direction need to be improved. Another possible reason is the quality of the mesh. The small size of the experiment acts as a constraint in the number of nodes + layers to be used, especially during the mesh generation stage. Currently, the smallest size to be handled by the mesh generation software 'Bluekenue' is about 0.001 m, therefore it is difficult to build elements smaller than this size.

In general, it is possible to couple the immersed boundary method with TELEMAC-3D to represent the structures in the simulation. When dealing with an obstacle going from the bottom though the surface of the water, the immersed boundary method offers good accuracy in the prediction of surrounding flow structures. The submerged obstacles now can be simulated by TELEMAC-3D by implementing the immersed boundary method. Although the accuracy is limited currently, qualitative patterns can be still

obtained from the numerical model.

# Chapter 6

# Model Application

In this chapter, the prototype scale applications of the new turbulence model and immersed boundary method are discussed. Firstly, the 2eddy turbulence model is applied to simulate the hydrodynamic and environmental impact of the London Array offshore wind farm (OWF). The structures are represented in the mesh explicitly, i.e., the mesh is body-fitted. Then a comparison between the results obtained with the body-fitted mesh and the mesh for the immersed boundary method is carried out. Finally both the 2eddy LES model and immersed boundary method are applied to simulate a tidal turbine farm in an ideal channel.

## 6.1 Offshore wind farms in the Thames Estuary

To test the capability of the present model in predicting hydrodynamic and turbulence around large scale wind farm turbine foundations, the London Array Offshore Wind Farm site is used. It is one of the two largest operational OWF in the world: with a capacity of 630 MW and is in the southern North Sea (SNS).

The foundation of a typical offshore wind turbine may impact the physical processes within the water column and on the seabed, due to their interruption of the flow of wind and currents and hence may affect mixing processes such as sediment transport. These effects have not been well researched, although the development of scour pits around OWF foundations, particularly in sandy sediments has been intensively studied lately. [126, 127].

Recently, more evidence suggest that such impacts may extend far beyond the spatial scale estimated by conventional methods in a natural marine environment. For example, remote sensing data at London Array site suggests that suspended particulate matter can be found in the reflection of the sea surface color over several kilometers distance, which indicates the signatures of wakes extending behind individual wind farm monopiles by Landsat-8 imagery [36] (figure 6.1).

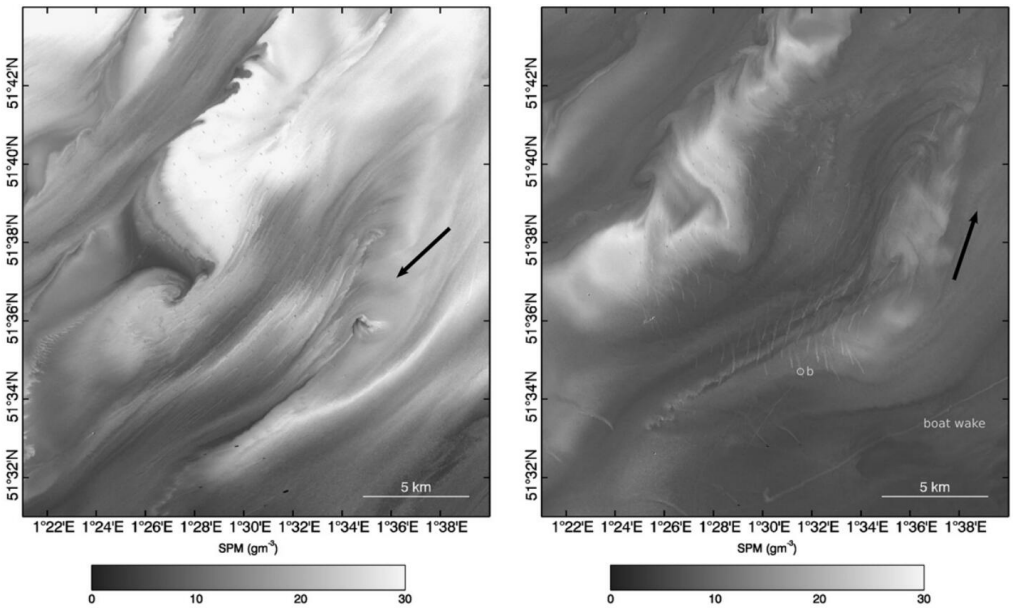


**Figure 6.1:** Details of wake around the London Array site as shown in the processed Landsat image (after Vanhellemont and Ruddick 2014)

This phenomenon is thought to be due to enhanced suspended particulate matter (SPM) concentration in the surface waters. The present model was tested on this particular site to verify whether this is a possible underlying mechanism(s) for these observations, as well as test the applicability of the present model to prototype conditions.

### 6.1.1 Test conditions

The London Array OWF (see figure 6.2) is located at the east of the Thames estuary mouth, Southern North Sea, and consists of 175 monopile turbines. Each monopile has a typical diameter of 4-5m. The bathymetry of the test domain is shown in figure 6.3 where the details of the grid around the structures have been highlighted. The average

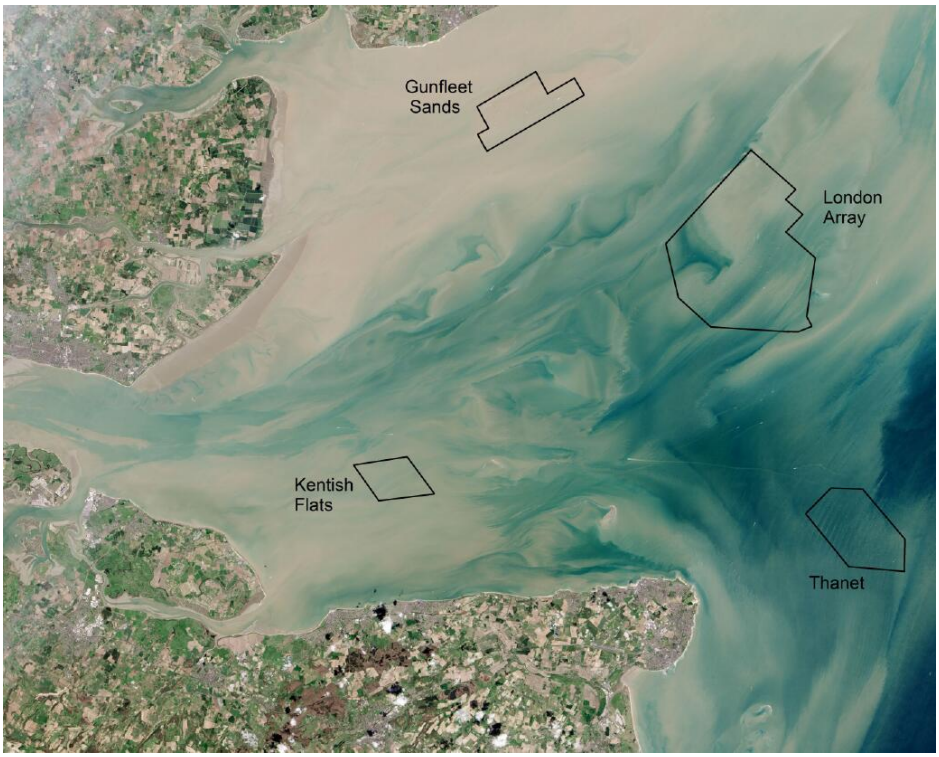


**Figure 6.2:** Thames Estuary and Wind Farms from Space (NASA, with annotations)

distance between each turbine structure along the flow main direction is about 700m. This area includes few sand banks where the local water depth is shallow.

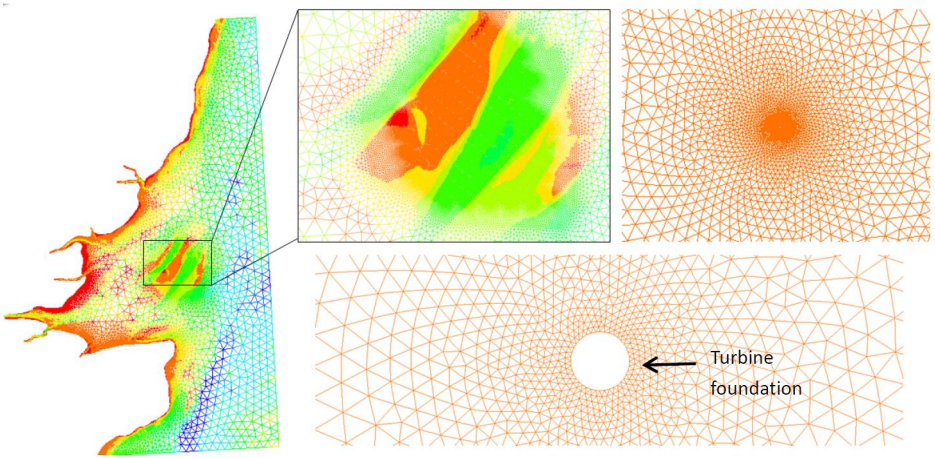


**Figure 6.3:** Numerical model domain and computational mesh for the Thames Estuary

The computational domain is generated in the horizontal plane using an unstructured triangular mesh with elements of different sizes. A sigma-coordinate transformation is used in the vertical direction to resolve the spatial variation of water depth. Each

individual turbine foundation is explicitly represented in the mesh as a solid structure. The mesh size varies from 0.4 m adjacent to the structure to 3 km at the offshore boundary. In total the computational mesh contains 1,074,995 elements in the 2-D (horizontal) plane and 20 layers through the depth in the vertical direction.

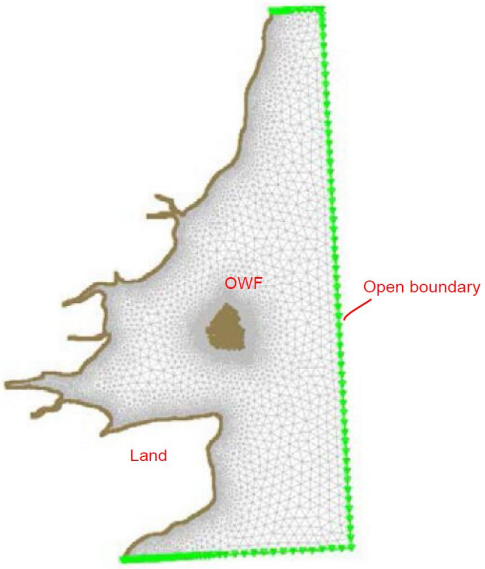


**Figure 6.4:** Model boundary conditions: green denotes the open boundary, grey means the solid (shore) boundary

The model was driven by time varying tidal water levels set at the offshore open boundaries (green dots in Figure 6.4) derived by the Oregon State University inverse tidal model [128]. A radiation boundary condition is used along the open boundary to compute the flow velocities based on given surface elevations. Riverine discharges are not included as their impact on the OWF is considered to be minor.

In order to satisfy the stability criteria and to cover a long period of time, the simulation is carried out in 2 stages including a hydrodynamic step and a sediment transport step. In the first step, the simulation lasts for 5 days dealing only with the hydrodynamic calculation. The time step was set to 1 s. The second step then deals with both hydrodynamic and sediment transport, and is a follow-up of the previous simulation, but with a lower time step set to 0.1 s. The simulation is run for 24 hours. The time step was set to 0.1 s.

Because the WALE turbulence model relies on high mesh resolution in both hori-

zontal and vertical directions, it is difficult in case of large applications, to combine a very fine vertical mesh and cover such a large simulation domain. Therefore only the 2eddy LES turbulence model is used in this chater.

### 6.1.2 Model calibration

To calibrate the model, a simulation is carried out over one month from $22^{nd}$ April to $21^{st}$ May 2013, covering the date corresponding to figure 6.1. The surface elevation variations in three different locations are shown in figure 6.5. P1 is an open boundary point at the South-East corner of the model domain, P2 is the location of the Sheerness tide gauge site, and P3 is at the London Array site. The computed tidal range at P3 is about 8 metres which is close to the observed data [36].

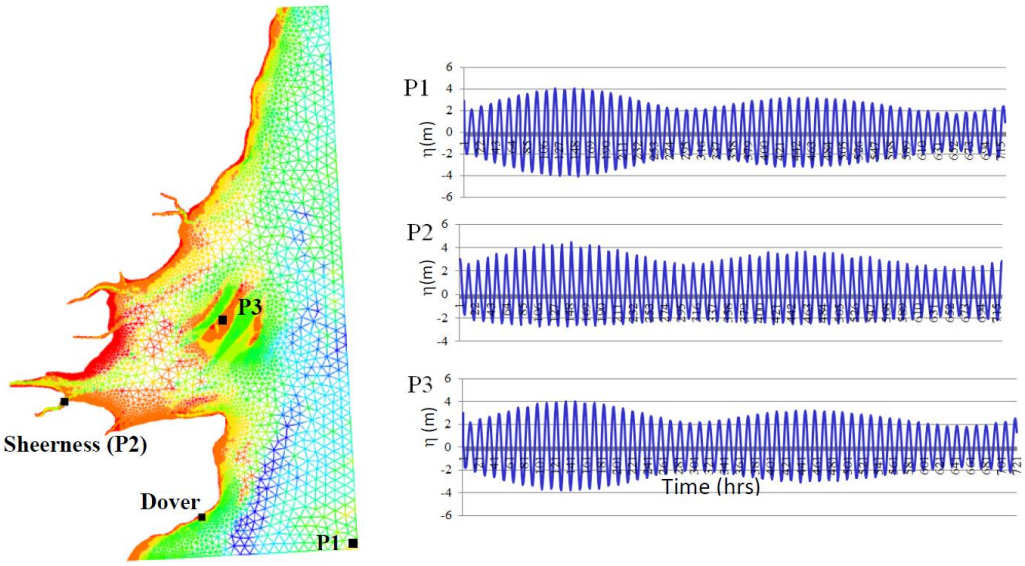


**Figure 6.5:** Surface level obtained by predicted data

Figure 6.6 shows a detailed comparison of the water surface elevation at Sheerness and Dover tide gauge stations over a 16 hrs period. The solid lines are model results and the symbols are measurements. It can be seen that the model results follow the measurements quite well. There is a slight under-prediction in the neap tide and over-prediction in the spring tide. It is considered that it is due to local variations in the bathymetry (not fully resolved in the model) that may influence the computation. In addition, other factors, such as wind and waves, are not included in the simulations,

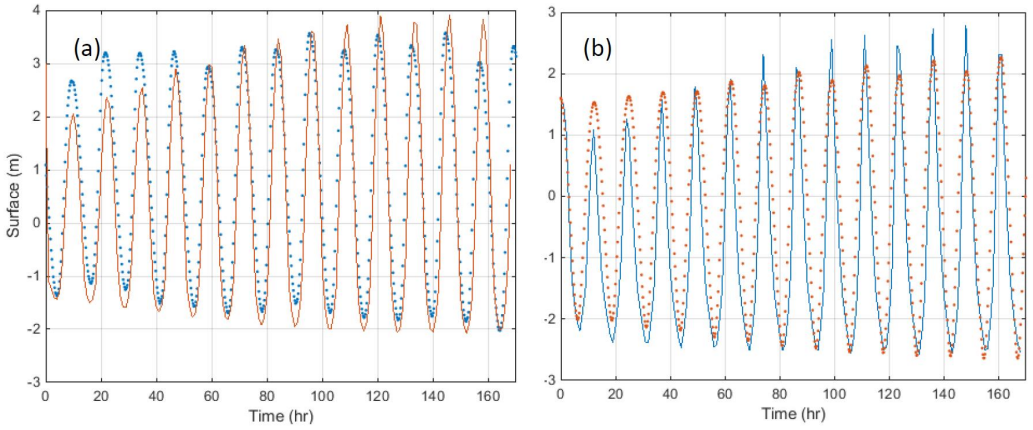


**Figure 6.6:** Comparison of computed and measured free surface elevations over 160 hrs at Dover (a) and Sheerness (b) tide gauges. The model results are denoted by solid lines and the symbols represent measurement.

which may also contribute to the differences. Moreover, another source of error is the boundary conditions that the riverine discharges are not taken into consideration in this case. The overall agreement, however, is considered good.

### 6.1.3 Hydrodynamic

The hydrodynamic and sediment transport results shown in this section cover a 24 hours period. The water surface level variation obtained from the numerical model is shown in figure 6.7.

In the figure it can be seen that two high peak tides and two low peak tides are captured during the 24 hours at the centre of the OWF. The amplitude of the tide during this period exceeds 8 meters.

The depth averaged velocity magnitude at 6 instances, including two flooding, two high peak tides, one ebb and one low peak tide (highlighted in figure 6.7) are illustrated in the figure 6.8 respectively. Streamlines are also used to illustrate the circulation patterns.

Figure 6.8 (a) and (e) show the mean velocity magnitude during the peak flood period. The streamlines indicate that the main tidal current flows from the east to the west during this period. Figure 6.8 (c) is the result for a peak ebb. Opposite flow direction to that of the flood is seen that the main flow goes from the west to the east.

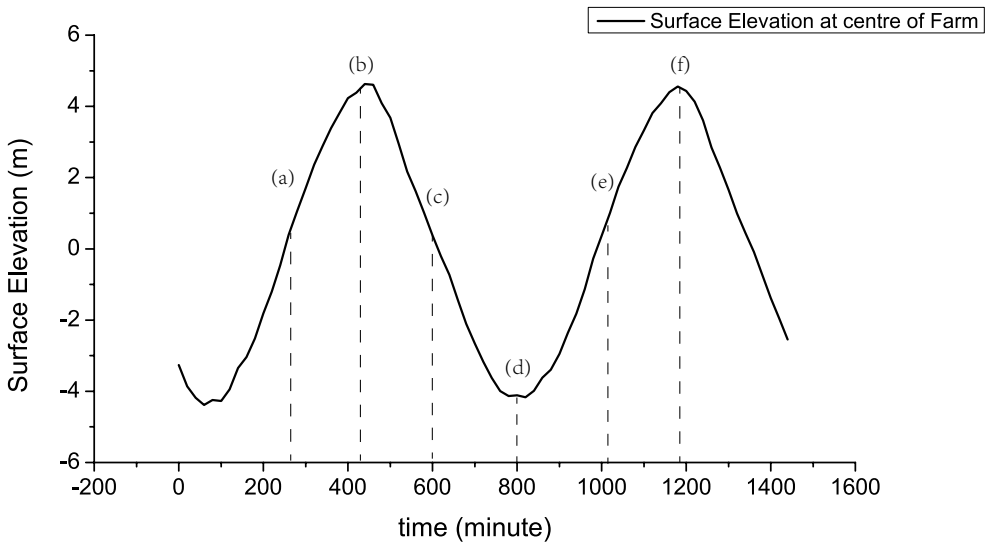


**Figure 6.7:** The surface elevation at the centre of the London Array offshore wind farm

Figure 6.8 (b) (d) and (f) represent the velocity distribution at two High Water (HW) and one Low Water (LW) respectively. During these instances large scale vortices are found in the farm area as the flow changes the direction. Comparing these 6 figures, it is clear that the flow velocities in the flood and ebb period are much higher than the ones during the peak tide period. It is noticed that high speed flow is found around the sandbanks area where the depth is shallow.

Figure 6.9 zooms in the numerical results shown in figure 6.8, focusing on the flow distribution around individual structures. A remarkable decrease in the velocity magnitude can be found in the wake behind each monopile at flood and ebb period. The averaged wake tail observed in figure 6.9 can be found with a length in excess of 1.5 km.

Figure 6.10 shows the computed flow vectors together with the corresponding streamlines around individual monopiles at these 6 instances. These figures have recorded the unsteady flow state around a single pile every 4 seconds, during a peak flood tide. The vortex shedding during the strong flow passing these structures can be seen clearly as indicated by the streamlines. The instantaneous velocities in 100 s behind this single pile is shown in figure 6.11. In this figure, the fluctuation of velocity is well represented with a general downtrend. The Re in the peak flood is about $10^7$ at the sandbank

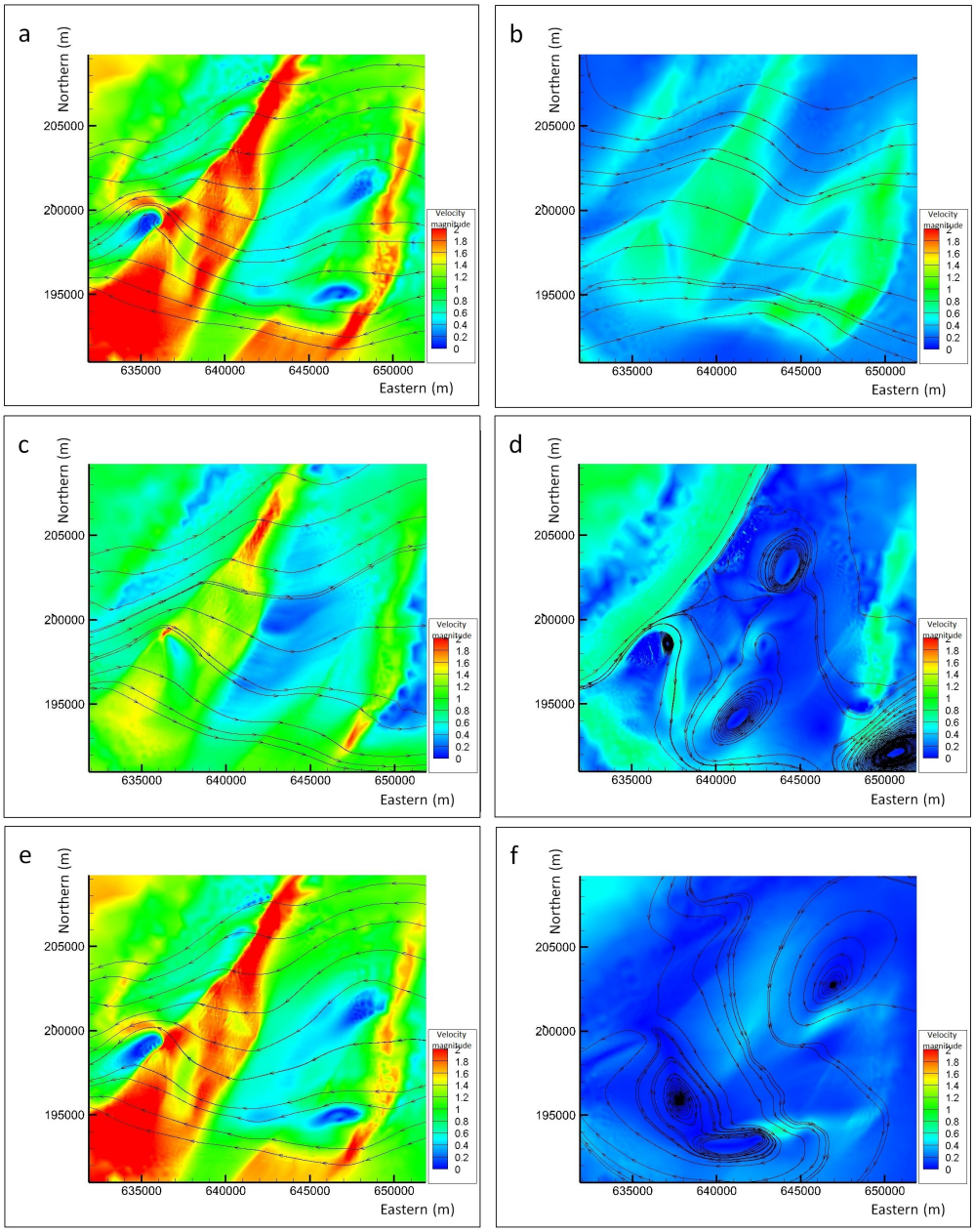


**Figure 6.8:** Depth averaged velocity magnitude (UV in $ms^{-1}$) at the London Array OWF site during 6 instances

and $1.5 \times 10^6$, in which case the flow region is in fully developed turbulence behind the monopole according to [124]. According to figure 6.11, the oscillatory frequency is about 20 s, however the St is still in the proper range [124] which is about 3.5. These results suggest that the model is well capable of capturing the fine details of the flow immediately around the monopiles at the large field scale, similar to that shown

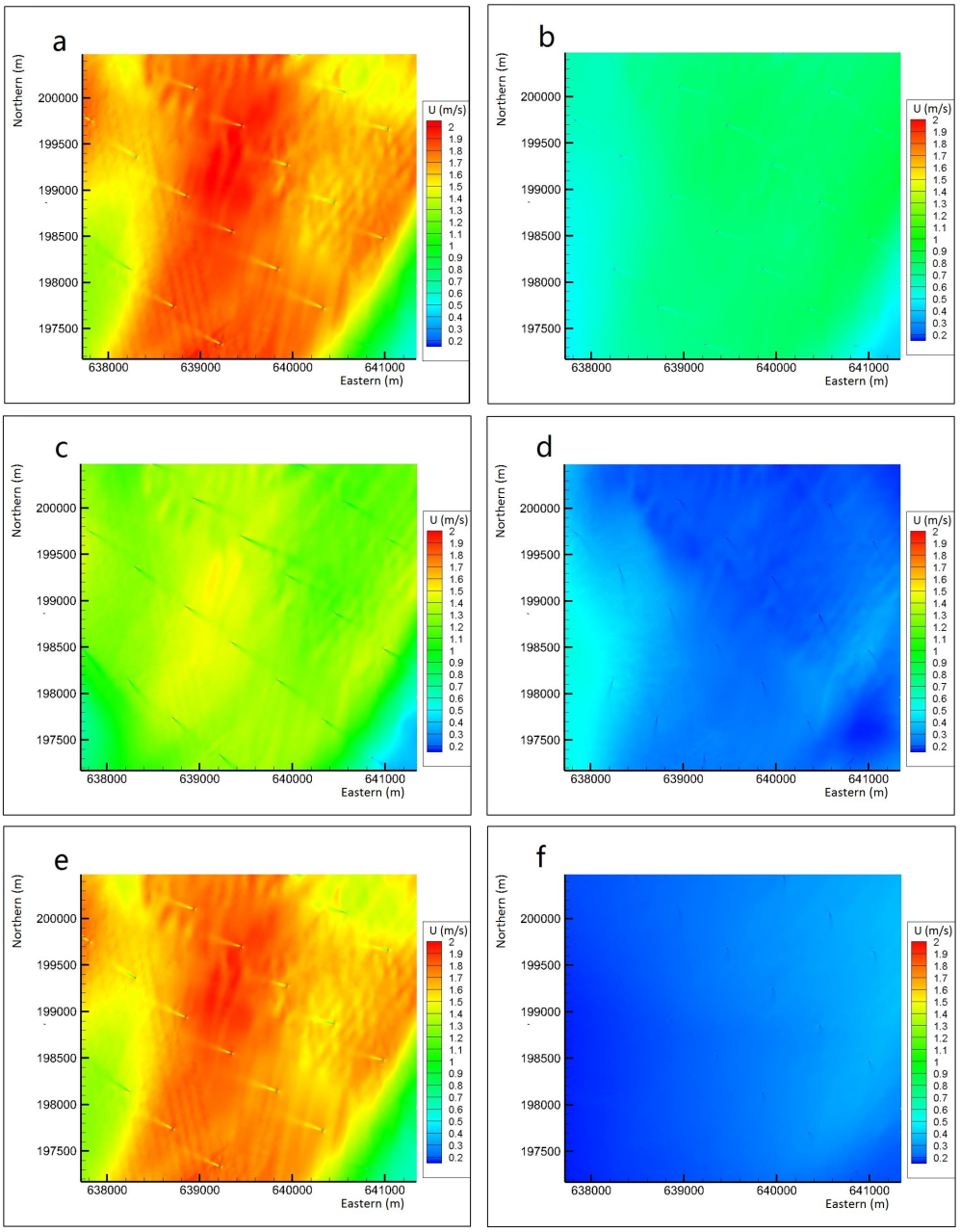


**Figure 6.9:** Depth averaged velocity magnitude ($ms^{-1}$) at the London Array OWF site during 6 instances

previously at the laboratory scale.

Figure 6.12 presents the computed surface flow speed magnitude around the OWF site during the peak ebb flow. The flow speed varies from 0.3 $ms^{-1}$ to 2.4 $ms^{-1}$ due to topographic variations. The wakes behind the structures are clearly visible as shown by the arrow A in the channel area and B on the sandbank where the depth is shallow. The

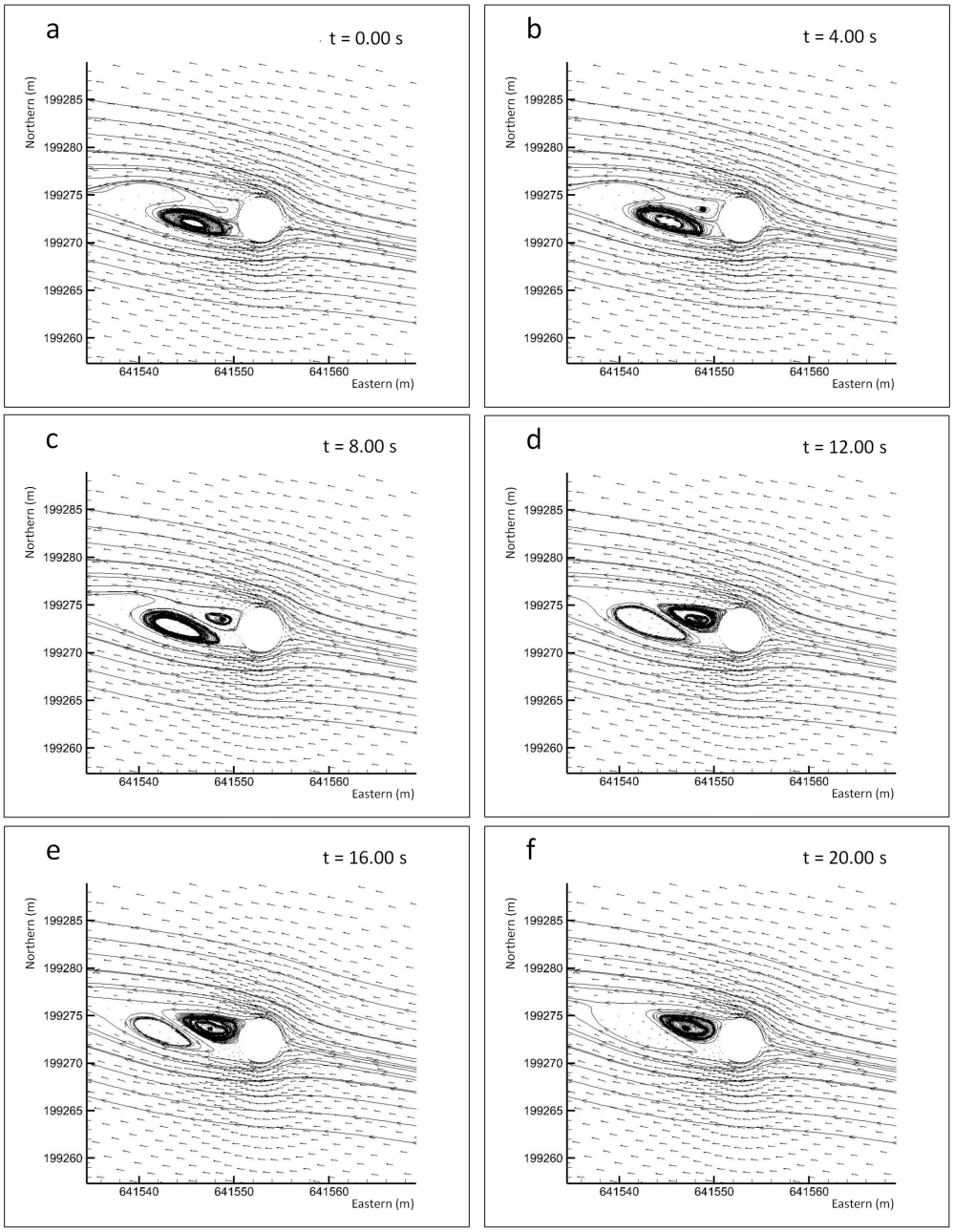


**Figure 6.10:** Flow structure around an individual pile shown by vectors and streamlines

flow velocity in the channel area varies from 0.3 $ms^{-1}$ to 0.8 $ms^{-1}$ approximately and 0.8 $ms^{-1}$ to about 1.6 $ms^{-1}$ in the sandbank area. The average length of these wake tails is again more than 1 km. It is noted that the flow at the sandbank is dominated by an eddy to the north-west. In the channel, however, the flow direction turns to the north-east. This phenomenon is due to the effect of shallow water which leads to the

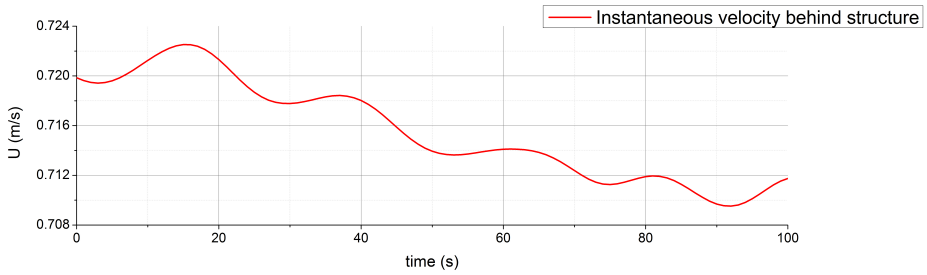


**Figure 6.11:** Instantaneous velocities over a 100 s period, behind one cylinder during peak flood tide

change in flow directions in shallow water stems from the direct dependence of flow speed on depth.

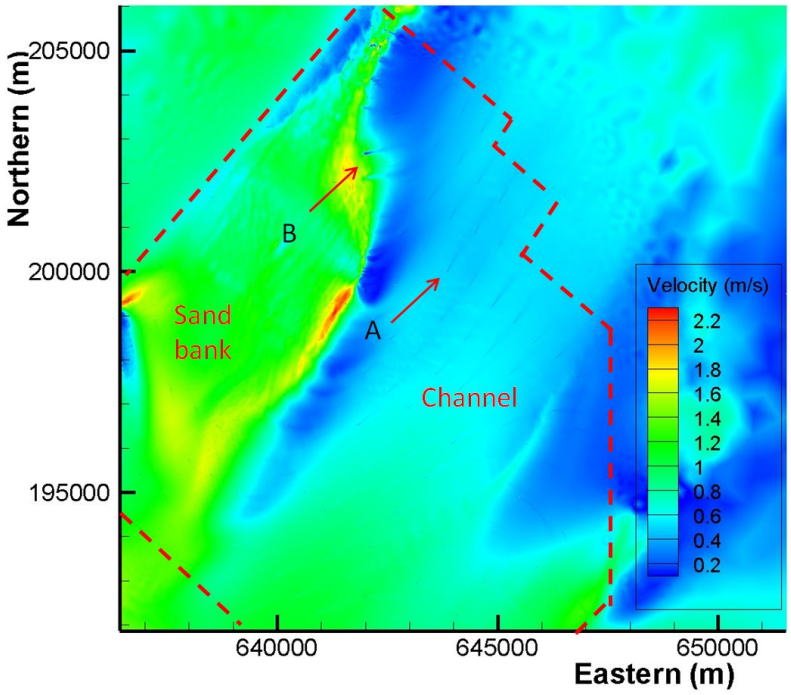


**Figure 6.12:** Surface velocity magnitude ($ms^{-1}$) at the London Array OWF site during peak flow

Figure 6.13 shows more detail of the computed flow speed magnitude around individual monopiles (close to points A and B respectively in figure 6.12). The long wake behind the structures can be found clearly in both sites. The speed magnitude reduction behind the monopile in the sandbank area in (b) seems larger than that in the channel area in (a). However the total length of the wake in (b) (about 600 m) is less

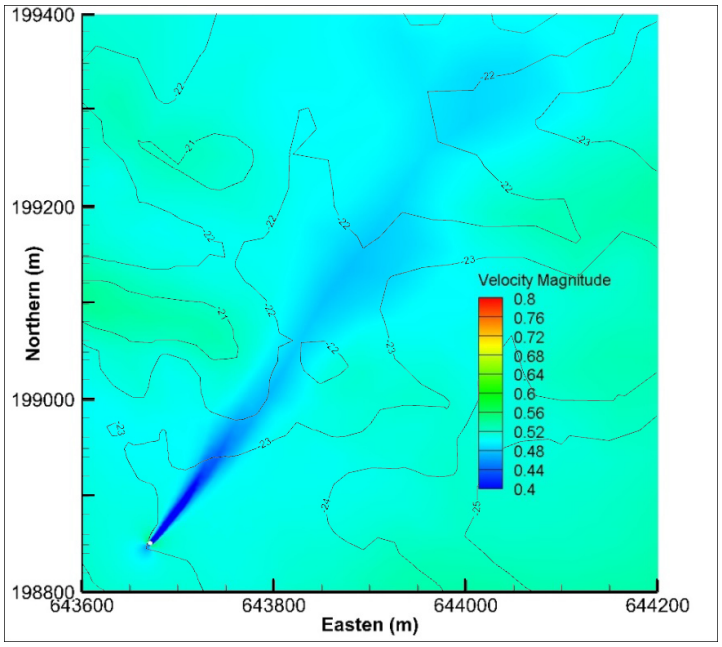


(a) Channel area

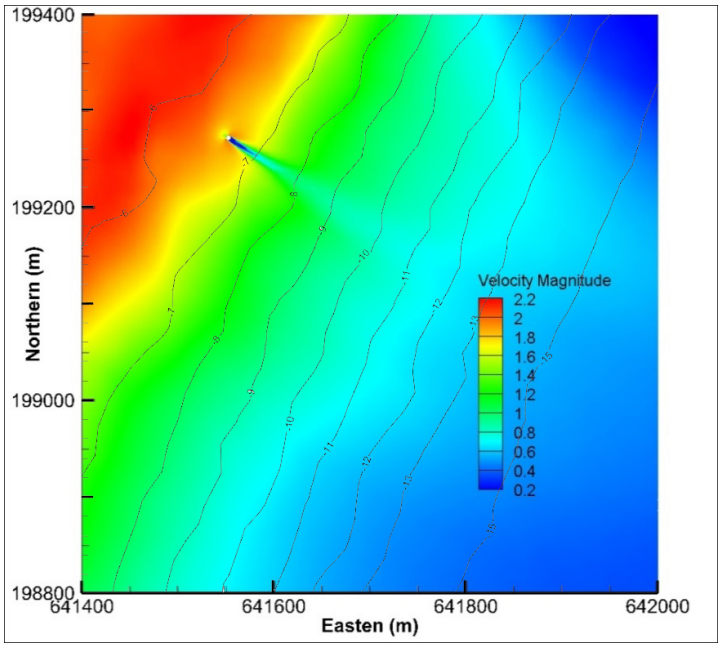


(b) Sandbank area

**Figure 6.13:** Peak ebb flow speed magnitude around one monopile in Channel (a) and at sandbank area (b)

that in (a) (about 1,600 m), suggests stronger shallow water effects.

To further illustrate these features, the magnitude of the depth-mean flow velocity

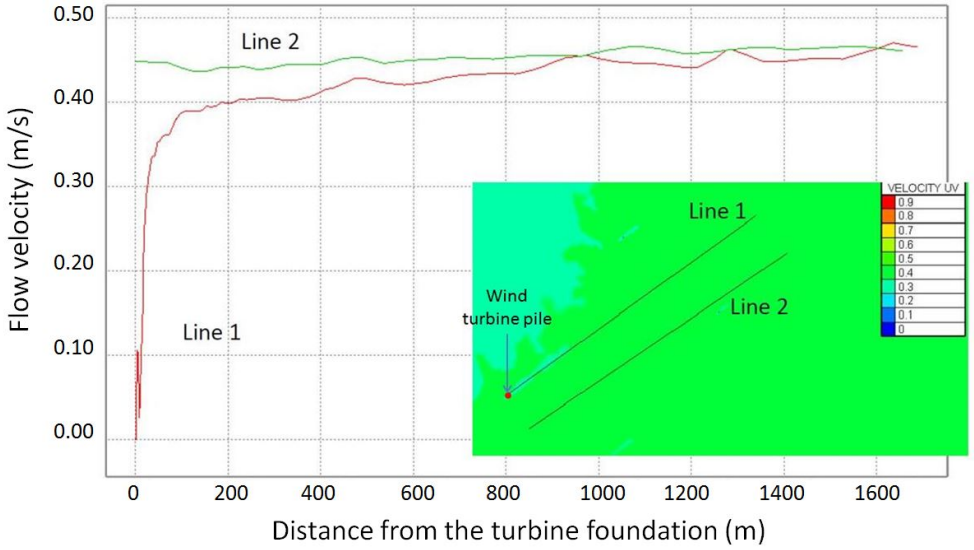


**Figure 6.14:** Depth average velocity magnitude along Line 1 in red (crossing the turbine foundation in the streamline direction) and Line 2 in green (a parallel line in the ambient flows)

behind a turbine foundation is compared with the ambient flow in figure 6.14. The red curve shows the velocity magnitude along Line 1 which is behind a circular pile. The ambient flow velocity magnitude along a parallel Line 2 is represented by the green curve. The water depths are similar for the two lines and the gap between them is 100 m. According to the figure, the reduced flow velocity immediately behind the structure (red curve) recovers fairly quickly in the first 200 metres, then increases gradually to the background value downstream. It is not until 1,600m downstream that the flow velocity recovers to its ambient values. Such a result clearly illustrates the potential long distances of the wake behind the OWF turbine foundation during peak flows at the site, which may contribute to the turbid plume as seen in [36].

The turbulence kinetic energy (TKE) around the London array during a peak flood and peak ebb period are presented in figure 6.15 and figure 6.16 respectively. Both figures show that high TKE is always gathered in the area where the flow past the sand banks. However around part of an individual turbine monopile, the changes in TKE can be clearly observed. It can be seen that the presence of the monopile creates a high TKE region close the sides of the structure, together with a lower value of TKE region behind covering a long distance downstream.

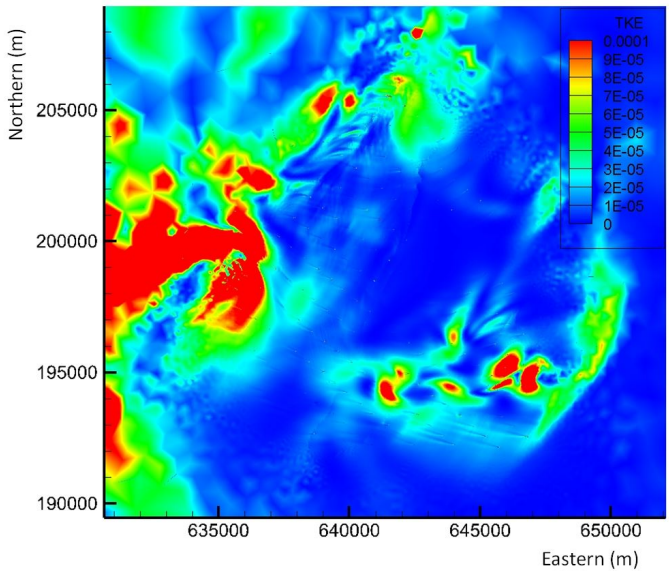


(a) the view of whole London Array OWF

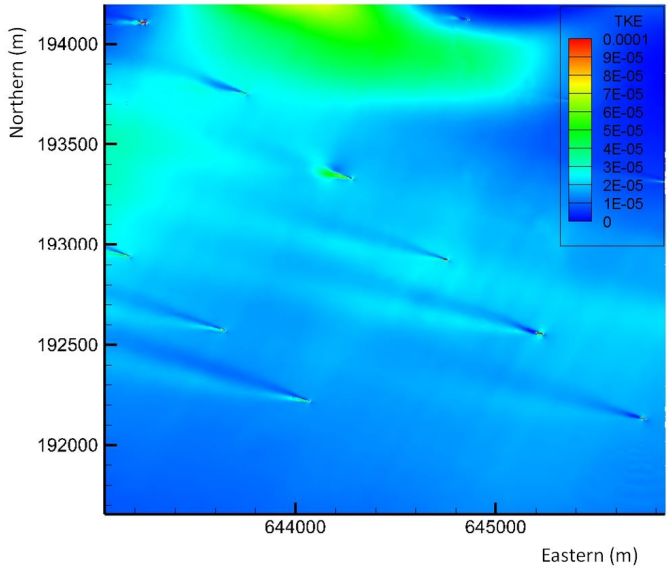


(b) the view of partial London Array OWF

**Figure 6.15:** TKE around the London Array during a peak flood period

### 6.1.4 Sediment transport

According to BGS (British Geological Survey) sediment maps, the bed material in the London Array OWF area is dominated by non-cohesive sediments. Computational tests are then carried out based on 0.1 mm and 0.3 mm diameter sand, which are commonly

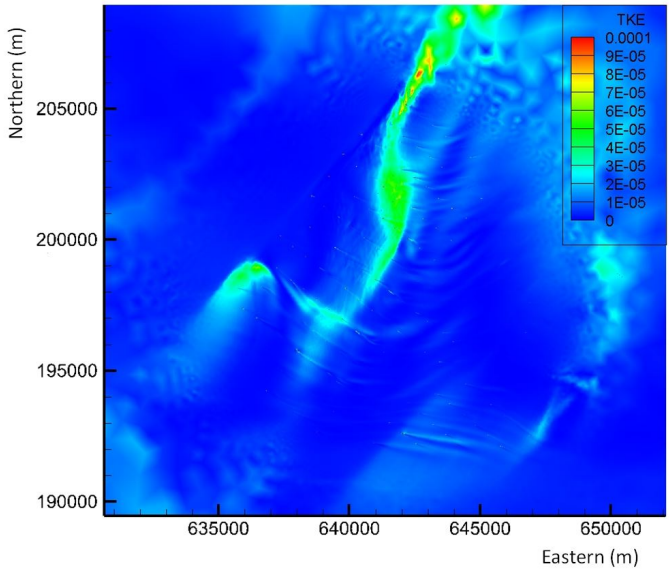


(a) the view of whole London Array OWF

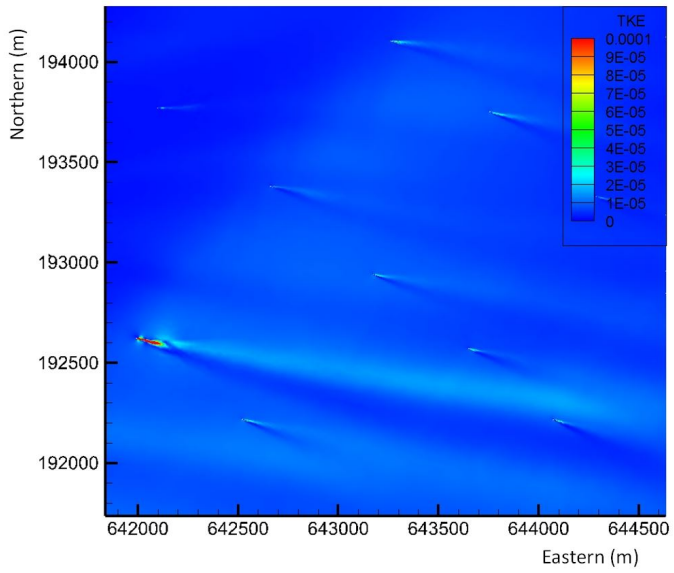


(b) the view of partial London Array OWF

**Figure 6.16:** TKE around the London Array during a peak ebb period

found in this area. The settling velocity and near bed critical shear parameters are computed based on Soulsby approach [129]. The near bed reference concentration is computed using Zyserman and Fredsoe method [130]. The initial thickness of sediment layers at the OWF is considered to be uniform and is set to 0.8 m in the numerical

model to provide sufficient sediment for suspension in the site. Note that 100 microns is the smallest sediment grain size permitted in the model (avoiding cohesive behaviour) but it is likely that the visible streaks are due to even finer fractions.

Figure 6.17 presents the computed suspended sediment concentration in the surface layer for 0.1 mm sand diameter (a) and 0.3 mm sand diameter (b) respectively at peak flood tide. Although both results show similar concentrations in the channel area, in the sandbank area, however, higher concentrations can be found in the finer sand case than in the coarser one. It is obvious that the finer sand is more easily re-suspended in shallow water and consequently leads to higher concentrations at the surface. The wakes of high sand concentration behind individual structures are clearly visible in both figures. In the finer sand case, the wake length seems longer and exceeds more than 1.5 km in distance.

To illustrate the vertical distribution of concentration, figure 6.18 zooms in the figure 6.17 (a) and shows the computed results around a group of monopiles at the surface layer in (a) and bottom layer in (b) respectively. Overall, the sediment concentration at the bottom shows higher values than that at the surface as expected in normal sediment transport situation. Although wakes of the variation of sand concentration can be found at both surface and bottom, their distribution profiles are the opposite. Figure 6.17 a shows that the wake behind each structure at the surface is composed by higher sand concentration than the surroundings. However, at the bottom, lower sand concentrations than the ambient values can be found in the wake region behind the monopile as shown in figure 6.18(b). The explanation of this phenomenon is that sand at the surface comes from the sea bed, picked up by the strong vertical vortex behind an individual cylinder, which is visualised across a vertical x-z plane as in figure 6.19.

Figure 6.19 presents the suspended sediment concentration along a vertical x-z cross-section through the centreline of the monopile during peak flood tide. The arrow-lines represent the flow path from left hand side to right hand side. A strong vertical eddy can be seen behind the turbine cylinder. According to the figure, high sediment concentration is located on the bed surface in front of the monopile. When the flow encounters the structure, with the increased bed shear stress at the sides of the structure, the strong eddy around the structure picks up sediment from the bed layer and

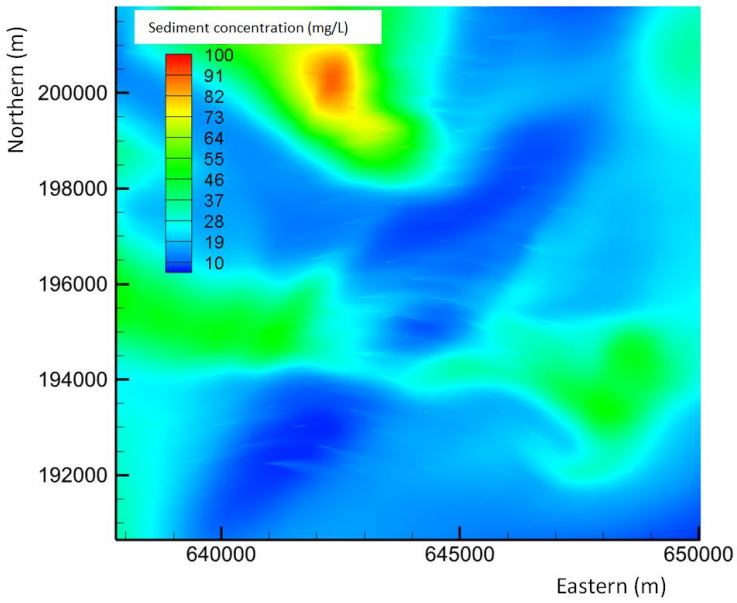


(a) $d50 = 0.1mm$

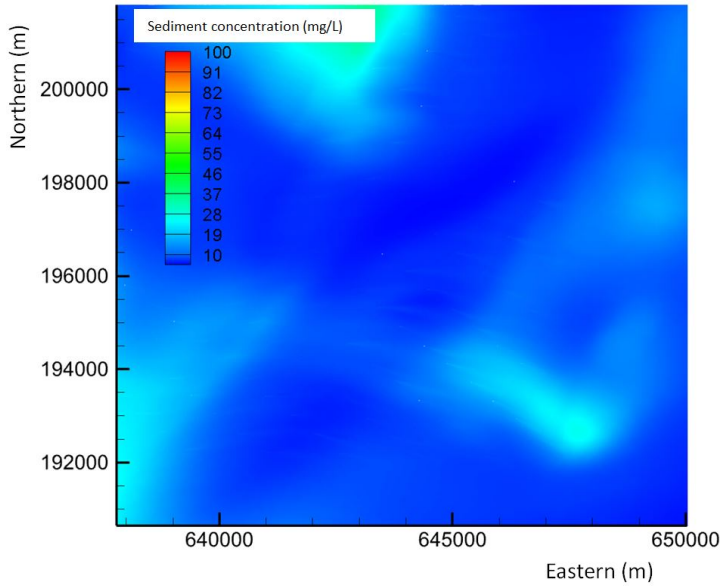


(b) $d50 = 0.3mm$

**Figure 6.17:** Suspended sediment concentrations at the surface layer at the London Array OWF site with different $d_{50}$ (a) 0.1 mm (b) 0.3 mm

transports it further downstream. Such a process reduces the sediment concentration at the sea bed behind the structure, but substantially increases the concentration in the

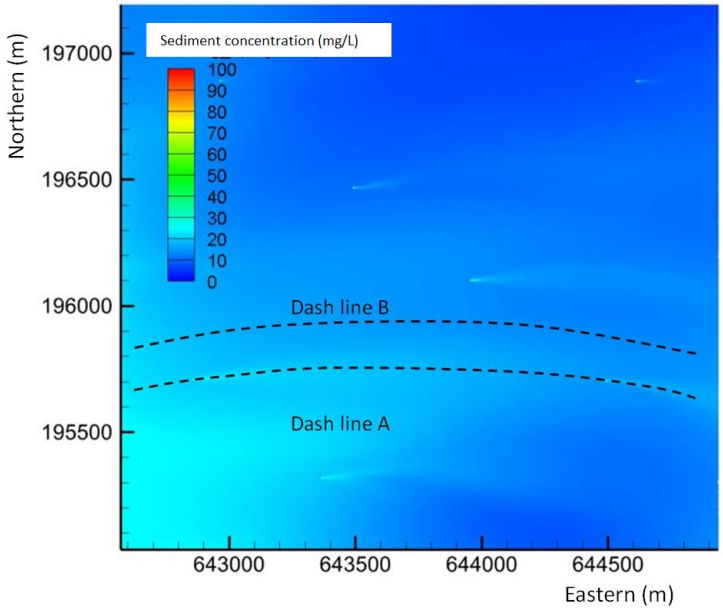


(a) surface layer

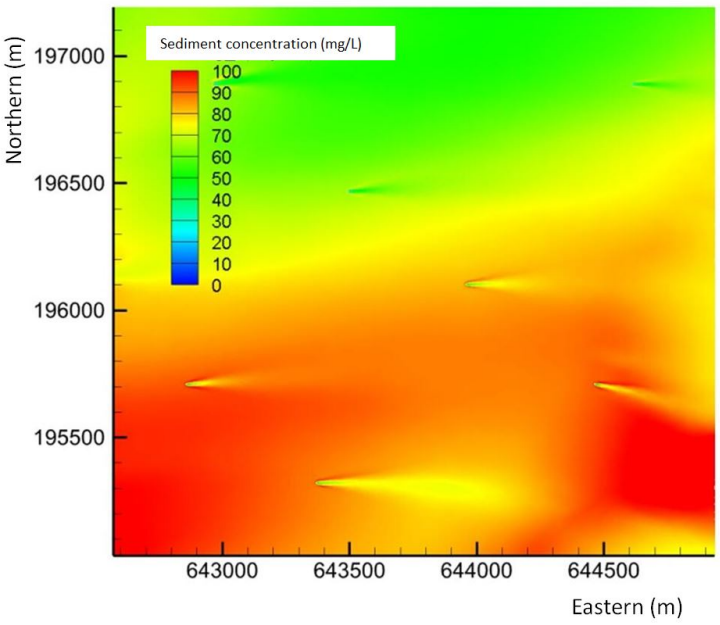


(b) bottom layer

**Figure 6.18:** Suspended sand concentrations around individual structures at surface (a) and bottom layer (b) with $d_{50}$ 0.1mm

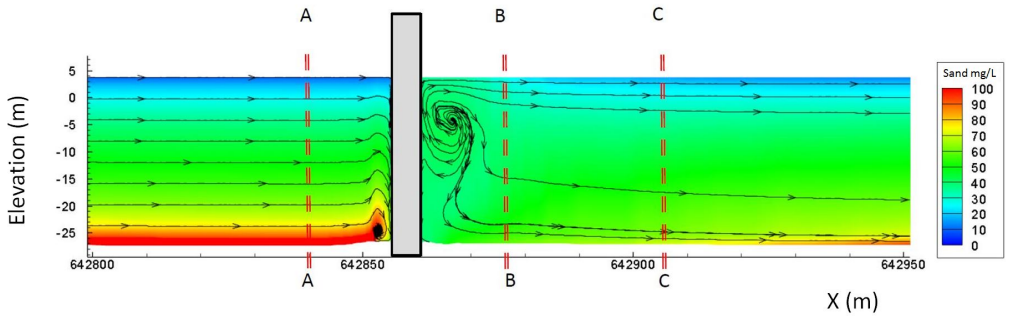


**Figure 6.19:** Vertical cross section sand concentration profiles, at one London Array monopile turbine

water column and creates the high concentration area at the sea surface immediately behind the pile. The current carries the high concentration further downstream for a long distance as shown in previous figures.

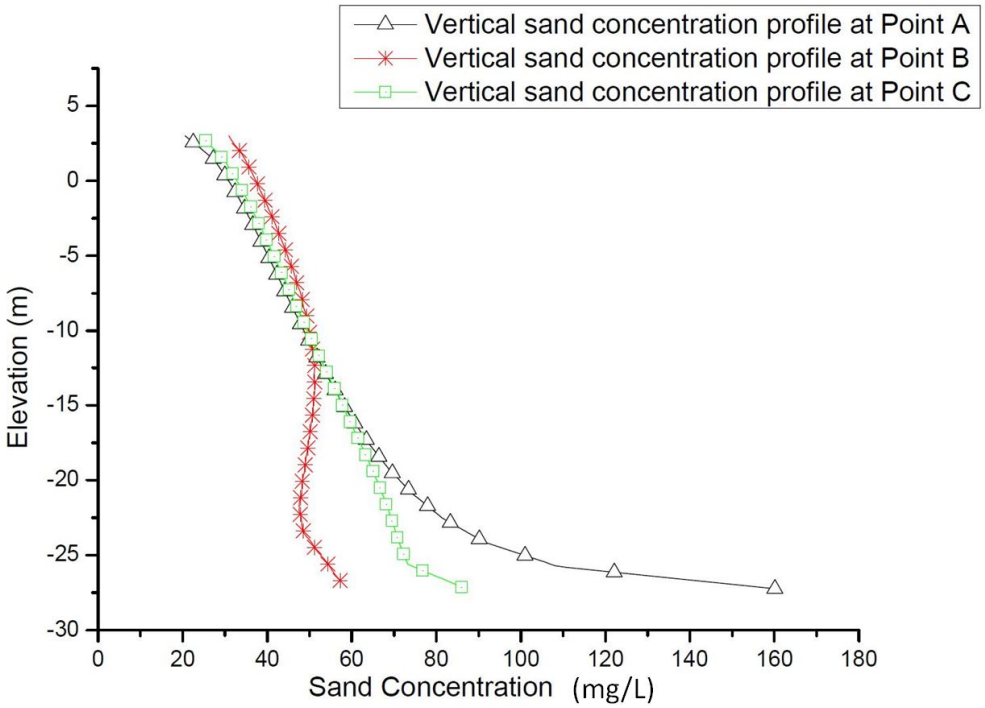


**Figure 6.20:** Vertical cross section sand concentration profiles, at one London Array monopile turbine

The vertical distributions of sediment concentration at points A, B and C in figure 6.20 are represented by black triangles, red crosses and green squares respectively. An

exponential vertical distribution can be found at point A, at 15 m in front of the monopile. The sediment concentration at this point reduces from 160 $gl^{-1}$ to 22 $gl^{-1}$ with increasing elevation. The differences in concentration distribution at point B (15 m downstream) and point C (45 m downstream) are significant. At point B, the sediment concentration is less than 55 $gl^{-1}$ near the bed, which is about 3 times less than it is at point A. the concentration at a higher level above the bed is actually larger than that near the bed at this point. This is caused by the strong vortex effects, with large amounts of sediment being entrained into the water column from the bed. At point C, the concentration gradually recovers back to the normal distribution although the near bed concentration is still smaller than that at point A.

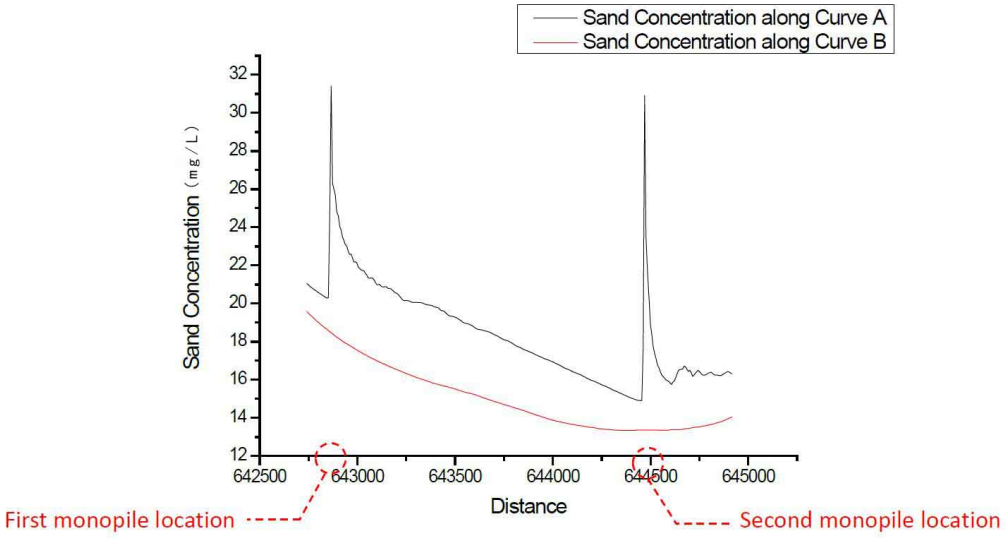


**Figure 6.21:** Surface suspended sediment concentrations along dash line A and dash line B of figure 6.18

The sediment concentration at the surface behind the turbine structures is compared with that in the ambient area in figure 6.21. The black curve and red curve represent the sediment concentration along the dashed line (A) and dashed line (B) in figure 6.18 separately. Line (A) intersects two monopiles and covers a whole wake between two structures. Although line (B) is only 200 m away from line (A), it covers the area which has not been affected by the monopile wakes. According to the figure, the sediment concentration along line (A) is higher than it is along line (B), in general. About 2 $gl^{-1}$ difference in sediment concentration can be found in front of the two monopiles.

However, due to the vortex effects, the sediment concentration increases dramatically behind the structures. The difference in sediment concentration at the first monopile increases by a factor of two, and at the second one by a factor of three, relative to the undisturbed value, approximately.

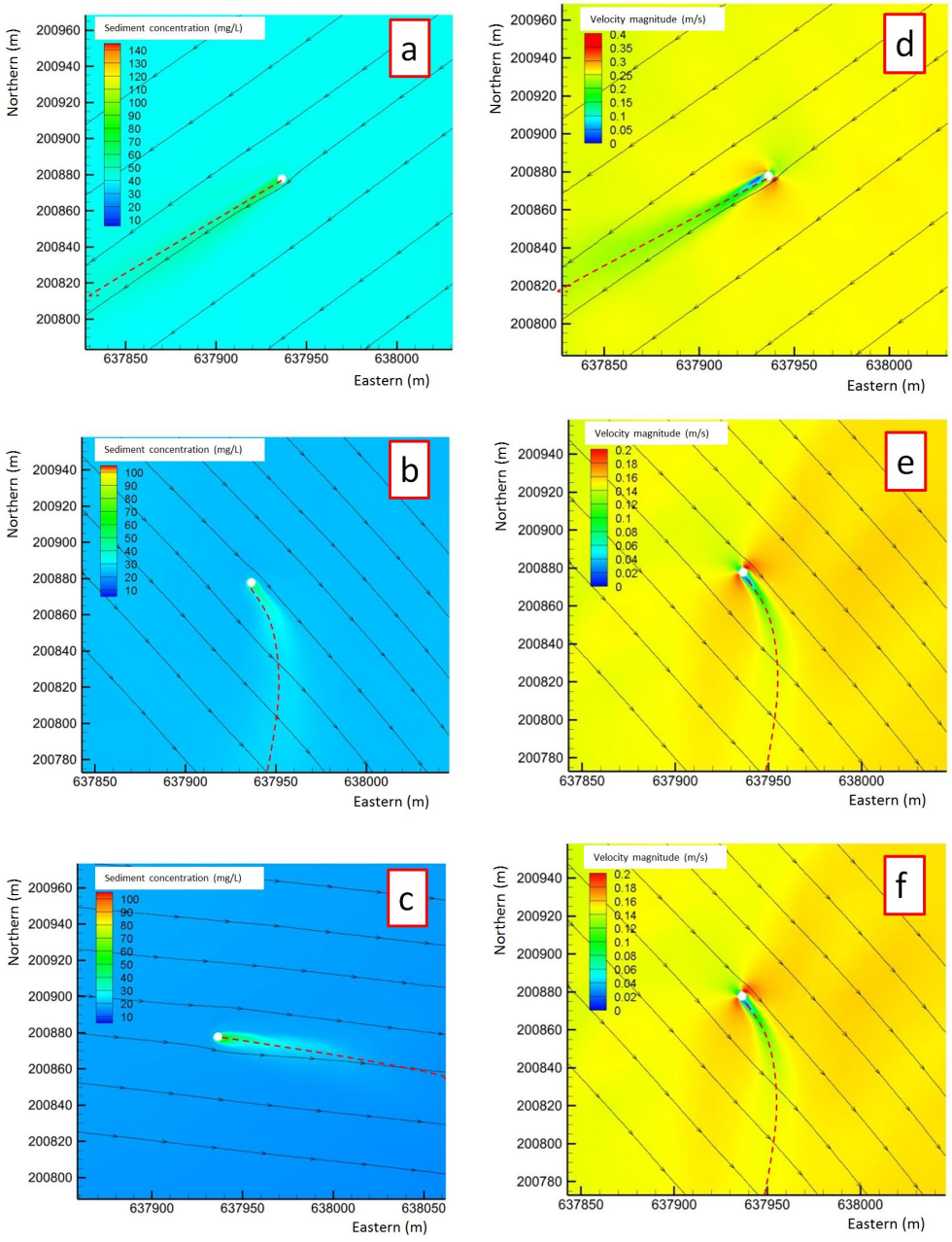


**Figure 6.22:** Surface sediment concentration profile (a), (b), (c) and velocity magnitude (d), (e), (f) around one pile

Figure 6.22(a), (b), (c) illustrate the distribution of surface sediment concentrations around a turbine structure at three different instances, with their corresponding current speeds in (d) (e) (f) separately. The arrow lines in figure 6.22 represent instantaneous flow directions which change from north-east to south-west (figure 6.22 (a), (d)) to west to east (figure 6.22 (c), (f)). The time difference between each figure is approximately 20 minutes. In the sediment concentration figures, the wake of high sediment concentration behind individual structures is clearly visible. Similar wake patterns, with a decrease in velocity, are also found in current speed profiles, which show noticeable flow acceleration at the side of the pile. In each instance, sediment concentration and current speed have the same wake directions (indicated by red dash curves). In a case in which tidal current is more or less uniform (figure 6.22 (a), (b), (c), (d)), the wake directions of the sediment transport and velocity magnitude follow the main flow directions, however a big deviation is found when there are strong variations in the current direction e.g. in the case of (b) and (e). Although in this time period, the main flow direction is from north-west to south-east, the wake of sediment transport and current speed behind the turbine monopile bends away from the flow direction towards the south. This phenomenon indicates that the sediment transport is affected largely by the wake of the turbulent eddy behind the structure. After suspended sediment particles are picked up into the fluid flow, the flow turbulence is damped due to the increase in concentration. Consequently, the diffusion process of the flow with high sediment concentration is weaker than in the ambient flow. Therefore a delay effect (hysteresis) is found in the wake of the sediment concentration and current speed when the current direction is changing.

The computed sediment concentration variation at surface in a 24-h period is shown in figure 6.23 at the centre of the London Array OWF based on a 5-day hydrodynamic model run. In total, five peaks in sediment concentration and current speed are found during the simulated 24 hours which covers two entire neap tides. As expected, the concentration curve correlates with the variation in the flow speed curve very well. But certain inter-cycle variations can be found, i.e. at 26/04/2013 which may well be related to the eddy shedding during that period which affects the advection of sediment particles.

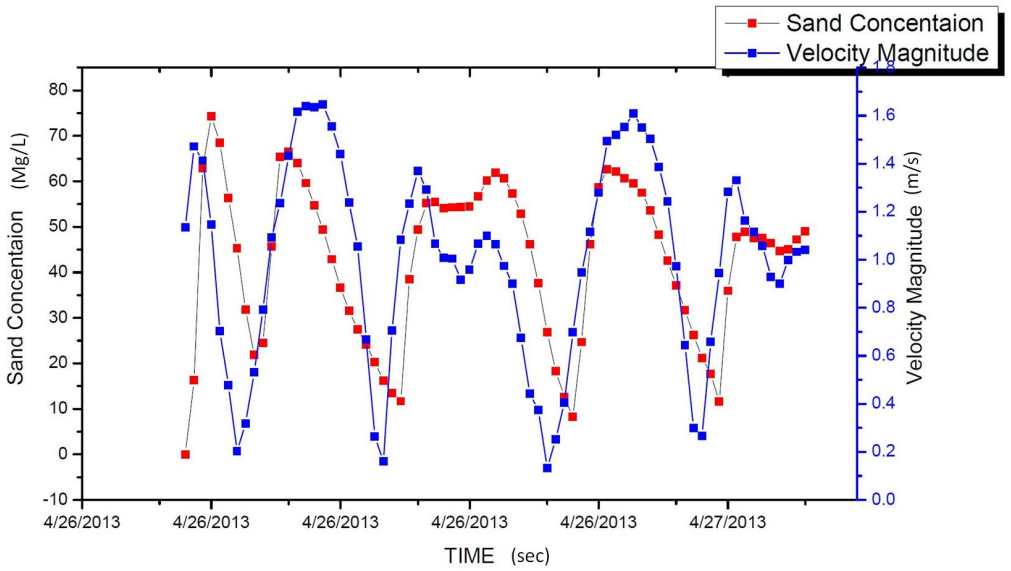


**Figure 6.23:** Surface sediment concentration and velocity magnitude over 24 hours in the centre of the London Array OWF

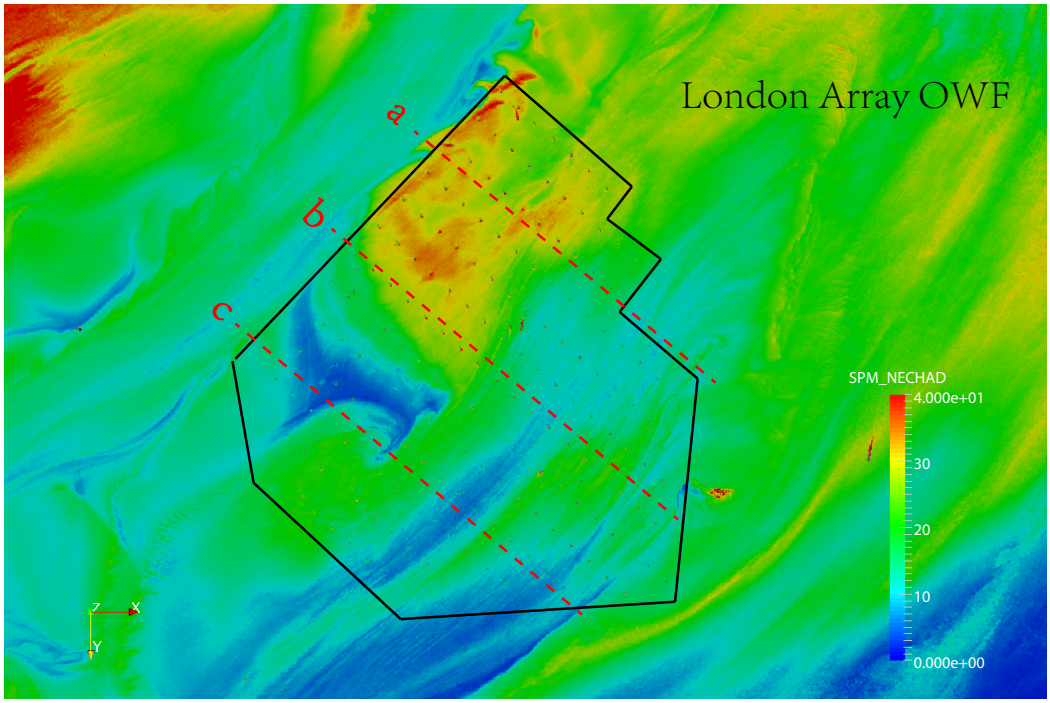


**Figure 6.24:** Landsat 8 satellite image of suspension concentration in the London Array OWF

Figure 6.24 shows the converted surface suspension concentration based on the Landsat 8 remote sensing images at the London Array. The comparison between satellite data and numerical results along 3 transects is presented in figure 6.25. Overall,

the computed results follow the satellite data reasonably well, although there are some differences in the magnitude of the concentration values. As line (a) crossing the sand bank and channel, the suspension concentration in figure 6.25(a) shows higher values than it at the channel. Similar results are also represented in figure 6.25(c). However there is a noticeable shift in the concentration peak at about 3,000 m in (c) which may due to the uncertainty of the bed bathymetry. The variation of the gain size in this area can also contributes to the divergence of the numerical model.

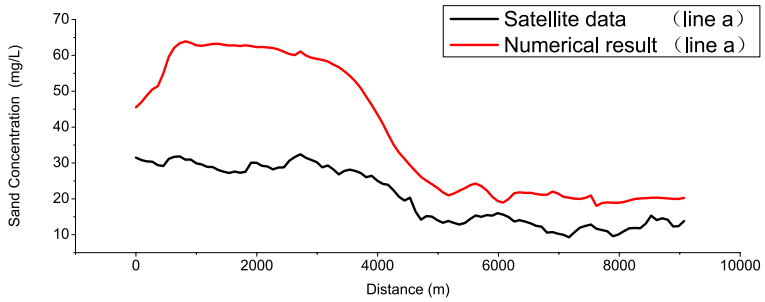


a: Comparison along line (a)

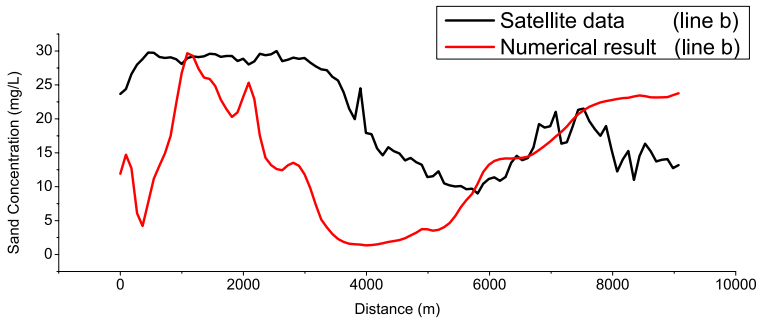


b: Comparison along line (b)

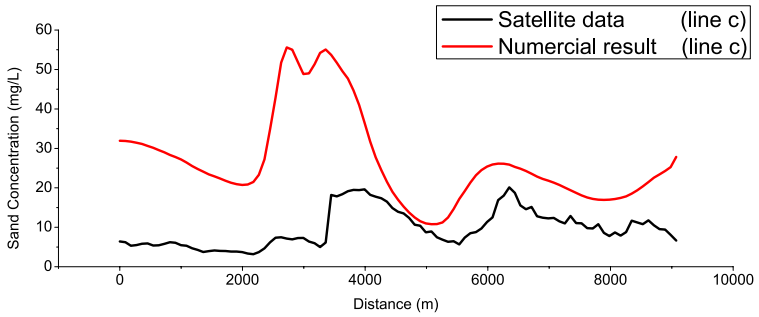


c: Comparison along line (c)

**Figure 6.25:** The comparison of the surface suspension concentration along line in figure 6.24

### 6.1.5 Implementation of the Immersed Boundary method

The immersed boundary method is also tested to investigate the impact of the London Array OWF.

Different from the previous cases, a total of 175 piles of the farm are accounted for by using immersed boundary forces. The mesh generated for the IB method test case is shown in figure 6.26 in which the whole domain is meshed, including the piles, but the footprint of each pile is represented, in order to be able to apply body forces without requiring any interpolation. All those boundary nodes are specially treated with the immersed boundary forces being applied on each of them.

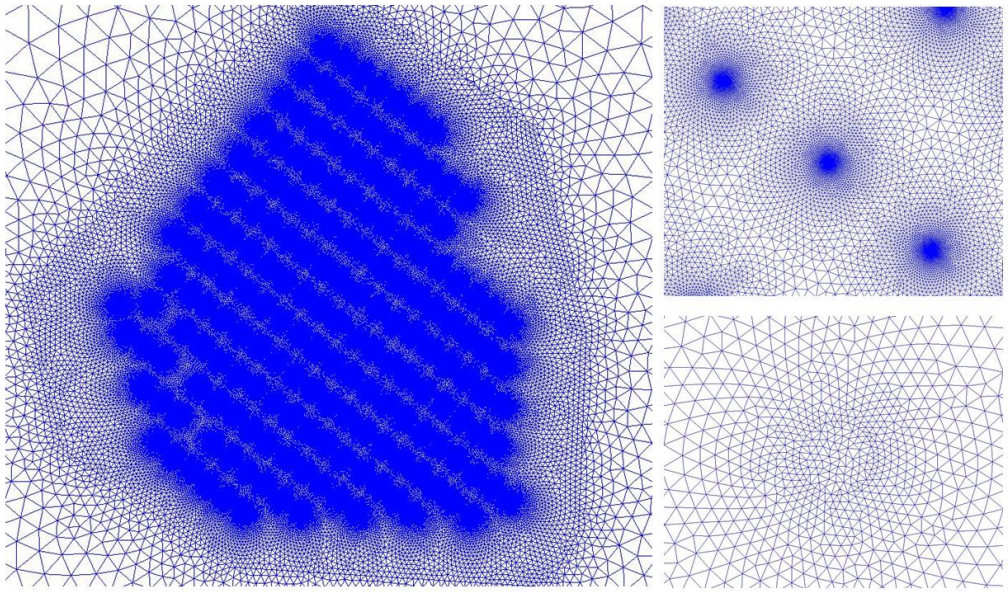

**Figure 6.26:** The mesh of London Array used for the immersed boundary method test

Figures 6.27 and 6.28 illustrate the depth averaged velocity magnitude at the London Array OWF in a peak flood and peak ebb period respectively. As shown in these figures, the wakes behind each individual structure are clearly visible as that in the previous cases, showing a length of more than 1 km.

The instantaneous velocity magnitudes along the centre line of three piles in the main flow direction are shown in figure 6.29 to compare them with that from the previous 'hollow mesh' cases. The black curve and red curve in the figure represent the numerical result obtained from 'hollow mesh' test and IB test respectively. Overall, the

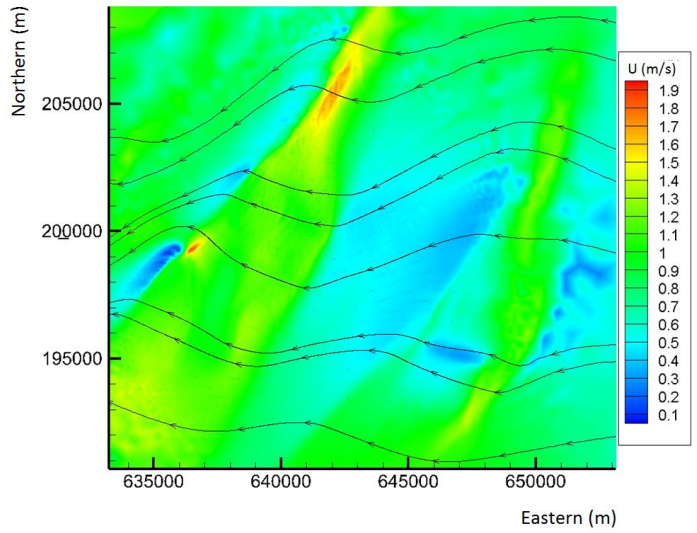


(a) surface layer

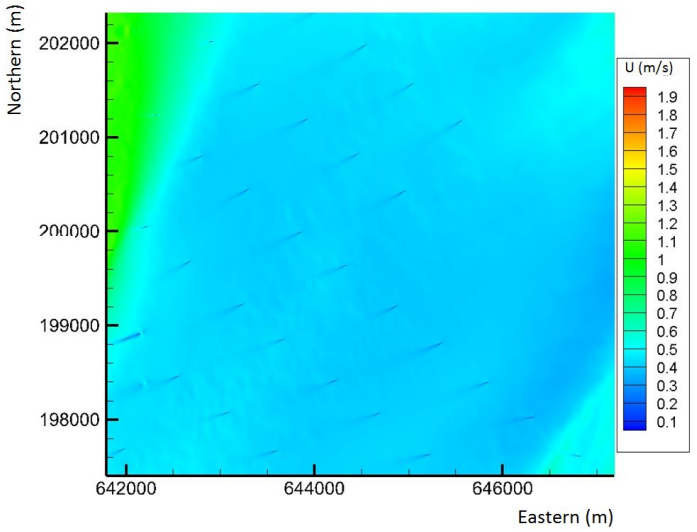


(b) bottom layer

**Figure 6.27:** Depth averaged velocity magnitude in the London Array OWF during a peak flood period. Immersed Boundary method test

results from these two methods are fairly similar, however the IB test result indicates a slightly faster recovery speed than the 'hollow mesh' case. In the far field, both models' results are close to each other.

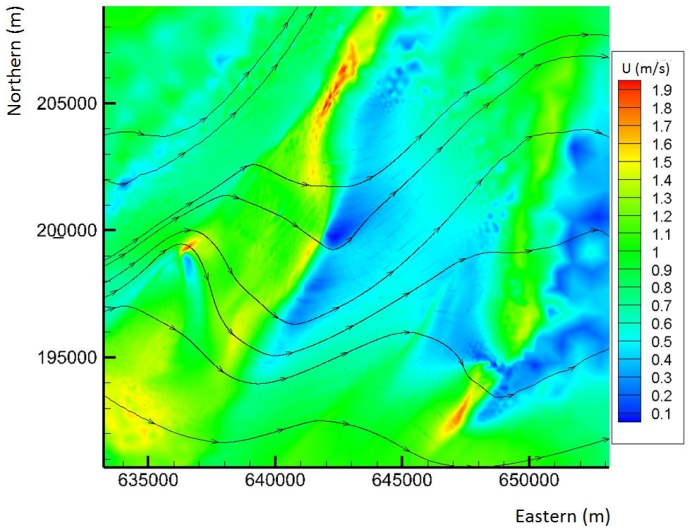


(a) surface layer

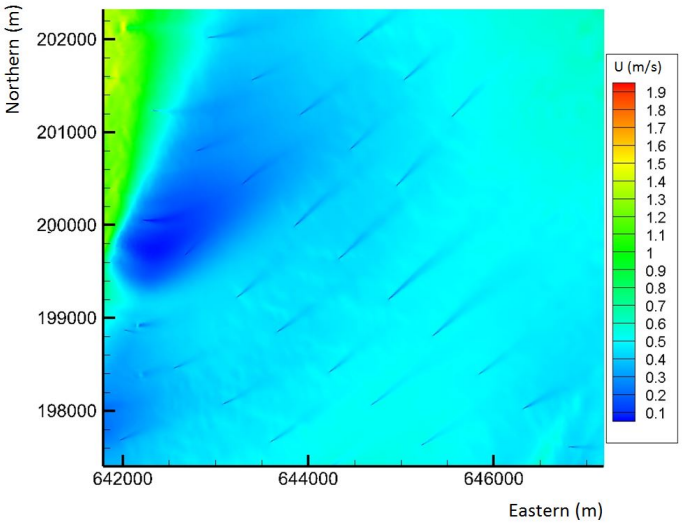


(b) bottom layer

**Figure 6.28:** Depth averaged velocity magnitude in the London Array OWF during a peak peak ebb period. Immersed Boundary method test

## 6.2 Tidal turbine farm in an ideal channel

The aim of this test case is to investigate the capability of immersed boundary method in dealing with submerged structure in prototype scale. An ideal channel was designed containing nine submerged circular cylinders. These structures can be considered as

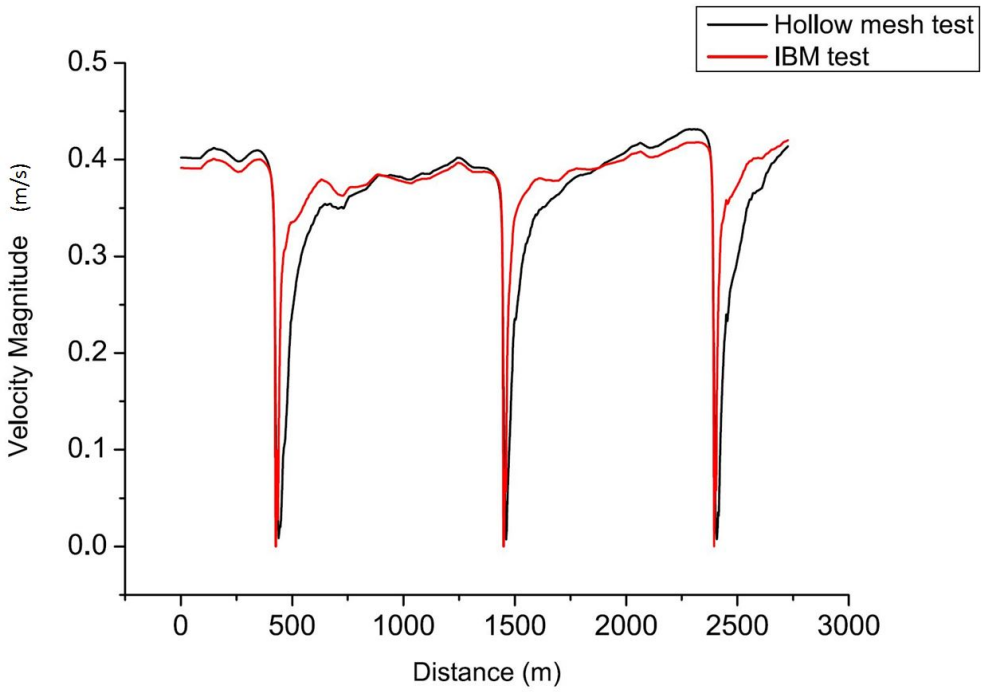


**Figure 6.29:** The instantaneous velocity magnitudes along centre line of three piles following main flow direction

the foundations of tidal turbine. Without considering the blades rotation effect, the flow impact around a tidal turbine structure can be simulated.

### 6.2.1 Test condition

The dimension of the ideal channel is set to 3,200m long and 1,400m wide. A constant water depth of 20 m is maintained during the calculation. Figure 6.30 shows the configuration of the simulation domain.

The tidal turbine structure in this simulation is considered as a finite height cylinder with a 5 m diameter and 4 m height. In total there are 9 turbine structures distributed in three rows placed. The first row is located at 500 m behind the inlet boundary and the next two rows are separated 700 m downstream. These conditions are designed to follow the a layout as in the OWF configuration.

The mesh of the test channel is illustrated in figure 6.31. In horizontal 2D plane, the mesh contains 80,711 elements. In the vertical direction, the numerical model uses 50 sigma transform layers including 16 fixed height layers for the representation of the

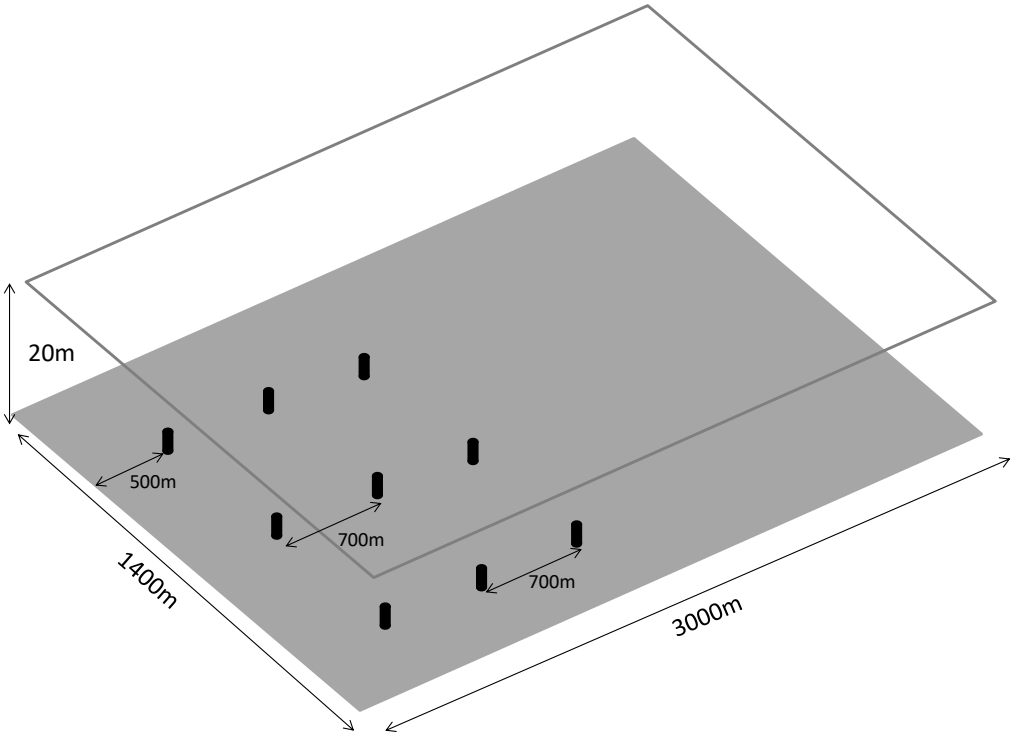


**Figure 6.30:** The simulation domain of the ideal channel

turbines.

Table 6.1 summarises the key parameters used in this case. The rigid rough bed with the coefficient of Nikuradse equivalent sand roughness 0.1 cm is assigned for the bottom bed condition. At the inlet boundary, a constant flow rate 14,000 $m^3$ is given. The outlet boundary maintains a constant water depth of 20 m during the calculation. The 2eddy LES turbulence model is used for the representation of the turbulence characteristics.

### 6.2.2 Results

The simulation is carried out for a period of 24 hours and the last hour result is selected for data analysis in this section.

Figure 6.32 represents the time-averaged horizontal velocity magnitude around the individual structures at the layer of Z = -18m and Z = 19m respectively. These layers are under the top of the turbines, which corresponds to 0.5 and 0.25 of the turbine

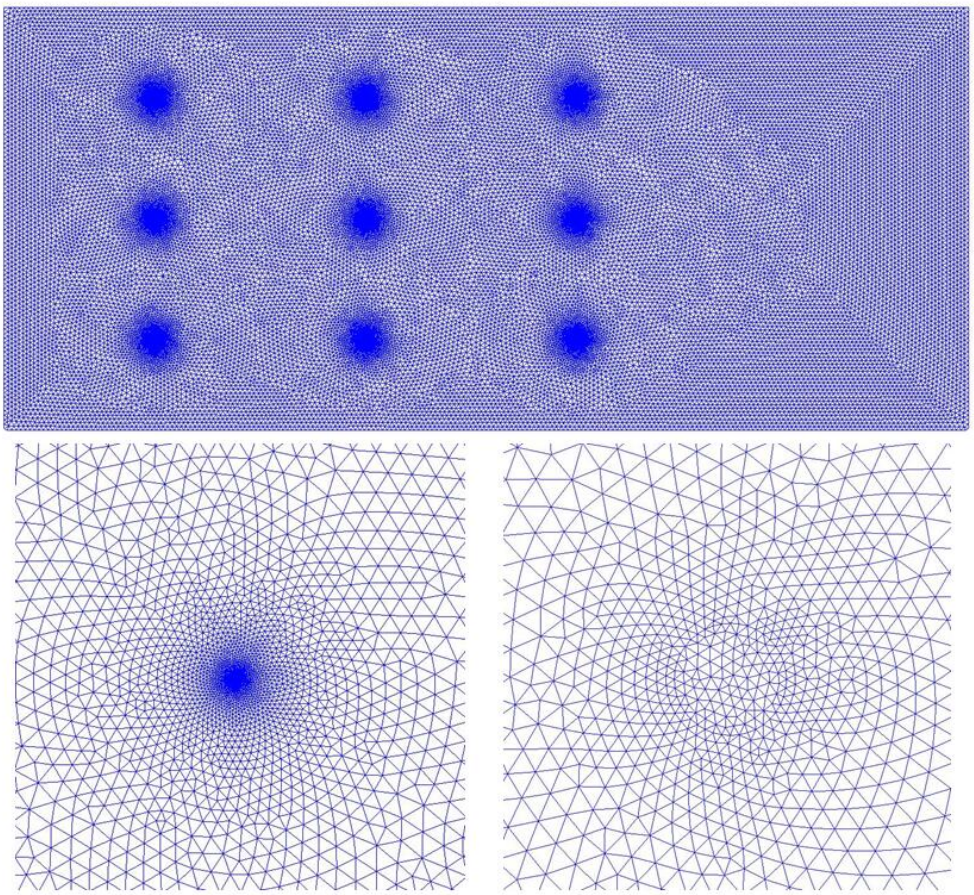

**Figure 6.31:** The mesh of the ideal channel

| Test | Tidal turbine farm in an ideal channel |
|---|---|
| Bed condition | Rigid rough bed |
| Water depth $h$ (cm) | 20 |
| Mean Flow velocity $U(ms^{-1})$ | 0.5 |
| Pile diameter $D(m)$ | 5 |
| Re Number | $2.5 \times 10^6$ |
| Bed Nikuradse equivalent sand roughness $ks(cm)$ | 0.1 |

**Table 6.1:** Test conditions for the tidal turbine case

height. The flow patterns obtained from numerical model are similar to the ones in the OWF case, a decreased velocities is found both upstream and downstream of the

turbine and the flow accelerations are seen at each side of the structure.

At a layer of 1 m above the top of the turbine structure (Z = -15 m), the velocity magnitude distribution is illustrated by figure 6.33. Without the presence of the submerged cylinder, the decreased flow upstream and downstream can still be seen clearly. There is no return flow in this layer and only the reduced flow speed is noticeable in the wake tail.

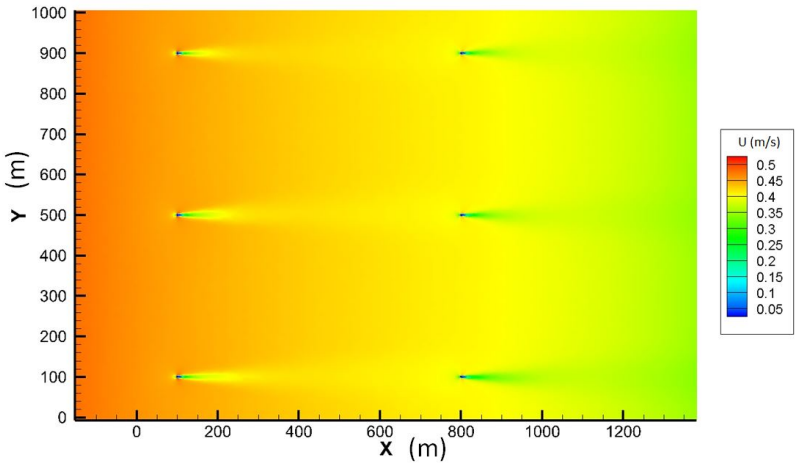


(a) the layer of z= -18m (0.5 of turbine height)

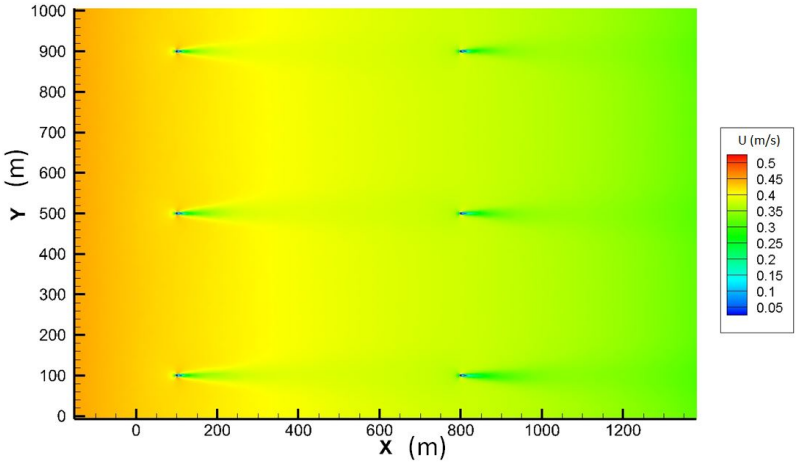


(b) the layer of z= -19m (0.25 of turbine height)

**Figure 6.32:** Time averaged (of 0.5 hours) velocity magnitude around tidal turbine farm in different water depth.

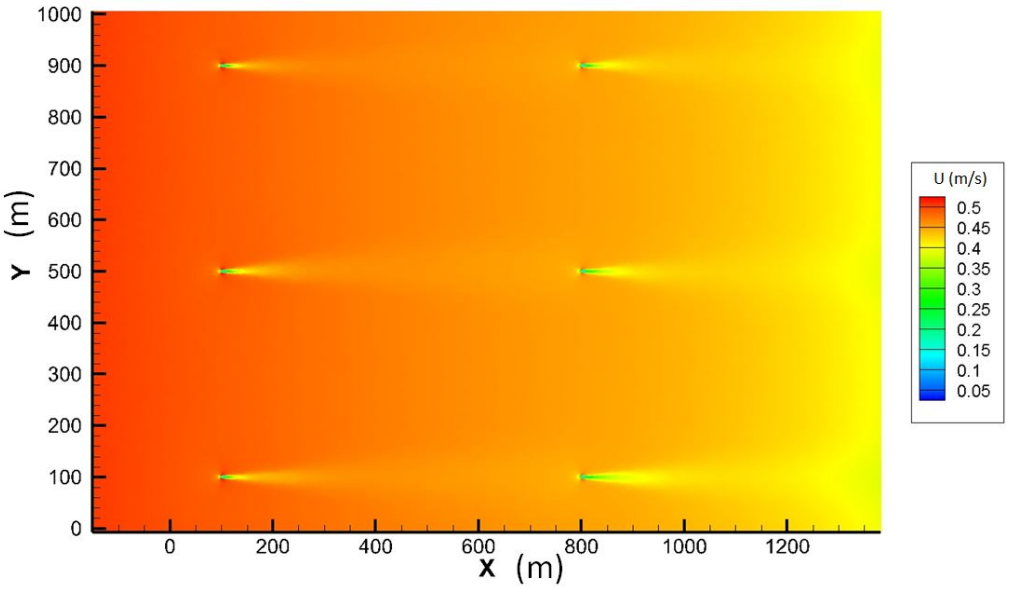


**Figure 6.33:** Averaged velocity magnitude around tidal turbine farm at the layer of z= -15m (1 m over the top of the turbine)

Further looking at the velocity distribution around the circular cylinder at half of the structure height, it is found that the velocity profile shows a very different distribution comparing with that in the laboratory scale simulation. In the figure 6.34, it is clear that the flow is split by the cylinder. The flow velocity is reduced in front of the cylinder and recovered behind the cylinder. The acceleration appears immediately at both side of cylinder which is the same as that in the case of the flow past an infinite cylinder.

Figure 6.35 presents the time averaged velocity magnitude along the vertical direction of the centre line of the channel. The impacts on the flow dynamics around three turbines are represented in figures 6.35 (a) (b) (c) respectively. The upstream flow in front of the turbine is separated nearly at the half height of the cylinder. Below this layer, the flow generates a horseshoe vortex at the bottom. Over this layer, the flow rises up and passes over the top of the turbine. A large vortex can be seen clearly at the back of the structure due to a low pressure zone in this area. But such a vortex remains close to the bed and never rises above the height of the structure. Due to the large distance between these structures, there is no apparent interaction in the flow wake for two consecutive (in the streamwise direction) submerged cylinders.

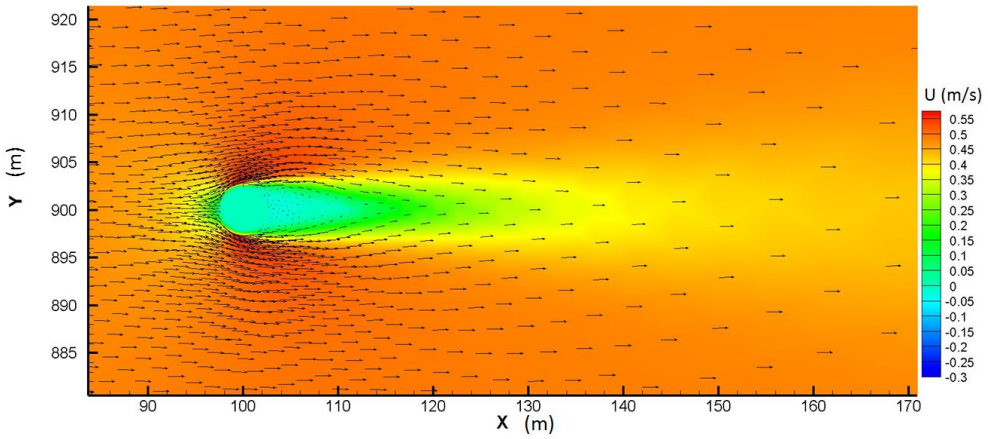


**Figure 6.34:** Averaged velocity magnitude around individual structure at the layer of z= -18 m

Figure 6.36 illustrates the sand concentration at the surface. Although there is no structure blockage at the surface level, the turbid wakes containing high concentrations of sand are still clearly visible. This is due to a very similar mechanism as that near the OWF structure, i.e. the accelerated flow at the side of the pile picks up a substantial amount of sand into suspension at higher level above the bed. Subsequently, the main flow advects these sands further downsteam across the whole water column.

The suspension sand concentration along the centre plane across the turbine is shown in figure 6.37. High sediment concentration is located at the bed surface in front of the turbines. When the flow hits the structure, the strong eddy around the structure picks up some sediment from the bed layer and transports them further downstream. The sand concentration in the water column substantially increases and creates a high concentration area above the turbine surface immediately. Under the action of the water flow, the high concentration of suspension sand keeps moving downstream and a long turbid wake appears as shown in previous figures.

## 6.3 Discussion

The flow in the London Array OWF is carried out by two different structure representation approaches. The first one is based on a 'hollow mesh' or body-fitted strategy and the second one relies on the immersed boundary method to account for the piles of the OWF. The numerical results indicate that when dealing with exposed structures

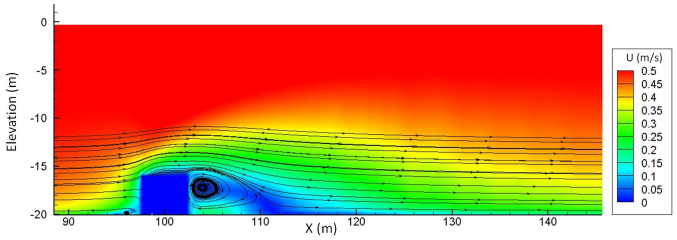


(a) the first turbine

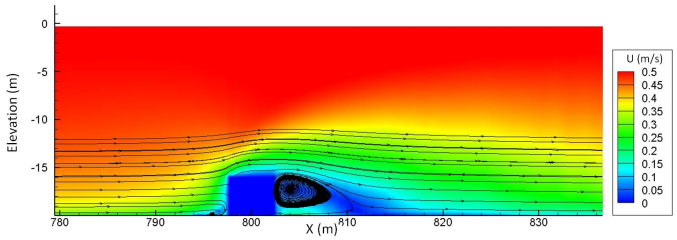


(b) the second turbine

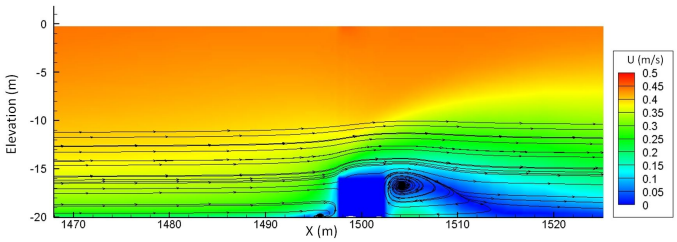


(c) the third turbine

**Figure 6.35:** Time averaged velocity magnitude in vertical cross section along the centre line.

such as the OWF, the immersed boundary method shows the same numerical result as the 'hollow mesh' approach. Currently, generating a 'hollow mesh' similar to the one in this study is very time consuming and might also be too much memory consuming. In such situation, therefore the immersed boundary is preferred.

This study also suggests that the 2eddy LES model is a suitable turbulence model for large scale applications. The complex 3-D flow structure crossing the OWF is well represented in this simulation. The wake behind an individual structure responds to the changing tidal current correctly. On average the wake during the peak tide period is found about 1.5 km long, which is about 300 times of the structure diameter. Furthermore, although the mesh density in this study is proportionally smaller than the one

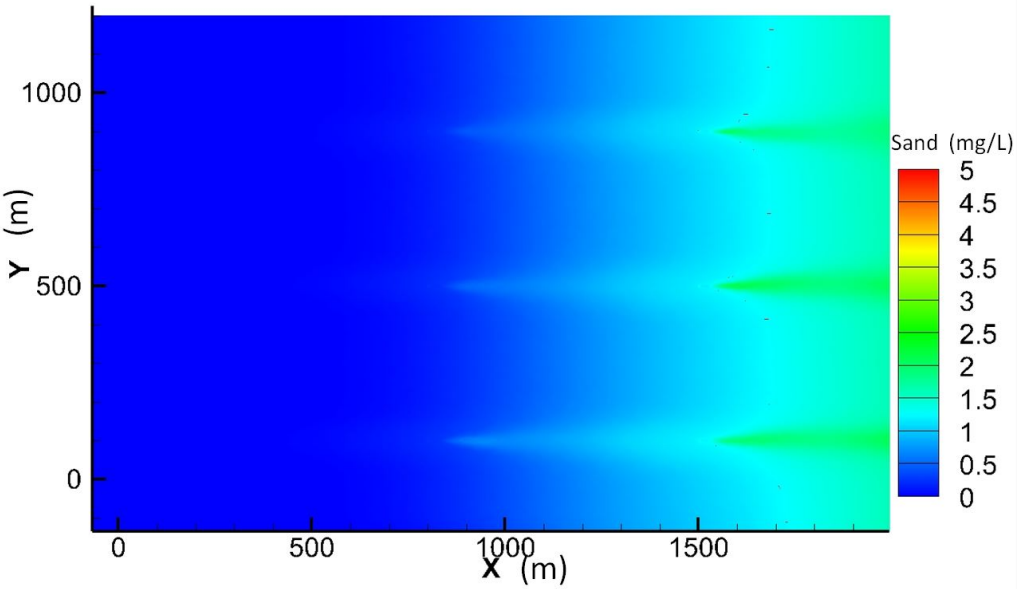


**Figure 6.36:** Suspension sand concentration profile at surface.

at laboratory scale case, the unsteady flow state is still captured well by the numerical model. Because the viscosities in the horizontal and vertical directions are calculated separately, the vertical vortices can be identified clearly in the result alongside the horizontal vortex that is on a very different length scale.

In the investigation of fine sediment transport, it is found that the vertical vortex behind each individual structure plays a significant role in picking up sediment from the bed surface, which increases the local fine sediment concentration in the water body. In high speed tidal current, such a high sediment concentration region extends downstream for a long distance. This generates a wake that is clearly visible at the surface of the see and is also found in the satellite. However comparing the quantity of fine sediment concentration, the numerical model shows a relative higher value than a remote sensing data. The first reason is that due to a lack of in-situ measurement data, the grain size distribution is not well represented. Secondly, the bathymetry in the simulation is based on the interpolation of large scale survey data from various sources, which is not designed for the simulation at this particular site. The London Array OWF is located on an complicated bathymetry with about half sandbanks and the rest in a deep channel. Lastly, the simulation period is limited for sediment transport

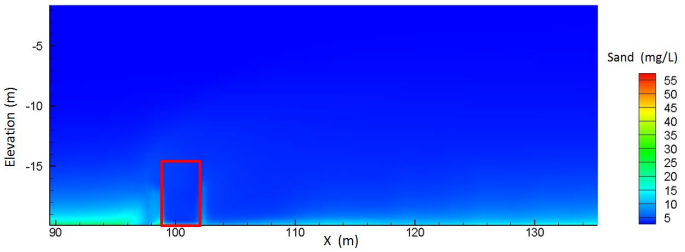


(a) the first turbine

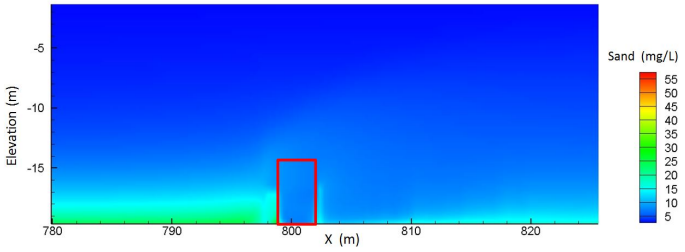


(b) the second turbine

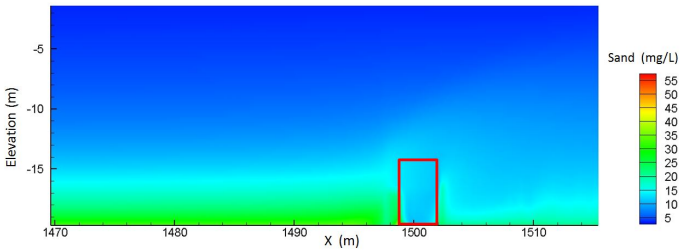


(c) the third turbine

**Figure 6.37:** Suspension sand concentration profile in vertical cross-section view.

process. Due to the small time-step required, the simulation of fine sediment transport is run for 24 hours. However for the fine sediment which is just disturbed into water, the time to allow the particles to settle and diffuse across the water column can be considerable. It is believed that if the model can be carried out for a longer period, the accuracy can be improved.

Currently, to represent a submerged structure, the only way is to use the immersed boundary method. In order to use this method for a large scale application, an ideal flume test is used which contains nine circular cylinders. This is used to investigate the far-field impact of tidal turbine farms. It is found that the immersed boundary method

is a good option to deal with submerged structures and that is suitable in large applications. Comparing with a laboratory scale test, a more classical flow pattern around the cylinder is predicted, a decrease flow in front of the cylinder, acceleration at sides of the cylinder and a recovery behind the cylinder. The qualitative analysis indicates that, the turbulence behind a structure also has a strong impact of the fine sediment transport and the wake of high sediment concentration can be seen for kilometres.

# Chapter 7

# Conclusions and future work

The main aim of this thesis is to review, develop and evaluate methodologies for modelling the impact of offshore structures on coastal seas. Two large-eddy simulation models (the 2eddy viscosity LES model and the Wall-Adapted Large Eddy model) have been incorporated into TELEMAC-3D to achieve a more realistic and effective representation of the turbulence mixing and to account for the unsteadiness of the flow past the structures. The immersed boundary method improves the capability of the 3-D unstructured mesh system and the submerged structures can be directly recognised by a fine mesh. These implementations are successfully tested against laboratory measurement and then applied to simulate the London Array site showing good agreement with in-situ and remote sensing data. An array of 9 submerged cylinders is used to test the immersed boundary approach and the simulations clearly showing the structure-induced far-wake. Overall, the model development and testing have achieved the designed objectives.

This thesis starts with a brief introduction of the background of offshore structure modelling. The importance of understanding the impact of offshore structures on hydrodynamics and environment is pointed out. Then the aims and objectives are designed and the methodology briefly discussed.

This is followed by a chapter of literature review. This chapter presents an overview of recent researches of offshore structure impacts and related numerical modellings. Reviews show that offshore structure has significant impacts on its surrounding environment. The tidal current and waves in the near field can be strongly disturbed

by an existing offshore structure, hence the surrounding flow might become very turbulent. That increased flow speed near the structure would enhance the bed shear stress immediately which plays an important role in entrainment of sediment. Among many types of offshore structures, wind farms and marine turbine farms are selected as the main model object due to their simple geometrical shape (their foundation can be represented as a circular cylinder and blades effect can be largely neglected in far-field simulation) which can be easily handled by numerical modelling. Moreover these structures have been widely installed around UK coast and it is worthwhile investigating their applications.

Many numerical simulations of offshore wind turbine and marine turbine have been reviewed. That includes modelling the flow past a single turbine structure and the flow past a turbine farm. Most of the near-field studies focused on the hydrodynamics adjacent to the structure (the distance is normally smaller than 5 diameters of the turbine pile). The details of the structure (not only foundation but also the blades) can be recognised by an extreme fine 3-D mesh, however due to the computational efforts, such models cannot take tide or wave effect into account effectively, and only simple flow condition is considered. The simulations of the flow past a turbine farm often focuses on 'far-field' simulation, e.g. impact in a large domain. There are two main challenges currently facing these modelling. The first one is that most of coastal models are based on a RANS approach to simulate turbulence phenomenon therefore the turbulence generation and dissipation are limited to certain length scales. The second one is related to the structure representation. Most of current numerical models are using additional friction or force to represent offshore wind farms or marine turbines in which the flow dynamics are not properly represented around the structures. Besides, the most commonly used sigma transform 3-D mesh limits the recognisation of a vertical boundary on the bottom, therefore the structure cannot be simulated.

Driven by the aforementioned requirements on the model development, TELEMAC-3D is selected as the development platform because of a number of advantages comparing with other solvers: firstly it is open-source which means it is programming friendly for users; secondly it has a good performance in parallel computation which means very fine meshes might be used for large scale simulation (large domain and long model

period); lastly, this numerical model contains multiple modules which enable user to simulate various physical processes.

Regarding to the turbulence models, two new turbulence models are developed, including the 2eddy viscosity LES model and the WALE model. The two models optimise the traditional constant Smagorinsky model in two different ways. The 2eddy LES model remedies the limitation of the classical LES approach that the turbulence flow has to be treated isotropically. By using different length-scales in the horizontal and vertical directions respectively, the new turbulence model can deal with the flow in a large horizontal domain but with a smaller vertical depth. The WALE turbulence model overcomes the drawback of the traditional Smagorinsky model, by taking account for both strain rate and rotation rate of the turbulent structures.

The implementation of two new turbulence models is validated for a laboratory scale test case showing the impact of the flow past a cylinder. Comparing with results based on the existing constant Smagorinsky turbulence model in TELEMAC-3D, both the new 2eddy LES and WALE models show less mesh dependence. The vortex shedding in the wake area is well captured in the instantaneous results. Based on the same coarse mesh, results from the 2eddy LES model show a continuous wake however a discontinuous wake is found in the result of the WALE model. This is due to the fact that many small vortex structures are captured by the WALE model and it is considered that the rotation rate plays a significant role in this vortex representation. According to the comparison of the mean velocity components with the experimental data, the 2eddy LES model and the WALE model have similar numerical accuracy in the representation of the flow structure at layers ranging from the surface to the middle depth. However at layers close to the bottom, the 2eddy LES model performs better than the WALE model. We believe this is because the calculation of the WALE model still relies on the representation of the isotropic turbulence structure therefore it requires a very fine mesh in the vertical direction, as the same as the horizontal one. The feature of 2eddy LES model enables it to have a good balance between anisotropic mesh density and model accuracy, which makes it feasible to be applied to engineering studies.

As discussed, the existing models based on sigma tranformation in the vertical di-

rection can not consider a submerged structure in the water. In order to overcome this drawback, the immersed boundary (IB) method is developed based on direct forcing method which relies on forces applied to some nodes of the mesh, and impedes the flow along the solid boundaries. The additional IB force replaces the actual reaction force on the solid surface and is activated by using source terms in the momentum equations of the Navier-Stokes equations. Two laboratory scale cases including the flow past a full cylinder and the flow past a cylinder of finite-height are simulated to validate the approach. In the full cylinder case, both instantaneous and time-averaged velocity profiles are fairly well captured by the numerical model. In the cylinder with finite-height test case, the general flow feature can be captured by the numerical model. The vortex structures can be seen clearly in the results. However, in the representation of the flow above a submerged structure, there is a deviation between numerical model and experiment data. Overall, we believe it is possible to use the immersed boundary method with TELEMAC-3D to represent structures in a simulation. When dealing with an obstacle going from the bottom though the surface of the water, the immersed boundary method offers good accuracy in the prediction of the surrounding flow structures. For the submerged obstacles, they can be simulated using a sigma transform mesh by implementing the immersed boundary method.

After the validation of these new modules against laboratory case, two study cases are discussed including the investigation of the flow past the London Array farm and the flow past 9 submerged circular cylinders. In the London Array study, two methodologies are used to represent OWF structures respectively. The first one is to use a 'hollow' mesh to model the structure explicitly, in a body-fitted way. The second one is to implement the immersed boundary method. In the case of a submerged cylinder, the structure can only be represented by the immersed boundary method. Regarding the turbulence model, we find it is difficult to apply the WALE model because it requires a very fine mesh in the vertical direction, which is not viable at large scale. Mesh independent tests show that increasing the number of layers does help improve the numerical results, however this requires a large amount of computing resource. Therefore only the 2eddy LES model is applied in this study.

We discovered that the new turbulence model shows good behaviour in the far-field

simulation. Although the mesh used at this large scale is proportionally much coarser than the one used in the laboratory scale case, in the sense that less nodes are used to represent the 2-D boundary of the cylinders, the vortex shedding effect is clearly seen in the numerical results.

Similar results are obtained when using both the 'hollow mesh' and the immersed boundary method, with high resolution around each individual structure. A 7-day hydrodynamic model run for the study domain has been obtained which suggests that the tidal flow has complex 3-D structures across the depth, and the wake behind the individual turbine foundation is clearly seen in the results. The suspended sediment concentration are simulated based on a 5-day hydrodynamic result. Due to the large number of elements and their small size, a small time-step is required. The wake made of a high sediment concentration is clearly visible in the results. They suggest that turbulent eddies in the vertical direction are important in resuspending fine sediment from the sea bed and the tidal current plays a crucial role in the subsequent transport process. The peak of sediment concentration always occurs during the peak flood and peak ebb flow period. With the combined effects of the turbulent eddy and high speed current, some wakes around the individual structures of the London Array offshore wind turbines are found to be more than 2 kilometer-long (about 400 times of cylinder diameter) downstream.

The present study shows that the implementation of a new turbulence model and the immersed boundary method in TELEMAC-3D overcome the difficulty of the original model to represent a far-field impact of offshore structures. It is found that these approaches are efficient and their accuracy is acceptable. It is also found that using new turbulence models as well as the immersed boundary conditions do not impact the overall parallel performance of the code. The application of these tools generally requires fine mesh resolution and hence computational costs are high. All the tests in the present work are carried out using High Performance Computer and the iDataPlex Cluster located at STFC Daresbury Laboratory Hartree Centre and Archer, the Cray XC30 supercomputer in Edinburgh. Although the WALE model can not be applied for real scale simulation in its present state, we believe that with the development of computer science, it could become a good option to model turbulence at large scale.

## 7.1 Future work

This research has opened up a number of potential avenues for future investigation:

- Further looking at the direct forcing approach of the immersed boundary method for the free-surface Navier-Stokes equations. Although the current approach can well represent a simple structure such as for an OWF, the performance of simulating the submerged structure is still questionable. The main problems appear in the representation of the flow structure above the top of structure. This may be related to the inherent numerics in the software. For example, different advection schemes need to be investigated or the integration step along the vertical direction need to be improved.

- The problem mentioned above may be also because of the turbulence model itself. In the current models, no special treatment is applied to the horizontal boundary of the submerged cylinder, and considering using a wall function for the turbulence model could be an option. Therefore a better turbulence model to represent the eddy around submerged structures can be considered.

- Implementation of the immersed boundary method coupled with the sediment transport can be further investigated including both bed load sediment transport and suspension sediment transport. Currently, the immersed boundary method is only applied to the hydrodynamic module. For the sediment transport simulation, the current code cannot ensure that there is no sediment particle going through the immersed boundary and this would result in errors in the simulation.

- Wave propagation is another important physical process for ocean/coastal engineering environment which should be taken into account. The TELEMAC system offers the user a module, namely TOMOWAC, to investigate the wave phenomenon. However, the coupling between TOMAWAC and TELEMAC-3D using the new developments has to be investigated further as some stability issues currently occur. Further code optimisation is required.

- Considering another approach than the immersed boundary method, by masking the elements. As the derivations rely on the finite-element method, element

masking would be accounted for during the assembly stage of the matrix.

# References


[1] G. Palau-Salvador, T. Stoesser, J. Fröhlich, M. Kappler, and W. Rodi. Large eddy simulations and experiments of flow around finite-height cylinders. *Flow, turbulence and combustion*, 84(2):239–275, 2010.

[2] Wave and tidal energy: part of the UK's energy mix. `https://www.gov.uk/guidance/wave-and-tidal-energy-part-of-the-uks-energy-mix`. Accessed: 2016-07-30.

[3] Crown Estate. UK wave and tidal key resource areas project: Summary report. *Crown Estate. October*, 2012.

[4] D. C. Wilcox. Turbulent modelling for cfd. *DCW Industries Inc., California*, 1993.

[5] S. Kang, I. Borazjani, J. A Colby, and F. Sotiropoulos. Numerical simulation of 3d flow past a real-life marine hydrokinetic turbine. *Advances in water resources*, 39:33–43, 2012.

[6] W. M. J. Batten, A. S. Bahaj, A. F. Molland, and J. R. Chaplin. Hydrodynamics of marine current turbines. *Renewable Energy*, 31(2):249–256, 2006.

[7] W. M. J. Batten, A. S. Bahaj, A. F. Molland, and J. R. Chaplin. The prediction of the hydrodynamic performance of marine current turbines. *Renewable energy*, 33(5):1085–1096, 2008.

[8] T. McCombes, C. Johnstone, and A. Grant. Unsteady 3d wake modelling for marine current turbines. In *Proceedings of the 8th European Wave and Tidal Energy Conference, Uppsala, Sweden*, pages 548–557, 2009.

[9] C. Chen, R. C. Beardsley, and G. Cowles. An unstructured grid, finite-volume coastal ocean model: Fvcom user manual. *SMAST/UMASSD*, 2006.

[10] Delft Hydraulics. Delft3d-flow user manual. *Delft, the Netherlands*, 2006.

[11] OPERATING MANUAL. Telemac modelling system. 2007.

[12] R. Ahmadian, R. Falconer, and B. Bockelmann-Evans. Far-field modelling of the hydro-environmental impact of tidal stream turbines. *Renewable Energy*, 38(1):107–116, 2012.

[13] R. Ahmadian and R. A. Falconer. Assessment of array shape of tidal stream turbines on hydro-environmental impacts and power output. *Renewable Energy*, 44:318–327, 2012.

[14] P. A. Work, K. A. Haas, Z. Defne, and T. Gay. Tidal stream energy site assessment via three-dimensional model and measurements. *Applied Energy*, 102:510–519, 2013.

[15] D. Hasegawa, J. Sheng, D. A. Greenberg, and K. R. Thompson. Far-field effects of tidal energy extraction in the minas passage on tidal circulation in the bay of fundy and gulf of maine using a nested-grid coastal circulation model. *Ocean Dynamics*, 61(11):1845–1868, 2011.

[16] M. A. El-Reedy. *Offshore structures: design, construction and maintenance*. Gulf Professional Publishing, 2012.

[17] D. N. Veritas. Design of offshore wind turbine structures. *Offshore Standard DNV-OS-J101*, 6:2004, 2004.

[18] P. Higgins and A. Foley. The evolution of offshore wind power in the united kingdom. *Renewable and sustainable energy reviews*, 37:599–612, 2014.

[19] M. J. Khan, G. Bhuyan, M. T. Iqbal, and J. E. Quaicoe. Hydrokinetic energy conversion systems and assessment of horizontal and vertical axis turbines for river and tidal applications: A technology status review. *Applied Energy*, 86(10):1823–1835, 2009.

[20] P. Garman et al. Water current turbines. a field worker's guide. *Water current turbines. A field worker's guide.*, 1986.

[21] Black and Veatch. Phase ii. UK tidal stream energy resource assessment. *Carbon Trust Marine Energy, Challenge*, 2005.

[22] S. Kihoh and M. Shiono. Electric power generations from tidal currents by darrieus turbine at kurushima straits. *T. IEE Japan*, 112:530–538, 1992.

[23] S. Kiho, M. Shiono, and K. Suzuki. The power generation from tidal currents by darrieus turbine. *Renewable Energy*, 9(1):1242–1245, 1996.

[24] G. G. Portnov and I. Z. Palley. Application of the theory of naturally curved and twisted bars to designing gorlov's helical turbine 1. system of governing equations. *Mechanics of composite materials*, 34(4):343–354, 1998.

[25] L. I. Lago, F. L. Ponta, and L. Chen. Advances and trends in hydrokinetic turbine systems. *Energy for Sustainable Development*, 14(4):287–296, 2010.

[26] R. Bedard, M. Previsic, O. Siddiqui, G. Hagerman, and M. Robinson. Final survey and characterization tidal in stream energy conversion (tisec) devices. Technical report, EPRI–TP–004 NA Report November 9, 2005.

[27] A. Good, G. A. Hamill, T. Whittaker, D. Robinson, et al. Piv analysis of the near wake of a tidal turbine. In *The Twenty-first International Offshore and Polar Engineering Conference*. International Society of Offshore and Polar Engineers, 2011.

[28] S. Rose, S. Ordonez, K. H. Lee, C. Johnstone, C. H. Jo, T. McCombes, and A. Grant. Tidal turbine wakes: small scale experimental and initial computational modelling. In *Proc. 9th European Wave and Tidal Energy Conference (EWTEC)*, 2011.

[29] T. Stallard, T. Feng, and P. K. Stansby. Experimental study of the mean wake of a tidal stream rotor in a shallow turbulent flow. *Journal of Fluids and Structures*, 54:235–246, 2015.

[30] P. Mycek, B. Gaurier, G. Germain, G. Pinon, and E. Rivoalen. Experimental study of the turbulence intensity effects on marine current turbines behaviour. part i: One single turbine. *Renewable Energy*, 66:729–746, 2014.

[31] P. Mycek, B. Gaurier, G. Germain, G. Pinon, and E. Rivoalen. Experimental study of the turbulence intensity effects on marine current turbines behaviour. part ii: Two interacting turbines. *Renewable Energy*, 68:876–892, 2014.

[32] C. Hill, M. Musa, L. P. Chamorro, C. Ellis, and M. Guala. Local scour around a model hydrokinetic turbine in an erodible channel. *Journal of Hydraulic Engineering*, 140(8):04014037, 2014.

[33] C. Hill, M. Musa, and M. Guala. Interaction between instream axial flow hydrokinetic turbines and uni-directional flow bedforms. *Renewable Energy*, 86:409–421, 2016.

[34] Y. Chen, B. Lin, J. Lin, and S. Wang. Effects of stream turbine array configuration on tidal current energy extraction near an island. *Computers & Geosciences*, 77:20–28, 2015.

[35] S. Rao, H. Xue, M. Bao, and S. Funke. Determining tidal turbine farm efficiency in the western passage using the disc actuator theory. *Ocean Dynamics*, 66(1):41–57, 2016.

[36] Q. Vanhellemont and K. Ruddick. Turbid wakes associated with offshore wind turbines observed with landsat 8. *Remote Sensing of Environment*, 145:105–115, 2014.

[37] J. Thiébot, P. B. du Bois, and S. Guillou. Numerical modeling of the effect of tidal stream turbines on the hydrodynamics and the sediment transport–application to the alderney race (raz blanchard), france. *Renewable Energy*, 75:356–365, 2015.

[38] J. Zheng, R. Li, Y. Yu, and A. Suo. Influence of wave and current flow on sediment-carrying capacity and sediment flux at the water-sediment interface. *Water Science & Technology*, 70(6), 2014.

[39] S. Monserrat, I. Fine, A. Amores, and M. Marcos. Tidal influence on high frequency harbor oscillations in a narrow entrance bay. *Natural Hazards*, 74(1):143–153, 2014.

[40] F. G. Dellatorre, J. P. Pisoni, P. J. Barón, and A. L. Rivas. Tide and wind forced nearshore dynamics in nuevo gulf (northern patagonia, argentina): Potential implications for cross-shore transport. *Journal of Marine Systems*, 96:82–89, 2012.

[41] M. V. Mikhailova. Long-term variations in river and sea factors responsible for the hydrological regime and morphological structure of the thames river mouth area. *Water Resources*, 38(4):438–452, 2011.

[42] L. J. Vermeer, J. N. Sørensen, and A. Crespo. Wind turbine wake aerodynamics. *Progress in aerospace sciences*, 39(6):467–510, 2003.

[43] M. E. Harrison, W. M. J. Batten, L. E. Myers, and A. S. Bahaj. Comparison between cfd simulations and experiments for predicting the far wake of horizontal axis tidal turbines. *Renewable Power Generation, IET*, 4(6):613–627, 2010.

[44] S. Gant and T. Stallard. Modelling a tidal turbine in unsteady flow. In *Proceedings of the Eighteenth (2008) International Offshore and Polar Engineering Conference*, pages 473–480, 2008.

[45] T. Divett, R. Vennell, and C. Stevens. Channel-scale optimisation and tuning of large tidal turbine arrays using les with adaptive mesh. *Renewable Energy*, 86:1394–1405, 2016.

[46] A. J. MacLeod, S. Barnes, K. G. Rados, and I. G. Bryden. Wake effects in tidal current turbine farms. In *International conference on marine renewable energy-conference proceedings*, pages 49–53, 2002.

[47] L. Bai, R. R. G. Spence, and G. Dudziak. Investigation of the influence of array arrangement and spacing on tidal energy converter (tec) performance using a 3-dimensional cfd model. In *Proceedings of the 8th European wave and tidal energy conference, Uppsala, Sweden*, pages 654–660, 2009.

[48] X. Sun, J. P. Chick, and I. G. Bryden. Laboratory-scale simulation of energy extraction from tidal currents. *Renewable Energy*, 33(6):1267–1274, 2008.

[49] L. S. Blunden, W. M. J. Batten, M. E. Harrison, and A. S. Bahaj. Comparison of boundary-layer and field models for simulation of flow through multiple-row tidal fences. In *Proc. 8th European Wave and Tidal Energy Conf., Uppsala, Sweden, September 2009.*, 2009.

[50] J. F. Manwell, J. G. McGowan, and A. L. Rogers. *Wind energy explained: theory, design and application*. John Wiley & Sons, 2010.

[51] T. Burton, D. Sharpe, N. Jenkins, and E. Bossanyi. *Wind energy handbook*. John Wiley & Sons, 2001.

[52] P. J. Moriarty and A. C. Hansen. Aerodyn theory manual: National renewable energy laboratory. Technical report, TP-500-36881. NREL, CO, 2005.

[53] F. O'Rourke, F. Boyle, A. Reynolds, and D. M. Kennedy. Hydrodynamic performance prediction of a tidal current turbine operating in non-uniform inflow conditions. *Energy*, 93:2483–2496, 2015.

[54] S. P. Neill, E. J. Litt, S. J. Couch, and A. G. Davies. The impact of tidal stream turbines on large-scale sediment dynamics. *Renewable Energy*, 34(12):2803–2812, 2009.

[55] I. Bryden and G. T. Melville. Choosing and evaluating sites for tidal current development. *Proceedings of the Institution of Mechanical Engineers, Part A: Journal of Power and Energy*, 218(8):567–577, 2004.

[56] D. A. Randall. The shallow water equations. *Department of Atmospheric Science, Colorado State University, Fort Collins*, 2006.

[57] Y. Fan and D. Li. Research on 2-d ecological mathematical model of red tide. *Nature Environment and Pollution Technology*, 15(1):195, 2016.

[58] Ü. Suursaar, T. Kullas, and M. Otsmann. A model study of the sea level variations in the gulf of riga and the väinameri sea. *Continental Shelf Research*, 22(14):2001–2019, 2002.

[59] P. Vethamony, G. S. Reddy, M. T. Babu, E. Desa, and K. Sudheesh. Tidal eddies in a semi-enclosed basin: a model study. *Marine Environmental Research*, 59(5):519–532, 2005.

[60] A. B. Fortunato, X. Bertin, and A. Oliveira. Space and time variability of uncertainty in morphodynamic simulations. *Coastal Engineering*, 56(8):886–894, 2009.

[61] G. Umgiesser, C. Ferrarin, A. Cucco, F. De Pascalis, D. Bellafiore, M. Ghezzo, and M. Bajo. Comparative hydrodynamics of 10 mediterranean lagoons by means of numerical modeling. *Journal of Geophysical Research: Oceans*, 119(4):2212–2226, 2014.

[62] M. Zhang, I. Townend, Y. Zhou, and H. Cai. Seasonal variation of river and tide energy in the yangtze estuary, china. *Earth Surface Processes and Landforms*, 41(1):98–116, 2016.

[63] L. Balas and E. Özhan. Three-dimensional modelling of stratified coastal waters. *Estuarine, Coastal and Shelf Science*, 54(1):75–87, 2002.

[64] M. Keshtpoor, J. A. Puleo, F. Shi, and G. Ma. 3d numerical simulation of turbulence and sediment transport within a tidal inlet. *Coastal Engineering*, 96:13–26, 2015.

[65] M. De Marchis, G. Freni, and E. Napoli. Three-dimensional numerical simulations on wind-and tide-induced currents: The case of augusta harbour (italy). *Computers & Geosciences*, 72:65–75, 2014.

[66] S. M. Kashefipour, B. Lin, and R. A. Falconer. Modelling the fate of faecal indicators in a coastal basin. *Water Research*, 40(7):1413–1425, 2006.

[67] E. L. Harris, R. A. Falconer, and B. Lin. Modelling hydroenvironmental and health risk assessment parameters along the south wales coast. *Journal of Environmental Management*, 73(1):61–70, 2004.

[68] Z. Yang, T. Wang, and A. E. Copping. Modeling tidal stream energy extraction

and its effects on transport processes in a tidal channel and bay system using a three-dimensional coastal ocean model. *Renewable Energy*, 50:605–613, 2013.

[69] I. G. Bryden and S. J. Couch. Me1marine energy extraction: tidal resource analysis. *Renewable Energy*, 31(2):133–139, 2006.

[70] DHI User Guide. Reference manual of mike21, 2005.

[71] L. Prandtl. Bericht über untersuchungen zur ausgebildeten turbulenz. *Z. Angew. Math. Mech*, 5(2):136–139, 1925.

[72] W. P. Jones and B. E. Launder. The prediction of laminarization with a two-equation model of turbulence. *International journal of heat and mass transfer*, 15(2):301–314, 1972.

[73] P. Bradshaw. *An Introduction to Turbulence and Its Measurement: Thermodynamics and Fluid Mechanics Series*. Elsevier, 2013.

[74] C. Leupi, M. S. Altinakar, and M. Deville. Numerical modeling of cohesive sediments dynamics in estuaries: Part idescription of the model and simulations in the po river estuary. *International journal for numerical methods in fluids*, 57(3):237–263, 2008.

[75] A. N. Kolmogorov. Equations of turbulent motion in an incompressible fluid. In *Dokl. Akad. Nauk SSSR*, volume 30, pages 299–303, 1941.

[76] J. Smagorinsky. General circulation experiments with the primitive equations: I. the basic experiment*. *Monthly weather review*, 91(3):99–164, 1963.

[77] G. L. Mellor and T. Yamada. Development of a turbulence closure model for geophysical fluid problems. *Reviews of Geophysics*, 20(4):851–875, 1982.

[78] G. Shapiro, M. Luneva, J. Pickering, and D. Storkey. The effect of various vertical discretization schemes and horizontal diffusion parameterisation on the performance of a 3-d ocean model: the black sea case study. *Ocean Science Discussions*, 9(6):3643, 2012.

[79] S. M. Griffies and R. W. Hallberg. Biharmonic friction with a smagorinsky-like viscosity for use in large-scale eddy-permitting ocean models. *Monthly Weather Review*, 128(8):2935–2946, 2000.

[80] F. Roman, G. Stipcich, V. Armenio, R. Inghilesi, and S. Corsini. Large eddy simulation of mixing in coastal areas. *International Journal of Heat and Fluid Flow*, 31(3):327–341, 2010.

[81] A. Petronio, F. Roman, C. Nasello, and V. Armenio. Large eddy simulation model for wind-driven sea circulation in coastal areas. *Nonlinear Processes in Geophysics*, 20(6):1095–1112, 2013.

[82] E. Meyer-Peter and R. Müller. Formulas for bed-load transport. IAHR, 1948.

[83] F. Engelund and E. Hansen. A monograph on sediment transport in alluvial streams. Technical report, TEKNISKFORLAG Skelbrekgade 4 Copenhagen V, Denmark., 1967.

[84] H. A. Einstein. *The bed-load function for sediment transportation in open channel flows*. Number 1026. US Department of Agriculture, 1950.

[85] L. C. Van Rijn. Sediment transport, part i: bed load transport. *Journal of hydraulic engineering*, 110(10):1431–1456, 1984.

[86] E. W. Bijker. Mechanics of sediment transport by the combination of waves and current. Technical report, ICCE 1992 local organising committee, 1992.

[87] J. P. Chollet and J. A. Cunge. New interpretation of some head loss-flow velocity relationships for deformable movable beds. *Journal of Hydraulic Research*, 17(1):1–13, 1979.

[88] J. A. Bailard. An energetics total load sediment transport model for a plane sloping beach. *Journal of Geophysical Research: Oceans*, 86(C11):10938–10954, 1981.

[89] M. Dibajnia and A. Watanabe. Sheet flow under nonlinear waves and currents. *Coastal Engineering Proceedings*, 1(23), 1992.

[90] I. Fairley, I. Masters, and H. Karunarathna. The cumulative impact of tidal stream turbine arrays on sediment transport in the pentland firth. *Renewable Energy*, 80:755–769, 2015.

[91] I. Celik and W. Rodi. Modeling suspended sediment transport in nonequilibrium situations. *Journal of Hydraulic Engineering*, 114(10):1157–1191, 1988.

[92] L. M. Ashall, R. P. Mulligan, and B. A. Law. Variability in suspended sediment concentration in the minas basin, bay of fundy, and implications for changes due to tidal power extraction. *Coastal Engineering*, 107:102–115, 2016.

[93] C. S. Peskin. Flow patterns around heart valves: a numerical method. *Journal of computational physics*, 10(2):252–271, 1972.

[94] J. Mohd-Yusof. Combined immersed-boundary/b-spline methods for simulations of ow in complex geometries. *Annual Research Briefs. NASA Ames Research Center= Stanford University Center of Turbulence Research: Stanford*, pages 317–327, 1997.

[95] E. A. Fadlun, R. Verzicco, P. Orlandi, and J. Mohd-Yusof. Combined immersed-boundary finite-difference methods for three-dimensional complex flow simulations. *Journal of computational physics*, 161(1):35–60, 2000.

[96] E. Arquis and J. P. Caltagirone. Sur les conditions hydrodynamiques au voisinage dune interface milieu fluide-milieu poreux: applicationa la convection naturelle. *CR Acad. Sci. Paris II*, 299:1–4, 1984.

[97] D. K. Clarke, H. A. Hassan, and M. D. Salas. Euler calculations for multielement airfoils using cartesian grids. *AIAA journal*, 24(3):353–358, 1986.

[98] X. Y. Hu, B. C. Khoo, N. A. Adams, and F. L. Huang. A conservative interface method for compressible flows. *Journal of Computational Physics*, 219(2):553–578, 2006.

[99] H. S. Udaykumar, R. Mittal, and W. Shyy. Computation of solid–liquid phase fronts in the sharp interface limit on fixed grids. *Journal of computational physics*, 153(2):535–574, 1999.

[100] H. S. Udaykumar, W. Shyy, and M. M. Rao. Elafint: a mixed Eulerian–Lagrangian method for fluid flows with complex and moving boundaries. *International journal for numerical methods in fluids*, 22(8):691–712, 1996.

[101] S. Popinet. Gerris: a tree-based adaptive solver for the incompressible Euler equations in complex geometries. *Journal of Computational Physics*, 190(2):572–600, 2003.

[102] A. S. Almgren, J. B. Bell, P. Colella, and T. Marthaler. A cartesian grid projection method for the incompressible Euler equations in complex geometries. *SIAM Journal on Scientific Computing*, 18(5):1289–1309, 1997.

[103] R. J. Leveque and Z. Li. The immersed interface method for elliptic equations with discontinuous coefficients and singular sources. *SIAM Journal on Numerical Analysis*, 31(4):1019–1044, 1994.

[104] J. E. Jones and A. M. Davies. Application of a finite element model (telemac) to computing the wind induced response of the irish sea. *Continental Shelf Research*, 26(12):1519–1541, 2006.

[105] E. H. Fernandes, K. R. Dyer, and L. F. H. Niencheski. Calibration and validation of the telemac-2d model to the patos lagoon (brazil). *Journal of Coastal Research*, pages 470–488, 2001.

[106] A. Malcherek. Application of telemac-2d in a narrow estuarine tributary. *Hydrological processes*, 14(13):2293–2300, 2000.

[107] C. Pham and V. A. Martin. Tidal current turbine demonstration farm in paimpol-brehat (brittany): tidal characterisation and energy yield evaluation with telemac. In *Proceedings of the 8th European Wave and Tidal Energy Conference, Uppsala, Sweden*, volume 710, 2009.

[108] C. Moulinec, C. Denis, C-T. Pham, D. Rougé, J-M. Hervouet, E. Razafindrakoto, R. W. Barber, D. R. Emerson, and X-J. Gu. Telemac: An efficient hydrodynamics suite for massively parallel architectures. *Computers & Fluids*, 51(1):30–34, 2011.

[109] A. J. Chorin. Numerical solution of the Navier-Stokes equations. *Mathematics of computation*, 22(104):745–762, 1968.

[110] F. Ducros, F. Nicoud, and T. Poinsot. Wall-adapting local eddy-viscosity models for simulations in complex geometries. In *International Conference on Computational Conference*, pages 293–300, 1998.

[111] J. Pedlosky. *Geophysical fluid dynamics*. Springer Science & Business Media, 2013.

[112] F. Nicoud and F. Ducros. Subgrid-scale stress modelling based on the square of the velocity gradient tensor. *Flow, turbulence and Combustion*, 62(3):183–200, 1999.

[113] J. Kim, D. Kim, and H. Choi. An immersed-boundary finite-volume method for simulations of flow in complex geometries. *Journal of Computational Physics*, 171(1):132–150, 2001.

[114] A. Roulund, B. M. Sumer, J. Fredsøe, and J. Michelsen. Numerical and experimental investigation of flow and scour around a circular pile. *Journal of Fluid Mechanics*, 534:351–401, 2005.

[115] Y. Yin, M. Li, C. Moulinec, and D. R. Emerson. In-depth hpc-les investigation for the flow around a circular cylinder using telemac3d. In *Proceedings of the XXI TELEMAC-MASCARET User Conference, Grenoble, France*, 2014.

[116] Y. Yin, M. Li, C. Moulinec, and D. R. Emerson. Wall-adapting local eddy-viscosity tubulence model for telemac3d. In *Proceedings of the XXII TELEMAC-MASCARET User Conference, STFC Daresbury Laboratory, UK*, 2015.

[117] B. M. Sumer and J. Fredsøe. *The mechanics of scour in the marine environment*. World Scientific, 2002.

[118] T. A. Waniewski, C. E. Brennen, and F. Raichlen. Bow wave dynamics. *Journal of Ship Research*, 46(1):1–15, 2002.

[119] G. Haller. An objective definition of a vortex. *Journal of Fluid Mechanics*, 525:1–26, 2005.

[120] V. Kolář. Vortex identification: New requirements and limitations. *International journal of heat and fluid flow*, 28(4):638–652, 2007.

[121] S. Kida and H. Miura. Identification and analysis of vortical structures. *European Journal of Mechanics-B/Fluids*, 17(4):471–488, 1998.

[122] J. Jeong and F. Hussain. On the identification of a vortex. *Journal of fluid mechanics*, 285:69–94, 1995.

[123] J. C. Hunt, A. A. Wray, and P. Moin. Eddies, streams, and convergence zones in turbulent flows. 1988.

[124] B. M. Sumer and J. Fredsøe. *Hydrodynamics around cylindrical strucures*, volume 26. World scientific, 2006.

[125] P. Hjorth. *Studies on the nature of local scour*. Inst. för Teknisk Vattenresurslära, Lunds Tekniska Högskola, Lunds Univ., 1975.

[126] R. J. S. Whitehouse, J. M. Harris, J. Sutherland, and J. Rees. The nature of scour development and scour protection at offshore windfarm foundations. *Marine Pollution Bulletin*, 62(1):73–88, 2011.

[127] E. Christie, M. Li, and C. Moulinec. Comparison of 2d and 3d large scale morphological modeling of offshore wind farms using hpc. *Coastal Engineering Proceedings*, 1(33):42, 2012.

[128] G. D. Egbert and S. Y. Erofeeva. Efficient inverse modeling of barotropic ocean tides. *Journal of Atmospheric and Oceanic Technology*, 19(2):183–204, 2002.

[129] R. Soulsby. *Dynamics of marine sands: a manual for practical applications*. Thomas Telford, 1997.

[130] J. A. Zyserman and J. Fredsøe. Data analysis of bed concentration of suspended sediment. *Journal of Hydraulic Engineering*, 120(9):1021–1042, 1994.

# Appendix A

# Publications

This appendix contains the papers which are published during the PhD study.

Y. Yin, E. Christie, M. Li, C. Moulinec and D. R. Emerson, 2014. 3D morphological impact modelling of Offshore Wind Farms using LES and HPC. *International Conference on Coastal Engineering 2014.* (peer reviewed)

Y. Yin, M. Li, C. Moulinec and D. R. Emerson, 2014. In-depth HPC-LES investigation for the flow around a circular cylinder using TELEMAC-3D. *TELEMAC User-Conference 2014.*

Y. Yin, M. Li, C. Moulinec and D. R. Emerson, 2015. Wall-Adapting Local Eddy-Viscosity turbulence model for TELEMAC-3D. TELEMAC User-Conference 2015.

Y. Yin, M. Li, C. Moulinec and D. R. Emerson, 2016. Simulation of the flow around a submerged structure using the Immersed Boundary Method. *TELEMAC User-Conference 2016.*

# 3D MORPHOLOGICAL IMPACT MODELLING OF OFFSHORE WIND FARMS USING LES AND HPC

Yue Yin[1], Elizabeth Christie[1], Ming Li[1], Charles Moulinec[2] and David R. Emerson[2]

A model based on TELEMAC 3D using Large Eddy Simulation has been developed to simulate of complex flows and sediment transport around offshore wind farm foundations. The model was tested against available laboratory experimental data with satisfactory agreement. The model results reveal that with fine resolution, using Large Eddy Simulation allows to capture the turbulence eddy shedding behind the structure better than using conventional RANS models. Application of the model to the Burbo Bank OWF in Liverpool Bay, in North West England helps capturing the strong 3D structures across the depth, which can have considerable influence on sediment suspension and transport around the structure, particularly for fine sediments.

*Keywords: offshore wind farms; TELEMAC3D; large eddy simulation*

## INTRODUTION

With recent fast development of offshore wind farms (OWF), it is important to understand any impacts they might have on large scale coastal hydrodynamics and morphodynamics. A recent study by Christie et al (2012) has shown that it is possible to include the OWF structure directly in the oceanographic model with high grid resolution around each individual monopile. Unfortunately, the conventional Reynolds Averaged Navier-Stokes (RANS) turbulence closures, such as k-ε and k-ω, become inefficient to describe turbulence generation and dissipation immediately adjacent to the monopile as well as the large scale wake tailing behind the whole OWF. To satisfy stability criteria, the computational time step has also to be small, which limits the model's capability for long term simulations. The present research therefore intends to substitute the RANS turbulence closure with Large Eddy Simulation (LES) and investigate its performance and accuracy for far field modelling.

The aim of this paper is to demonstrate the capability of the coastal morphodynamic model TELEMAC3D (Hervouet, 2007; http://www.opentelemac.org) to predict the flow and sediment transport around offshore wind farm foundations. Prior to this investigation, TELEMAC3D is first validated at laboratory scale by simulating the flow around a cylinder lying on the bottom of a channel. Results are compared to the experimental data obtained by Roulund et al (2005), using their configuration.

## NUMERICAL METHOD

### Governing equations

An open source hydrodynamic suite, TELEMAC, is used to simulate the hydrodynamics impact of offshore wind farms. The 3D module, TELEMAC3D is a three-dimensional computational code solving either the hydrostatic or non-hydrostatic equations. In this work the hydrostatic approximation is used both at laboratory scale and field scale. The code solves the three-dimensional hydrodynamic equations based on the following assumptions (courtesy of Hervouet (2007)):

1. Three-dimensional Navier-Stokes equations with a free surface changing in time,
2. Negligible variation of density in the conservation of mass equation (incompressible fluid),
3. Pressure-hydrostatic assumption (that assumption results in that the pressure at a given depth is the sum of the air pressure at the fluid surface plus the weight of the overlying water body),
4. Boussinesq approximation for the momentum (the density variations are not taken into account in the gravity term)

Due to these assumptions, the three-dimensional equations being solved are:

$$\frac{\partial U}{\partial x}+\frac{\partial V}{\partial y}+\frac{\partial W}{\partial z}=0 \tag{1}$$

$$\frac{\partial U}{\partial t}+U\frac{\partial U}{\partial x}+V\frac{\partial U}{\partial y}+W\frac{\partial U}{\partial z}=-g\frac{\partial Z_s}{\partial x}+\nu\Delta U+F_x \tag{2}$$

$$\frac{\partial V}{\partial t}+U\frac{\partial V}{\partial x}+V\frac{\partial V}{\partial y}+W\frac{\partial V}{\partial z}=-g\frac{\partial Z_s}{\partial y}+\nu\Delta V+F_y \tag{3}$$

$$p=\ p_{atm}+\rho_0 g(Z_s-z)+\rho_0 g\int_Z^{Z_s}\frac{\Delta\rho}{\rho_0}dZ \tag{4}$$

[1] School of Engineering, University of Liverpool, L69 3GQ, Liverpool, U.K.
[2] Science and Technology Facilities Council, Daresbury Laboratory, WA4 4AD, U.K.

where *U*, *V* and *W* are three-dimensional components of velocity; $Z_s$ is the free surface elevation and $F_x$, $F_y$ are source terms. Pressure is calculated in Eq. 4 where $\rho_0$ and $\Delta\rho$ are reference density and variation of density respectively.

Based on these assumptions, TELEMAC3D model can be split up in three fractional steps:

-The first step consists in finding out the advected velocity components by only solving the advection terms in the momentum equations.

-The second step computes, from the advected velocities, the new velocity components taking into account the diffusion terms and the source term in the momentum equations. These two solutions enable to obtain an intermediate velocity field.

-The third step is provided for computing the water depth from the vertical integration of the continuity equation and the momentum equations only including the pressure-continuity terms (all the other terms have already been taken into account in the earlier two steps). The resulting two-dimensional equations (analogous to the Shallow Water equations without diffusion, advection and source terms) are written as:

$$\frac{\partial h}{\partial t} + \frac{\partial (uh)}{\partial x} + \frac{\partial (vh)}{\partial y} = 0 \tag{5}$$

$$\frac{\partial u}{\partial t} = -g \frac{\partial Z_s}{\partial x} \tag{6}$$

$$\frac{\partial v}{\partial t} = -g \frac{\partial Z_s}{\partial y} \tag{7}$$

The *u* and *v* in lower case denote the two-dimensional variables of the vertically integrated velocity. These two-dimensional equations are solved by the libraries in the TELEMAC-2D code and enable to obtain the vertically averaged velocity and the water depth. The water depth makes it possible to re-compute the elevations of the various mesh points and then those of the free surface. Lastly, the computation of the *U* and *V* velocities is simply achieved through a combination of the equations linking the velocities. Finally, the vertical velocity *W* is computed from the continuity equation.

**Turbulence model**

In this study, the LES closure based on the Smagorinski sub-grid scheme has been selected as the turbulence model for the horizontal directions. Smagorinski (1963)'s idea is to add to the molecular viscosity a turbulent viscosity deduced from a mixing length model. This mixing length corresponds to the size of the vortices smaller than that of the mesh size.

$$v_t = {C_s}^2 \Delta^2 \sqrt{2 D_{ij} D_{ij}} \tag{8}$$

where $C_s$ is a dimensionless coefficient to be calibrated and $\Delta$ is the mesh size derived in 2D or 3D from the surface or from the volume of the element. The value of $C_s$ is set to 0.1 for canal condition.

A mixing-length model is used as a turbulence model for the vertical direction. This model, proposed by Prandtl (1925) gives the value of the viscosity coefficient as:

$$v_t = {L_m}^2 \sqrt{2 D_{ij} D_{ij}} \tag{9}$$

where $D_{ij}$ is the strain rate tensor of average motion, with:

$$D_{ij} = \frac{1}{2}\left(\frac{\partial \overline{U_i}}{\partial x_j} + \frac{\partial \overline{U_j}}{\partial x_i}\right) \tag{10}$$

$L_m$ is the "mixing length" parameter equal to *kz* at a distance *z* from the bottom, and *k*=0.41 (von Karman constant).

It is expected that the seabed boundary and the structure wall will influence the results. In particularly, the important parameters are the shear velocity, defined by $\tau = -\rho(U^*)^2$ and the dimensionless distance to the wall $y^+ = \frac{yU^*}{v}$, where $y$ is the distance to the wall. $z^+$ is defined as $z^+ = \frac{zU^*}{v}$ at the bottom. In this study, the mean value of $y^+$ is 240 and of $z^+$ is 130, which stats that boundary condition are in the logarithmic range. In this condition, the turbulent viscosity is then written as $v_t = kU^*y$. The velocity profile takes the following form:

For hydraulically smooth flow:

$$\frac{U}{U^*} = \frac{1}{k} ln\left(\frac{yU^*}{v}\right) + 0.52 \tag{11}$$

For hydraulically rough flow:

$$\frac{U}{U^*} = \frac{1}{k} ln\left(\frac{33y}{k_s}\right) = \frac{1}{k} ln\left(\frac{y}{k_s}\right) + 0.85 \quad (12)$$

where $k$ is the von Karman constant and $k_s$ is the roughness size.

## MODEL VALIDATION

TELEMAC3D is widely used by the coastal engineering community. Accurately modeling turbulence with these coastal models is often proven to be challenging. Therefore the accuracy of the coastal model in the simulation of such complex flow condition is always one of the main users' focuses. In order to obtain reasonable results from simulations, numerical model is validated against laboratory experiment, involving steady flow around a circular cylinder as described in Roulund et al. (2005).

Following the experimental setup in Roulund et al. (2005), the simulation domain as shown in Figure 1 is set to be 50 m long by 4 m wide. The bed is assumed to be flat with a constant depth of 0.54 m. A cylinder with diameter of 0.53 m is placed at 13 m downstream of the inlet. The 3D mesh of the simulation domain contains 282,740 elements in 2D and has 20 unevenly distributed horizontal layers.

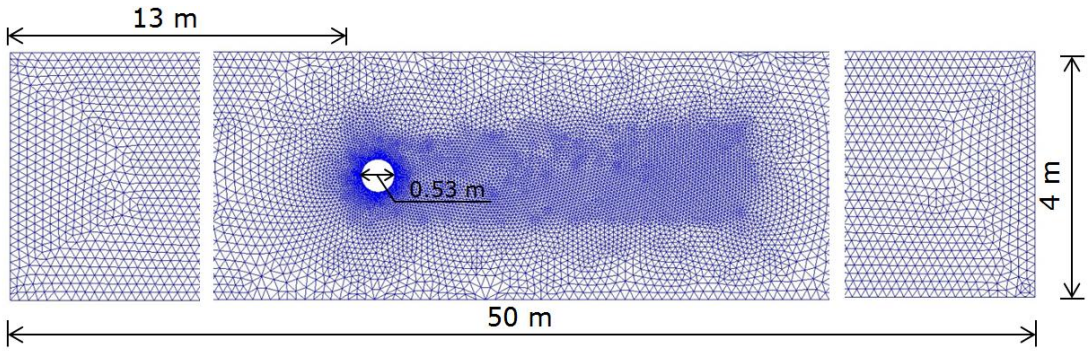


**Figure 1. Geometry of the computed domain.**

Two conditions from the experiment are used to test the model, one for a smooth bed and another one for a rough bed. In both cases, the simulations are carried out at Re=1.7×10$^5$, with inlet velocity U = 0.326 m/s. The time step of 0.01 s is chosen to keep the maximum Courant number below 0.8.

In order to compare the measured mean flow velocities obtained in the experiment, the computed instantaneous velocities are averaged over 10,000 time steps after the initial settle down period in the numerical model.

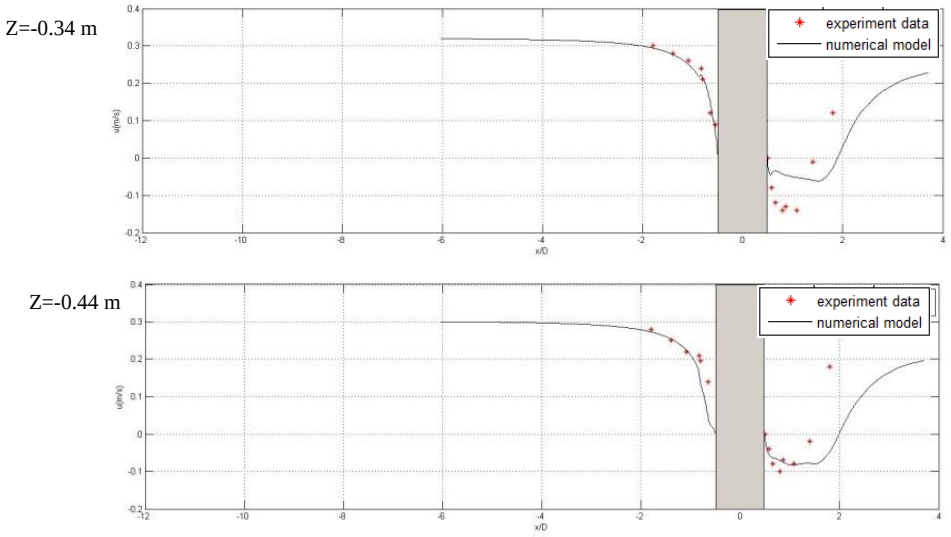

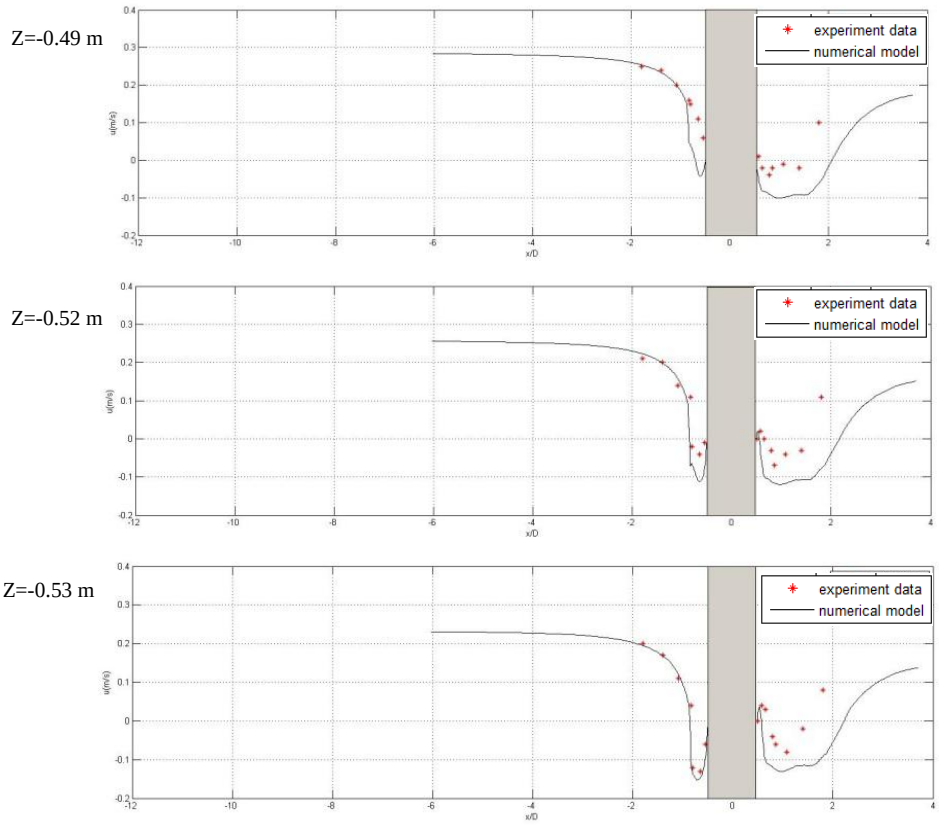


**Figure 2. Mean horizontal velocity in the streamwise plane of symmetry at different distances from the bed using a smooth rigid bed condition**

Figure 2 compares the computed mean horizontal velocity distributions with experimental data at different layers for the smooth bed condition. Overall, the velocity profile in front of cylinder shows a better agreement in comparison with the experimental data. Small deviations can be observed in the area which is close to the structure. At the layer Z=-0.44 m, the flow velocity decreases slightly faster than for the experimental data. At the layer Z=-0.49 m, the minimum flow speed in the experiment is around 0 m/s. However in the numerical model, velocities reduce to negative values first and then recover to 0 m/s at the wall of the cylinder. At the layers Z= -0.52 m and -0.53 m, negative velocities are both found in numerical model and experimental data. In the wake part, at the layer Z= -0.34 m the minimum flow velocity of the numerical model does not reach to the peak observed in the experimental data. At the layer Z= -0.44 m the minimum flow velocity of numerical model is close to the peak of experimental data but a small difference can still be found. At the layers Z= -0.49 m, -0.52 m and -0.53 m, the minimum flow velocity of the numerical model is over- predicted. Although in the wake part the length of the wake is over-estimated, the tendency of the flow recovery behind the structure still shows a reasonable agreement. At the layer Z = = -0.34 m, -0.44 m and -0.49 m, both numerical model and experimental data show a down and up trend. At the layer Z = -0.52 m and 0.53 m, experimental data shows a significant feature that flow velocity slightly increases before reducing to negative values, then recovers to outlet speed, which is represented by the numerical model.

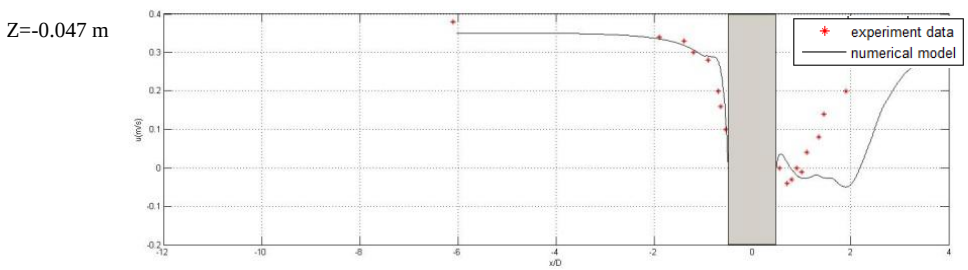

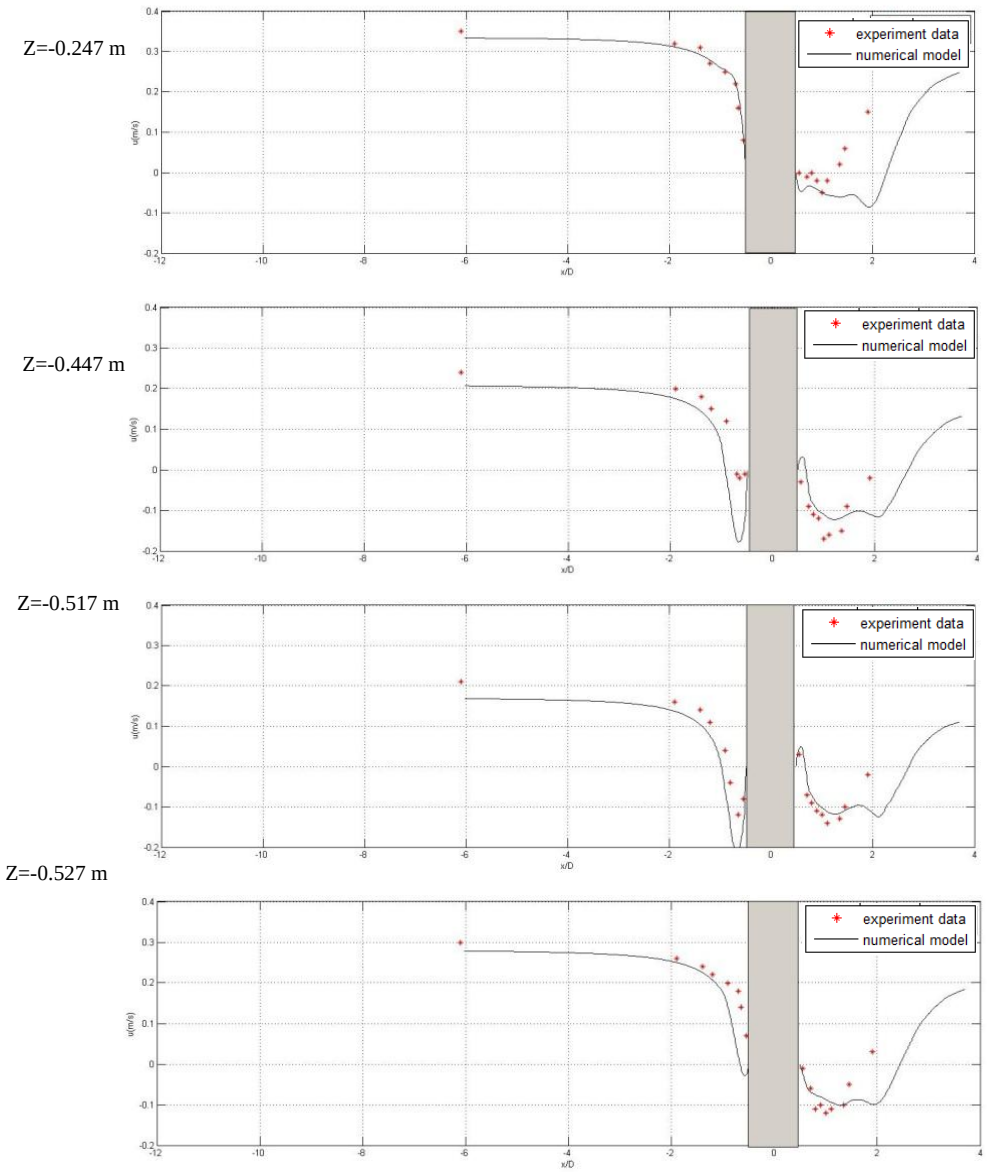


**Figure 3. Mean horizontal velocity in the plane of symmetry at different distances from the bed using a rough rigid bed condition**

Similarly, Figure 3 shows the mean horizontal velocity distributions obtained for a rough bed test using the same mesh as for the previous case. The velocity profile in front of the cylinder shows a good agreement with the experimental data, which is also observed for the smooth bed test case. However in layers Z = -0.517 m and -0.527 m, the measured velocities are slightly under-estimated by the numerical model. In the wake part, the minimum mean velocities are closed to the peak of the experimental data, but the wake length is clearly over-predicted. In the numerical models, it takes longer for the flow to recover to the flow. The difference in wake length between numerical model and experimental data reduces from the surface layer to the bottom layer and a much closer agreement can be found at Z = -0.527m level.

## MODEL APPLICATION

The model is then used for far field simulations at Liverpool Bay, Eastern Irish Sea where three OWFs exist, namely Burbo Bank, North Hoyle and Rhyl Flats, consisting of 25, 30 and 25 monopile turbines respectively. The fine mesh is shown in Figure 4 where the details of the grid around the structures have been highlighted. The mesh contains 323,830 elements in 2D and has 15 horizontal layers. The cell size varies from 0.4 m on cylinder walls to 5500 m at the open boundary. The monopile

has a typical diameter of 4-5m. The average distance between each turbine structure is about 350 m to 540 m.

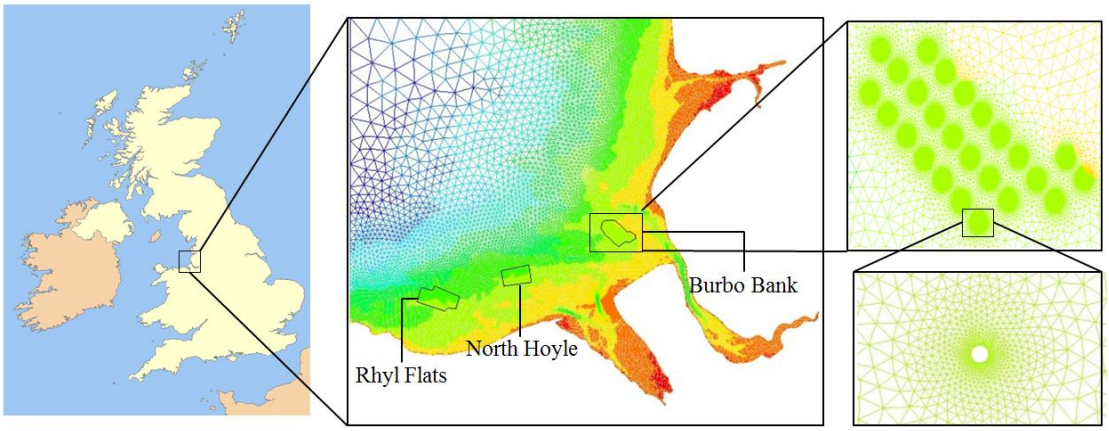


**Figure 4. Mesh of Liverpool Bay**

Boundary conditions used include offshore open boundary with the tidal water level or riverine discharge specified and solid wall shoreline boundaries. The model is driven by scaled representative tides calculated by the Tidal Model Driver (Egbert & Erofeeva, 2002) for 7 tidal constituents (M2, S2, N2, K2, P1, O1, K2). Riverine discharge is also included as a model input with annual mean flow rate specified at the boundaries of the Dee, Mersey, Douglas and Ribble estuaries as 33.70m3/s, 37.22 m3/s, 4.16 m3/s, 33.04 m3/s respectively. Bottom friction is calculated by the Chézy formula with a Chézy coefficient of 24. Sediment transport is modeled with the Meyer-Peter bed load transport formula with a single sediment size class of diameter 0.23mm, and the morphology is updated with the Exner equation.

## Results

Both the hydrodynamics and morphological impacts of OWF are investigated by numerical simulations. For the hydrodynamics study, the model is run over a full spring-neap tidal cycle (over 30 days) to catch the peak flow. For the morphological study, TELEMAC3D is coupled with SISYPHE the sediment transport module and run for less than 7 days due to time step limitation.

Figure 5 shows the computed depth averaged velocity around OWF during a peak flow spring tide. Remarkable decrease in the depth averaged velocity can be found in the wake of each monopile foundation. At spring tide, the wake tail behind certain structures at Burbo Bank is over 200 meters long. However this distance is still shorter than the average distance between each cylinder. Consequently, it is difficult to see the flow interaction between adjacent piles.

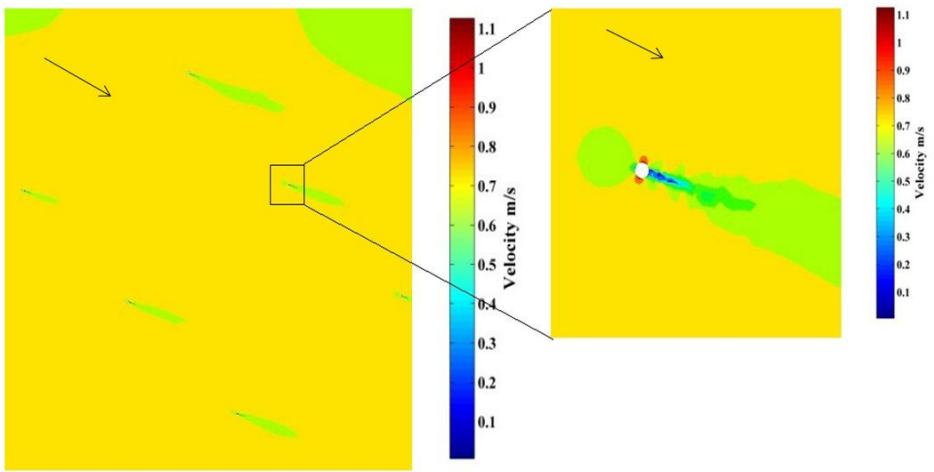


**Figure 5. Depth averaged velocity over part of the Burbo Bank OWF (highlighted) obtained from a 3-D model simulation**

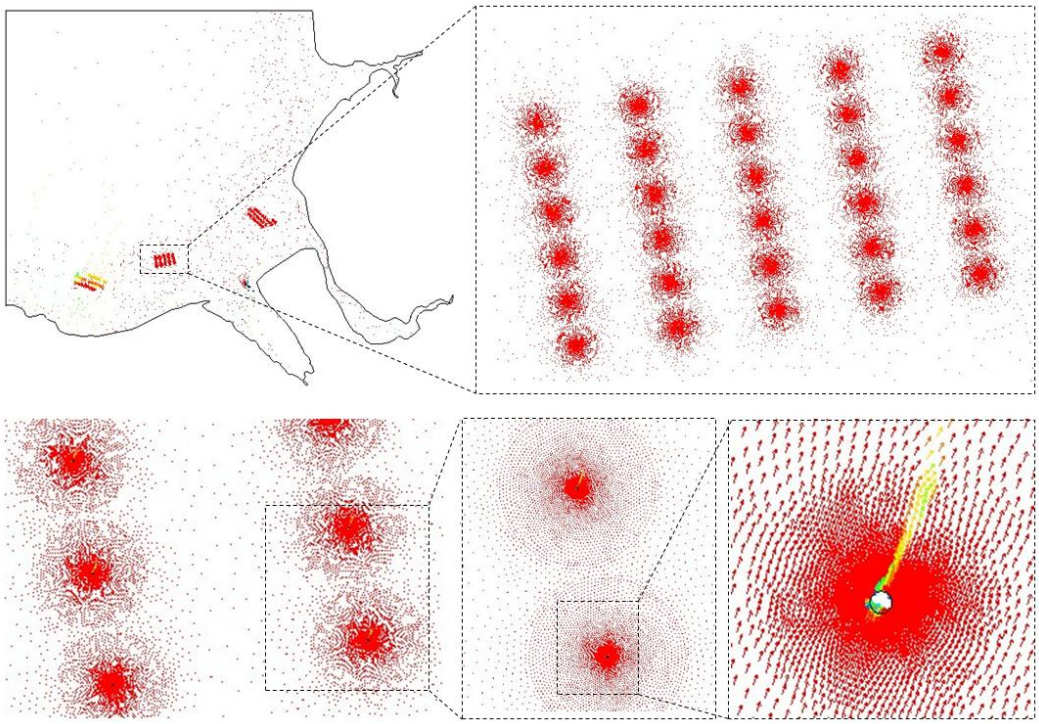

**Figure 6. Flow profile displayed by "Arrows" style**

Figure 6 presents the distribution of flow vectors in the whole test domain. The flow pattern is represented by "arrow" style, in which the length and color of arrows represent the magnitude of the flow velocity and the direction of arrows is consistent with flow direction. As can be observed in this figure, the interaction between adjacent pile wakes is weak. The flow impact of the whole wind turbine farm cannot be represented so far.

Due to the element-size dependence of the LES turbulence closure, the model is tested with two different meshes. Figure 7 compares the flow pattern for different mesh at the same time period and the difference can be clearly seen. Figure 7(a) is the result for the mesh of 323,830 elements and Figure 7(b) is that for the mesh of 1,295,230 elements. The mesh in Figure 7 (b) is refined from previous mesh by mesh multiplication. Although noticeable wake tail behind piles can be found in both results, the length of the wake for the refined mesh is much longer than the one for the initial mesh. Flow interaction between two piles can be found in Figure 7(b).

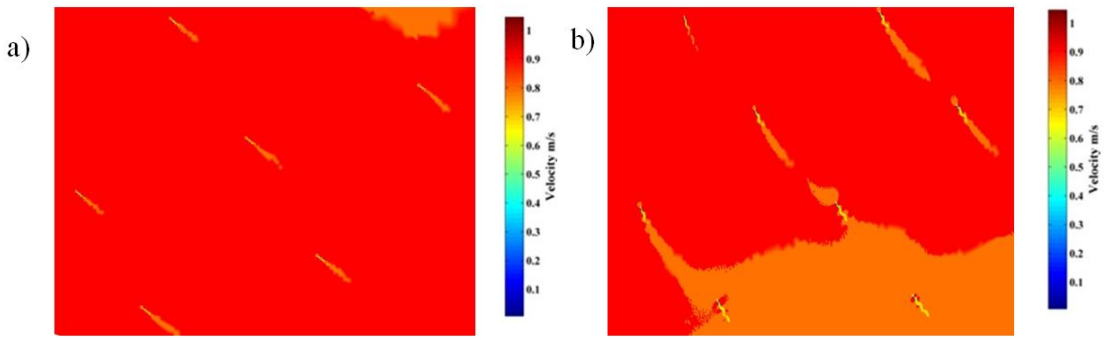


**Figure 7. Depth averaged velocity over part of the Burbo Bank wind farm with different size of mesh. a) 323,830 2D elements; b) 1,295,320 2D elements**

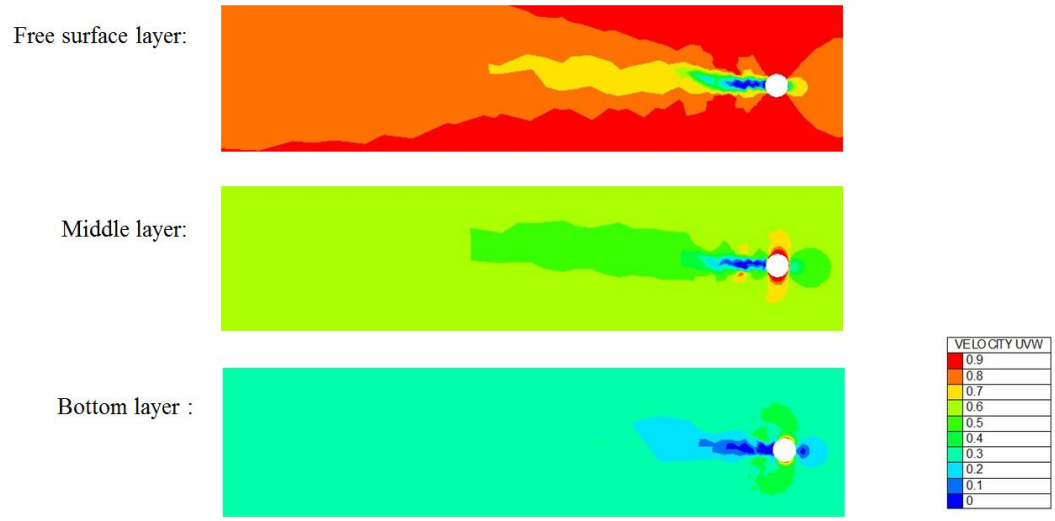


**Figure 8. Velocity distribution at one monopile turbine at the North Hoyle wind farm for the 3-D model simulation at different layers**

Figure 8 shows the distribution of the magnitude of the instantaneous velocity around a turbine at free surface layer, middle layer and bottom layer separately. In all three layers, similar flow patterns can be found with a decrease in velocity in the wake of the pile and flow acceleration at the side of the pile. However it is obvious that the wake illustrated in the free surface layer is much longer than the wake in the bottom layer. The wake in the middle layer is twice as long as for the bottom layer wake. With the increase of water depth, velocity accelerations at both sides of the pile play more significantly roles in hydrodynamics.

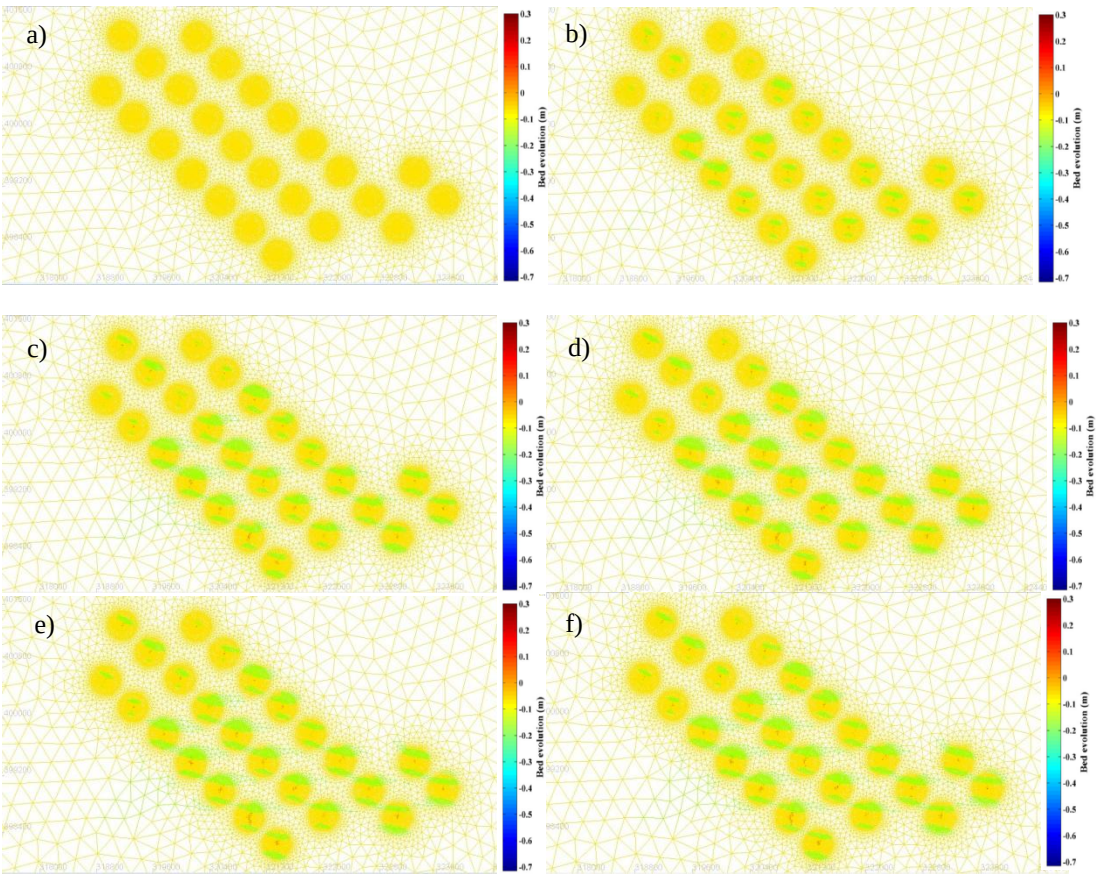


**Figure 9. Bed evolution around OWF of Burbo Bank**

In Figure 9, the computed bed evolution is presented around the OWF of Burbo Bank over a 5 days period. Figure 9(a) shows the initial state of the seabed and the following figures illustrate the seabed evolution for each day. Comparing the six figures, scour on the seabed develops rapidly in the first three days and then begin to remain stable. Marked scour area can be found in both sides of each monopole turbine which is parallel to the flow direction. However the areas of deposition cannot be observed, which suggests that the sediment being eroded from the structure site and subsequently transported away from the site leads to the net erosion at the OWF.

## CONCLUSIONS

In this study, TELEMAC3D is used to simulate the flow around a circular cylinder at laboratory scale and model both hydrodynamics and morphological impact of OWF at large scale. At laboratory scale, LES gives a reasonable agreement with the experimental data for a flow around a cylinder. Although TELEMAC3D cannot reach the same accuracy as a CFD solver would, it can still catch and represent the flow's key features. For most engineering propose, the accuracy of TELEMAC3D is acceptable.

At the prototype scale, the model is tested at the OWF at Liverpool Bay in which the OWF foundation structures are represented by the mesh directly with high resolution around each individual structure. The initial model test suggests the tidal flow has complex 3D structures across the depth and the weak behind the individual turbine foundation is clearly seen in the results. However the interaction between adjacent pile wakes is not obvious, but can be found in very high resolution configurations.

## ACKNOWLEDGMENTS

The current study is supported by EPSRC and EDF Energy through an iCASE studentship. The technical supports from Computing Services of the University of Liverpool and from the Hartree Centre are also greatly appreciated.

## REFERENCES

Christie E., M. Li, C. Moulinec. 2012. Comparison of 2d and 3d large scale morphological modeling of offshore wind farms using HPC. *International Conference on Coastal Engineering 2012 Proceedings.* World Scientifics, Santander pp sediment.42

Hervouet J-M. 2007. Hydrodynamics of free surface flows: modelling with the finite element method, *Wiley*

The TELEMAC system. <http://www.opentelemac.org>

Roulund, A., B.M. Sumer, J. Fredsøe, J. Michelsen. 2005. Numerical and experimental investigation of flow and scour around a circular pile. *Journal of Fluid Mechanics*, 534, pp. 351-401

Smagorinski, J. 1963 General circulation experiments with the primitive equations. I. The basic experiment. Monthly Weather Review, 91,99-164

Prandtl, L., 1925. Über die ausgebidete Turbulenz. Zeitschrift für augewandte Mathematik und Mechanik. 5, pp. 136-139

# In-depth HPC-LES investigation for the flow around a circular cylinder using TELEMAC3D

Mr Yue Yin, PhD student
School of Engineering,
University of Liverpool
Liverpool, UK
yue.yin@stfc.ac.uk

Dr Ming Li,
School of Engineering,
University of Liverpool
Liverpool,UK
Mingli@liverpool.ac.uk

Dr Charles Moulinec,
Scientific Computing Department,
STFC Daresbury Laboratory,
Warrington, UK
charles.moulinec@stfc.ac.uk

Professor David R. Emerson,
Scientific Computing Department,
STFC Daresbury Laboratory,
Warrington, UK
david.emerson@stfc.ac.uk

***Abstract*—Flow around a circular cylinder in laboratory scale is simulated by coastal model TELEMAC3D. The aim of this paper is to investigate the performance and accuracy of TELEMAC3D, hydrostatic mode, at laboratory scale. The model is tested on both smooth bed and rough bed conditions. The turbulence characteristics are modelled using Large Eddy Simulation and the Smagorinsky sub-grid scale model. The model results, including velocity profiles and the Strouhal number are compared with experimental data. Three different mesh sizes are used in these tests. According to the comparison, the finest mesh gives a better agreement of the model exhibiting the right trend in the wake part, comparing to the experimental data.**

## I. INTRODUTION

With the repaid expansion of offshore wind farm industry, it has become important to the coastal engineers to be able to predict the impact of array of monopiles on offshore waves, tides and sediment transport. Traditionally, due to the small diameter of the single monopile (~5-10m) comparing with the mesh size in the coastal engineering model (~100m), these cylinder-like structures are treated as sub-grid features and represented simply as enhanced roughness. In recent years, benefiting from the increase of computing power, access to High End machines and flexible mesh system, the computational resolution in these coastal models has demonstrated that it is able to account for the cylinders, which means that is it possible to represent the offshore turbine foundations directly. The present study therefore aims at exploring the potential of an existing coastal model system, TELEMAC3D to simulate the flow around a single cylinder with various settings, in its hydrostatic mode.

In the last decade, many successful studies have been carried out using CFD models to simulate flow around cylinders at laboratory scale. Roulund et al. [1], for instance numerically simulated a flow around a circular pile at laboratory scale, using EllipSys3d. Their results were fairly good in comparison to experimental data. However application of coastal and ocean models at laboratory scale is still limited. Apart from the difficulty of resolving hydrodynamics around structures, accurately modeling turbulence with these coastal models is also often proven to be questionable. Therefore the accuracy of the coastal model in the simulation of such complex flow condition is always one of the main users' focuses.

TELEMAC [2, 3], as an efficient hydrodynamics suite, has been widely used in coastal engineering community. In the author's previous work to be published in [4], the flow around offshore wind farms was simulated using TELEMAC3D with the Large-Eddy Simulation (LES) closure. The results suggest that TELEMAC3D is capable of reproducing complex flow reasonably well with high grid resolution around the individual structure. However due to a lack of experimental data in the test domain, the accuracy of the numerical model is questionable.

The main objective of the present work therefore is to use TELEMAC3D to simulate the flow around a circular cylinder at laboratory scale and, to examine potential factors that might influence the results. In this work, sensitivity simulations are performed using several 2-D horizontal mesh sizes and number of vertical layers. The model is tested in both smooth and rough bed conditions and turbulence is modeled by the LES closure. In the end the numerical results are benchmarked with the experiment made by Roulund et al. [1].

## II. NUMERICAL METHOD

### A. *Governing equations*

An open source, TELEMAC3D, was used to simulate the flow around a circular cylinder. TELEMAC3D is a three-dimensional computational code describing the 3D velocity field (u, v, w) and the water depth h (and, from the bottom depth, the free surface S) at each time step. In this work the hydrostatic approximation is used at laboratory scale, as it is going be used later at field scale, because the simulations would be too computationally demanding otherwise.

### B. Turbulence models

In this study, the LES closure with Smagorinsky sub-grid scheme has been selected as the turbulence model for the horizontal directions. Smagorinski [5]'s idea is to add to the molecular viscosity a turbulent viscosity deduced from a mixing length model. This mixing length corresponds to the size of the vortices smaller than that of the mesh size.

$$v_t = {C_s}^2 \Delta^2 \sqrt{2D_{ij}D_{ij}} \quad (1)$$

where $C_s$ is a dimensionless coefficient to be calibrated and $\Delta$ is the mesh size derived in 2D or 3D from the surface or from the volume of the element. The values of $C_s$ is set to 0.1 for canal condition.

A mixing-length model is used as the turbulence model for the vertical direction. This model, proposed by [6] gives the value of the viscosity coefficient as:

$$v_t = {L_m}^2 \sqrt{2D_{ij}D_{ij}} \quad (2)$$

where $D_{ij}$ is the strain rate tensor of average motion, with:

$$D_{ij} = \frac{1}{2}\left(\frac{\partial \overline{U_i}}{\partial x_j} + \frac{\partial \overline{U_j}}{\partial x_i}\right) \quad (3)$$

$L_m$ is the "mixing length" parameter equal to $kz$ at a distance $z$ from the wall, and k=0.41 (von Karman constant), till the size of eddies is no longer influenced by the bottom and remains constant.

The velocity profile can be influenced by the boundary layer which is above the bottom or in the vicinity of walls. The important parameters are the shear velocity, defined by $\tau = -\rho(U^*)^2$ and the dimensionless distance to the wall or bottom $y^+ = \frac{yU^*}{v}$, where $y$ is the distance to the wall or bottom. In this study, the average $y^+$ on the bottom and wall are 130 and 240 respectively, which stats that boundary layers are in the logarithmic range. In this condition, the turbulent viscosity is then written as $v_t = kU^*y$ . The velocity profile takes the following form:

For hydraulically smooth flow:

$$\frac{U}{U^*} = \frac{1}{k}\ln\left(\frac{yU^*}{v}\right) + 0.52 \quad (4)$$

For hydraulically rough flow:

$$\frac{U}{U^*} = \frac{1}{k}\ln\left(\frac{33y}{k_s}\right) = \frac{1}{k}\ln\left(\frac{y}{k_s}\right) + 0.85 \quad (5)$$

where $k$ =0.41 (von Karman constant) and $k_s$ is the roughness size.

### C. Boundary conditions

The boundaries of the computational domain include inlet, outlet and walls.

*1) Inlet:* At the inlet, flow rate Q was specified. The value of Q was calculated by the horizontal velocity, which following similar flow settings in the Roulund's experiment.

*2) Outlet:* At the outlet, prescribed elevations was given.

*3) Walls:* The walls of flume and pile were set as solid wall. Sidewall friction was not applied in this study, therefore all walls are smooth. For bottom, both smooth bed and rough bed conditions are considered.

### D. Computational mesh

The computational mesh was generated by software Bluekenue. Following the experimental setup in Roulund et a. [1], the simulation domain as shown in Figure 1 is set to be 50 m long by 4 m wide. The bed is assumed to be flat with a constant depth of 0.54 m. A cylinder with diameter of 0.53 m is placed at 13 m downstream of the inlet. An initial mesh, called *mesh1* is generated using 47,546 triangle elements in the 2-D horizontal plane and 20 non-equally distributed vertical layers across the water depth. Subsequently, *mesh2* and *mesh3* are obtained by refining mesh1 up to 91,628 elements and 282,740 elements separately in 2-D by mesh multiplication.

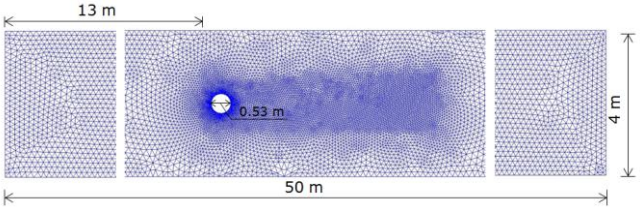


Figure 1. Geometry of the computed domain

### E. Model setup

Two conditions from the experiment in [1] are used for the model testing, one for a smooth bed and the other for a rough bed. In both cases, the simulations are carried out at Re=$1.7\times10^5$, with inlet velocity U = 0.326 m/s. The time step of 0.01 s is chosen to keep the maximum Courant number below 0.8. The Courant number is defined as (4)

$$C = U\frac{\Delta t}{\Delta x} \quad (4)$$

where U is the depth-mean flow velocity and Δx is the smallest mesh size.

In rough bed simulations, the bottom friction was modelled by Nikuradse law and the friction coefficient $k_s$ is set to 0.01.

## III. MODEL RESULTS

To test the model's sensitivity to the mesh resolution, computations have been performed with three different size meshes, i.e. *mesh1* has 47,546 2-D triangular elements, *mesh2* 91,628 2-D triangular elements and *mesh3* 282,740 2-D triangular elements. All three meshes deal with 20 horizontal layers unevenly distributed.

### A. Mean velocity analysis (smooth bed)

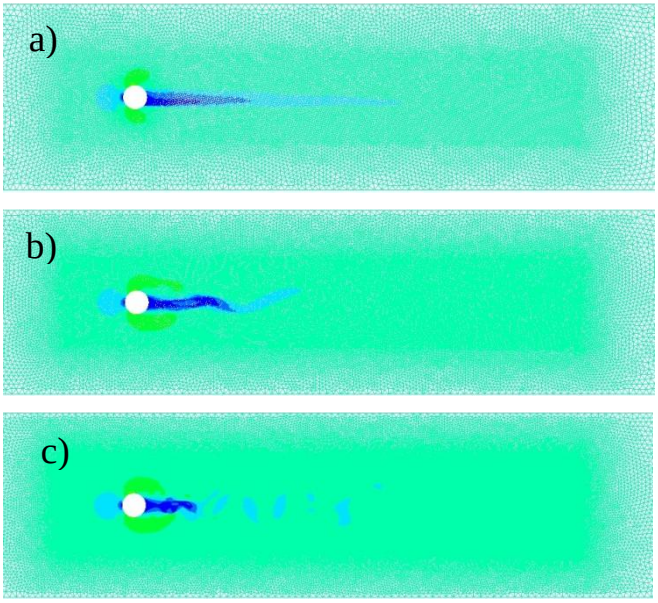


Figure 2. Instantaneous velocity field around a circular pile in a flume (smooth bed test). a) *mesh1*, b) *mesh2*, c) *mesh3*

The images in Figure 2 illustrate the instantaneous velocity distribution around a circular pile for the smooth bed test using three different meshes. In all three test cases, similar flow patterns can be found with a decrease in velocity in the wake of the pile and flow acceleration at the side of the pile. However it is obvious that the wake obtained by *mesh1* is much longer than the wake in *mesh3*. The wake in *mesh2* is about half of *mesh3* wake length. The vortex shedding is clearly noticeable in both *mesh2* and *mesh3* results, although the vortex size seems much smaller in *mesh3*.

In order to get details of the mean flow, the instantaneous velocities are averaged over 10,000 time steps after ensuring flow development.

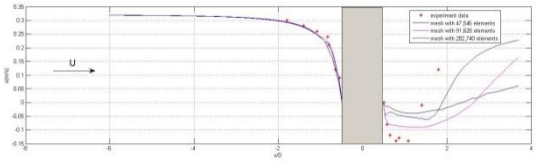

Figure 3. Mean horizontal velocity component obtained by LES using different mesh size (smooth bed test)

Figure 3 compares the mean horizontal velocity profiles over the central cross section with different mesh sizes for the smooth bed test. The red dots denote the experimental data obtained by Roulound et al. [1]. Black, red and blue curve represent the numerical results obtained from *mesh1*, *mesh2* and *mesh3* respectively. It is clear that, the three computed velocity profiles in front of the circular cylinder show a very good agreement with experimental data. Flow speed reduced from 0.36 m/s at inlet boundary to 0 m/s at the cylinder wall. However, in the wake area behind the structure the 3 cases clearly deviate from each other. Although the three results all show flow recovery, the length of the recovery is very different.

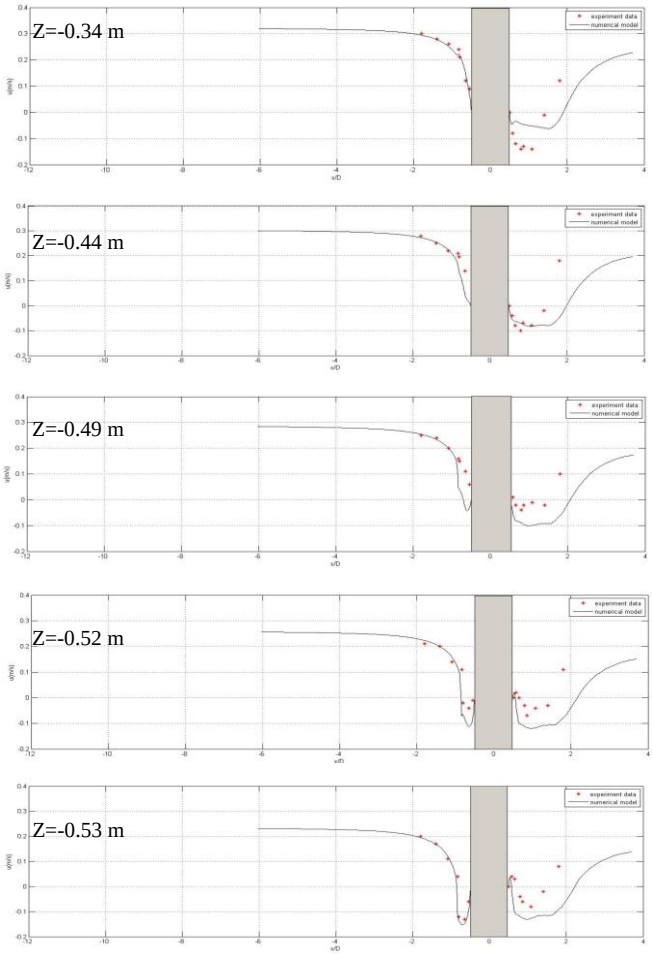


Figure 4. Mean horizontal velocity in the plane of symmetry at different distances from the bed. Smooth rigid bed with *mesh3*

Figure 4 compares the computed mean horizontal velocity distributions with experimental data for different layers for *mesh3* case for the smooth bed condition. Generally, the velocity profile in front of cylinder shows a good agreement in comparison with the experimental data. Small deviations can be found in the area which is close to the structure. At the layer Z=-0.44 m, the flow velocity decreases slightly faster than for the experimental data. At the layer Z=-0.49 m , the minimum flow speed in experiment is around 0 m/s, however in the numerical models, velocities reduce to negative values first and then recover to 0 m/s at the wall of the cylinder. At the layers Z= -0.52 m and -0.53 m, negative velocities are both found in numerical and experimental data. In the wake part, at the layer Z= -0.34 m the minimum flow velocity of numerical model doesn't reach to the peak of experimental data. At the layer Z= -0.44 m the minimum flow velocity of numerical model is close to the peak of experimental data but small difference can still be found. At the layers Z= -0.49 m, -0.52 m and -0.53 m, the minimum flow velocity of the numerical model is over-predicted. Although in the wake part the length the of wake is over-estimated, the tendency of the flow recovery behind the structure still shows a reasonable agreement. At the layer Z =

= -0.34 m, -0.44 m and -0.49 m, both numerical model and experimental data show a down and up trend. At the layer Z = -0.52 m and 0.53 m, experimental data shows a significant feature that flow velocity slightly increases before reducing to negative values, then recover to outlet speed, which is represented by numerical model.

The type and size of elements used for *mesh3* are definitely required to get a good description of the flow and even using TELEMAC3D in hydrostatic mode shows very good results in this case compared to the experiment.

### B. *Mean velocity analysis (rough bed)*

An analysis is now conducted when a rough bed is used.

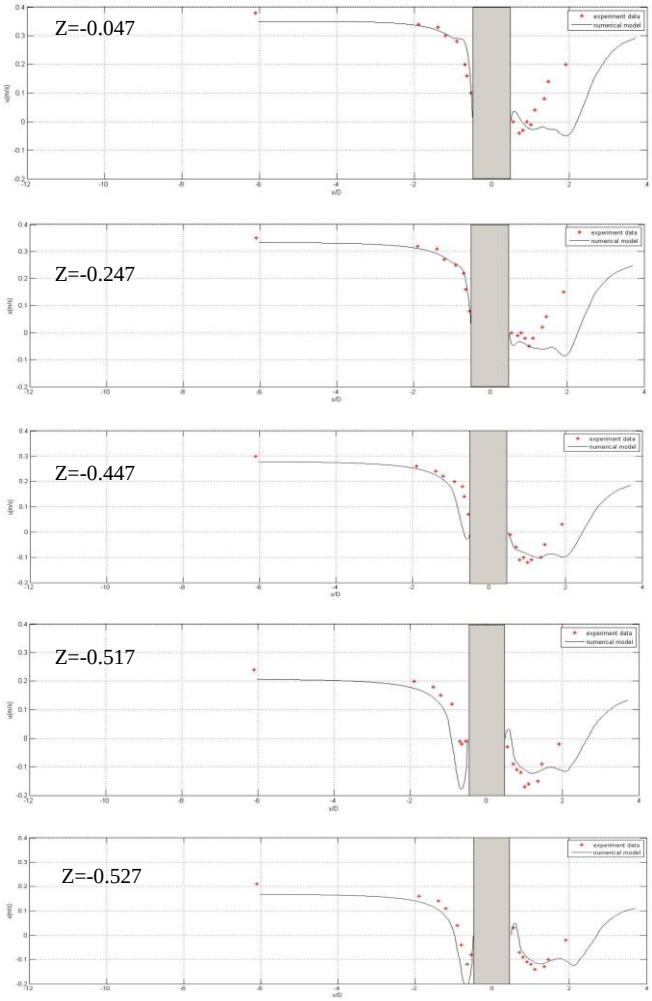


Figure 5. Mean horizontal velocity in the plane of symmetry at different distances from the bed. Rough rigid bed with *mesh3*

Figure 5 shows mean horizontal velocity distributions obtained for a rough bed test using *mesh3* 2-D triangular element distribution with several vertical layer distributions. The mean velocity profile in front of the cylinder shows a good agreement with the experimental data, which is also observed for the smooth bed test case. However in layers Z = -0.517 m and -0.527 m, the mean velocities are slightly under-estimated by numerical model. In the wake part, the minimum mean velocities are close to the peak of the experimental data, but the wake length is still over-predicted. In the numerical models, it takes longer for the flow to recover to the previous flow. The difference in wake length between numerical model and experimental data reduces from the surface layer to the bottom layer and a much closer agreement can be found between the model prediction and laboratory data.

### C. *Strouhal number (smooth bed)*

As the flow is oscillatory, it is also crucial to know if its period is well predicted by TELEMAC3D.

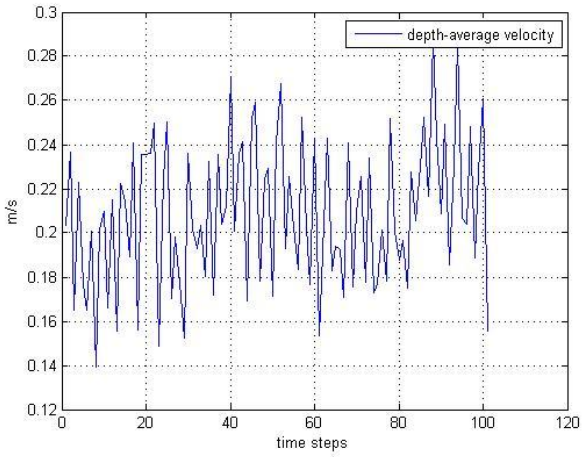


Figure 6. Time evolutions of the instantaneous depth-averaged velocity at point A ($x$=2, $y$=0.5D), obtained by smooth bed test with *mesh3*

Figure 6 represents the time evolutions of the instantaneous depth-averaged velocity at point A, which is located at (2.0, 0.5D). Strong fluctuating velocities can be found in the test with mesh3.

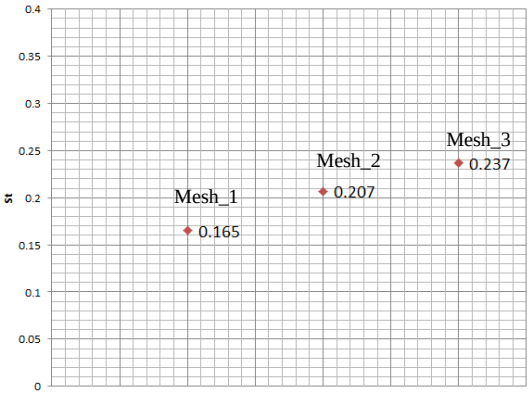


Figure 7. Strouhal number with different mesh size, obtained by smooth bed test

Figure 7 compares the Strouhal number (*St*) for the three different mesh sizes based on the smooth bed tests. The Strouhal number (*St*) represents a normalised value of

shedding frequency (see 5), where $f$ is the shedding frequency in Hz, $D$ is hydraulic diameter and $U$ is the depth-mean flow velocity.

$$St = \frac{fD}{U} \quad (5)$$

In this study, time step is set to 0.01 s and print-out period is set to 100 time steps. Therefore, $\pm 1$ Hz is taken into consideration when calculating the shedding frequency.

Comparisons for the Strouhal number were not available for the exact same flow as aforementioned. However, Stringer et al. [7] compared the Strouhal number at different Reynolds numbers ranking from 40 to $10^6$ for the flow around an infinite cylinder (different from the current configuration which is similar to a flow around a cantilever). According to their study, *St* should be of the order of 0.25 at Re $=1.8\times10^5$. The Strouhal number in the current study varies from 0.165 to 0.237 for the largest mesh. In consideration of numerical error, the finest mesh shows a good agreement oofvortex shedding frequency and Richardson extrapolation would exhibit a Strouhal number of about 0.29, which is close to what Stringer et al. observed.

## IV. CONCLUSIONS - PERSPECTIVES

In this study, TELEMAC3D is used to simulate the flow around a circular cylinder in laboratory scale using the hydrostatic approach. Running ocean model at such a small scale is challenging. In this particular test case, it is found that the TELEMAC3D can be used in laboratory scale simulations. It performs well when simulating steady flows, such as the flow at the front of the structure. In complex flow conditions, although TELEMAC3D cannot reach the same accuracy as CFD solver does, it can still catch and represent the flow's key features. Vortex shedding frequency can be simulated properly by very fine mesh.

The turbulence coefficient of LES closure in TELEMAC3D is linked to the area of each triangle cell. Therefore mesh size of model domain affects the accuracy of simulations. According to the comparison, it is clear that the finest mesh gives a better agreement of the model with experiment data. Mesh size does affect the numerical error in simulations, but it does not affect the whole velocity trend. In consideration that TELEMAC3D is normally used in engineering applications, the accuracy of this model is more than acceptable.

This work gives us experience and confidence to build good meshes for offshore wind farms, with extra refinement in the mean direction of the flow, both before and past each of the monopiles.

## ACKNOWLEDGEMENTS

The current study is supported by EPSRC and EDF Energy through an iCASE studentship. The technical supports from Computing Services of the University of Liverpool and from the Hartree Centre are also greatly appreciated.

## REFERENCES

[1] Roulund, A., Sumer, B.M., Fredsøe, J., Michelsen, J. "Numerical and experimental investigation of flow and scour around a circular pile," Journal of Fluid Mechanics, 534, 2005, pp. 351-401

[2] Hervouet J-M. "Hydrodynamics of free surface flows: modelling with the finite element method", Wiley, 2007

[3] The TELEMAC system. <http://www.opentelemac.org>.

[4] Yin, Y., Li, M., & Moulinec, C., Emerson, D. R., "3D modelling morphological impact of Offshore Wind Farms using LES model in HPC", submitted to ICCE 2014.

[5] Smagorinski, J., "General circulation experiments with the primitive equations". I. The basic experiment. Monthly Weather Review, 91,99-164.

[6] Prandtl, L., 1925. Über die ausgebidete Turbulenz. Zeitschrift für augewandte Mathematik und Mechanik. 5, pp. 136-139

[7] Stringer, R.M., Zang, J., Hillis, A.J., "Unsteady RANS computations of flow around a circular cylinder for a wide range of Reynolds number", Ocean Engineering, 2014, pp. 1-9

# Wall-Adapting Local Eddy-Viscosity Turbulence Model for TELEMAC3D

Yue Yin
School of Engineering,
University of Liverpool
Liverpool, UK
yue.yin@stfc.ac.uk

Ming Li
School of Engineering,
University of Liverpool
Liverpool,UK
Mingli@liverpool.ac.uk

Charles Moulinec
Science and Technology Facilities Council,
Daresbury Laboratory,
Warrington, UK
charles.moulinec@stfc.ac.uk

David R. Emerson
Science and Technology Facilities Council,
Daresbury Laboratory,
Warrington, UK
david.emerson@stfc.ac.uk

***Abstract***—TELEMAC3D offers the user several options for turbulence modelling, including Reynolds-Averaged Navier-Stokes modelling and Large Eddy Simulation based on the Smagorinsky constant model. Complex turbulent flow problems can be computed using various levels of approximation, yielding a more or less detailed description of the flow state. The aim of this work is to implement the Wall-Adapting Local Eddy-Viscosity (WALE) turbulence model from the existing TELEMAC3D code and to compare it to the Smagorinsky constant model. There are two major advantages associated with the choice of the WALE model: firstly, the invariant of the symmetric part of $\bar{S}_{ij}$ is related to both the strain rate of the turbulent structure and the rotation rate. Secondly, it offers a proper wall-scaling to get a good prediction of the friction coefficient. The aforementioned advantages will help improve the representation of the complex turbulent flow. Numerical results are benchmarked against two experiment tests including the flow around a circular cylinder test case and the flow in a U-shape bend channel.

## I. INTRODUTION

Turbulent flows are commonly encountered in engineering and are of considerable interests in a variety of industrial applications. In coastal engineering, to resolve the combined tides and waves induced by constant changes in flows around offshore structures, using a computer model is particularly important to coastal protection and development.

The 3-D module of the TELEMAC suite, i.e. TELEMAC3D [1] offers the user several options for turbulence modelling. The most widely used approximation is based on the Reynolds-averaged Navier-Stokes equations (RANS) which has one main drawback: i.e. the fact that all the scales are modelled in the same way dispite the fact that the small scales tend to depend only on the viscosity whereas the large ones are very strongly affected by the boundary conditions.

An alternative to RANS is Large Eddy Simulation (LES). It is based on the assumption that the large eddies of the flow are dependent on the geometry while the smaller scales more universal. The turbulent flow is split into large and small parts by a filtering process based on an energy cascade. The large eddies are simulated by the calculation, while the small eddies are ignored by using a sub grid-scale model. However there are two major drawbacks associated with to the choice of the Smagorinsky constant model, for instance: firstly, the invariant of the symmetric part of $\bar{S}_{ij}$ is only related to the strain rate of turbulent structure but not the rotation rate. Secondly, it does not offer a proper wall-scaling to get a good prediction of the friction coefficient.

To overcome the aforementioned drawbacks, the Wall-Adapting Local Eddy-Viscosity (WALE) turbulence model has been developed by Ducros et al. [2] and implemented in TELEMAC3D. In order to investigate the behaviour of the new turbulence model and examine potential factors which affect the results, the Smagorinsky constant and WALE models are compared with two laboratory scale cases, including the flow around a circular cylinder test case of Roulund et al [3] and the flow in a U-shape bend channel [4].

## II. NUMERICAL MODEL

### A. Governing Equations

The calculations are performed using the open source hydrodynamic suite TELEMAC and more specifically its 3-D module, TELEMAC3D. It is a three-dimensional computational code solving either the hydrostatic or non-hydrostatic equations. In this work the hydrostatic approximation is used for both the circular cylinder test case and the U-shape bend channel case. The code solves the three-dimensional mass and momentum conservation equations [5] :

$$\frac{\partial U}{\partial x}+\frac{\partial V}{\partial y}+\frac{\partial W}{\partial z}=0 \quad (1)$$

$$\frac{\partial U}{\partial t}+U\frac{\partial U}{\partial x}+V\frac{\partial U}{\partial y}+W\frac{\partial U}{\partial z}=-g\frac{\partial Z_s}{\partial x}-\frac{\partial \tau}{\partial x}+F_x \quad (2)$$

$$\frac{\partial V}{\partial t}+U\frac{\partial V}{\partial x}+V\frac{\partial V}{\partial y}+W\frac{\partial V}{\partial z}=-g\frac{\partial Z_s}{\partial y}-\frac{\partial \tau}{\partial y}+F_y \quad (3)$$

$$p=p_{atm}+\rho_0 g(Z_s-z)+\rho_0 g\int_Z^{Z_s}\frac{\Delta\rho}{\rho_0}dZ \quad (4)$$

where U, V and W are the three-dimensional components of velocity; $\tau$ is the stress tensor; $Z_s$ is the free surface elevation and $F_x$, $F_y$ are source terms. The pressure is calculated in Eq. 4 where $\rho_0$ and $\Delta\rho$ are the reference density (1024kg/m3) and the variation of density respectively. The stress tensor is computed as $\tau=-\nu\nabla U$, in which $\nu$ is the effective viscosity that needs to be computed by a turbulence model.

### B. Turbulence Models

In order to obtain a better representation of complex turbulent flows, numerical model is computed using Large Eddy Simulation employing two turbulence models including the constant Smagorinsky model [6] and the 'Wall-Adapting Local Eddy-Viscosity (WALE)' model [2].

Using the Smagorinsky model, the viscosity is computed as:

$$v_t=C_s{}^2\Delta^2\sqrt{2S_{ij}S_{ij}} \quad (5)$$

where $C_s$ is a dimensionless coefficient to be calibrated and $\Delta$ is the mesh size derived in 2-D or 3-D from the surface or from the volume of the element. The value of $C_s$ is set to 0.1 for after calibration. More details of the constants can be found in User Manual [1].

In LES, the eddy-viscosity $v_t$ must not change when the frame of reference is changed. Clearly the velocity gradient tensor $\bar{g}_{ij}=\partial\bar{u}_i/\partial x_j$ is a good choice to represent velocity fluctuations at the length scale $\Delta$. The Smagorinsky model is based on the second invariant of the symmetric part $\bar{S}_{ij}$ of this tensor. However there are two major drawbacks associated with this choice:

- This invariant is only related to the strain rate of the turbulent structure but not the rotation rate.
- It does not offer a proper wall-scaling to get a good prediction of the friction coefficient.

For the aforementioned reasons, Ducros et al. uses a better operator with the traceless symmetric part of the square of the velocity gradient tensor as follows:

$$S_{ij}^d S_{ij}^d=\frac{1}{2}\left(\bar{g}_{ij}^2+\bar{g}_{ji}^2\right)-\frac{1}{3}\delta_{ij}\bar{g}_{kk}^2 \quad (6)$$

where $\bar{g}_{ij}^2=\bar{g}_{ik}\bar{g}_{kj}$ and $\delta_{ij}$ is the Kronecker symbol. Einstein summation is used here. If $\bar{\Omega}$ is used to represent the anti-symmetric part of $\bar{g}$ :

$$\bar{\Omega}_{ij}=\frac{1}{2}\left(\frac{\partial\overline{u_i}}{\partial x_j}-\frac{\partial\overline{u_j}}{\partial x_i}\right) \quad (7)$$

the tensor $S_{ij}^d$ can be rewritten in terms of $\bar{S}$ and $\bar{\Omega}$ :

$$S_{ij}^d=\bar{S}_{ik}\bar{S}_{kj}+\bar{\Omega}_{ik}\bar{\Omega}_{kj}-\frac{1}{3}\delta_{ij}[\bar{S}_{mn}\bar{S}_{mn}-\bar{\Omega}_{mn}\bar{\Omega}_{mn}] \quad (8)$$

By construction, the trace of $S^d$ is zero and its second invariant remains finite and proportional to $S_{ij}^d S_{ij}^d$. By using the relation above and making use of the Cayley-Hamiltion theorem of linear algebra, this quantity can be developed as:

$$S_{ij}^d S_{ij}^d=\frac{1}{6}(S^2S^2+\Omega^2\Omega^2)+\frac{2}{3}S^2\Omega^2+2IV_{S\Omega} \quad (9)$$

with the notations:

$$S^2=\bar{S}_{ij}\bar{S}_{ij},\ \Omega^2=\bar{\Omega}_{ij}\bar{\Omega}_{ij},\ IV_{S\Omega}=\bar{S}_{ik}\bar{S}_{kj}\bar{\Omega}_{jl}\bar{\Omega}_{li}$$

From the last relation, a LES model based on $S_{ij}^d S_{ij}^d$ will detect turbulence structures with either strain rate, rotation strain or both. In the case of pure shear (e.g., $\bar{g}_{ij}=0$, except $\bar{g}_{12}$ ), it yields $S^2=\Omega^2=4\bar{S}_{12}$ and $IV_{S\Omega}=-\frac{1}{2}S^2S^2$, so that the considered invariant, $S_{ij}^d S_{ij}^d$, is zero. This point is in agreement with the fact that the shear zones contribute to energy dissipation to a smaller extent than convergence zones and eddies. Moreover, this means that almost no eddy viscosity would be produced in the case of wall-bounded laminar flow. Thus the amount of turbulence diffusion would be negligible in such a case and development of linearly unstable waves would be possible. This is a great advantage over the Smagorinsky model. The expression for $v_t$ is computed as:

$$v_t=\frac{\left(s_{ij}^d s_{ij}^d\right)^{3/2}}{\left(\bar{s}_{ij}\bar{s}_{ij}\right)^{3/2}+\left(s_{ij}^d s_{ij}^d\right)^{5/4}} \quad (10)$$

## III. CASE I: FLOW AROUND A CIRCULAR CYLINDER

Both the constant Smagoringsky turbulence model and the WALE model are used in the simulation of the flow around a circular cylinder and their results compared to the laboratory measurement of Roulund et al [3].

### A. Model Setup

Following Roulund et al [3], the simulation domain is set to be 50 m long by 4 m wide. The bed is assumed to be flat with a constant depth of 0.54 m. A cylinder with a diameter of 0.53 m (D) is placed at 13 m downstream the inlet as in Fig. 1. The computational mesh is generated by the software Bluekenue using 47,546 triangle elements in the 2-D horizontal plane and 20 non-equally distributed vertical layers across the water depth.

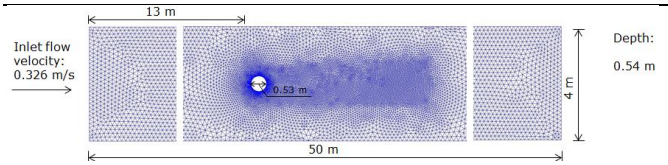


Figure 1. Model mesh layout for the validation test (top view)

The boundaries of the computational domain include inlet, outlet and walls. At the inlet, the flow rate Q is specified to 0.68 $m^3/s$ following similar flow settings in Roulund's experiment. At the outlet, prescribed elevation is given to 0 m. The walls of the flume and pile are set as solid walls. Sidewall friction is not applied in this study, therefore all the walls are smooth. The bottom friction is modelled by the Nikuradse law and the friction coefficient $k_s$ is set to 0.01.

*B. Results*

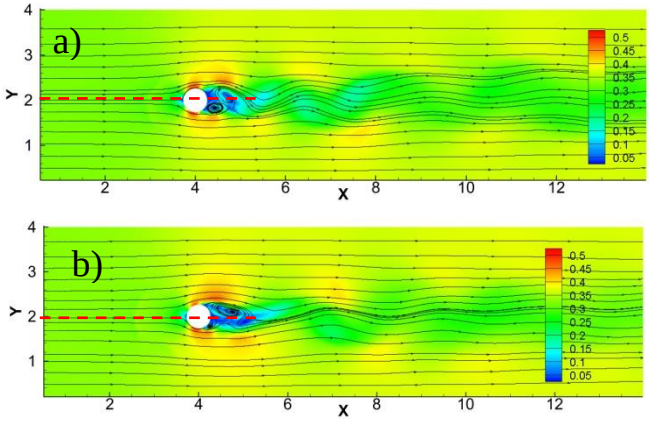


Figure 2. Instantaneous velocity field around a circular pile in a flume a) WALE model, b) LES Smagorinsky model.（01:00:00）

Figure 2 illustrates the instantaneous velocity distribution around a circular pile using the constant Smagorinsky model and the WALE model respectively. Similar flow patterns can be found with a decrease in velocity in the wake of the cylinder and flow acceleration at the side of the pile. The vortex shedding is clearly noticeable in both turbulence model results, although the vortex size in WALE model test seems smaller than it in the constant Smagorinsky model results.

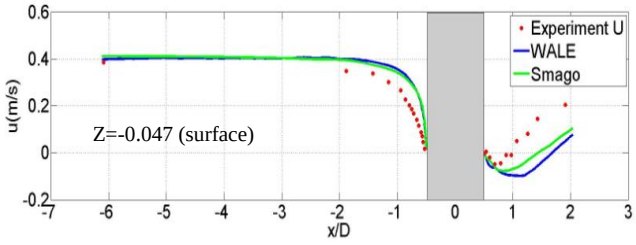


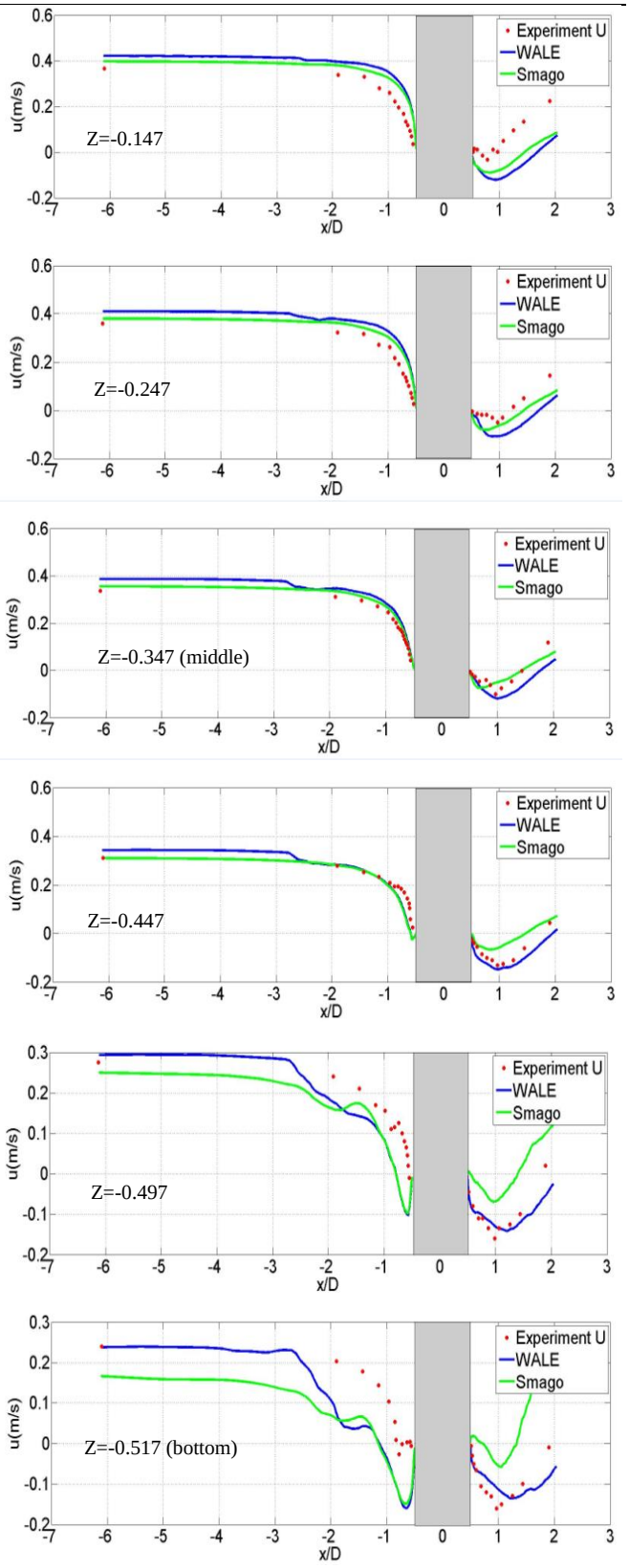


Figure 3. Mean horizontal velocity in the plane of symmetry at different distances from the bed obtained by both turbulence models.

To further illustrate the velocity distribution around the circular cylinder, instantaneous velocities are averaged over 10,000 time steps after ensuring flow development. Time-averaged horizontal velocity at different levels above the bed over the stream-wise centre plan of symmetry (the red broken line in Fig. 2) are compared with experimental data for one of the Roulund et al [3] experimental condition in Fig. 3. The red dots denote the experimental data obtained by Roulund et al. [3]. The blue and green curves represent the numerical results obtained using the Smagorinsky model and the WALE model respectively. Generally, both turbulence models show good agreement comparing with the experiment data. Although a slight over-prediction is found at levels close to the surface (z=-0.047 m and -0.147 m), the velocities at bottom levels are under-estimated by the numerical models. In the wake part, all the results show flow recovery, however the WALE model show better agreements at Z= -0.447m, -0.497m and -0.517m (which are close to the bottom) than the Smagorinsky model.

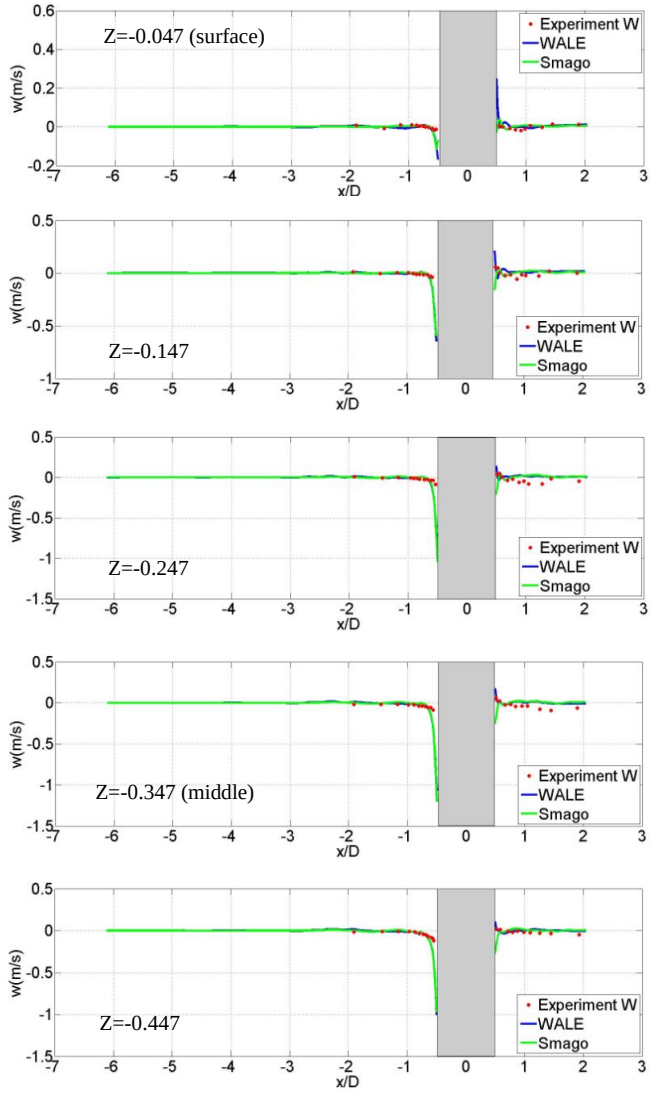


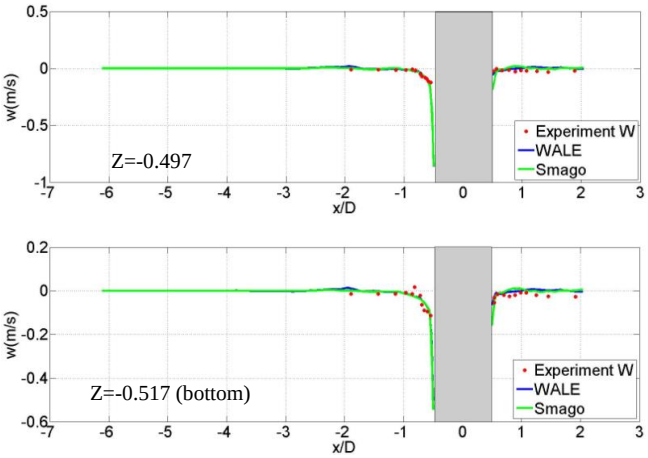


Figure 4. Mean vertical velocity in the plane of symmetry at different distances from the bed obtained by both turbulence models.

Figure 4 compares the averaged vertical velocity along the centre line at different levels. It is clear that, the vertical velocity profiles obtained by both the Smagorinsky model and the WALE model show very good agreement comparing with the experimental data. Small deviations are only found in the wake part which is very close to the cylinder wall and water surface. The Smagorinsky model shows negative velocities in this area, however positive velocities are obtained by the WALE model.

## IV. CASE II: FLOW IN A U-SHAPE BEND CHANNEL

To further investigate the capability of the two turbulence models, the flow in a U-shaped bend channel is simulated. Numerical results are benchmarked with flow measurements in a curved rectangular channel made by H.J. de Vriend 1979 [4].

### *A. Model Step*

The simulation domain of numerical model (shown in Fig. 5) matches the experiment of H.J. de Vriend [4]. The test flume is composed of two straight channels and one curved channel. The whole channel maintains a uniform width of 1.7 m. The inner radius of the curved channel is 0.34 m and its outer radius is 0.51 m. In De Vriend's experiment, both straight channels connecting with inlet and outlet are 6 meters long. However in the numerical model, the straight channel at outlet side is extended to 56 meters to reduce the impact of the outlet boundary setting.

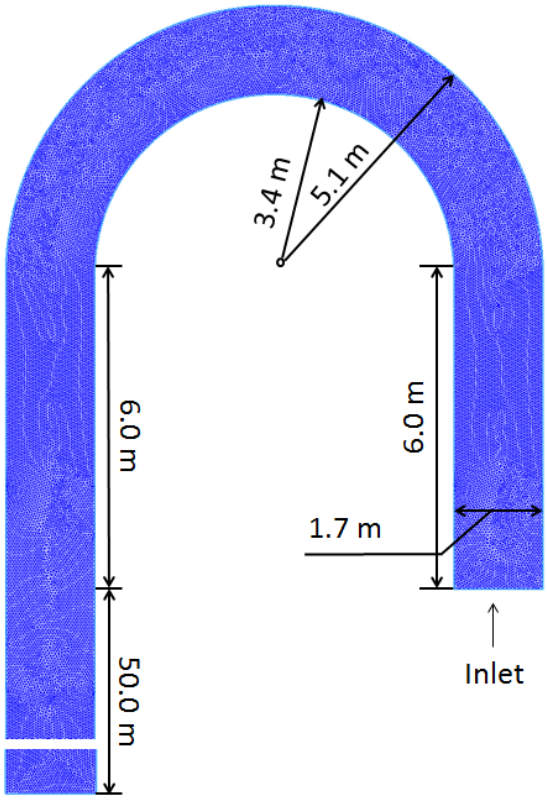


Figure 5. The geometry of U-shaped bend Channel.

The computational mesh was generated by software Bluekenue containing 117,664 elements in 2-D. Thirty non-equally distributed layers are used in the vertical direction.

For the boundary conditions, a constant flow rate of 0.184m/s at inlet boundary is specified and a prescribed water elevation of 0.18m is given at outlet. The walls of the flume are set as solid walls.

*B. Results*

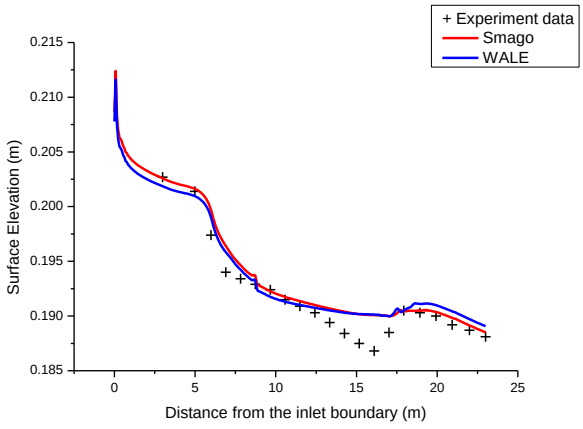


Figure 6. Comparsion between measured surface elevation and numerical results along channel at the inner bank.

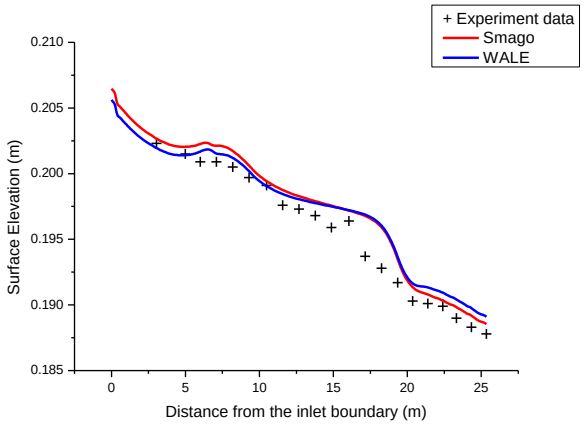


Figure 7. Comparsion between measured surface elevation and numerical results along channel at the centre.

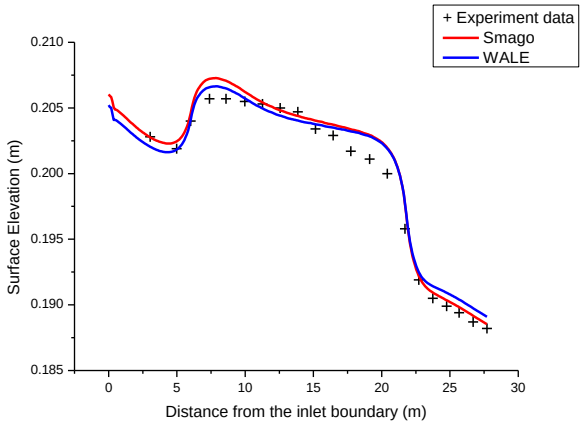


Figure 8. Comparsion between measured surface elevation and numerical results along channel at the outer bank..

Figures 6, 7 and 8 compare measured free surface elevations with numerical results along the channel at the inner bank, the centre and the outer bank respectively. Experiment data are represented by '+' and the numerical results obtained by the constant Smagorinsky model and the WALE model are displayed by red and blue curves respectively. According to the figures, free surface elevations show decrease trends from the inlet boundary to the outlet boundary throughout the channel. However a small increase can be found at the beginning of the curved channel at the centre and outer bank.

Comparing with two numerical results, all three figures show a similar feature: the free surface elevation obtained by WALE model is slightly lower than that of the constant Smagorinsky model at the inlet straight channel (0 m-6 m downstream the inlet) and first half of the curved channel (6 m -12.5 m downstream the inlet). Although both models

show similar results at the second half of the curved channel (12.5 m – 18 m downstream the inlet), small differences are still found at the outlet part. The surface elevation obtained by the constant Smagorinsky model is lower than that of the WALE model at 18 m-25 m downstream the inlet.

According to the comparison between numerical results and experiment data, the WALE model has a better representation of the surface elevation than the constant Smagorinsky model at the first half of the test channel (0 m-12.5 m downstream the inlet). Over-predicted surface elevation is found at 12 m – 18 m downstream the inlet by both two models, however it thes difference at outer bank is smaller than that at inner bank. At the outlet part (18 m-25 m downstream the inlet), both Smagorinsky and WALE models show good agreement. Lower surface elevation obtained by the constant Smagorinsky model matches experiment better.

## V. CONCLUSIONS – FUTURE WORK

In this study, the behaviour of two turbulence models including the constant Smagorinsky model and the WALE model is investigated against two laboratory scale cases: the flow around a circular cylinder and the flow in a U-shape bend channel. In the circular cylinder test case, good agreement is observed for both turbulence models in front of the cylinder. However behind the cylinder, the result of the WALE model is clearly better than that of the constant Smagorinsky model. In the U-shaped bend channel case, the results of the WALE model match experimental data better in the first half of the est channel however the constant Smagorinsky model demonstrates a slightly better agreement at the outlet part.

Generally, the WALE model is a good turbulence model for the type of flows investigated here, according to the results of the benchmarks. Big improvement can be found when simulating complex turbulent flow close to structure walls.

The U-bend channel test case will be investigated further with a focus on the velocity field, to assess both turbulence models.

## ACKNOWLEDGEMENT

The current study is supported by EPSRC and EDF Energy through an iCASE studentship. The technical supports from Computing Services of the University of Liverpool and from the Hartree Centre are also greatly appreciated.

## REFERENCES

[1] The TELEMAC system. http://www.opentelemac.org

[2] Ducros F, Nicoud F, Poinsot T. Wall-adapating local eddy-viscosity models for simulations in complex geometries. In: Baines MJ, editor. ICFD; 1998. p. 293–300.

[3] Roulund, A., Sumer, B.M., Fredsøe, J., Michelsen, J. “Numerical and experimental investigation of flow and scour around a circular pile,” Journal of Fluid Mechanics, 534, 2005, pp. 351-40

[4] D. J. De Vriend, “Flow measurements in a Curved Rectangular Channel”, Laboratory of Fluid Mechanics, Department of Civil Engineering, Delft University of Technology, Internal Report No. 9-79, 1979

[5] Hervouet J-M.. Hydrodynamics of free surface flows: modelling with the finite element method, Wiley. 2007

[6] Smagorinski, J., “General circulation experiments with the primitive equations”. I. The basic experiment. Monthly Weather Review, 91,99-164

# Simulation of the flow around a submerged structure using the Immersed Boundary Method

Yue Yin*, Ming Li†, Charles Moulinec‡, David R. Emerson§
*School of Engineering, University of Liverpool
Email: yue.yin@stfc.ac.uk
†School of Engineering,University of Liverpool
Email: mingli@liverpool.ac.uk
‡Science and Technology Facilities Council
Daresbury Laboratory,Warrington, UK
Email: charles.moulinec@stfc.ac.uk
§Science and Technology Facilities Council
Daresbury Laboratory,Warrington, UK
Email:david.emerson@stfc.ac.uk

***Abstract*—In the current version of TELEMAC3D (7.0+), triangular 2-D unstructured body-fitted meshes are used to represent the computational domain as for example river banks or coastal lines. However due to the sigma mesh transformation in the vertical direction, flows around submerged obstacles with vertical walls can not be easily handled. In this study, the Immersed Boundary method is implemented to represent the obstacles in the water. The principle of the Immersed Boundary method is to simulate the flow around structures by applying forces which impede the flow along the solid boundaries. The numerical results are benchmarked with two laboratory scale cases, including the flow around a circular cylinder [12] and the flow over a submerged structure [8].**

## I. Introduction

TELEMAC has been widely used to simulate river and maritime hydraulics. In the current version of the TELEMAC system (7.0+), and more specifically TELEMAC3D, triangular 2-D unstructured body-fitted meshes are used to represent the computational domain as for example river banks or coastal lines. However due to the sigma mesh transformation in the vertical direction, flows around submerged obstacles with vertical walls can not be easily handled.

The strategy based on triangular elements to mesh the bottom of the field, and using layers of triangle elements to simulate 3-D flows is a clear limitation to tackle flows around submerged obstacles, as each water column contains the same number of prisms. It is then possible to generate a mesh around obstacles such as island or bridge piles which go through the free surface, but not around submerged structures, for instance. In order to account for obstacles in water, an Immersed Boundary (IB) method has been used. The principle of the Immersed Boundary method is to simulate the flow around structures by applying forces which impede the flow along the solid boundaries. An additional IB force, which is to replace the actual reaction force on the solid surface, is applied in the momentum equations of the Navier-Stokes equations.

The IB method was firstly introduced by Peskin [9] in 1973 to simulate the blood flow in the heart. This approach was used to model elastic capillary and artery walls. Nowadays, a variety of approaches have been developed to simulate fluid-structure interaction (FSI) problems, for instance. The IB method used by Peskin [9] is a classic IB method in which IB forces are represented by appropriate constitutive laws depending on the realistic force condition. This approach is more suitable for the simulation of elastic boundaries as the spring feature of the boundary can be introduced by Hook's law. For a rigid boundary, the immersed boundary can be represented by a direct forcing method [4], [7]. The idea of this approach is to calculate the IB force based on the temporally discretised momentum equations. To incorporate direct forcing in the original diffused interface IB method, the quantities on the background and immersed boundary meshes can be materialised by employing discrete delta functions in the classical formulation.
Another commonly used IB method is the cut-cell method. In this approach, the mesh cells are cut at the interface to fit the immersed boundary. The fluxes across the faces of the cut-cells are reconstructed from the surrounding regular cells and immersed boundaries [3]. Due to the difficulty managing of the topology of the cut-cells (for instance, after cutting a rectangle cell, the shape of the remaining cell can be either a pentagon, a quadrangle or a triangle), this approach is easier to be used in 2-D [5], [13], [14] than in 3-D [1], [10].

In this study a direct forcing IB method has been developed and implemented in TELEMAC3D to simulate the structures submerged in the water. The 2-D mesh is generated in a way that the footprint of the obstacle on the bottom is accounted for. This allows to avoid adding extra interpolations when computing fluxes, for instance. The numerical results are compared with two laboratory scales experiment including the flow around a circular cylinder [12] and the flow over a submerged cylinder [8].

## II. Numerical model

### A. Governing equations

In this study, TELEMAC3D is used to simulate the flow impact on a full cylinder and a submerged cylinder respectively. TELEMAC3D is a three-dimensional computational

code which solves the 3-D Navier-Stokes equations using the Boussinesq approximation. The 3-D Navier-Stokes equations read:

$$\frac{\partial u_1}{\partial x_1} + \frac{\partial u_2}{\partial x_2} + \frac{\partial u_3}{\partial x_3} = 0 \tag{1}$$

$$\frac{\partial u_1}{\partial t} + u_1\frac{\partial u_1}{\partial x_1} + u_2\frac{\partial u_1}{\partial x_2} + u_3\frac{\partial u_1}{\partial x_3} = -\frac{1}{\rho}\frac{\partial p}{\partial x_1} + \nu\left(\frac{\partial^2 u_1}{\partial x_1^2} + \frac{\partial^2 u_1}{\partial x_2^2} + \frac{\partial^2 u_1}{\partial x_3^2}\right) + F_{x_1} \tag{2}$$

$$\frac{\partial u_2}{\partial t} + u_1\frac{\partial u_2}{\partial x_1} + u_2\frac{\partial u_2}{\partial x_2} + u_3\frac{\partial u_2}{\partial x_3} = -\frac{1}{\rho}\frac{\partial p}{\partial x_2} + \nu\left(\frac{\partial^2 u_2}{\partial x_1^2} + \frac{\partial^2 u_2}{\partial x_2^2} + \frac{\partial^2 u_2}{\partial x_3^2}\right) + F_{x_2} \tag{3}$$

$$\frac{\partial u_1}{\partial t} + u_2\frac{\partial u_3}{\partial x_1} + u_2\frac{\partial u_3}{\partial x_2} + u_3\frac{\partial u_3}{\partial x_3} = -\frac{1}{\rho}\frac{\partial p}{\partial x_3} - g + \nu\left(\frac{\partial^2 u_3}{\partial x_1^2} + \frac{\partial^2 u_3}{\partial x_2^2} + \frac{\partial^2 u_3}{\partial x_3^2}\right) + F_{x_3} \tag{4}$$

where $(x_1, x_2, x_3)$ are the Cartesian coordinates, $(u_1, u_2, u_3)$ is the velocity vector, $t$ the time, $\nu$ is the dynamic viscosity, $p$ is pressure, $g$ is the gravity constant, $(F_{x_1}, F_{x_2}, F_{x_3})$ a potential extra force (it could be the wind, the Coriolis force, or an IB force for instance).

The pressure term is divided into hydrostatic pressure $p_h$ and dynamic pressure $p_d$. The hydrostatic pressure is defined by the following equation:

$$p_h = p_{atm} + \rho_0 g(\eta - x_3) + \rho_0 g \int_{x_3}^{\eta} \frac{\Delta\rho}{\rho_0} dx_3 \tag{5}$$

where $\rho_0$ and $\Delta\rho$ are reference density (1,024kg/m3) and variation of density respectively; $p_{atm}$ is the atmospheric pressure, $\eta$ is the water surface elevation.

The dynamic pressure $p_d$ is solved by Chorin and Teman projection scheme [2].

TELEMAC3D supports both hydrostatic and non-hydrostatic options. In the hydrostatic version, the pressure is only related to the water depth, i.e. Eqs. (1) (2) (3) (5) are solved. In the non-hydrostatic version, the full Navier-Stokes equations (Eqs. (1) (2) (3) (4)) with both hydrostatic pressure $p_h$ and dynamic pressure $p_d$ are solved.

In this study, the hydrostatic version is used to simulate the flow past a full cylinder and the non-hydrostatic version is used to simulate the flow past a submerged cylinder.

### *B. Immersed boundary condition*

The Immersed Boundary method used here corresponds to a direct forcing method which relies on forces applied to some nodes of the mesh, which impedes the flow along the solid boundaries. The additional IB force replaces the actual reaction force on the solid surface and is activated by using source terms in the momentum equations of the Navier-Stokes equations. The forcing step is added in the pressure-continuity step which is the last step of solving the moment equations.

The forcing step in the current modified model can be represented as:

$$\frac{u_1^{n+1} - u_1^c}{\Delta t} = -g(\frac{\partial \eta}{\partial x_1}) + \nu\left(\frac{\partial^2 u_1}{\partial x_1^2} + \frac{\partial^2 u_1}{\partial x_2^2} + \frac{\partial^2 u_1}{\partial x_3^2}\right) + F_{x_1} \tag{6}$$

$$\frac{u_2^{n+1} - u_2^c}{\Delta t} = -g(\frac{\partial \eta}{\partial x_2}) + \nu\left(\frac{\partial^2 u_2}{\partial x_1^2} + \frac{\partial^2 u_2}{\partial x_2^2} + \frac{\partial^2 u_2}{\partial x_3^2}\right) + F_{x_2} \tag{7}$$

where $u_i^c$ are the velocity components obtained from previous advection step of calculation and $F_{x_i}$ contains the buoyancy terms

Following [6], the force terms are obtained by rearranging Eqs.[6] and Eqs.[7] and substituting $u_1^{n+1}$, $u_2^{n+1}$, $u_3^{n+1}$ with the desired velocity at the solid node. By applying non-slip boundary conditions on the solid surface, the IB force terms are defined as:

$$f_{x_1}^{ibm} = \begin{cases} \dfrac{0 - u_1^c}{\Delta t} + g(\dfrac{\partial \eta}{\partial x_1}) \\ -\nu\left(\frac{\partial^2 u_1}{\partial x_1^2} + \frac{\partial^2 u_1}{\partial x_2^2} + \frac{\partial^2 u_1}{\partial x_3^2}\right) - F_{x_1} \text{ , on the boundary node} \\ 0 \text{ , elsewhere} \end{cases}$$

$$f_{x_2}^{ibm} = \begin{cases} \dfrac{0 - u_2^c}{\Delta t} + g(\dfrac{\partial \eta}{\partial x_2}) \\ -\nu\left(\frac{\partial^2 u_2}{\partial x_1^2} + \frac{\partial^2 u_2}{\partial x_2^2} + \frac{\partial^2 u_2}{\partial x_3^2}\right) - F_{x_2} \text{ , on the boundary node} \\ 0 \text{ , elsewhere} \end{cases}$$

TELEMAC3D uses the finite element method for the equation discretisation. The value of one node relies on the values of the surrounding nodes. Therefore, although the velocities on the IB nodes can be set to zero by applying the additional force (this is because of the assumption that the boundary of an obstacle is accounted for during meshing), small velocity fluctuations can still be observed inside the obstacle. In order to keep the model stable, a zero velocity condition is applied on all the nodes inside of the obstacle at each time-step. When dealing with submerged structures in the water, the vertical zero velocity condition is used at all Immersed Boundary nodes.

### *C. Turbulence modelling*

In order to simulate more accurately the turbulence impact of a structure, focusing mainly on the wake, a two-eddy viscosity LES turbulence model was implemented by considering horizontal and vertical characteristic length-scales separately [11].

The two-eddy LES turbulence model shares similar ideas as the Smagorinsky model, but using different length-scales in the horizontal and vertical directions respectively. This approach is more suitable for highly anisotropic filtering cells rather than using a single characteristic length-scale. Two turbulence viscosities $\nu_{t,h}$ and $\nu_{t,v}$ are commonly used in geophysical fluid dynamics, with $h$ and $v$ representing the horizontal and the vertical components respectively. The diffusive term for the Navier-Stokes equations is calculated as:

$$D_i = \frac{\partial}{\partial x_1}\left(\nu_h \frac{\partial u_i}{\partial x_1}\right) + \frac{\partial}{\partial x_2}\left(\nu_v \frac{\partial u_i}{\partial x_2}\right) + \frac{\partial}{\partial x_3}\left(\nu_h \frac{\partial u_i}{\partial x_3}\right) \quad (8)$$

where $\nu_h = \nu + \nu_{t,h}$ and $\nu_v = \nu + \nu_{t,v}$, and $\nu$ is the water viscosity. Adopting the two-eddy LES model to reproduce the sub-grid stress through a Smagorinsky model gives:

$$\nu_{t,h} = (C_h L_h)^2 |S_h| \quad (9)$$

$$\nu_{t,v} = (C_v L_v)^2 |S_v| \quad (10)$$

where $C_h$ and $C_v$ are the coefficients of the model and $L_h$ and $L_v$ are 2 length-scales for the horizontal and vertical directions respectively. Here $L_h$ and $L_v$ are computed as:

$$L_h = \sqrt{\Delta_{x_1}^2 + \Delta_{x_2}^2} \quad (11)$$

$$L_v = \Delta_{x_3} \quad (12)$$

$\Delta_{x3}$ is obtained by calculating the vertical distance between two nodes. Because in the current code, the element volumes have been considered as the integral of test functions on the domain, $L_h$ can be easily obtained by using an approximate value of $L_h = \sqrt{Volume/\Delta_{x3}}$

The strain rates tensor $|S_h|$ and $|S_v|$ are decomposed as:

$$|S_h| = \sqrt{2S_{11}^2 + 2S_{33}^2 + 2S_{13}^2} \quad (13)$$

$$|S_v| = \sqrt{2S_{12}^2 + 2S_{22}^2 + 2S_{23}^2} \quad (14)$$

where $S_{ij}$ is calculated by the Einstein summation convention, reading as:

$$S_{ij} = \frac{1}{2}\left(\frac{\partial u_i}{\partial x_j} + \frac{\partial u_j}{\partial x_i}\right) \quad (15)$$

The coefficients of the model need calibration and this is still an open issue because of the lack of large range of available test cases. In this study, $C_h$ and $C_v$ are set to 0.005 and 0.25 respectively which is similar to the recommended value in [11].

## III. CASE I: FLOW PAST A FULL CYLINDER

Firstly, a laboratory experiment (see Roulund [12]) is used to validate the implementation of the IB method. The numerical model is built to simulate the flow past a full cylinder in a flume.

### A. Computational domain and mesh

Following Roulund's experiment [12], the simulation domain is set to be 50 m long by 4 m wide. The bed is assumed to be flat with a constant depth of 0.54 m. A cylinder with a diameter of 0.53 m (D) is placed at 13 m downstream the inlet as in figure 1.

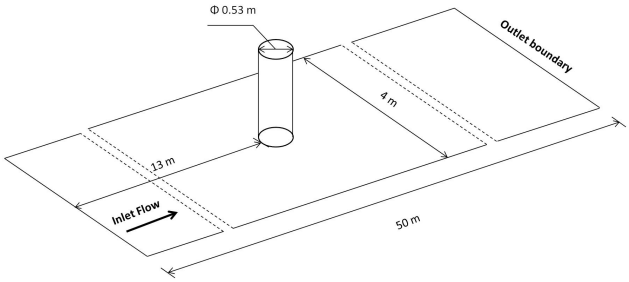


Fig. 1: Geometry of the computed domain

The area containing the cylinder and the wake part are refined. The mesh of the simulation domain contains 48,764 elements in 2-D and has 50 evenly distributed horizontal layers. As shown in figure 2, the hollow mesh is not used to represent the cylinder directly, however the boundary nodes of cylinder are marked as immersed boundary nodes which can be seen clearly (the boundary between blue mesh and red mesh is the immersed boundary).

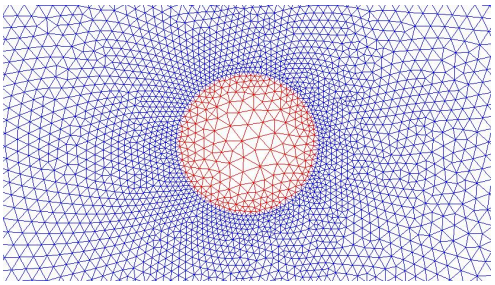

Fig. 2: Geometry of the computed domain with the immersed boundary

### B. Model setup

Table I summrises the test conditions for the cylinder case. The smooth bed condtion from the experiment of [12] is used for the model testing.

In the table, $Re$ is the Reynolds number based on the pile diameter,

$$Re = \frac{UD}{\nu} \quad (16)$$

| Test | Flow past full cylinder |
|---|---|
| Bed | Rigid |
| Smooth bed/rough bed | Smooth |
| Water depth $h$ (m) | 0.54 |
| Mean Flow velocity $U(ms^{-1})$ | 0.326 |
| Pile diameter $D(m)$ | 0.53 |
| Re Number | $1.7 \times 10^5$ |
| Fr Number | 0.14 |

TABLE I: Test conditions for the numerical modelling

where $U$ is the mean flow velocity and $D$ is the diameter of the cylinder. Also in the table, $Fr$ is the Froude number defined by

$$Fr = \frac{U}{\sqrt{gh}} \tag{17}$$

in which $h$ is the water depth.

A time step of 0.01s is chosen to keep the maximum Courant below 0.8. The Courant number is defined as:

$$C = U\frac{\Delta t}{\Delta x} \tag{18}$$

where $U$ is the depth-mean flow velocity and $\Delta x$ is a given mesh size.

### C. Results

The numerical model was run for 30 minutes and the last 100 seconds of the instantaneous results were collected for analysis and comparison.

The instantaneous horizontal flow distributions obtained from the numerical model are illustrated in figure 3. Three figures show the velocity profile at the surface, middle and bottom layer respectively. The oscillating flow due to the cylinder obstacle can be seen clearly in the surface and middle layers. All the figures show slow velocity regions in front of and behind the cylinder. A dramatic acceleration is also observed at each side of the cylinder. At the bottom layer, rather than the long oscillating wake, an accelerated velocity at the sides of the cylinder plays a more significant role in the flow structure.

In the further investigation of the horizontal flow distribution, the averaged horizontal velocity magnitude is calculated by averaging 100 instantaneous data. The result is represented in figure 4

As shown in this figure, the velocities inside the cylinder are kept to zero. The streamlines indicate the route of the flow past the cylinder. Under the effect of the immersed boundary forces which are applied on the cylinder boundary nodes, the upstream flow splits in front of the cylinder and then accelerates at each side. After stream detaching the cylinder, a pair of symmetric vortices is clearly found behind the cylinder.

The unsteady flow state is shown in figure 5 which covers a full vortex shedding period. From these figures, the unsteady behaviour of the wake is evident. The flow route is represented by both vectors and streamlines. The shedding of the vortices from the two sides of cylinder is clearly present.

Quantitatively, the numerical results obtained using the immersed boundary method are benchmarked with Roulund's

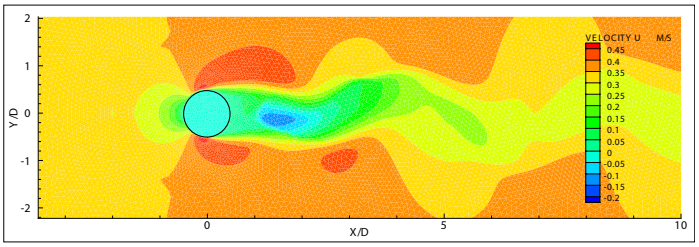


a: Surface

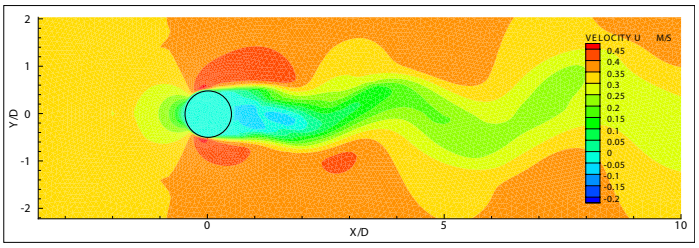


b: Z=-0.27m

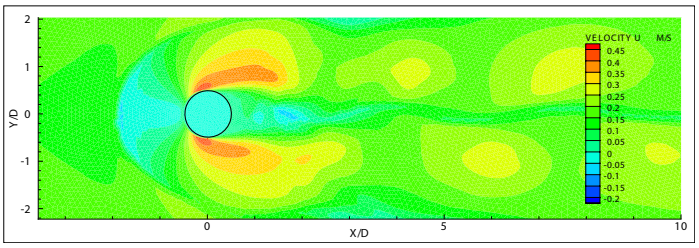


c: Bottom

Fig. 3: Horizontal velocity distribution at different layers

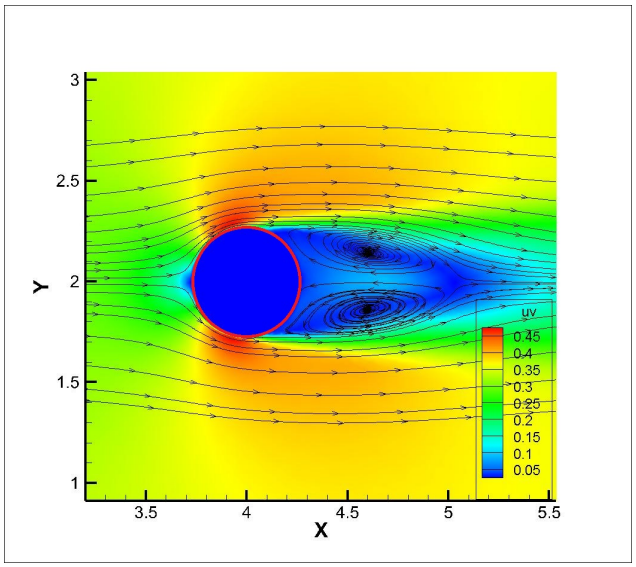


Fig. 4: Averaged horizontal velocity magnitude and streamlines at Z = -0.27 m

experiment [12]. Comparison results are shown in figures 6, 7:

The averaged horizontal and vertical velocities at layer Z=-0.34m are presented in the aforementioned figures. Experimen-

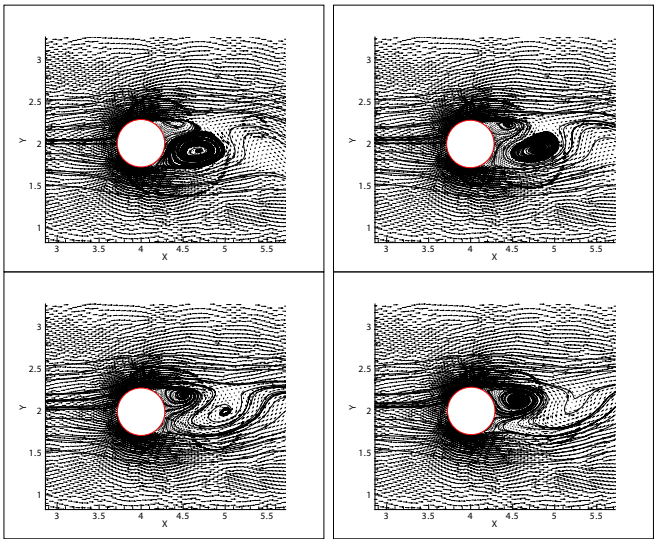

Fig. 5: Horizontal velocity vectors and streamlines for the unsteady flow simulation during one period of vortex shedding. Horizontal cross-section at z = -0.27 m

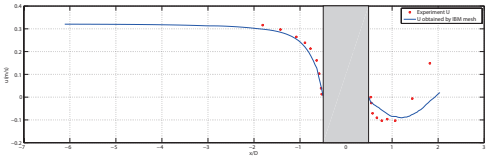

Fig. 6: Mean horizontal velocity at Z = -0.34m. Smooth rigid bed

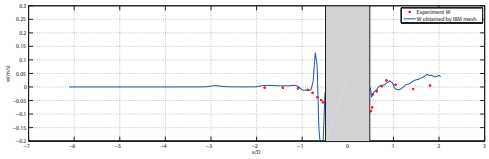

Fig. 7: Mean vertical velocity at Z = -0.34m. Smooth rigid bed

tal data and numerical model results are illustrated by red dots and blue curves respectively. The horizontal velocity distribution shows very good agreement between numerical model and experiment in front of the cylinder. The upstream flow reduces from about 0.32 $ms^{-1}$ to approximately 0 $ms^{-1}$ in front of the cylinder wall. Behind the cylinder, both experimental data and numerical model show a recovery flow, however the distance for recovery is slightly over-predicted by the numerical model. The vertical velocities obtained using the numerical model agree with the experiment measurement both in front of and behind the cylinder except for a big spike found in front of the cylinder. This spike is due to the water surface elevation raising in front of cylinder.

A comparison between the numerical results obtained by the immersed boundary condition and hollow mesh is presented in figure 8.The mean horizontal velocity obtained from the immersed boundary test and hollow mesh test are represented by a red line and a black line respectively. As shown in this figure, both IB test and hollow mesh test show the same result in front of the cylinder, although a small difference is found in the wake region. Between 0.5 D to about 18 D, the flow obtained by the immersed boundary test exhibits a faster recovery, however from 18D downstream on, the velocity predicted by the hollow mesh test is higher than the one of the IB test.

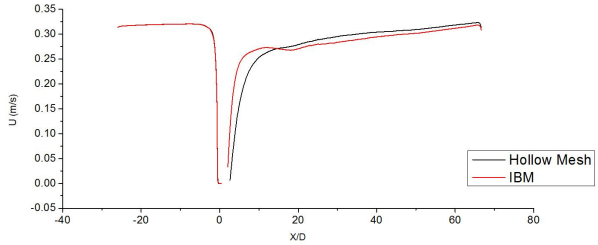


Fig. 8: Mean horizontal velocity along the center line at the layer of Z = -0.27

## IV. CASE II: FLOW PAST A SUBMERGED CYLINDER (WITH FINITE HEIGHT)

In the second test case, the immersed boundary method is used to simulate the flow around a finite height cylinder. Following Palau-Salvador's experiment [8], cylinders with h=0.2 m height and two different diameters (0.040 m and 0.080 m respectively) are computed using the immersed boundary method.

### A. *Computational domain and mesh*

Palau-Salvador's experiment [8] was performed in a tank with a constant water level of 3 meter and this water depth was also used in the numerical models. As shown in figure 9, the width and length of the numerical model was set to 4 $h$ (0.8 m) and 13 $h$ (2.6 m) respectively. The cylinder was placed at 3 $h$ (0.6 m) downstream the inlet.

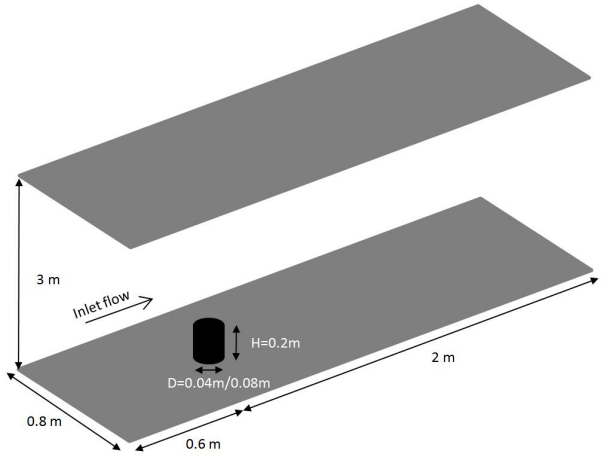


Fig. 9: Computational domain of the flow passing a finite height cylinder

| Test | 1 | 2 |
|---|---|---|
| Bed condition | Smooth Rigid | Smooth Rigid |
| Water depth $h$ (m) | 3 | 3 |
| Mean Flow velocity $U(ms^{-1})$ | 0.54 | 0.54 |
| Pile diameter $D(m)$ | 0.04 | 0.08 |
| Re Number | $2.2 \times 10^4$ | $4.4 \times 10^4$ |

TABLE II: Test conditions for the numerical modelling

In total, the mesh of the numerical model contains 37,372 elements in 2-D and 50 layers in the vertical direction. Similar to the mesh used in case I, there are 100 nodes located on the cylinder boundaries. The mesh around the cylinder is refined. In the vertical direction, as shown in figure 10, the height of the first 30 layers from the bottom are fixed, thus the cylinder can maintain a constant height during the simulation.


Fig. 10: Snapshot of the vertical mesh used in the numerical model of the flow passing a finite height cylinder

### B. Model setup

The key parameters of the numerical model are summarised in table II.

A constant flow velocity of 0.54 $ms^{-1}$ is set at the inlet boundary. The Reynolds number based on the pile diameter is $2.2 \times 10^4$ and $4.4 \times 10^4$ for both cylinders respectively. The time step equal to 0.001 s is chosen to keep the maximum Courant number below 0.6.

### C. Results

The horizontal velocity distributions at the layer of $x_3 = h/2$ are illustrated in figure 11 and figure 12. The numerical results obtained from the 0.04 m diameter cylinder case and 0.08 m diameter cylinder case show similar pattern that the flow reduces speed in front of the cylinder and then recovers behind it. Streamlines in figures indicate that the upstream flow is separated by the structure and then pushed to the side of cylinder. After the flow detaches from the cylinder wall, small vortices are generated in the wake area. Comparing to the instantaneous pictures of Palau-Salvador's experiment, the width of the wake tail in the numerical results is slightly over-predicted.

The horizontal velocity distributions in the vertical cross-section along the centre line is shown in figure 13 . The numerical results show that the flow accelerates at the top of the cylinder and a deceleration is observed in the wake part. The vertical vortex behind the cylinder is seen clearly both in

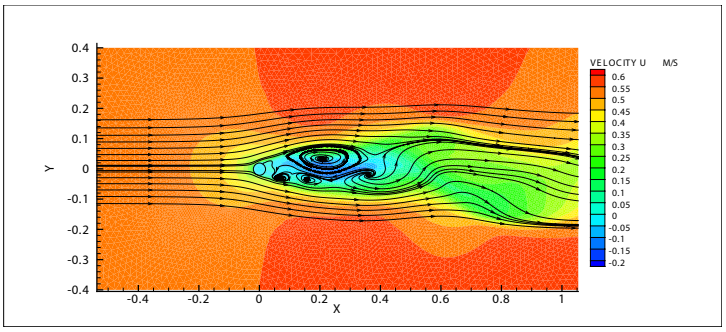


a: numerical model

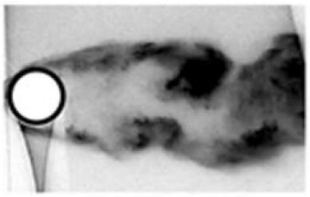

b: Experiment

Fig. 11: Horizontal velocity distribution at layer of $h/2$ of the cylinder d= 0.04m. (a)Numerical results. (b)Instantaneous pictures of Palau-Salvador's experiment [8]

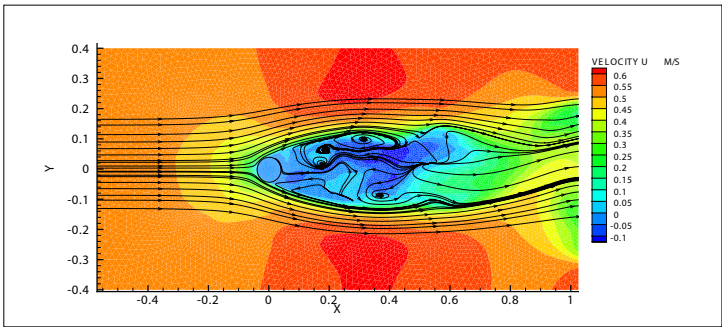


a: numerical model

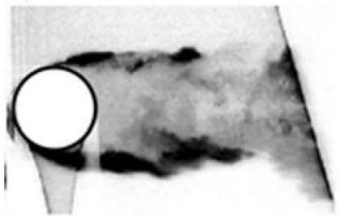

b: Experiment

Fig. 12: Horizontal velocity distribution at layer of $h/2$ of the cylinder d= 0.08m. (a)Numerical results. (b)Instantaneous pictures of Palau-Salvador's experiment [8]

the 0.04 m diameter cylinder case and 0.08 m diameter cylinder case. However in the figure of the 0.04m diameter cylinder result, the horizontal velocity colour bands indicate that there is a strong velocity fluctuation in front of the cylinder. The

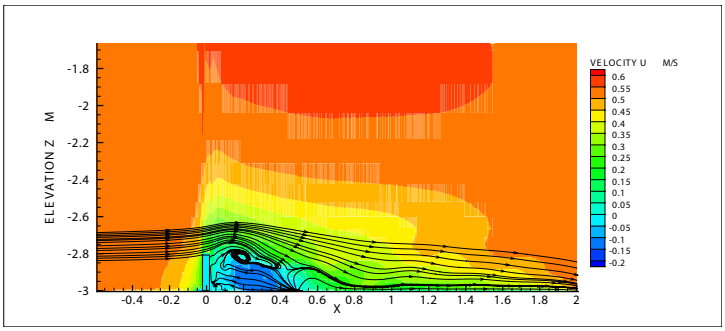


a: D=0.04m

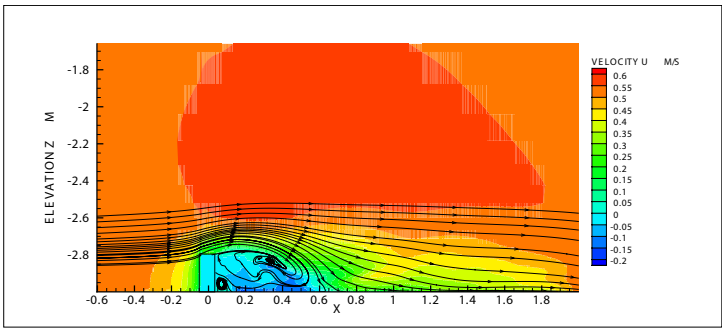


b: D=0.08m

Fig. 13: Horizontal velocity distribution along the center line in the vertical cross-section view.

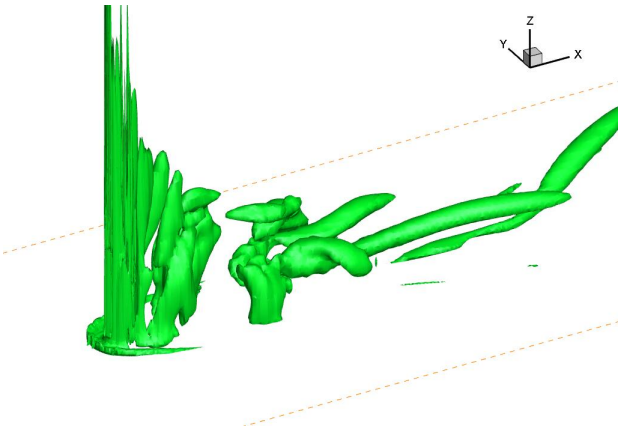


a: D=0.04m

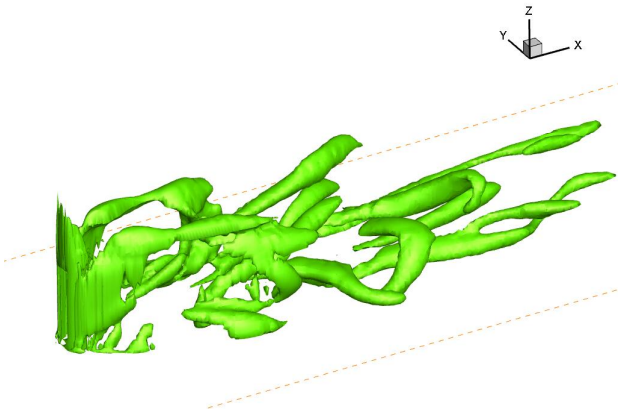


b: D=0.08m

Fig. 14: Horizontal velocity distribution along the center line in the vertical cross-section view

reason of this impact is not clearly understood at the moment. Due to the same configuration used in both cylinder cases, this velocity fluctuation may come from the quality of the mesh used in the 0.04 m diameter cylinder case.

Figure 14 shows the Q-criterion to visualise the vortex structure obtained by both simulations. Q is the second scalar invariant of the velocity derivative tensor and has been widely used for vortex visualisation. The spike shown in Fig. 14 (a) proves the founding in Figure 13(a) that there is a strong velocity fluctuation in front of the cylinder. Exept this unknown phenomenon, the vortex structures including horseshoe vortex at the bottom in front of the cylinder, tip vortex above the cylinder and trailling vortex behind the cylinder are represented clearly in the simulations. Because the larger cylinder diameter case shows an increased Reynolds number based on the diameter, more vortices can be found in the result of the 0.08 m diameter cylinder case.

## V. Conclusions - Perspectives

In this study, the Immersed Boundary method is implemented and applied to TELEMAC3D. Two laboratory scale cases including the flow passing a full cylinder and the flow passing a finite-height cylinder are simulated. In the full cylinder case, both instantaneous velocity profiles and mean velocity profiles are fairly well captured by the numerical model. In the finite-height cylinder test case, the general flow feature can be captured by the numerical model. The vortex structures can be seen clearly in the results.

Generally, it is possible to couple the Immersed boundary method with TELEMAC3D to represent structures in the simulation. When dealing with an obstacle going from the bottom though the surface of the water, the immersed boundary method offers good accuracy in the prediction of surrounding flow structures. For the submerged obstacles, they can be simulated by TELEMAC3D by implementing immersed boundary method. Although the accuracy is limited currently, the result of the qualitative analysis can be still obtained from the numerical model.

In future works, the immersed boundary method used for submerged structure simulation will be further investigated. Not only qualitative analysis but also quantitative analysis will be done by benchmarking numerical results with laboratory measurement data.

## Acknowledgment

The current study is supported by EPSRC and EDF Energy through an iCASE studentship. The technical supports from Computing Services of the University of Liverpool and from the Hartree Centre are also greatly appreciated.

## VI. References

### References


[1] A. S. Almgren, J. B. Bell, P. Colella, and T. Marthaler, "A cartesian grid projection method for the incompressible euler equations in complex geometries," *SIAM Journal on Scientific Computing*, vol. 18, no. 5, pp. 1289–1309, 1997.

[2] A. J. Chorin, "Numerical solution of the navier-stokes equations," *Mathematics of computation*, vol. 22, no. 104, pp. 745–762, 1968.

[3] D. K. Clarke, H. Hassan, and M. Salas, "Euler calculations for multi-element airfoils using cartesian grids," *AIAA journal*, vol. 24, no. 3, pp. 353–358, 1986.

[4] E. Fadlun, R. Verzicco, P. Orlandi, and J. Mohd-Yusof, "Combined immersed-boundary finite-difference methods for three-dimensional complex flow simulations," *Journal of computational physics*, vol. 161, no. 1, pp. 35–60, 2000.

[5] X. Hu, B. Khoo, N. A. Adams, and F. Huang, "A conservative interface method for compressible flows," *Journal of Computational Physics*, vol. 219, no. 2, pp. 553–578, 2006.

[6] J. Kim, D. Kim, and H. Choi, "An immersed-boundary finite-volume method for simulations of flow in complex geometries," *Journal of Computational Physics*, vol. 171, no. 1, pp. 132–150, 2001.

[7] J. Mohd-Yusof, "Combined immersed-boundary/b-spline methods for simulations of ow in complex geometries," *Annual Research Briefs. NASA Ames Research Center= Stanford University Center of Turbulence Research: Stanford*, pp. 317–327, 1997.

[8] G. Palau-Salvador, T. Stoesser, J. Fröhlich, M. Kappler, and W. Rodi, "Large eddy simulations and experiments of flow around finite-height cylinders," *Flow, turbulence and combustion*, vol. 84, no. 2, pp. 239–275, 2010.

[9] C. S. Peskin, "Flow patterns around heart valves: a numerical method," *Journal of computational physics*, vol. 10, no. 2, pp. 252–271, 1972.

[10] S. Popinet, "Gerris: a tree-based adaptive solver for the incompressible euler equations in complex geometries," *Journal of Computational Physics*, vol. 190, no. 2, pp. 572–600, 2003.

[11] F. Roman, G. Stipcich, V. Armenio, R. Inghilesi, and S. Corsini, "Large eddy simulation of mixing in coastal areas," *International Journal of Heat and Fluid Flow*, vol. 31, no. 3, pp. 327–341, 2010.

[12] A. Roulund, B. M. Sumer, J. Fredsøe, and J. Michelsen, "Numerical and experimental investigation of flow and scour around a circular pile," *Journal of Fluid Mechanics*, vol. 534, pp. 351–401, 2005.

[13] H. Udaykumar, R. Mittal, and W. Shyy, "Computation of solid–liquid phase fronts in the sharp interface limit on fixed grids," *Journal of computational physics*, vol. 153, no. 2, pp. 535–574, 1999.

[14] H. Udaykumar, W. Shyy, and M. Rao, "Elafint: a mixed eulerian–lagrangian method for fluid flows with complex and moving boundaries," *International journal for numerical methods in fluids*, vol. 22, no. 8, pp. 691–712, 1996.